
A Compton Camera Prototype with γ -PET Imaging Capability: From Component Evaluations to Online Tests

Tim Maximilian Fitzpatrick



München 2022

A Compton Camera Prototype with γ -PET Imaging Capability: From Component Evaluations to Online Tests

Tim Maximilian Fitzpatrick

Dissertation
an der Fakultät für Physik
der Ludwig-Maximilians-Universität
München

vorgelegt von
Tim Maximilian Fitzpatrick
aus Regensburg

München, den 20. Dezember 2021

Erstgutacher/in: Prof. Dr. Peter G. Thirolf
Zweitgutachter/in: Prof. Dr. Otmar Biebel
Tag der mündlichen Prüfung: 22.02.2022

To my mother Helen, my sister Jenny, my grandparents Erika and Günter and my aunt Karin, who have been supporting me my whole life. You have always been and still are my motivation to reach my aims.

To my wife Erin Grace, my love, you gave me the strength to always go on.

Zusammenfassung:

Am Lehrstuhl für Medizinphysik der LMU wird ein szintillator-basierter Compton-Kamera-Prototyp mit SiPM-Auslese zur Reichweitenbestimmung von Ionenstrahlen in der Hadronentherapie (mit der Möglichkeit des Einsatzes im γ -PET-Modus) entwickelt.

Als Compton-Kamera-Streudetektor wird eine GAGG ($\text{Ce:Gd}_3\text{Al}_2\text{Ga}_3\text{O}_{12}$) Szintillatormatrix (16×16 Kristalle; 1.6 mm Abstand (Zentrum-zu-Zentrum)) verwendet. Die relative Energieauflösung dieser Kristallmatrix und die Ortsauflösung wurden in unterschiedlichen Auslesekonfigurationen mit SiPMs ausgiebig untersucht. Durch Vergleiche von SiPM-Modulen unterschiedlicher Hersteller (KETEK und HAMAMATSU) und verschiedener Mikrozellgrößen (15 μm , 25 μm , 35 μm und 50 μm), sowie zwei Arten der Kopplung zwischen Kristall und SiPM (optisches Fett und RTV Silikonschicht), konnte die leistungsfähigste Konfiguration ermittelt werden. In allen Auslesekonfigurationen konnten jeweils alle 256 Kristalle der GAGG Kristallmatrix identifiziert werden, woraus auf eine Ortsauflösung gleich dem Zentrumsabstand der Kristalle von 1.6 mm geschlossen werden kann. Die beste Energieauflösung von $\Delta E/E = 9.5 \%$ bei einer γ -Strahlenergie von 662 keV wurde unter Verwendung von KETEK SiPM-Modulen mit 35 μm Mikrozellgröße erreicht.

Als Compton-Kamera Absorberdetektor wurden monolithische $\text{LaBr}_3\text{:Ce}$ und CeBr_3 Szintillatoren ($51 \times 51 \times 30 \text{ mm}^3$) untersucht. Durch ihre stöchiometrische Ähnlichkeit versprechen beide Materialien eine vergleichbare Leistungsfähigkeit und folglich auch vergleichbare Szintillationseigenschaften (Lichtausbaute, Zerfallszeit, Dichte). Der CeBr_3 -Kristall besitzt jedoch keinen intrinsischen Untergrund, der im $\text{LaBr}_3\text{:Ce}$ vom radioaktiven Isotop ^{138}La verursacht wird.

Ausgelesen mit Multinoden Photoelektronen-Vervielfacher-Röhren (MA-PMT) konnte eine Zeitauflösung von beiden Szintillationsmaterialien von unter 300 ps erreicht werden ($250 \pm 2 \text{ ps}$ [$\text{LaBr}_3\text{:Ce}$] und $281 \pm 3 \text{ ps}$ [CeBr_3]), was die Fähigkeit dieser Detektoren zeigt, durch Flugzeitmessungen prompte γ -Strahlen von Untergrund-Neutronen zu unterscheiden. Die beste Energieauflösung wurde mit einem $\text{LaBr}_3\text{:Ce}$ Kristall, ausgelesen von einer KETEK SiPM-Matrix mit 50 μm SPADs, erreicht. $\Delta E/E = 4.1 \%$ (bei 662 keV) und $\Delta E/E = 1.8 \%$ (bei 6.13 MeV) wurden mit einer ASIC-basierten Signalauslese erreicht. Des Weiteren wurde eine alternative Methode zur Detektorauslese ("Hybrid-Ganging") für monolithische Kristalle entwickelt, die zu einer Verbesserung von ca. 0.5 Prozentpunkte im Vergleich zur ASIC-basierten Auslese geführt hat. In allen durchgeführten Studien war die relative Energieauflösung des CeBr_3 -Kristalls der jeweiligen des $\text{LaBr}_3\text{:Ce}$ Kristalls um 0.8 % bis 2.0 % unterlegen.

Ein erster Compton-Kamera-Prototyp mit monolithischem $\text{LaBr}_3\text{:Ce}$ Absorber und GAGG Szintillatormatrix als Streuer erreichte eine von der genauen Position der radioaktiven Quelle in der Ebene parallel zur Streukomponente (in einer Entfernung

von 50 mm zum Streuer) abhängige Winkelauflösung zwischen 5.4° und 6.2° . Eine Ortsauflösung zwischen 5.2 mm und 5.6 mm konnte demonstriert werden und dabei eine Genauigkeit der Quelllokalisierung von unter einem Millimeter erreicht werden.

Als alternativer Absorberdetektor für einen Compton-Kamera-Prototyp zur Bildgebung von γ -Strahlen mit Energien unterhalb von 1.5 MeV wurde eine dreilagige gepixelte LYSO Kristallmatrix ($0.9 \times 0.9 \times 6.6$ mm³ Kristallvolumen), ausgelesen von KETEK und HAMAMATSU 50 μ m SPAD SiPM-Modulen mit 8×8 Kanälen (3×3 mm² aktive Kanalfläche) und dem PETsys TOFPET v2v ASIC untersucht. Für beide untersuchten SiPM-Matrizen konnten alle einzelnen Kristalle aufgelöst werden. Die relative Energieauflösung wurde für die drei Lagen getrennt untersucht und trotz der starken Abhängigkeit von der jeweiligen Lage konnte ein mittlerer Wert von $\Delta E/E = 19.1$ % und $\Delta E/E = 21.2$ % bei 511 keV, für das KETEK-Modul bzw. das HAMAMATSU-Modul gemessen werden. Eine Koinzidenzzeitauflösung von unter 500 ps (bestimmt für die einzelnen Kristalllagen) wurde gemessen.

Ein zweiter Compton-Kamera-Prototyp wurde mit den GAGG-Matrizen (unter Verwendung eines KETEK SiPM-Moduls mit 25 μ m Mikrozellen) und einem dreilagigen LYSO-Block (unter Verwendung eines HAMAMATSU 50 μ m SPAD SiPM-Moduls). Mit diesem Prototypen konnte mit einer ²²Na Punktquelle in einer Distanz zum Streuer von 50 mm eine Winkelauflösung von 8.2° für Energien von einfallenden Photonen von 1274 keV und eine Ortsauflösung von 6.0 mm und 6.1 mm entlang der x- bzw. y-Achse erreicht werden.

Im Dreifach-Koinzidenz-Modus (durch kombinierte Ereignisse von separat ausgelösten PET und Compton-Ereignissen) konnte mit nur 77 Primäreignissen eine Ortsauflösung von 3.3 mm und 3.9 mm in der PET-Ebene und 12,9 mm in der dritten Dimension erreicht werden, was die daraus folgende Fähigkeit zur vollständigen dreidimensionalen Bildgebung und die hohe Empfindlichkeit des γ -PET-Modus demonstriert.

Mit einem Detektorsystem, das aus vier kreuzförmig angeordneten Compton-Kamera Armen besteht, wurden Messungen an (radioaktiven) Teilchenstrahlen (¹²C and ¹⁶O (stabil); ¹⁰C, ¹¹C and ¹⁵O (radioaktiv)) durchgeführt. Die gute Zeitaufklärung der Kamera konnte verwendet werden, um die zeitliche Struktur des Strahls zu beobachten. Ausserdem konnten prompte γ -Strahlen in Koinzidenzspektren zwischen Streuer und Absorber detektiert werden. Die sehr geringe geometrische Effizienz dieses ersten Prototypen und der hohe strahlinduzierte Untergrund ließen jedoch keine zuverlässige Rekonstruktion des Ionenstrahls durch die Detektion von prompten γ -Strahlen zu.

Abschließend ist zu sagen, dass eine SiPM-basierte Auslese von verschiedenen Compton-Kamera Komponenten und dazugehörige Kamerakonfigurationen als Alternative zu einer konventionellen PMT-basierten Auslese etabliert werden konnte.

Abstract

At the Chair for Medical Physics at LMU a scintillator-based Compton camera prototype is under development with SiPM read out for ion beam range monitoring in hadron therapy (with the capability to be operated in a γ -PET imaging mode).

As Compton camera scatterer detector a GAGG ($\text{Ce:Gd}_3\text{Al}_2\text{Ga}_3\text{O}_{12}$) scintillator array (16×16 crystals; 1.6 mm crystal pitch) was investigated. The relative energy resolution of this crystal array and the spatial resolution were intensively studied in various readout configurations using SiPMs. Comparing SiPM modules from two different vendors (KETEK and HAMAMATSU) and of various microcell sizes (15 μm , 25 μm , 35 μm and 50 μm) as well as two types of crystal-to-SiPM couplings (optical grease and RTV silicon rubber sheet), the best component configuration was found. While in all readout configurations all 256 individual crystals of the GAGG crystal array could be identified from which a spatial resolution equal to the crystal pitch of 1.6 mm was concluded, the best energy resolution of $\Delta E/E = 9.5 \%$ at a γ -ray energy of 662 keV was found using the KETEK 35 μm microcell size SiPM array.

As Compton camera absorber detector monolithic $\text{LaBr}_3\text{:Ce}$ and CeBr_3 scintillator blocks ($51 \times 51 \times 30 \text{ mm}^3$) were under investigation. Both materials promise comparable performance, due to their stoichiometric similarity and therefore scintillation properties (light yield, decay time, density). The CeBr_3 crystal, however, does not suffer from an internal background component due to the abundance of the radioactive isotope ^{138}La in $\text{LaBr}_3\text{:Ce}$.

Read out using multi-anode photomultiplier tubes (MA-PMT), a time resolution of both crystal materials of well below 300 ps was achieved (250 ± 2 ps [$\text{LaBr}_3\text{:Ce}$] and 281 ± 3 ps [CeBr_3]) which demonstrated the capability of these absorber detectors to discriminate prompt γ -rays from neutron background that occurs during ion beam irradiation, by means of time-of-flight (TOF) measurements.

The best energy resolution was measured using the $\text{LaBr}_3\text{:Ce}$ crystal read out by a KETEK SiPM array with 50 μm SPADs. $\Delta E/E = 4.1 \%$ (at 662 keV) and $\Delta E/E = 1.8 \%$ (at 6.13 MeV) was achieved using an ASIC-based signal processing. Furthermore, an alternative detector readout method (by hybrid-ganging) for the monolithic crystals was developed, which resulted in an improvement of $\approx 0.5 \%$ points compared to the ASIC-based readout.

In all performed studies, the relative energy resolution of the CeBr_3 crystal was inferior by between 0.8 % and 2.0 % compared to the one of the $\text{LaBr}_3\text{:Ce}$.

A first Compton camera prototype comprising a monolithic $\text{LaBr}_3\text{:Ce}$ crystal as absorber and a GAGG scintillator array as scatterer resulted in an ARM value between 5.4° and 6.2° depending on the exact radiation source location in the plane parallel to the scatterer component (at a distance of 50 mm to the scatterer). A spatial resolution

between 5.2 mm and 5.6 mm could be demonstrated with an accuracy to localize a ^{22}Na point source of below 1 mm.

As an alternative absorber detector for a Compton camera prototype for γ -ray imaging below 1.5 MeV, a three-layered pixelated LYSO crystal array ($0.9 \times 0.9 \times 6.6 \text{ mm}^3$ crystal volume) was studied in a readout configuration using KETEK and HAMAMATSU $50 \mu\text{m}$ SPAD SiPM arrays with 8×8 channels ($3 \times 3 \text{ mm}^2$ active channel area) and the PETsys TOFPET v2c ASIC.

For both investigated SiPM arrays all crystals could be individually resolved and identified. The relative energy resolution was studied individually for the three crystal layers and despite a strong dependency of the layer, in which the interaction took place, an average value of $\Delta E/E = 19.1 \%$ and $\Delta E/E = 21.2 \%$ at 511 keV was found for the KETEK and HAMAMATSU SiPM arrays, respectively. A coincidence-resolving time of below 500 ps (determined for individual crystal layers) was found for both SiPM arrays.

A second Compton camera prototype was commissioned from the GAGG crystal array (using a KETEK $25 \mu\text{m}$ SPAD SiPM array) and a three-layered LYSO crystal block (using a HAMAMATSU $50 \mu\text{m}$ SPAD SiPM array). This prototype could achieve an angular resolution measure (ARM) of 8.2° at an incident photon energy of 1274 keV and a spatial resolution of 6.0 mm and 6.1 mm along the x- and y-dimension, respectively, using a ^{22}Na point source at a distance to the scatterer of 50 mm.

A γ -PET proof-of-principle study was carried out in which a spatial resolution of 2 mm in a PET-only imaging mode was achieved using a simple backprojection for image reconstruction.

In a triple-coincidence imaging mode (by combined events of a individually triggered PET and Compton events) using only 77 primary events a spatial resolution of 3.3 mm and 3.9 mm in the PET detector plane was achieved and 12.9 mm in the third plane, resulting in full three-dimensional imaging capability and high sensitivity of the γ -PET imaging mode was demonstrated.

Using a detector system comprising four of Compton cameras in a cross-like arrangement online measurements at a (radioactive) ion beams (^{12}C and ^{16}O (stable); ^{10}C , ^{11}C and ^{15}O (radioactive)) were performed. The good camera time resolution could be used to image the ion beam's spill structure and prompt γ -rays were detected in a coincidence mode (between scatterer and absorber). The very low geometrical efficiency of this first prototype and the high beam induced background, however, did not allow to obtain a reliable reconstruction of the ion beam by means of prompt γ -rays. In an PET-imaging mode using the scatterers of opposing Compton cameras a ^{16}O beam could be monitored.

In conclusion, a SiPM-based readout of various Compton camera components and related camera configurations could be established as high-performance alternative to conventional PMT-based readout.

List of Abbreviations and Acronyms

3D-CRT	3-Dimensional Conformal Radiation Therapy
ASIC	Application Specific Integrated Circuit
CeBr ₃	Cerium Bromide
CFD	Constant Fraction Discriminator
CRT	Coincidence Resolving Time
CT	Computed tomography
DOI	Depth of Interaction
EBRT	External Beam Radiation Therapy
ESR	Enhanced Specular Reflector
eV	electron Volt (unit of energy defined as kinetic energy an electron gains from a potential difference of 1 V)
FOV	Field-of-view
FPGA	Field Programmable Gate Array
FRS	Projectile FRagment Separator
FWHM	Full width at half maximum
GAGG	Gadolinium Aluminium Gallium Garnet (Ce:Gd ₃ Al ₂ Ga ₃ O ₁₂)
LaBr ₃ :Ce	Cerium-doped Lanthanum Bromide
LOR	Line of Response
LY	Light Yield
LYSO	Cerium-doped Lutetium Yttrium Orthosilicate (Lu _x Y _y SiO _z :Ce)
MLEM	Maximum Likelihood Expectation Maximization
OAR	Organs-at-risk
OV	overvoltage
PA3315WB-0808	KETEK SiPM Array: 3 × 3 mm ² active channel area; 15 μm SPADs; 8 × 8 channels, Waferlevel package; Blue-sensitive series
PA3325WB-0808	KETEK SiPM Array: 3 × 3 mm ² active channel area; 25 μm SPADs; 8 × 8 channels; Waferlevel package; Blue-sensitive series
PA3335WL-0808	KETEK SiPM Array: 3 × 3 mm ² active channel area; 35 μm SPADs; 8 × 8 channels, Waferlevel package; Low noise series
PA3347WL-0808	KETEK SiPM Array: 3 × 3 mm ² active channel area; 47 μm SPADs; 8 × 8 channels, Waferlevel package; Low noise series
PA3350WB-0808	KETEK SiPM Array: 3 × 3 mm ² active channel area; 50 μm SPADs; 8 × 8 channels, Waferlevel package; Blue-sensitive series
PCB	Printed Circuit Board
PET	Positron-Emission Tomography
PMT	Photomultiplier Tube
PRV	Planning RiskVolume
PTV	Planning Target Volume
QDC	Charge (Q)-to-Digital Converter

S/B	Signal-to-Background
S/N, SNR	Signal-to-Noise (Ratio)
S14161 3050HS-08	HAMAMATSU SiPM array; $3 \times 3 \text{ mm}^2$ active channel area; 50 μm SPADs; 8×8 channels; 14161 series
SD	Standard deviation
SiPM	Silicon Photomultiplier
TDC	Time-to-Digital Converter
TIA	Transimpedance amplifier
TOF	Time of Flight
TPS	Treatment planning system
V_{bd}	Breakdown Voltage



Contents

I. Introduction and Motivation	1
1. Cancer: Its Increasing Contribution to the Mortality Rate and its Treatment Methods	3
1.1. Cancer and its treatments	4
1.2. Radiation therapy	5
1.2.1. Photon therapy	5
1.2.2. Charged particle therapy	6
1.3. Content and Thesis Organization	12
II. Physics and Technological Background	15
2. The Physics of Ionizing Radiation	17
2.1. Ionizing radiation: definition, examples and its interactions	18
2.2. Direct ionization: Interactions of charged particles with matter	19
2.2.1. Heavy charged particles' interactions with matter	19
2.2.2. Ion beam range	22
2.2.3. Interactions relevant for range verification (prompt- γ imaging and PET)	23
2.3. Indirect ionization: Interactions of photons with matter	24
2.3.1. Photoelectric absorption	26
2.3.2. Compton scattering	28
2.3.3. Pair creation	31
3. Radiation Detector Physics	33
3.1. (Inorganic-) Scintillators	34
3.2. Photosensors: Types and working principles	37
3.2.1. Photomultiplier tubes (PMTs)	37
3.2.2. Silicon photomultiplier (SiPM)	40
3.3. Scintillation detectors: photosensor's readout configurations	45
4. Signal Processing and Digitization	49
4.1. General concepts of signal processing for radiation detectors	50

4.2.	TOFPET v2c ASIC by PETsys Electronics	51
4.3.	Hybrid-ganging readout board (HGRB)	53
5.	Electronically Collimated Medical (γ ray) Imaging Systems	57
5.1.	Positron-emission-tomography (PET)	58
5.2.	The Compton camera	62
5.3.	γ -PET imaging	65
III.	Experimental Methods and Results	67
6.	Compton Camera Components' Characterization	71
6.1.	Characterization of the scatterer component	72
6.1.1.	Scintillators, photosensors and measurement configuration	72
6.1.2.	Crystal identification (flood maps) and spatial resolution	73
6.1.3.	Energy Resolution of the GAGG Scatterer	78
6.1.4.	Summary	90
6.2.	Characterization of the Compton camera absorber component	92
6.2.1.	Scintillators and photosensors	92
6.2.2.	Time resolution of the absorber detectors components	95
6.2.3.	Energy resolution of the absorber detector components	102
6.3.	Conclusion	121
7.	Characterization of a Trapezoidal Pixelated Detector with Intrinsic DOI Resolution as PET and Alternative Compton Camera Absorber for Energies Below 1.5 MeV	125
7.1.	Experimental setup and electronics settings	127
7.2.	Measurements & results	131
7.2.1.	SiPM arrival time distribution	131
7.2.2.	Spatial information and crystal identification	132
7.2.3.	Energy resolution	136
7.2.4.	Inter crystal scattering (ICS)	139
7.2.5.	Analysis of the time difference spectra	141
7.2.6.	Coincidence resolving time	144
7.3.	Discussion and conclusion	148
8.	Compton Camera Commissioning and Characterization	151
8.1.	Offline characterizations	153
8.1.1.	A scintillator-based Compton camera with DOI capable LYSO absorber for γ -PET imaging (Prototype #1)	153
8.1.2.	A LaBr ₃ :Ce/CeBr ₃ - and GAGG based Compton Camera for Prompt- γ Imaging (Prototype #2)	166

8.2. Online Camera Characterizations	171
8.2.1. Measurement campaign at GSI in February 2021	172
8.2.2. Measurement campaign at GSI in June 2021	176
8.3. LaBr ₃ :Ce- and GAGG based Compton Camera for Prompt- γ Imaging based on the latest KETEK low-noise SiPM series (Prototype #3)	185
IV. Summary, Future Perspectives and Appendix	193
9. Summary and Conclusions	195
10. Future Perspectives	201
11. Appendix	203
11.1. 6 mm ² active area SiPMs	204
11.2. Comparison of GAGG arrays of two batches	205
11.3. List of publications, conference contributions and submitted manuscripts .	214
12. Bibliography	217

List of Figures

1.1. Estimated cancer cases in 2018	4
1.2. 2D beam profiles: photons, protons and carbon ions	6
1.3. Progress in radiotherapy	8
1.4. Range uncertainties	9
1.5. β^+ activity vs. dose deposit	11
2.1. Ionizing electromagnetic radiation	19
2.2. Ion stopping	21
2.3. Proton stopping power in water	22
2.4. Bragg peak	23
2.5. Relative importance of τ , σ and κ	26
2.6. LaBr ₃ /GAGG linear attenuation coefficients: model	27
2.7. Photoabsorption	28
2.8. Compton scattering	28
2.9. Compton scattering: angular distribution	30
2.10. Pair creation	31
3.1. Scintillator: band model	35
3.2. PMT: model	38
3.3. Photodiode: model	41
3.4. GM APD: quenching Schematics	42
3.5. SiPM: Scheme and electrical model	43
3.6. Scintillation detectors: modes of coupling	46
4.1. Signal processing	51
4.2. PETsys Electronics: ASIC channel scheme	52
4.3. PETsys Electronics: event triggering	53
4.4. Hybrid-ganging readout board: picture	54
5.1. DOI PET: reconstruction of the LOR	61
5.2. DOI PET: improvement of the image resolution	61
5.3. Compton camera: working principle	62
5.4. Compton camera: intersecting cones	64
5.5. Compton camera: angular resolution measure	64
5.6. γ -PET principle	66

6.1. GAGG scatterer: picture	72
6.2. GAGG scatterer: flood maps and projections	75
6.3. GAGG scatterer: comparison of the number of firing SiPMs	76
6.4. GAGG scatterer: comparison of the GAGG array's energy spectra (KETEK vs. HAMAMATSU)	78
6.5. PA3315WB-0808: 662 keV peak position map	79
6.6. GAGG scatterer: calibration workflow chart	79
6.7. GAGG scatterer: relative energy resolution vs. over voltage (PA3325WB-0808, GAGG array)	81
6.8. Spatially dependence of the relative energy resolution: PA3315WB-0808 and PA3325WB-0808	84
6.9. Spatially dependence of the relative energy resolution: PA3350WB-0808	85
6.10. Spatially dependence of the relative energy resolution: S14161 3050HS-08	86
6.11. PA3335WL-0808: non-linearity map	88
6.12. PA3335WL-0808: flood map	89
6.13. PA3335WL-0808: spatially resolved energy resolution	90
6.14. PA6650-0808: picture	93
6.15. Monolithic absorber: picture	94
6.16. Monolithic absorbers: CRT Setup	96
6.17. Monolithic absorbers: CRT (MA-PMT)	98
6.18. Time skew: pulse shape	98
6.19. Time skew: arrival times	99
6.20. Monolithic absorbers: CRT (SiPM)	100
6.21. Monolithic absorbers: Hit Time distribution	105
6.22. PA3350WB-0808: breakdown voltage	108
6.23. Energy resolution vs. overvoltage: CeBr ₃ + KETEK PA6625WV-0808	110
6.24. Energy spectra of ¹⁵² Eu, ²² Na and ¹³⁷ Cs	112
6.25. Spatially resolved energy resolution: CeBr ₃ + PA6625WB-0808	113
6.26. PA6647WL-0808 (HGRB): energy spectra and energy resolution	114
6.27. MLL Tandem Accelerator: setup	116
6.28. MLL Tandem accelerator: prompt- γ spectra	118
6.29. MLL Tandem accelerator: energy resolution at prompt- γ energies	120
6.30. Prompt- γ spectrum: LaBr ₃ :Ce crystal + HAMAMATSU S14616-3050HS-08 SiPM array	121
6.31. Prompt- γ spectrum: CeBr ₃ crystal + KETEK PA6625WB-0808 SiPM array	122
7.1. DOI LYSO: picture of the CRT setup	128
7.2. DOI LYSO: covered solid angle in CRT configuration (schematic)	128
7.3. DOI LYSO: arrival Time Distribution	132
7.4. DOI LYSO: flood maps (KETEK)	134
7.5. DOI LYSO: flood maps (HAMAMATSU)	135

7.6. DOI LYSO (1.3 mm pitch): flood map (HAMAMATSU)	136
7.7. DOI LYSO: energy resolution summary	138
7.8. DOI LYSO: background spectrum and first layer ^{22}Na spectrum	139
7.9. DOI LYSO: ^{22}Na spectra of front and back-side irradiation	140
7.10. DOI LYSO: arrival-time difference spectra	144
7.11. DOI LYSO: summary of the CRT	146
7.12. DOI LYSO: layered CRT Summary	147
8.1. Compton camera with DOI: setup	154
8.2. γ -PET prototype: flood maps	155
8.3. γ -PET prototype: ^{137}Cs energy spectra	156
8.4. Coincidence events: 2D energy deposition	156
8.5. Compton camera with DOI absorber: ARM	158
8.6. Compton camera with DOI absorber: point source reconstruction at 511 keV	159
8.7. Compton camera with DOI absorber: point source reconstruction at 1274 keV	160
8.8. γ -PET prototype: PET-only point spread functions	162
8.9. γ -PET prototype: PET-only point spread function and projection (central position)	163
8.10. γ -PET: PET-only image	164
8.11. γ -PET: Compton-only image	165
8.12. γ -PET: γ -PET image	167
8.13. Prototype 2: components and housing	168
8.14. Prototype 2: 2D energy correlation	169
8.15. Prototype 2: ARM	170
8.16. Prototype 2: ^{22}Na point spread function	171
8.17. GSI: February 2021 setup	173
8.18. GSI: February 2021 Compton cameras	174
8.19. GSI: ^{11}C beam spill structure	175
8.20. GSI: ^{10}C prompt γ spectrum	176
8.21. GSI: ^{11}C prompt γ spectrum	176
8.22. GSI: setup schematics (June 2021)	178
8.23. GSI: picture of the setup	179
8.24. GSI: spill structure of a ^{16}O beam	180
8.25. GSI: prompt γ spectra	181
8.26. GSI: enhanced prompt γ spectrum	182
8.27. GSI: energy spectrum (^{15}O irradiation) on camera #3	183
8.28. GSI: coincidence spectrum (PET)	183
8.29. GSI: reconstruction (PET)	184
8.30. Prototype 3: SiPM	185
8.31. Prototype 3: setup schematics	187

8.32. Prototype 3: setup picture	188
8.33. Prototype 3: 2D energy correlation	188
8.34. Prototype 3: coincidence energy spectrum	189
8.35. Prototype 3: ARM	189
8.36. Prototype 3: compton image	191
8.37. Prototype 3: two source image	192
11.1. Flood map of four GAGG scatterers on one KETEK PA6647WL-0808	205
11.2. ^{137}Cs spectrum acquired with four GAGG scatterers on one KETEK PA6647WL-0808	206
11.3. Integral ^{22}Na spectra of GAGG arrays #2 and #4 (PA3350WB-0808)	206
11.4. Flood maps of crystal arrays #2 and #4 (PA3350WB-0808)	207
11.5. Integral ^{22}Na spectra of GAGG arrays #2 and #4 (PA3350WB-0808)	208
11.6. PA3325WB-0808 photopeak distribution	209
11.7. Inclusive ^{137}Cs energy spectrum and zoom	209
11.8. PA3350WB-0808: firing SiPMs at 662 keV (comparison between two crys- tals)	210
11.9. Integral ^{22}Na spectra of GAGG arrays #2 and #4 (PA3350WB-0808)	210
11.10 Top and bottom view of the GAGG scintillation array aligned centrally and shifted with respect to the SiPM array	212
11.11 Flood maps of crystal array #1 with acquired with aligned/shifted crystal	212
11.12 Comparison of GAGG crystal array #1 and #2	213

List of Tables

2.1. β^+ emitters (induced by proton irradiation of human tissue)	24
2.2. Prompt- γ emitters	25
3.1. Key characteristics of LaBr ₃ :Ce, CeBr ₃ , LYSO and GAGG	37
6.1. ASIC configuration (GAGG arrays)	73
6.2. GAGG: energy resolution summary	82
6.3. PA3335WL-0808: energy resolution	91
6.4. Monolithic absorber: CRT	101
6.5. ASIC configuration: monolithic absorbers	104
6.6. Energy resolution of the absorber detector component	107
6.7. Summary of the energy resolution of the absorber detector components above 1.5 MeV	117
7.1. Summary of the energy resolution of the 0.9 mm crystal pitch DOI LYSO detector block	139
7.2. Summary of the energy resolution of the 1.2 mm crystal pitch DOI LYSO detector block	141
7.3. Comparison of the CRT by first and brightest firing SiPM	143
7.4. Summary of the CRT: DOI LYSO	147
8.1. Compton camera prototype: coincidence energy resolution	157
8.2. Summary on the Compton camera performance of Prototype # 1	160
8.3. PET-only imaging mode: spatial resolution	163
8.4. γ -PET imaging-mode: summary	166
8.5. GSI: coincidence energy resolution	170
8.6. Prototype 3: performance summary	190

Part I.

Introduction and Motivation

Cancer: Its Increasing Contribution to the Mortality Rate and it's Treatment Methods

Contents

1.1. Cancer and its treatments	4
1.2. Radiation therapy	5
1.2.1. Photon therapy	5
1.2.2. Charged particle therapy	6
1.3. Content and Thesis Organization	12

This first part of this thesis is meant as a brief introduction to radiation therapy and, more specifically, for ion therapy as an alternative approach to conventional photon therapy to treat tumors. The interest in this research field is briefly motivated by pointing to the expected increase in cancer diagnosis and the inequality between higher and lower income countries.

Radiation therapy as the overarching topic of the research results presented in this thesis work is presented in greater detail. The potential advantages of ion therapy compared to photon therapy are worked out and the required technological improvements in order to exploit its full power are stated.

At the end of this chapter, the organization of the thesis is given.

1.1. Cancer and its treatments

Over the past 60 years, an epidemiological transition took place. Deaths from infectious diseases have decreased, while deaths caused by non-communicable diseases, such as heart attacks, strokes and cancer, have increased. For cancer, the World Health Organization (WHO) estimated 18.1 million new cases of cancer and 9.6 million deaths worldwide in 2018. Lower income countries and people of the lowest economic levels are affected stronger. Furthermore, the WHO expects cases to almost double until 2040 predominantly in lower and mid-income countries¹ [WHO 2020]. The distribution of the most common types of cancer in men and women are displayed in Fig. 1.1.

Also in terms of cancer mortality rates, lower income countries are affected more severely. While the rate of premature cancer deaths could be reduced by 20 % between 2000 and 2015 in higher income countries, in lower income countries the reduction accounted only to 5 % [WHO 2020].

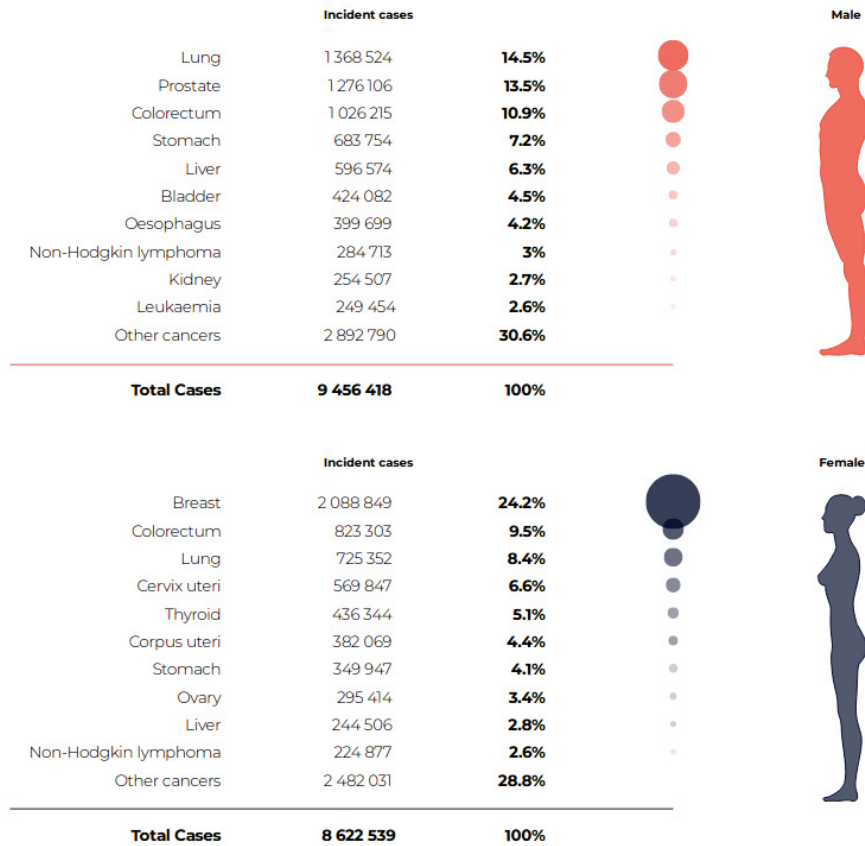


Fig. 1.1: Estimated cancer cases in 2018. Image reprinted from [WHO 2020].

In order to reduce the cancer mortality rate, screenings for precancerous lesions and

¹e.g. due to longer life expectancy and demographic transitions [Ferlay 2019].

early detection systems are required, since in early stages the treatment is not only less aggressive, but also long-term survival rates and life quality is higher [WHO 2020]. Once cancer is diagnosed, various treatment modalities are available. The three big columns of cancer treatment are (i) surgery, where the cancer is removed from the body in a surgical intervention, (ii) chemotherapy, where drugs are used to kill cancer cells and (iii) radiation therapy, where high doses of radiation are used to kill cancer cells. Often a combination of these treatment methods is used [NCI 2021].

1.2. Radiation therapy

Radiation therapy (radiotherapy) has become one of the three main treatment modalities for malignant tumors and has the advantage of being non-invasive (except Brachytherapy). In this context it is also often referred to as radiation oncology [Karger 2018]. First usage of X-rays for cancer treatment dates back to 1896, shortly after Röntgen's discovery of X-rays in 1895 [Grubbe 1933, Bernier 2004, Connell and Hellman 2009]. The rationale for radiation oncology is the potential cell killing by ionizing radiation by destroying the cell's DNA directly and irreversibly. Apparently, cells with high division rates, such as tumor cells, are more sensitive to radiation damage than regular tissue cells [Bernier 2004, Baskar 2014].

The application of the radiation can be realized by placing radiation sources in the body close to the tumor (**Brachytherapy**) [Bernier 2004] or externally by irradiation. For external methods (**EBRT**: external beam radiation therapy) it is generally differentiated between photon therapy, using X-rays, or charged particle (hadron/ion) therapy, using predominantly protons or heavier ions such as carbon ions.

Today, about two-thirds of cancer patients are treated with radiotherapy [Thariat 2012, Durante 2017]. Photon therapy, with more than 80% of treated patients receiving X-rays, is the dominant modality over hadron therapy [Durante 2017].

1.2.1. Photon therapy

The treatment of tumors in deeper body regions, such as the prostate or pancreas, requires photon energies in the low MeV region, i.o. to deposit a sufficiently high dose to the tumor. Starting in the end of the 1940s, these photons came from the radioactive decay of ^{60}Co (1.173 MeV and 1.332 MeV) and allowed to deposit doses of up to 60 Gy in deeply seated tumors. Starting mid of the 1950s also linear accelerators (linacs) were used and have become the main source of photons² in the energy range between 6 MeV and 25 MeV [Podgorsak 2005, Thariat 2012].

However, the attenuative nature of photon-matter interactions results in an exponential decrease (in first order) of dose deposit with increasing penetration depth (see Fig. 1.4(a) and Fig. 1.2) and thus an unavoidable exposure of healthy tissue to radiation dose, in front of, but also behind (exit exposure) of the treatment volume. By end of

²These photons are produced by Bremsstrahlung and therefore are X-rays

the 1990s, three-dimensional conformal radiation therapy (3D-CRT) had become widely used in clinical EBRT worldwide. 3D-CRT uses multiple X-ray beams under different irradiation angles to conform the three-dimensional shape of the tumor (see Fig. 1.3 (bottom row, central image)), which has the potential to allow for dose escalation at the tumor while keeping dose delivery to healthy tissue and organs at risk (OAR) low. In practice, however, good conformity is only achieved for relatively simple shapes³. One way to achieve higher conformity is to use intensity modulated beams (IMRT: intensity modulated radiation therapy) (see Fig. 1.3 (top row, third from the left)) [Verhey 1999]. Both methods reduce toxicity to healthy tissue and OAR. The nature of photon-matter interactions, however, still limits the maximum dose that can be delivered to tumor cells [Liu and Chang 2011] and still raises the desire to methods that deliver dose in a more localized manner.

1.2.2. Charged particle therapy

Heavy charged particles interact with matter via different physical processes than photons (see Sec. 2) and as such show a localized dose deposit in media: Ions, such as protons and carbon ions, almost deposit no dose close to the surface (entrance plateau), when their velocities are still high. But with decreasing speed, the dose deposit builds up, with a steep rise, resulting in a dominant peak with a distal fall-off (Bragg peak) at the end of their range (Figs. 1.2 and 1.4(a)). Most of the dose is delivered within the sharp Bragg peak (Fig. 1.2).

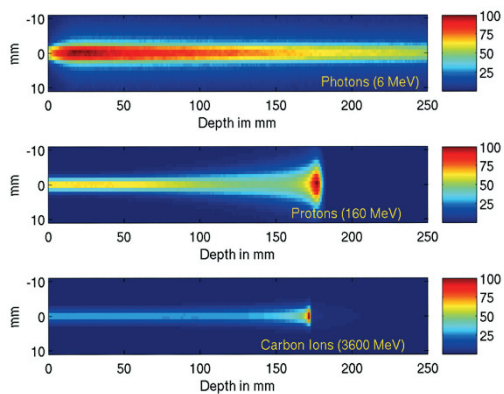


Fig. 1.2: 2D beam dose distribution profiles of Gaussian-shaped pencil-like beams in water (as percentage of the maximum dose). A collimated photon (6 MeV, top), proton (160 MeV, center) and carbon ion beam (300 MeV/u, bottom) is displayed. The beams enter the target from the left. Image taken from [Parodi 2012].

the Berkeley Radiation Laboratory [Lawrence 1958, Jensen 2013]. By the end of 2020,

This results in a lower integral dose with potentially higher doses in the tumor volume compared to photon therapy [McGowan 2013] and the ability to spare healthy tissue and organs at risk (OAR). In Fig. 1.2 the 2D dose distribution profiles in water are displayed for Gaussian-shaped pencil beams (entering from the left) of collimated photons (top), protons (center) and carbon ions (bottom).

Initially proposed for cancer treatment by Robert R. Wilson in 1946 [Wilson 1946], charged particles (protons) were first clinically used in 1954 at

³This is because for complex three-dimensional objects a large number of beams is required, which may be prohibited by the patients anatomy (e.g. by OARs).

more than 290 000 patients have been treated with ion therapy worldwide. Over 85% of patients were treated with protons and almost 40 000 with carbon ions [PTCOG 2021].

Beam delivery A further advantage of charged particle therapy is that the penetration depth (and Bragg peak position) is correlated to the particles' initial energy, which also allows to adjust the Bragg peak to the tumor's depth. For protons, typical energies between 60 MeV and 250 MeV and for carbon ions about 120 MeV/u to 430 MeV/u are required to treat tumors in human bodies [Stock 2018, Grau 2020]. Thus, treatment facilities need to be equipped with their own accelerator. While for protons usually cyclotrons are used that accelerate the protons to a maximum beam energy and range shifters are used to decrease the energy to the required level, carbon beam treatment facilities use synchrotrons. Synchrotrons have the advantage that the beam can be extracted at any energy, so that passive elements such as range shifters are obsolete [Grau 2020].

After the extraction, passive scattering is used to widen the pencil beam's energy deposit (a very narrow beam) to a so-called spread-out Bragg peak (SOBP) [Durante 2017, Grau 2020] in order to irradiate a 3D tumor volume. In recently established facilities, however, another technique is in practice, the so-called pencil beam scanning. Here, magnetic fields are used to deflect the beam in 2D to scan the tumor's projection. Longitudinal scanning is achieved by varying the beam's energy [Grau 2020]. The absence of passive elements, from which unwanted secondary particles like neutrons may be ejected due to interactions with the beam particles, pencil beam scanning results in a reduced integral dose, especially to healthy tissue [Schneider 2016, Grau 2020] and good conformity. Fig. 1.3 shows the improvement of conformity in radiotherapy on the example of prostate cancer achieved by technological progress. Starting from early usage of photons in the few hundred keV region achieving 40 Gy in the treatment volume, to treatment by using carbon ions with up to 100 Gy dose deposit, the dose escalation in the target volume is nicely demonstrated.

Range Uncertainties The biological advantages of hadron therapy compared to photon therapy and the technological quality of modern beam delivery systems can only be fully exploited if the dose is delivered accurately to the targeted volume in the body. Dose-delivery is commonly calculated by the treatment planning system (TPS) based on either semi-empirical analytical formalisms [Mohan and Grosshans 2017] or Monte Carlo simulations [Paganetti 2012] based on computed tomography (CT) images. However, even though Monte Carlo simulation is known to be the most accurate method to calculate dose delivery [Paganetti 2008], there are multiple sources to introduce inaccuracies in the exact dose deposit, resulting in range uncertainties. TPS related inaccuracies arise, for example, from the conversion of Hounsfield units into ion stopping

1.2. Radiation therapy

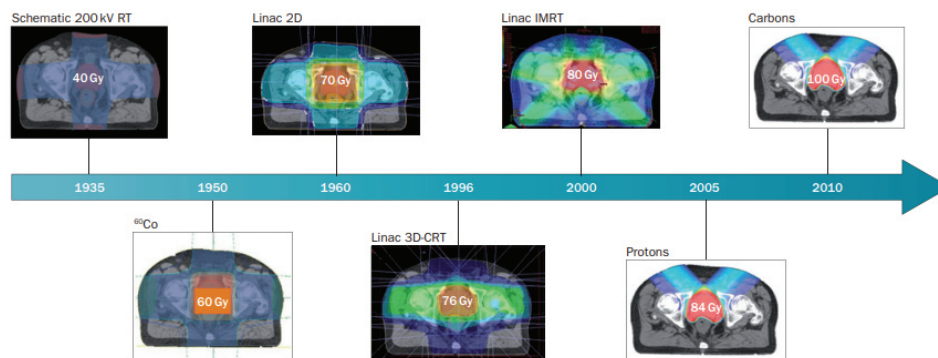


Fig. 1.3: Progress in radiotherapy treatment technologies demonstrated via the example of prostate cancer irradiation. Starting with early treatment plans in the 1930s using 200 keV photons up to nowadays used carbon ions, the dose escalation and irradiation conformity is nicely demonstrated. Image reprinted from [Thariat 2012].

power⁴ or CT-image noise, but may also be attributed to the dose calculation algorithm [McGowan 2013]. In addition to TPS related inaccuracies, also discrepancies between the planned and the delivered dose lead to range uncertainties. Reasons may be of geometric nature like organ motion (e.g. breathing patient) or the patient set-up, or be caused by weight loss or even density heterogeneities of the irradiated tissue [Paganetti 2012, McGowan 2013].

It is the well localized dose delivery and steep dose gradient at the distal edge of the range of hadrons that make the treatment method more sensitive to these inaccuracies in dose deposition compared to photons (Fig. 1.4). Hence, current clinical practice follows the International Commission on Radiation Units and Measurements' (ICRU) recommendation [ICRU 2007], and uses safety margins to prevent too high doses from being delivered to healthy tissue and OAR (overdosage) on one side, and no or too low dose being delivered to the tumor (underdosage) on the other side. These safety margins are typically determined as a function of the tumor's depth range plus a constant value and result in a planning target volume (PTV) and a planning risk volume (PRV) [Paganetti 2012, McGowan 2013]. As an example, the Massachusetts General Hospital (MGH) assumes 3.5% of the beam's range plus 1 mm as uncertainty, the Loma Linda University Medical Center assumes 3.5% plus 3 mm and the University of Florida Proton Therapy Institute assumes 2.5 % plus 1.5 mm as stated by Paganetti [Paganetti 2012]. However, these margins jeopardize the initial rationale for hadron therapy, i.e the Bragg peak with its distal fall-off [Mohan and Grosshans 2017]. Furthermore, the usefulness of the concept of PTV in hadron therapy is strongly discussed, especially for scanning beam delivery [Albertini 2011, Knopf and Lomax 2013]. Both motivates the research for *in vivo* methods to assess the ion beam's range and dose delivery from measurements [Knopf and Lomax 2013, Parodi and Polf 2018].

⁴from CT images

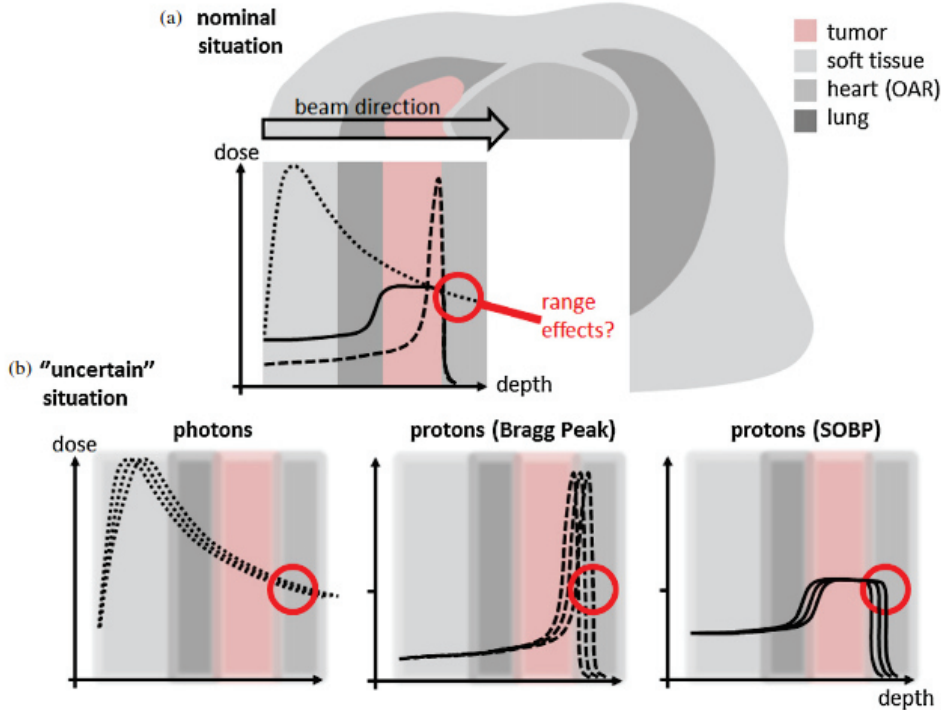


Fig. 1.4: (a) Potential benefit of protons (monoenergetic: dashed line, SOBP: solid line) compared to photons (dotted line) in terms of dose deposit and integral delivered dose. (b) Range uncertainties and their influence on the dose deposit for photons (left), protons (monoenergetic; center) and a SOBP (right). Image reprinted from [Knopf and Lomax 2013].

1.2.2.1. *In vivo* beam range verification

Methods for *in vivo* range and dose delivery verification can be categorized by means of different characteristics. Typically it is distinguished between online and offline methods or direct and indirect access to the beam range. Direct methods rely on interactions of at least a part of the ion beam with a detector, which needs to be considered in the treatment plan by itself. In contrast, indirect methods rely on secondary emissions, typically from nuclear interactions of the beam with the target tissue. Within the field of indirect range verification different concepts have been proposed and followed over the past years. Many rely on the detection of γ rays such as positron emission tomography (PET) [Bennet 1975, Parodi 2002, Parodi 2015a] and prompt- γ spectroscopy [Min 2006, Polf 2009a, Polf 2009b] or prompt- γ timing [Golnik 2014], but methods based on other effects as, e.g., the ionoacoustic effect are investigated, too [Parodi and Assmann 2015].

Positron Emission Tomography (PET) The assessment of an ion beam's range via PET imaging is based on β^+ emitters that are correlated to the beam itself. The most straightforward mode would be the irradiation by positron emitting isotopes (e.g. ^{10}C , ^{11}C) [Enghardt 2004a, Urakabe 2001] as has been investigated, e.g., at the Heavy ion

medial accelerator (HIMAC) in Chiba, Japan, for almost 20 years [Kanazawa 2002]. Due to low production rates of the required radioactive secondary isotopes and the resulting low achievable beam intensities, this method is hardly of practical relevance so far [Enghardt 2004a, BARB 2021]. However, research efforts at the HIMAC are still going on and, e.g., optical beam imaging has been applied for visualization of the RIB, recently [Kang 2019b]. Also at GSI (Darmstadt, Germany), it is back in the focus of research within the BARB (Biomedical Application of Radioactive Ion Beams) project (PI: M. Durante) that builds on the intensity upgrade of the SIS-18 synchrotron at the GSI Helmholtz Centre for Heavy Ion Research in Darmstadt, which allows for sufficiently high radioactive beam (RIB) intensities to treat tumors [BARB 2021].

The more often followed approach, however, is using secondary positron emitters by beam induced production from nuclear interactions (fragmentation). The half-life of the most abundant isotopes (^{10}C ($T_{1/2} = 19$ s), ^{11}C ($T_{1/2} = 20.4$ min), ^{15}O ($T_{1/2} = 122$ s)) generated in human tissue irradiation ranges from a few seconds to minutes and determines the timescale on which the PET scans can be taken. Therefore, ideally "in beam" PET implementation is used, i.e. the data acquisition takes place during the irradiation and the feasibility (in the pauses of pulsed beams) was demonstrated end of the 1990s [Pawelke 1997, Litzenberg 1999]. Until 2008, (the so far most extensive) studies were conducted in a clinical implementation at GSI based on carbon ion therapy [Enghardt 2004a, Enghardt 2004b]. Also in more novel implementations, the data are still taken during the inter-spill phases [Ferrero 2018]. Another type are "in-room" installations, which allow for data acquisition directly after the patient's irradiation. For "offline" PET imaging, the patient is brought to a scanner installation outside the treatment room [Parodi 2007].

In terms of PET imaging for dose control in hadron therapy, two differences between protons and heavier ion projectiles are worth mentioning: (a) lower partial cross-sections of nuclear processes that produce the β^+ emitters and (b) an accumulation of β^+ emitters at the end of the heavier ion beams's range. The latter is attributed to fragmentation not only of the target nuclei, but also of the projectiles. These fragments stop in the same range as the initial beam constituents, resulting in an accumulation thereof at the end of the beam's range [Parodi and Enghardt 2000, Parodi 2012]. Fig. 1.5 shows the correlation between β^+ activity and (normalized) dose deposit from an in-beam PET measurement of a proton (110 MeV) irradiation of PMMA (left) and with carbon ions (212.12 MeV/u) (right).

In general, PET is the most mature of all investigated imaging techniques to perform *in-vivo* range control, however, most likely a combination of different complementary techniques will provide the accuracy that is required to fully exploit the potential of ion beam therapy [Parodi 2012].

Prompt- γ spectroscopy Another *in vivo* method to monitor the distal fall-off of the Bragg curve is given by detecting and counting prompt γ rays, a modality that was pro-

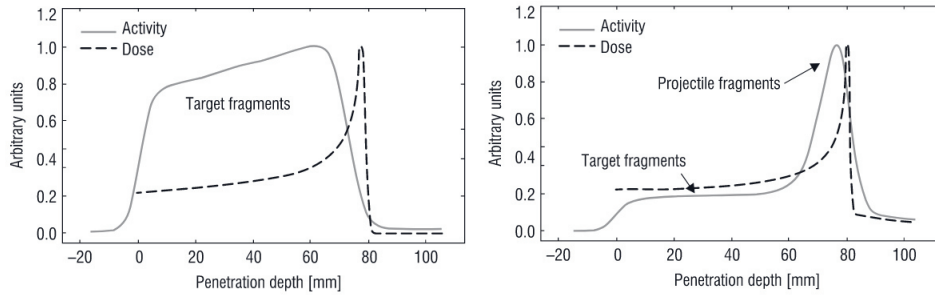


Fig. 1.5: Correlation between β^+ activity and dose obtained from in-beam PET measurements. Left: data taken from a proton (110 MeV) irradiation of PMMA. Right: data acquired from a carbon (212.12 MeV/u) irradiation of PMMA. Image taken from [Parodi 2012].

posed and demonstrated by Min *et al.* in 2006. In two publications they could show the correlation between the distal fall-off and the number of prompt- γ emissions experimentally [Min 2006] and based on simulations [Kim 2007]. While the β^+ emitters emerge from nuclear fragmentation of either the target (dominant for protons) or the projectile (dominant for heavier ions such as carbon) [Min 2006], the relevant interactions for prompt- γ ray emissions are the ones that excite the target nuclei, but leave them intact [Polf 2009a]. The energy of those prompt- γ rays from human body irradiations is in the few MeV region. The highest energies are typically 10.8 MeV ($^{14}\text{N}(n,\gamma)^{15}\text{N}$)⁵ and 15.10 MeV ($^{12}\text{C}(p,p')^{12}\text{C}^*$) [Sutcliffe 1996, Kozlovsky 2002, Polf 2009a]. Despite the multiplicity of prompt- γ -ray peaks in the energy spectra, only the ones originating from beam induced (i.e. by the primary particles) target nuclei deexcitations are of relevance for range verification.

The first proposed and realized concept by Min *et al.* was based on a mechanically collimated system (lead collimator (including paraffin and B_4C powder to suppress neutron background)). It used a single CsI(Tl) scintillator placed under a 90° angle relative to the beam, and was later further developed to an array-type detector coupled to photodiodes and used a multi-slit collimator [Min 2008, Min 2012]. Another system based on multi-slit collimation was investigated and optimized by Pinto *et al.* [Pinto 2014]. Besides multi-slit collimator systems also pinhole systems, as known from classical optics, are under investigation [Kim 2009] allowing, in principle, for 2D imaging [Krimmer 2015a]. For 1D imaging, as is sufficient to monitor the hadron beam's profile, also single knife-edge slits can be used (for 1D profiles) and have already been used in clinical treatment [Richter 2016].

Comparative studies of multi-slit collimator systems on one side and pinhole/knife-edge systems on the other side were conducted by Smeets *et al.* who found comparable performances [Smeets 2016]. Also Lin *et al.* concluded from a simulation study the potential of both systems to monitor the range of proton beams, but also inferred that multi-slit systems are stronger impacted by neutron background contamination

⁵Neutron capture of secondary neutrons

[Lin 2016].

One disadvantage common to all mechanically collimated systems is the limited detection efficiency. Electronically collimated systems, Compton cameras (but also PET), have the potential of overcome these limitations. In a Compton camera, the emission vertex of γ rays is not determined by only allowing straight incident angles and blocking all other photons, but on (at least) two successive interactions (Compton scattering and photo absorption) in a detector system. For such events, the kinematics of Compton scattering allows to localize the emission of γ rays. This is the approach that motivates all investigations and work done in this thesis.

A more detailed and technical description of PET systems and Compton cameras (including γ -PET as a combination of both techniques) will be given in the dedicated chapter 5.

1.3. Content and Thesis Organization

The studies, measurements, evaluations and developments presented in this thesis are an integral part of the ongoing work at the Chair for experimental and medical physics of the Ludwig-Maximilians-University Munich to build a Compton camera prototype that will allow to be operated in Compton-only and γ -PET imaging mode. Both, in the individual Compton camera and in γ -PET-mode the prototype is intended to be used to monitor the range of ion beams in hadron therapy. Especially, radioactive beams of, e.g., ^{10}C or ^{15}O do not only produce prompt γ rays by exciting tissue nuclei into a higher energy level which subsequently decays via the prompt emission of a γ ray. Some isotopes may also undergo a β^+ decay resulting in a daughter nucleus left in an excited state. The transition into the ground state happens under the emission of a prompt γ ray. The positron will annihilate (after thermalization) into two 511 keV γ rays, which can be detected as triple-coincidence together with the γ originating from the deexcitation of the decay's daughter nucleus by a Compton camera arrangement operated in γ -PET mode.

This first chapter has motivated and introduced the concept of ion beam therapy and the need for accurate online range verification. Chapters 2 to 5 introduce the basic physical concepts and theories underlying the work presented in this thesis. Starting with the interaction of charged particles with matter as the central rationale of range verification in hadron therapy via prompt- γ imaging, also a description of the interaction mechanisms of photons with matter will be given. The latter forms the basis to the understanding of how radiation detectors work, can be built and optimized for specific needs. These concepts will be used in Ch. 3 to provide an overview of different types of radiation detectors and to motivate the choice of detectors used in the framework of this thesis.

Ch. 4 briefly presents electronic readout concepts for radiation detectors. Furthermore, the signal processing electronics used to characterize the detectors presented in this thesis will be described.

Ch. 5 deals with electronically collimated detector systems suitable for spatially resolved γ detection and their basic working principles such as positron emission tomography (PET) scanners and Compton cameras. This focus is in accordance with the overall thesis focus on systems used in a medical environment. In a brief discourse also the concept of γ -PET imaging is introduced.

A major part of this project has been done in the framework of the MultiSiP project funded by the Bayerische Forschungsstiftung in a joint effort between the LMU Chair for Medical Physics and the company KETEK GmbH. The aim of this project was to introduce a semiconductor-based photosensor (silicon photomultiplier (SiPM)) that is able to substitute the photomultiplier tubes (PMTs) that have been used so far to read out scintillation crystals. SiPMs are of particular interest in applications in a medical environment, where magnetic stray fields prevent the use of PMTs, which rely on electrons (primary and secondary) being focused towards dynodes. The presence of magnetic fields would deflect the electrons from their initial trajectories, so that eventually only a fraction of electrons would reach the anode and only a corrupted electrical signal could be picked up.

Consequently, Ch. 6 deals with the characterization of potential Compton camera components with SiPM read out. Its first part is dedicated to the characterization of a pixelated 16×16 GAGG scintillation scatterer matrix with $1.45 \times 1.45 \times 6 \text{ mm}^3$ crystals, and the second one to a monolithic absorber crystal block ($51 \times 51 \times 30 \text{ mm}^3$). The investigated absorber scintillation compounds are $\text{LaBr}_3:\text{Ce}$ and CeBr_3 , which provide comparable properties in terms of crystal structure, decay constant and emission wavelength. The superior energy resolution of about 1 % - 2 % of $\text{LaBr}_3:\text{Ce}$ crystals compared to CeBr_3 could also be observed in the evaluations presented in this chapter. All crystals under investigation were read out with SiPMs of different microcell size types and of two different vendors (KETEK and HAMAMATSU) and a detailed comparison of the achievable performance is given.

Ch. 7 introduces an alternative absorber detector, initially developed for small animal PET. This staggered three-layered LYSO crystal block has been characterized with respect to its energy and time resolution, and its capability to identify the individual crystals of the scintillator array. This high-resolution detector block is a suitable alternative to the monolithic absorbers, especially in applications where γ -ray energies do not exceed 1 – 1.5 MeV, as is the case in γ -PET imaging modalities.

The detector components studied in Ch. 6 and 7 were used to build two types of Compton cameras, one using a monolithic absorber detector and one using the pixelated DOI LYSO detector (also in γ -PET mode). The characterization of these Compton cameras is presented in Ch. 8. The characterizations also include a study of the imaging quality in a PET-only mode of the used GAGG scatterers (for γ -PET mode). A four armed Compton camera (γ -PET) prototype that was commissioned within the framework of this thesis project and applied in online RIB measurements at GSI, Darmstadt, will also be presented in Ch. 8.

In the final Ch. 9, the thesis findings and results are summarized and set in the context of the ongoing work at the LMU Chair for Medical Physics. Furthermore, a crosslink to other ongoing projects will be given and an outlook to further planned investigations and projects will be presented.

Part II.

**Physics and Technological
Background**

The Physics of Ionizing Radiation

Contents

2.1. Ionizing radiation: definition, examples and it's interactions	18
2.2. Direct ionization: Interactions of charged particles with matter	19
2.2.1. Heavy charged particles' interactions with matter	19
2.2.2. Ion beam range	22
2.2.3. Interactions relevant for range verification (prompt- γ imaging and PET)	23
2.3. Indirect ionization: Interactions of photons with matter	24
2.3.1. Photoelectric absorption	26
2.3.2. Compton scattering	28
2.3.3. Pair creation	31

This chapter is intended to give an overview of the physics of different kinds of ionizing radiation and the underlying theories thereof.

Starting with a definition of ionizing radiation and its distinction from non-ionizing radiation, the different types of ionizing radiation and their interactions with matter will be reviewed.

In the context of radiotherapy, the stopping and attenuation behavior of heavy charged particles (e.g. protons, carbon or oxygen ions) and photons (especially X-rays), respectively, when impinging onto matter, are key features to understand the concepts. Furthermore, understanding photon-matter interactions also give access to the question of how radiation detectors work and how to build them.

2.1. Ionizing radiation: definition, examples and its interactions

The first classification of penetrating radiation was proposed by E. Rutherford in 1899 [Rutherford 1899]:

- **α radiation:** High energetic He^{2+} nuclei, also referred to as α particles¹;
- **β radiation:** High energetic electrons (β^-) or positrons (β^+);
- **γ radiation:** high energetic (several tens of keV to MeV) photons originating from nuclear deexcitation processes.

Rutherford, however, by that time only distinguished between two types of radiation (emitted from uranium), "[...] one that is readily absorbed [...] and the other of a more penetrative character [...]" [Rutherford 1899], according to their potential to be absorbed. While the less-penetrating particles were named α particles, the β particles were considered to be the deeper penetrating ones [Britannica 2021a]. This classification had been generalized and extended to include a third, even more penetrating, type of radiation than β particles, consistently called γ rays by Rutherford [Trenn 1976].

A fourth, less prominent, type are **delta (δ) rays**. Delta rays are recoil electrons, ejected in an ionization process from interactions between charged particles and nuclei of an absorbing material, with a sufficient amount of energy to cause secondary ionization [Britannica 2021c, Podgorsak 2005]. This classification of radiation, however, is incomplete from today's perspective. A more complete overview on radiation is given in the following.

Ionizing and non-ionizing radiation Radiation in a physical meaning can be regarded as the motion of energy, which can either be in form of a particle flux or in form of electromagnetic waves [Britannica 2021b]. Among these two types of radiation the term "ionizing radiation" relates to the energy, rather than in which manifestation (particle or electromagnetic wave) the energy is carried. *Ionizing radiation* generally refers to radiation that contains sufficient energy to ionize atoms or matter [BfG 2019], i.e. that transfers energy larger than the respective binding energy to shell electrons with the consequence that the electron is released from its bound state. As summarized by Tschurlovits, there is no unambiguous definition that defines a clear threshold energy above which radiation is referred to as ionizing, but generally an energy of the order of few (for alkali elements) to few tens of eV (e.g. 24.5 eV for helium) is sufficient to cause ionization [Tschurlovits 2021, Podgorsak 2005]. For electromagnetic radiation energetic ultraviolet, X-, and γ radiation, but also Bremsstrahlung and annihilation photons are considered ionizing, while optical and infrared light, micro and radio waves do not carry sufficient energy to ionize matter and are, therefore, referred to as non-ionizing radiation.

¹Rutherford in 1899 only distinguished two types of radiation. The exact nature of the radiation was discovered later.

Ionizing particle radiation covers α and β particles, but also high energetic neutrons, protons and heavier particles [NRC 2021, Podgorsak 2005].

Ionizing radiation can be further categorized by distinguishing between charged particles, causing direct ionization, and uncharged particles (such as neutrons) which transfer their energy indirectly. Electromagnetic radiation can be attributed to the category of uncharged particles, since the photon, as the mediator of the electromagnetic force, carries no electrical charge.

While direct ionization and the interaction of charged particles with matter is a key to understand processes in hadron therapy, indirect interactions, especially that of photons with matter, provide an understanding of radiation detectors like the ones presented in later chapters (see Sec. 3).

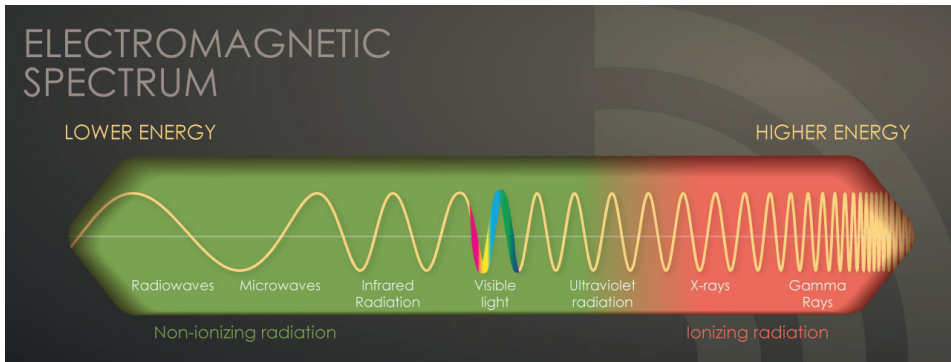


Fig. 2.1: Electromagnetic energy spectrum and categorization of radiation types into non-ionizing (green) and ionizing (red) radiation. Image taken from [CDC 2021].

2.2. Direct ionization: Interactions of charged particles with matter

Ionizing **charged particle radiation** distinguishes between **heavy charged particles**, such as protons, α particles and ions, and **fast electrons**. While fast electrons play a minor role in the context of this thesis, heavy charged particles, especially hydrogen (proton), carbon and oxygen ions, are a central part. The detectors presented within this thesis are built and characterized as Compton camera components for range verification in hadron therapy. An essential feature that motivates the potential advantages of particle therapy compared to photon therapy is the stopping behavior of heavy charged particles in matter. The physics of such interactions is discussed in the following sections.

2.2.1. Heavy charged particles' interactions with matter

Heavy charged particles (as projectiles) interact via Coulomb forces between their positive charge, and the negative (shell electrons) or positive charge (nuclei) of the absorbing

material's atoms [Frauenfelder 1999, Knoll 2010]. Nuclear interactions, named after the nucleus as interaction partner and also referred to as Bremsstrahlung interactions, are radiative interactions. However, these nuclear interactions are typically experienced by light charged particles (electrons, positrons), but occur rarely with heavy charged particles. Their contribution is only significant for very low particle energies (< 1 keV/u) [Liprandi 2018].

Therefore, heavy charged particles interact primarily in electronic interactions, which may cause excitation or ionization of the atom. As a result, charged particles lose energy when impinging onto a medium. The differential energy loss (dE) of the impinging particle per differential path length (dx) in the medium is called **linear stopping power** $S(E)$

$$S(E) = -\frac{dE}{dx} \quad (2.1)$$

From the linear stopping power, the mass stopping power can be obtained by division with the absorbing medium's density ρ .

The Bethe-Bloch formula A first description of the **stopping power** for charged particles (light and heavy) was already derived by N. Bohr in 1913 through a semi-classical procedure, where he parameterized collisions according to the closest distance of the incident particle to the center of an atom (the impact parameter b) [Bohr 1913]. Bethe later classified the collisions via the momentum transfer \mathbf{q} , instead of the impact parameter b . Beginning of the 1930s, he provided a quantum mechanical non-relativistic description [Bethe 1930, Bloch 1933a, Fano 1963]. Shortly after, also extended models for particles at relativistic velocities have been proposed by Bethe and Møller [Bethe 1932, Moller 1933].

A more general model was derived by Bloch, that converges towards the formulae described by Bethe and Møller for small momentum transfers ($eE/\hbar v$) and towards Bohr's formula for large values of $eE/\hbar v$ [Bloch 1933a]. While Bethe's approach only included the projectile's atomic number Z_p to second order, by using quantum mechanical perturbation treatments these models have been further extended to higher orders of Z_p (Barkas-Anderson effect)² and refined by Fano and Sigmund amongst others [Fano 1963, Sigmund 1975, Ziegler 1999]. Including shell corrections $(C/Z_2)^3$ and

²Named after Walter Barkas, who found deviations in the stopping powers of positively charged particles compared to their antiparticle [Barkas 1956, Barkas 1963], and Hans Henrik Anderson, who found a velocity-dependent deviation for light ions from Bethe's quadratic dependency on the atomic number Z [Anderson 1969].

³Corrections for the motion of shell electrons

density effect corrections ($\delta/2$), the relativistic Bethe-Bloch⁴ formula can - according to Fano [Fano 1963, Ziegler 1999] - be given as

$$S(E) = -\frac{dE}{dx} = \frac{4\pi e^4 Z_a Z_p^2}{m_e v^2} \left[\ln \frac{2mv^2}{\langle I \rangle} - \ln(1 - \beta^2) - \beta^2 - \frac{C}{Z_a} - \frac{\delta}{2} \right] \quad (2.2)$$

with e the charge of an electron, m_e the mass of the electron, Z_p the charge of the projectile, Z_a the atomic number of the absorbing material, $\beta = \frac{v}{c}$ and $\langle I \rangle$ the mean excitation potential. Using Eq. (2.2.1) including the above mentioned corrections, the stopping power can be calculated with an accuracy of a few percent for sufficiently large ion energies [Liprandi 2018].

For the mass stopping power, as plotted in Fig. 2.2, depending on the projectile's energy, three regimes can be distinguished.

For low projectile energies (region 1), the mass stopping power rises almost linearly until a maximum at approximately $250 \cdot \langle I \rangle$. For intermediate energies (region 2), $S(E)$ decreases with the square of the particles velocity ($S(E) \sim \frac{1}{v^2}$). This reciprocal dependency on β^2 is correlated with shorter interaction times Δt for faster particles [Kolanoski and Wermes 2016].⁵

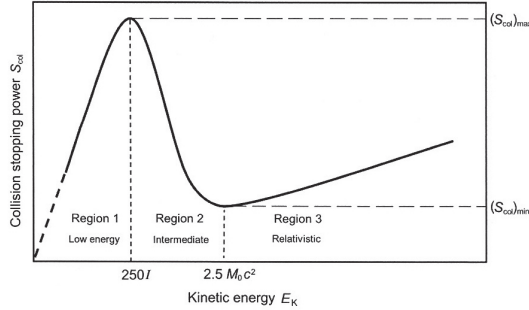


Fig. 2.2: Schematic of the collision stopping power of ions as a function of the projectile's kinetic energy. Image taken from [Podgorsak 2010].

At approx. 2.5 times the rest energy

of the projectile M_0c^2 $S(E)$ reaches a minimum. Particles at these (approximate) energies are referred to as **minimum ionizing particles** (MIPs). For (simply charged) MIPs, $S(E)$ is typically of the order of $2 \frac{MeV}{g \cdot cm^2}$ [Liprandi 2018]. The velocity of MIPs typically ranges between $3-3.5 \cdot (\beta - \gamma)^6$ or $\beta \approx 0.95$ [Kolanoski and Wermes 2016]. Beyond the minimum $S(E)$ rises with increasing kinetic energy of the projectile as the relativistic terms $\{ \ln(1 - \beta^2) - \beta^2 \}$ become dominant.

Stopping power in hadron therapy In the framework of this thesis, various experiments at accelerator facilities were conducted. The projectiles were either protons, carbon or

⁴Bloch's contribution Z-dependent estimate for the mean excitation value $\langle I \rangle$ [Bloch 1933a, Bloch 1933b, Sigmund and Schinner 2020].

⁵ Δt is proportional the momentum transfer [Kolanoski and Wermes 2016]

⁶with $\gamma = 1/\sqrt{1 - \beta^2}$

oxygen ions, respectively. The target materials were water (H_2O), polymethylmethacrylat (PMMA; $(\text{C}_5\text{H}_8\text{O}_2)_n$) and polyethylen (PE; $(\text{C}_2\text{H}_4)_n$) (see Sec. 6.2.3.1 and 8.2). The stopping power for protons impinging into water, as a constellation used in experiments at the Maier-Leibnitz-Laboratory’s Tandem accelerator in Garching with 20 MeV protons, is shown in Fig. 2.3. The stopping power is plotted for proton energies between 10 keV and 10 GeV. The electronic stopping power is indicated by the red dashed line, while the solid black line represents the overall stopping power ($S(E)_{\text{tot}} = S(E)_{\text{electronic}} + S(E)_{\text{nuclear}}$).

For a typical proton beam energy of 250 MeV, the particle velocity amounts to $\beta \approx 0.6$. Thus, we deal with relativistic particles. In terms of stopping power, however, we deal with the regime on the low energetic side of the MIP minimum [Kraan 2015].

For ions with velocities in the same order of orbital electrons’ velocities, the Bethe-Bloch formula (Eq. (2.2.1)) is no longer valid. In this energy regime, the Lindhard region, $S(E)$ becomes proportional to β [Kraan 2015]. Another energy region, between the Lindhard and the Bethe-Bloch region, is called Anderson-Ziegler region, named after their model [Ziegler 1977] that describes the stopping power of ions in this energy regime [Kraan 2015].

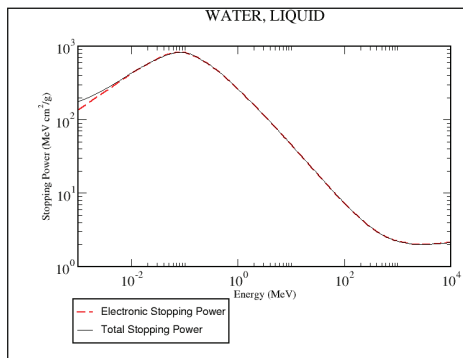


Fig. 2.3: Stopping power of protons in water for proton energies between 10 keV and 10 GeV. The red dashed line represents the modeled electronic stopping power, while the solid black line indicates the total stopping power. Image created on [NIST 2021b].

2.2.2. Ion beam range

According to the $1/v^2$ -dependency $S(E)$, the stopping power or the energy transfer (dose deposit) from the particle to the medium, respectively, increases while the projectile slows down. This causes the low entrance plateau and leads to a steep increase of the stopping power right before the ion is fully stopped, with a subsequent sharp fall-off, which is known as **Bragg peak** [Bragg and Kleeman 1904, Knopf and Lomax 2013].

The shape of such a Bragg peak for protons and carbon ions is illustrated in Fig. 2.4. Also the attenuation of photons (X-rays), as will be discussed in the subsequent section, is illustrated.

The distance a charged particle needs to travel until it has lost all of its energy is called **range R**. Under the assumption that the energy loss along the full track is equal to the mean energy loss, which is referred to as continuous-slowing-down approximation (csda) [Berger 1964], the csda range can be calculated as the energy integral over the reciprocal stopping power [Berger 1964].

$$R_{csda} = \int_{E_0}^0 \frac{1}{S(E)} dE = \int_{E_0}^0 -\frac{dx}{dE} dE \quad (2.3)$$

R_{csda} describes the path length of a charged particle in an homogeneous medium that loses its energy with a rate, that equals the mean rate of energy loss [Berger 1964]. R_{csda} is not to be confused with other range concepts such as the *mean range*⁷, which might be shorter than R_{csda} due to deflections, and describes the length of the covered track of a charged particle in the absorber medium [Berger 1964]. For heavy charged particles, however, deflections due to elastic scattering are negligible and a particle's path is basically rectilinear.

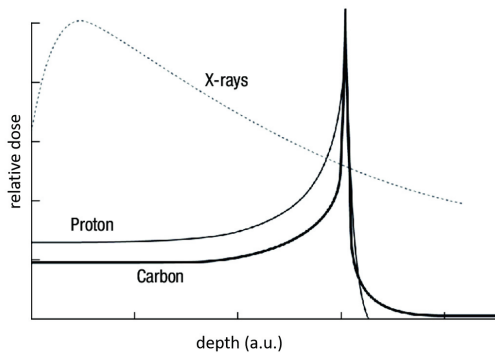


Fig. 2.4: Illustrative image of the range of protons and carbon ions (solid lines) and X-rays (dashed line) when impinging onto an absorber material (in a.u.). Image reprinted from [Choi and Cho 2016].

range). Yet, most therapy facilities use the 90% fall-off line to define a beam's range [Paganetti 2012].

Consequently, R_{csda} is in good agreement with the average range for heavy charged particles [Liprandi 2018]. In the context of particle therapy, however, where the range differs from ion to ion (even though having identical energy) due to range straggling. Hence, the range of an ion beam (e.g. of protons) needs to be defined for a broadened Bragg peak. A natural choice could be the depth at which the dose has decreased to 80% of the maximum dose deposit, which coincidences with the range at which half of the protons have stopped (mean projected range).

2.2.3. Interactions relevant for range verification (prompt- γ imaging and PET)

While it is electronic stopping that predominantly determines the dose deposition of hadrons in matter, it is inelastic nuclear collisions that are exploited for online range verification in hadron therapy. For a proton beam in water, about 1% of protons per cm undergo inelastic collisions with nuclei of the absorber medium, until a few millimeters before the Bragg peak [Knopf and Lomax 2013, Lozano 2018].

The absorber medium may be left in an excited state as result of the interaction. The de-excitation takes place on very short timescales (< nanosecond) and is accompanied

⁷absorber thickness that reduces the initial amount of particles by a factor of 2 [Knoll 2010].

β^+ emitter	reaction channel	Half-life (min)
^{11}C	$^{12}\text{C}(\text{p},\text{n})^{11}\text{C}$ $^{14}\text{N}(\text{p},2\text{p}2\text{n})^{11}\text{C}$ $^{16}\text{O}(\text{p},3\text{p}3\text{nn})^{11}\text{C}$ $^{16}\text{O}(\text{p},\alpha\text{ d})^{11}\text{C}$	20.385
^{13}N	$^{16}\text{O}(\text{p},2\text{p}2\text{n})^{13}\text{N}$ $^{14}\text{N}(\text{p},\text{pn})^{13}\text{N}$	9.965
^{15}O	$^{16}\text{O}(\text{p},\text{pn})^{15}\text{O}$	2.037

Tab. 2.1.: Most frequently induced (exclusive) β^+ emitters from proton irradiation of human tissue⁹ [Beebe-Wang 2003].

by photon emission (prompt- γ). Above a certain projectile threshold energy⁸ also other ejectiles, such as neutrons, protons or α particles are possible. The resulting nuclei of such a fragmentation process might again be in an excited state and decay via the emission of a prompt γ ray [Polf 2009a, Polf 2009b, Verburg 2012]. Another source of (beam-induced) secondary radiation are β^+ particles emitted from short-lived positron-emitting isotopes as a result of fragmentation [Parodi 2002, Knopf and Lomax 2013]. The most prominent β^+ emitters caused by proton irradiation of human tissue and prompt- γ decay channels are listed in Tab. 2.1 and Tab. 2.2, respectively.

The devices that exploit these beam-induced emission of secondary particles (prompt γ rays and annihilation photons as result of the β^+ emission) will be presented in Ch. 5.

2.3. Indirect ionization: Interactions of photons with matter

As stated, charged particles lose energy in many consecutive interactions. Photons, in contrast, undergo only one (or very few) interactions, before being fully stopped. Therefore, other than for charged particles, the range of photons in matter is not determined by a stopping power, but by the linear attenuation. The probability of a photon to undergo any interaction when impinging onto matter is a function of μ , the linear

⁸For protons, e.g., 16.79 MeV for $^{16}\text{O}(\text{p},\text{pn})^{15}\text{O}$ or 20.61 MeV for $^{12}\text{C}(\text{p},\text{n})^{11}\text{C}$ reactions [Beebe-Wang 2003].

⁸(p,2p2n) includes (p, α) and (p,3p3n) includes (p, α pn)

⁹(p,2p2n) includes (p, α) and (p,3p3n) includes (p, α pn)

prompt- γ emitter	reaction channel	Transition	Energy (MeV)	Half-life (s)
		I_i^π, E_i (MeV) \rightarrow I_f^π, E_f (MeV)		
$^{11}\text{C}^*$	$^{12}\text{C}(\text{p},\text{x})^{11}\text{C}^*$	$\frac{1}{2}^-, 2.00 \rightarrow \frac{3}{2}^-, \text{g.s.}$	2.00	1.0×10^{-14}
$^{12}\text{C}^*$	$^{12}\text{C}(\text{p},\text{p}')^{12}\text{C}^*$	$2^+, 4.44 \rightarrow 0^+, \text{g.s.}$	4.44	6.1×10^{-14}
	$^{16}\text{O}(\text{p},\text{x})^{12}\text{C}^*$	$2^+, 4.44 \rightarrow 0^+, \text{g.s.}$	4.44	6.1×10^{-14}
$^{14}\text{N}^*$	$^{14}\text{N}(\text{p},\text{p}')^{14}\text{N}^*$	$1^+, 3.95 \rightarrow 0^+, 2.31$	1.64	6.9×10^{-15}
		$0^+, 2.31 \rightarrow 1^+, \text{g.s.}$	2.31	6.9×10^{-15}
		$2^-, 5.11 \rightarrow 1^+, \text{g.s.}$	5.11	6.3×10^{-12}
$^{15}\text{N}^*$	$^{16}\text{O}(\text{p},\text{x})^{15}\text{N}^*$	$\frac{5}{2}^+, 5.27 \rightarrow \frac{1}{2}^-, \text{g.s.}$	5.27	2.6×10^{-12}
$^{16}\text{O}^*$	$^{16}\text{O}(\text{p},\text{p}')^{16}\text{O}^*$	$2^-, 8.87 \rightarrow 3^-, 6.13$	2.74	1.8×10^{-13}
		$3^-, 6.13 \rightarrow 0^+, \text{g.s.}$	6.13	2.7×10^{-11}
		$2^+, 6.92 \rightarrow 0^+, \text{g.s.}$	6.92	6.8×10^{-14}
		$1^-, 7.12 \rightarrow 0^+, \text{g.s.}$	7.12	1.2×10^{-19}

Tab. 2.2.: Most frequent prompt- γ emitters and reaction channels for a proton irradiation of human body tissue. g.s. denotes the ground state [Kozlovsky 2002, Verburg 2012].

attenuation coefficient.

Beer-Lambert law A γ ray's intensity $I(x)$ at a depth x is generally given as

$$I(x) = I_0 e^{-\mu x} \quad (2.4)$$

with I_0 being the initial intensity.

As a consequence, the energy deposit of photons in matter is essentially different than that of heavy charged ions. Fig. 2.4 shows a comparison between the relative energy deposit of photons (X-rays) compared to protons and carbon ions.

For photons impinging onto an absorbing medium a variety of interactions are physically possible with either orbital electrons or nuclei as the counterparts of the interaction. For the interaction two potential outcomes can occur: a) the photon transfers its entire energy to a light charged particle and disappears (photoelectric effect); b) the photon is scattered and the resulting photon's energy either remains unchanged (e.g. Rayleigh scattering) or is of lower energy than the incident photon (Compton and Thompson scattering) with energy being transferred to a light charged particle.

Among all possible photon-matter interaction channels three are of main relevance in radiation measurements. These interactions are

- photoelectric absorption,
- Compton scattering,
- and pair production.

While the photoelectric absorption describes the physical process that is most important for spectroscopic γ detection in detectors, Compton scattering is the underlying process that is exploited by Compton cameras¹⁰ (see. Sec. 5.2). Pair creation has a rather subordinate role, but is crucial to describe observations from γ rays with energies above the pair creation threshold of 1.022 MeV.

The linear attenuation coefficient μ can be expressed as the sum of the individual interaction probabilities of the three aforementioned effects [Knoll 2010]:

$$\mu = \tau(\text{photoelectric}) + \sigma(\text{Compton}) + \kappa(\text{pair}) \tag{2.5}$$

Relative importance of interactions The relative importance for photons to interact via one of the above mentioned processes strongly depends on the absorbing material’s atomic number Z and the photon’s energy, which is illustrated in Fig. 2.5. Here, the respective dominant regime is plotted as a function of the photon energy $h\nu$ and the absorber’s atomic number Z .

Also from Fig. 2.5 it is evident that photoelectric absorption is only a dominant process for low photon energies. To reach a decent photo absorption probability, high Z materials are required [Evans 1955]. For higher photon energies (few tens to few hundreds of keV) Compton scattering becomes the dominant process until, starting at γ energies of 1022 keV¹¹, pair creation becomes the more and more dominating process.

For two scintillation compounds evaluated within this thesis, LaBr₃:Ce and GAGG, the linear attenuation coefficient μ and the attenuation coefficients τ (photoelectric absorption), σ (Compton/incoherent scattering) and κ (pair creation) are shown in Fig. 2.6 for γ energies between 20 keV and 7 MeV as the energy range that is most relevant in the context of this thesis.

In the following section, the three main interaction mechanisms of photons with matter are described in more detail.

2.3.1. Photoelectric absorption

The term photoelectric effect (or photoeffect) describes the release of a shell electron (typically from the K or L shell in an atom) by full absorption of an incident photon.

¹⁰In this case, a second interaction (typically a full absorption of the scattered photon) is required.

¹¹two times the electron’s rest mass

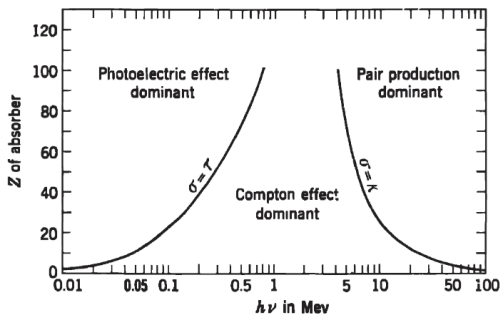


Fig. 2.5: Relative importance of photo absorption, Compton scattering and pair creation plotted as a function of Z and the photon energy $h\nu$. The drawn lines represent regions where two of the respective linear attenuation coefficients are equal. Image reprinted from [Evans 1955].

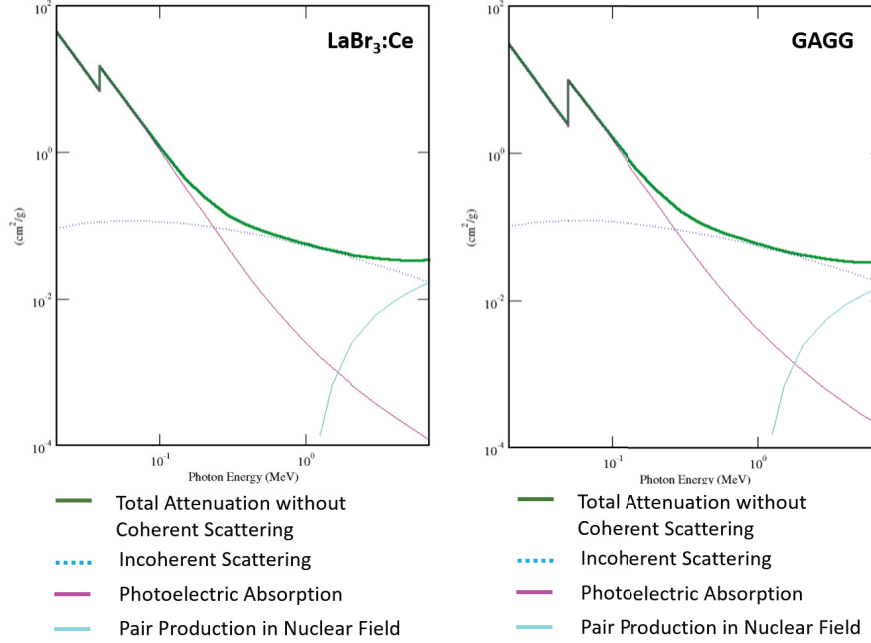


Fig. 2.6: Linear attenuation coefficient μ of LaBr₃:Ce (left) and GAGG (right). The individual interaction probabilities for photoelectric absorption (magenta line), Compton scattering (dashed blue line) and pair creation (mint colored line) are also displayed. Graph produced from [NIST 2021a].

From considerations of momentum and energy conservation, it can be derived that photo absorption cannot occur on free electrons, but needs bound electrons. The momentum is transferred not only to the rejected electron but also to the residual atom [Evans 1955]. During the interaction, the photon's initial energy $h\nu$ is transferred predominantly to a K-shell electron (in roughly 80% of the cases). The electron is ejected with a kinetic energy that equals the difference between the photon's ($h\nu$) and the electron's binding energy E_B

$$E_{kin} = h\nu - E_B \quad (2.6)$$

The vacancy in the atom's shell is resolved by either a deexcitation of the atom, i.e. the vacancy is filled by an electron of a higher shell, or by the capture of a free electron.

Either way, the energy difference between the initial energy of the electron that fills the vacancy and the binding energy of the vacant state is released in form of one or more characteristic X-rays.

Another (rare) case of atomic deexcitation involves the emission of an Auger electron that carries away the atoms excitation energy instead of a characteristic X-ray [Auger 1925, Fontana 2018].

As mentioned before, the photoeffect is the predominant interaction mode for γ - and X-rays of low energy ($< \text{few hundreds of keV}$). However, absorber materials with high atomic numbers Z can enhance the probability for photo absorption (Fig. 2.5). Although no single expression for the probability of photoelectric absorption τ over all γ energies E_γ and atomic numbers Z can be given, it can roughly be approximated to

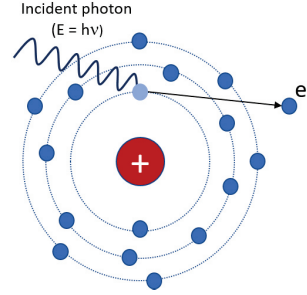


Fig. 2.7: Schematic of photoelectric absorption

$$\tau \cong \text{const} \times \frac{Z^n}{E_\gamma^3} \quad (2.7)$$

with n varying between 4 and 5 [Evans 1955, Knoll 2010].

2.3.2. Compton scattering

While an interaction via photoelectric absorption causes the incident photon to disappear, photons may also scatter. In scintillation detectors, the most prominent scatter mechanism is **Compton scattering**. In 1922 (published in 1923) A. H. Compton provided a theoretical explanation for the "softening", i.e. an increase of the wave length, of scattered X- and γ rays by light elements [Compton 1923]. He received the Nobel prize in 1927 for "the discovery of the effect named after him" [Nobel prize 2021].

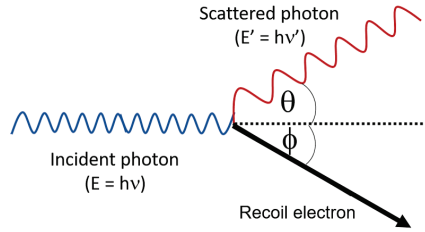


Fig. 2.8: Schematic of Compton scattering. Own work, inspired from [Knoll 2010],

(with energy $E_{\gamma,i}$ and momentum $\mathbf{p}_{\gamma,i}$) and an outer shell electron ($E_{e,i}^{rel}$, $\mathbf{p}_{e,i}$ ¹²) of the detector material. The photon transfers a part of its energy to the electron, which is ejected as recoil electron under an angle ϕ . Typically, the electron is assumed to be at rest prior to the interaction. The photon itself is deflected by an angle θ (Compton scattering angle). Fig. 2.8 illustrates schematically the Compton scatter process.

Compton cameras exploit this scatter mechanism to spatially resolve the origin of γ rays. As this thesis is dedicated to build a Compton camera prototype, Compton scattering is discussed here in more detail.

Compton scattering is an interaction, or more precisely, an incoherent, inelastic scattering between an incident photon

¹²which are unknown for the bound electron and for the kinematical considerations the electron is therefore assumed to be at rest [Zoglauer 2005].

Kinematics of Compton scattering The reduction of the scattered photon's energy ($E'_\gamma = h\nu'$) is derived from energy and momentum conservation considerations:

$$E_{\gamma,i} + E_{e,i}^{rel} = E'_\gamma + E_e'^{rel}$$

$$\mathbf{p}_{\gamma,i} + \mathbf{p}_{e,i} = \mathbf{p}'_\gamma + \mathbf{p}'_e$$

Under the assumption of the electron being at rest, $E_{e,i}$ becomes E_0 and $\mathbf{p}_{e,i}$ is zero. Exploiting the relativistic energy-momentum correlation for the electron

$$E_e'^{rel} = \sqrt{E_0^2 + p_e'^2 c^2} = E_e' + E_0$$

and the energy-momentum relation of the photon

$$E_{\gamma,i} = \mathbf{p}_{\gamma,i} c$$

the initial photon's direction and energy can be derived to

$$\mathbf{e}_{\gamma,i} = \frac{\sqrt{(E_e')^2 + 2E_e' E_0 \mathbf{e}_e + E_\gamma' \mathbf{e}_g}}{E_e' + E_\gamma'}$$

$$E_{\gamma,i} = E_e' + E_\gamma'$$

Eventually, the energy of the scattered photon can be written as a function of the scattering angle and the incident photon's energy (Compton formula)

$$E'_\gamma = \frac{E_{\gamma,i}}{1 + \frac{E_{\gamma,i}}{m_0 c^2} (1 - \cos\theta)} \quad (2.8)$$

with $m_0 c^2$ the rest mass of the electron (511 keV) [Zoglauer 2005]. The minimum energy transfer from the photon to an electron is defined to be at $\theta = 0^\circ$, which means the photon is only minimally deflected and $h\nu' \simeq h\nu$ [Liprandi 2018]. According to

$$\cos\theta = 1 - m_e c^2 \left(\frac{1}{E_A} - \frac{1}{E_S + E_A} \right) \quad (2.9)$$

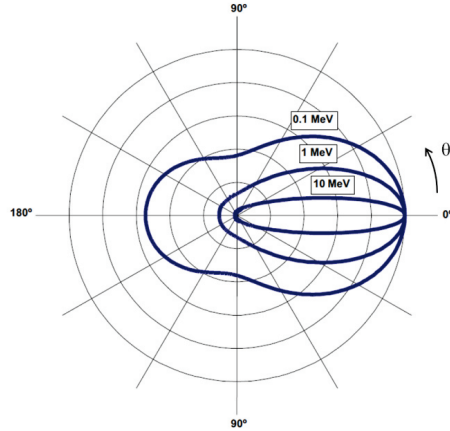
most energy is transferred to the electron for scattering angles $\theta = \pi$ and is referred to back scattering. In energy spectra these photons represent a prominent edge on the lower energy side prior to the photo peak, which is referred to as "**Compton edge**". On the other side, fully absorbed photons that had been Compton scattered prior to their absorption form another prominent feature in energy spectra, the **back-scatter peak** [Knoll 2010].

The angular distribution of scattered photons The angular distribution of scattered photons¹³ has already been derived in 1928 by Klein and Nishina based on Dirac's relativistic quantum electrodynamics. According to the **Klein-Nishina formula** the differential cross section $d\sigma/d\Omega$ is given as [Klein Nishina 1929]:

$$\frac{d\sigma}{d\Omega} = Zr_0^2 \left(\frac{1}{1 + \alpha(1 - \cos(\theta))} \right)^2 \left(\frac{1 + (\cos(\theta))^2}{2} \right) \left(1 + \frac{\alpha^2(1 - \cos(\theta))^2}{(1 + (\cos(\theta))^2)(1 + \alpha(1 - \cos(\theta)))} \right) \quad (2.10)$$

with Z the target's atomic number, $\alpha = h\nu/m_e c^2$ and r_0 the classical electron radius (≈ 2.82 fm [Podgorsak 2010]).

Fig. 2.9 shows the angular distribution plotted for photons with three different initial energies (0.1 MeV, 1 MeV and 10 MeV). The clear trend of high energetic photons to predominantly scatter in forward direction can nicely be seen.



In a more realistic scenario the photon scatters at a bound electron, i.e. the electron is not at rest, but has kinetic energy. The influence of electronic motion on the scattering angle was first observed by DuMond as broadening of measured Compton spectra and interpreted as Doppler broadening effect [DuMond 1929]. Almost 50 years later, Ribberfors accounted for this effect when he derived an expression for the angular distribution for scattering at a bound electron in the i -th shell [Ribberfors 1975].

Fig. 2.9: Angular distribution for Compton scattered photons with initial energy of 0.1 MeV, 1 MeV and 10 MeV. Image reprinted from [Liprandi 2018].

$$\left(\frac{d\sigma}{d\Omega} \right)_{bound,i} = \left(\frac{d\sigma}{d\Omega} \right)_{unbound,i} S_i(E_i, \theta, Z) \quad (2.11)$$

¹³off electrons at rest

with S_i the incoherent scattering function of the i -th shell electron, E_i the initial energy of the photon, θ the scattering angle and Z the atomic number of the target [Zoglauer 2005]. $\left(\frac{d\sigma}{d\Omega}\right)$ represents the Klein-Nishina equation for a free electron (Eq. (2.10)).

As a consequence, (i) low energy photons (few tens of keV) have a minimal higher probability to scatter on bound electrons, compared to free electrons at rest, (ii) small and large scattering angles are slightly suppressed and (iii) the energy distributes slightly different than predicted by the calculations with electrons at rest. As a result, the calculated scattering angle (from Eq. 2.9) slightly differs from the measured one by the two interaction positions. This results in a broadening of the angular resolution measure (ARM) distribution (see Par. 5.2) and is therefore referred to as **Doppler broadening** [Zoglauer 2005].

However, deviations between the cross sections derived from Eqs. (2.10) and (2.11) occur mainly in the energy region below 300 keV. For γ -ray energies relevant for either γ PET (>700 keV) or range verification (3 MeV - 6.1 MeV) the deviations are negligible [Liprandi 2018].

2.3.3. Pair creation

A third relevant process is **pair creation**. For γ rays with energies above twice the electron rest mass (1022 keV) pair creation is energetically possible, however, the process gains more importance for energies above 2 MeV.

Pair creation is an interaction between a photon and the Coulomb field of a target nucleus. The initial photon disappears completely, while an electron-positron pair is created. The photon's excess energy is carried by the electron and positron as kinetic energy. The positron, however, will thermalize and annihilate.

In the context of this thesis, pair creation is a key to understand the energy spectra acquired at accelerator facilities, where prompt γ rays were detected.

The energy of these prompt- γ rays depends on the emitting nucleus, but ranges typically between 3 and 7 MeV (e.g. 4.44 MeV from the deexcitation of ^{12}C). If pair creation takes place in the detector with a significant probability, not only a single photo peak appears in the energy spectrum, but also a so called **single escape (SE)** and **double escape**

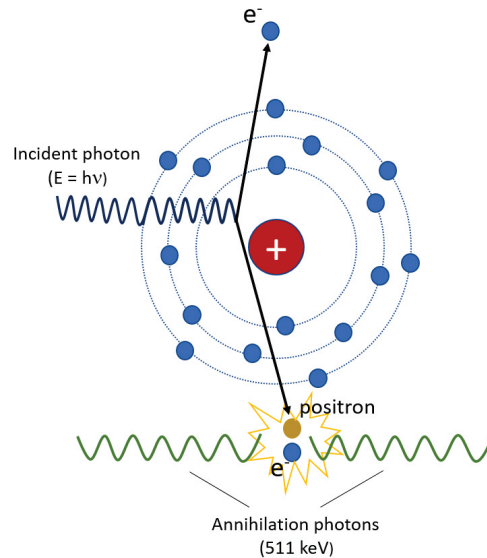


Fig. 2.10: Illustration of the pair creation process in the field of a nucleus with subsequent annihilation of the positron.

2.3. Indirect ionization: Interactions of photons with matter

peak (DE). These are attributed to pair creation with subsequent loss of either one or both of the two γ rays from the positron annihilation in the detector (see Fig. 6.28).

Radiation Detector Physics

Contents

3.1. (Inorganic-) Scintillators	34
3.2. Photosensors: Types and working principles	37
3.2.1. Photomultiplier tubes (PMTs)	37
3.2.2. Silicon photomultiplier (SiPM)	40
3.3. Scintillation detectors: photosensor's readout configurations	45

In the previous chapter, the interaction processes of charged particles and photons with matter have been reviewed. Based on the concepts introduced in the sections about photon-matter interactions (Sec. 2.3), devices to detect radiations, and specifically electromagnetic radiation, are presented in this chapter.

Many devices are capable of detecting ionizing radiation: Ionization chambers, for example, are used as proportional counters or to indicate the presence of ionizing radiation such as the Geiger-Müller counter. Semiconductor devices, like high-purity Germanium (HP-Ge) detectors or silicon drift detectors (SDD) are examples that provide an excellent energy resolution, which makes them ideal detectors for spectroscopic applications. Another type of radiation detector are scintillation detectors. These devices are relatively cost efficient, easy to handle (e.g. can typically be operated at room temperatures) and the various types of scintillating materials provide flexibility to build an optimized device for a wide range of applications. In this section, the physics of scintillation detectors, or more specific, inorganic scintillation crystals and potential photo sensors, is described.

3.1. (Inorganic-) Scintillators

Scintillation describes a material's property to emit a light flash after electronic excitation by ionizing radiation. Materials capable of undergoing such a process are called *scintillators*. Among the numerous scintillation materials such as gases, solid organic scintillators (e.g. plastic scintillators), and inorganic scintillation crystals (e.g. $\text{LaBr}_3\text{:Ce}$ and LYSO), the following section will focus on the latter as this type was intensively studied in the framework of this thesis.

In *inorganic scintillator* crystals the energy levels of the crystal lattice structure determine the scintillation process. Inorganic scintillators are typically classified as insulators. Electrons with sufficient energy to move quasi freely in the crystal are called to be in the conduction band, while electrons in the valence band are in bound states. The energy band between the valence band and the conduction band is a forbidden zone and referred to as the band gap (see Fig. 3.1). By interactions with ionizing radiation, electrons can be excited from the valence band into the conduction band, leaving holes in the valence band. Recombination of such electron-hole pairs is a rather inefficient process. Furthermore, the photons emitted by such a recombination are typically too energetic to be within the visible range of the electromagnetic spectrum [Knoll 2010], and the light output would suffer from self-absorption. By doping the base compound with so called so-called activator or color centers, i.e intentionally bringing defects into the crystal structure, states in the otherwise forbidden zone, the band gap, are created (see Fig. 3.1). Once electron-hole pairs are generated, the holes will drift (on very short time scales) to the activator center and ionize it. Electrons migrate through the conduction band until being trapped in an ionized activator state resulting in a neutral but excited activator state. This state can subsequently return to its ground state by the emission of a visible or near-UV photon [Knoll 2010]. Since this photon does not exceed the ionization threshold for the host compound material, self-absorption is strongly suppressed.

Generally, the scintillation process in inorganic scintillators can be subdivided into four phases

- Conversion of a γ into "hot" electron-hole pairs; followed by
- Thermalization of the "hot" electron-hole-pairs in inelastic interactions;
- Transfer to color centers and formation of excited activator states; and
- Deexcitation of activator states and scintillation light emission

with different time constants [Lecoq 2017].

For completeness it should be noted that the scintillation process in *organic scintillators* is essentially different from that in inorganic scintillators. In organic scintillators

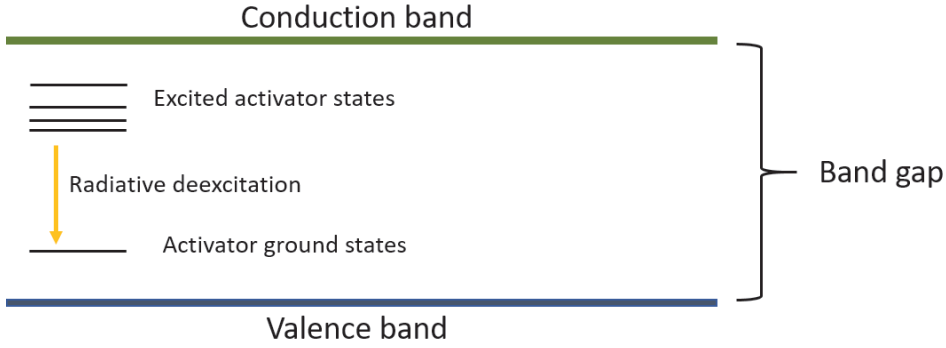


Fig. 3.1: Band model of an inorganic scintillation crystal including activator states.

such as plastic scintillators as used as fast reference detectors within this thesis (e.g. BC-413) the scintillation arises from the energy level structure of single molecules and electronic transitions between those energy states. The consequence is that the scintillation process can be observed independently from the physical state of the scintillator [Knoll 2010].

Scintillator properties Among the characterizing properties of scintillators, a high detection efficiency, high light output and short decay times are of special interest in the context of this thesis.

High detection efficiency can be realized by a high material density that ensures an efficient interaction with γ rays [Tavernier 2006]. Especially Lutetium compounds, such as LSO and LYSO, are favorable host materials due to their high densities [Weber 2002].

Decay time and activator state's lifetime For high count rate applications and good timing characteristics the scintillation process needs to happen on short time scales. The conversion ($\tau = 10^{-18}$ s - 10^{-9} s) and thermalization ($\tau = 10^{-16}$ s - 10^{-12} s) typically occur on very short time scales [Lecoq 2017]. The two main contributions to a scintillator's time behavior are a) the drift time of electrons/holes to the luminescence centers and b) the lifetime of the excited activator states [Tavernier 2006]. The time constant for the transfer phase to an activator center is of the order of 10^{-12} s - 10^{-8} s [Lecoq 2017] and is typically interrupted by trapping and detrapping. The decay rate of a state which dominates the scintillation process is generally given as [Henderson 1989]

$$\Gamma = \frac{1}{\tau} \propto \frac{n}{\lambda_{em}^3} \left(\frac{n^2+2}{3} \right)^2 \sum_f |\langle f | \mu | i \rangle|^2 \quad (3.1)$$

with n the refractive index of the compound, λ the emission wavelength and μ the dipole operator.

For the dipole operator μ to be of meaningful size, the two states i (initial) and f (final) need to be of different parity. The transition between the 5d and 4f state in Ce^{3+} and Pr^{3+} is an example of such states with different parity [Dorenbas 2002] occurring on timescales well below $1 \mu\text{s}$ [Weber 2002]. Besides a crystal's refractive index, the emission wavelength, which depends on the compound lattice structure and predominant type of bindings, determines the decay time (see Eq. (3.1)). Dorenbas has shown that for Ce^{3+} compound materials with a high refractive index and short emission wavelengths (such as $\text{LaBr}_3:\text{Ce}$) provide the shortest lifetimes among the evaluated compounds in the study [Dorenbas 2002]. A limit, however, to the shortest emission wavelengths is set by the lack of suitable photosensors with sufficient detection efficiency at these short wavelengths.

Light yield and energy resolution The absolute light yield (η) sets the total energy of scintillation photons (E_p) in relation to the energy deposit ($E_{deposit}$) in the scintillator [Sysoeva 2002]:

$$\eta = \frac{E_p}{E_{deposit}} \quad (3.2)$$

From a practical point of view, the amount of created electron-hole N_{e-h} pairs per γ interaction is of bigger interest than the absolute light yield. This number can be expressed as

$$N_{e-h} = \frac{E_{deposit}}{\beta \cdot E_g} \quad (3.3)$$

with E_g the band gap energy. The value of β is found to be close to 2.5 [Dorenbas 2002, Tavernier 2006]. For simple comparison between different scintillators in this work, the light yield (LY) refers to the amount of emitted scintillation photons per 1 MeV energy deposit in the crystal.

The achievable relative energy resolution of a scintillator is - neglecting non-proportionalities and other non-uniformities - determined by Poisson statistics [Dorenbas 2002]:

$$ER = \frac{\Delta E}{E} \propto \sqrt{\frac{1}{N_{e-h}}} \quad (3.4)$$

with ΔE being the FWHM of a photopeak and the E the photopeak energy. This dependency of the energy resolution on the number of generated scintillation photons

strongly motivates the choice of bright scintillators for applications where excellent energy resolution is required.

Tab. 3.1 lists the key properties of $\text{LaBr}_3\text{:Ce}$, CeBr_3 , LYSO and GAGG crystals, as the compounds used in this thesis.

Property	LaBr₃(Ce)	CeBr₃	LYSO	GAGG
Reference	[Saint Gobain 2021a]	[Scionix 2021] [Quarati 2013]	[Epic-Crystal 2021a]	[C&A 2020a]
Density (g/cm ³)	5.10	5.20	7.10	6.63
Light yield (photons/ MeV)	63'000	≈ 60'000	30'000	45'000-55'000 ¹
Hygroscopic	Yes	Yes	No	No
Peak emission (nm)	387	380	420	520
Internal radioactivity	Yes	No	Yes	No
Decay Time (ns)	19	18 - 20	42	≈ 90
Energy resolution (at 663 keV)	2.9 %	4.0 %	8.5 %	8 - 9 %

Tab. 3.1.: Properties of the four different scintillation materials used within the framework of this thesis ($\text{LaBr}_3\text{:Ce}$, CeBr_3 , LYSO and GAGG).

3.2. Photosensors: Types and working principles

The scintillation photons emitted by the scintillator need to be collected and transformed into an electronic signal. The component to perform this task is a photosensor. The used types of photosensors are either *Photomultiplier tubes* (PMT) or semiconductor detectors such as *Avalanche Photodiodes* (APD) or *Silicon Photomultiplier* (SiPMs). This section will present the technical structure and functional principles of PMTs and SiPMs. The APD will not be discussed separately, SiPMs are basically an array of APDs operated in Geiger mode and therefore the basic working principle for both detector types is identical. The focus of this section, however, will be on the SiPM as one of the core elements throughout the studies presented in this thesis.

3.2.1. Photomultiplier tubes (PMTs)

Since its invention and first realization in the 1930s, photomultiplier tubes (PMTs) have become the most popular vacuum electronic device with especially many applications in

¹50'000 photons/MeV for two GAGG crystals arrays used in the within this thesis work [C&A 2020b, C&A 2020c]

high energy physics and astrophysics [Lubsandorzhev 2006].

PMTs fulfill two tasks in radiation detectors: a) the conversion from optical (or near-UV) photons into an electronic signal and b) the amplification of the weak (typically few hundreds of photoelectrons) electronic signal [Knoll 2010]. The basic setup of a PMT is sketched in Fig. 3.2. The basic components of a PMT are 1) an entrance window 2) a photocathode 3) focusing electrodes 4) a series of electron multiplier stages (Dynodes) and 5) an anode. The components are placed in an evacuated tube [Hamamatsu 2007]. In addition to the internal parts, a high voltage supply (HV) (typ. 1 - 2 kV) and a voltage divider circuit are required (see Fig. 3.2). The voltage divider, typically a resistor chain, is responsible to apply the HV which is distributed to the dynodes such that a positive potential difference between a dynode and its successor is applied [Hamamatsu 2007, Knoll 2010].

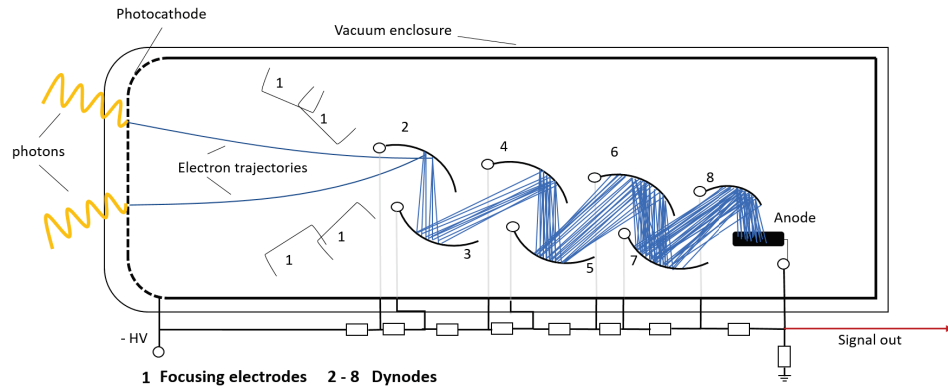


Fig. 3.2: Schematic of a photomultiplier tube (PMT). The incident light is converted into photoelectrons at the photocathode. Via focusing electrodes, the photoelectrons are accelerated towards the first dynode. One primary electron generates multiple secondary electrons via impact ionization at each dynode. Eventually all secondary electrons are collected at the anode and form the PMT signal.

Photon detection and signal efficiency The first step to be performed by a PMT is the conversion from an incident photon into a photoelectron. This process is described by the external photoelectric effect, i.e. a bound electron is released from a photo-sensitive surface and can be subdivided into three steps [Knoll 2010, Hamamatsu 2007]:

- the photon's energy (few eV) is transferred to an electron in the photocathode's valence band;
- the excited electron diffuses towards the material surface;
- the electron is released from the surface if its rest energy (after potential collisions) is sufficient to overcome the potential barrier (working function) between

the photocathode material and the surrounding environment (vacuum in case of a PMT).

The free photoelectron is subsequently accelerated towards the first dynode, where one initial electron causes multiple secondary electrons to be emitted via impact ionization. The process that leads to the emission of secondary electrons is similar to that of the photocathode emission. The energy, however, in this case is transferred from the primary electron to the dynode's material valence electrons [Knoll 2010].

The amplification factor δ of one dynode is limited by the kinetic energy of the primary electron and the bandgap energy of the dynode's material, since this energy barrier needs to be overcome by the electron to be released. Effects like energy loss of electrons not reaching the surface, however, cause δ to be smaller than the theoretically reachable up to 50 secondary electrons per 100 V potential difference applied to the dynode (for a bandgap of 2 eV). Typical values of δ are 4 - 6 for typical interdynode voltages [Knoll 2010].

The secondary electrons are collected at the anode to form the electrical output signal. Typically PMTs are very linear devices in terms of the amplification process and can retain the initial timing structure of the initial light signal [Knoll 2010].

Quantum efficiency (QE) and spectral response The quantum efficiency (QE) of a PMT can basically be described as the ratio of emitted photoelectrons and the number of incident photons. In a more detailed consideration the QE can be expressed as:

$$QE = (1 - R) \frac{P_\nu}{k} \cdot \left(\frac{1}{1 + 1/kL} \right) \cdot P_s \quad (3.5)$$

with R being the reflection coefficient, P_ν the probability that a photon with frequency ν excites an electron to a level greater than the vacuum level, k the full absorption coefficient of photons, L the mean escape length of excited electrons and P_s the probability that electrons reaching the photocathode will be emitted into the vacuum [Hamamatsu 2007].

Typical values of PMTs QE's are between 20 and 30% [Knoll 2010].

The spectral response of a PMT is on the lower energy edge determined by the minimum energy of the photon required to be able to excite an electron into the vacuum and on the higher energy side predominantly by the entrance window that an incident photon has to pass through to reach the photocathode [Knoll 2010]. Within these constraints the spectral response is basically determined by the material of the photocathode.

For scintillation detectors the choice of a PMT with a maximum QE close to the scintillator's emission wavelength is crucial to obtain good energy resolution.

The PMT gain The gain of a PMT is the product of the multiplication factor δ of each dynode. For a constant amplification factor for all N dynodes the PMT amplification can be expressed as δ^N . Typically, N amount to 10 - 12, but can also reach up to 19 [Hamamatsu 2007, Knoll 2010, Liprandi 2018]. Typical values for the PMT gain are of the order of 10^6 - 10^7 .

3.2.2. Silicon photomultiplier (SiPM)

The amplification process in PMTs relies on adequate focusing of the electrons from one dynode towards the successive one, which prohibits a conventional PMT from being used in an environment where magnetic fields are present.

A more recent type of photosensor, the silicon photomultiplier (SiPM), also referred to as multi-pixel photon counter (MPPC), is a semiconductor device. The amplification process of the initially generated electron(-hole pair) in such a SiPM is insensitive to magnetic fields. This allows scintillation detector read out by SiPMs to be applied even where magnetic fields are present. Especially in a medical environment (e.g. PET-MR) this is of big interest. Other advantageous properties compared to PMTs are compactness, robustness and a low operation voltage [Grundacker and Heering 2020].

The invention of SiPM The ground works for the Silicon Photomultiplier, as an array of Geiger-Mode Avalanche Photodiodes (GM-APD) [Golovin and Saveliev 2004, Renker and Lorenz 2009] was initially provided by Russian scientists Z. Sadygov and V. Golovin [Gasanov 1989, Golovin 1989, Golovin and Saveliev 2004, Engelmann 2018] with their studies of Silicon Metal Oxide Semiconductors (MOS) in an avalanche mode [Saveliev 2010]. Initial limitations with these early devices, which had to be recharged via an external circuit and had very limited sensitive areas, could be overcome by the implementation of Metal Resistive Semiconductors (MRS) [Saveliev 2010] with many local pn-junctions (in various designs) and common output as presented and also patented in the mid/end 90s [Saveliev 1995, Golovin 1998, Sadygov 1998]. Also the avalanche breakdown became controllable by the resistive layers of the MRS structures [Saveliev 2010]. In the following years different structures and realizations were presented with a common resistive layer [Saveliev and Golovin 2000, Sadygov 2006] and resulted in the modern design of SiPMs, where each pn-junction (micro-cell) has its own dedicated resistor [Golovin and Saveliev 2004, Saveliev 2010]. Today, the individual pn-junctions with their own quenching resistor (GM-APDs) are often also referred to as single-photon avalanche diodes (SPAD) or microcells.

The SiPM micro-cell/ single-photon avalanche diode (SPAD) Single-photon avalanche diodes (SPAD) are typically reversely biased diodes [Cova 1996, McIntyre 1985] and form the building blocks of an SiPM [Grundacker and Heering 2020] also referred to as

SiPM micro-cells. Fig. 3.3 shows the basic structure of a p-on-n type SPAD where the pn-junction is created by implementing shallow p-type regions on the n-type silicon bulk. While this structure has its peak sensitivity in the blue and near-UV light, an inverse structure (n-on-p) is more sensitive in the red [Renker and Lorenz 2009, Grundacker and Heering 2020]. In a p-on-n type structure the base is low resistivity Si on which a thin epitaxial layer will be grown, followed by an implantation of dopants to form a layer of n^+ type Si. The pn-junction is subsequently created by implantation of opposite charge dopants (p-type). This process is followed by the implantation of a heavily doped layer (p^{++}) to help a uniform distribution of the electrical potential over the full area of the APD. In further steps, the quenching resistor, signal lines and a passivation layer are added [Renker and Lorenz 2009].

By applying a reverse bias voltage (i.e. the anode will be the negative electrode, the cathode will be the positive electrode) a depleted region forms at the pn-junction. A photon that interacts predominantly via photoeffect in this depleted layer creates an electron-hole (e^- -h) pair. For sufficiently strong electric fields (of the order of $1.75 \cdot 10^5$ V/cm [McIntyre 1999]), the electron may gain enough kinetic energy while drifting towards the cathode to overcome the ionization energy and therefore can create further e^- -h pairs by impact ionization. Electrons created in this process again can create further e^- -h pairs and therefore trigger an avalanche. However, the avalanche is not self-sustainable and is quenched when all electrons have reached the cathode [Renker and Lorenz 2009, Saveliev 2010]. Diodes to detect photons operated in this regime are called avalanche photodiodes (APD). The typical gain of such APDs is of the order of few hundred [Renker and Lorenz 2009]. The self-sustainable Geiger breakdown can be interrupted by reducing the applied bias voltage below the breakdown voltage. This is typically realized by means of a quenching resistor with a resistance on the order of 100 k Ω to 1 M Ω [Saveliev 2010].

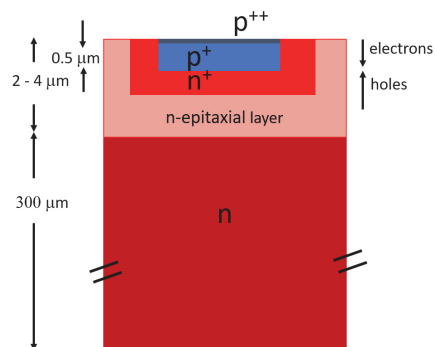


Fig. 3.3: Simplified schematic of a single GM-APD cell (p-on-n structure) without passivation layers, quenching resistor and connection lines. Reproduced from [Renker and Lorenz 2009].

Operation in Geiger-mode If one increases the applied bias voltage of the diode further, one can create even stronger electrical fields in the depleted region. For field strengths of the order of $2.5 \cdot 10^5$ V/cm also holes gain enough kinetic energy to create further e^- -h pairs [Lee 1964] and cause a Geiger discharge also known as breakdown. The bias voltage beyond which such a breakdown can occur is referred to as breakdown voltage (V_{bd}). An APD operated above the breakdown voltage is referred to be a Geiger-mode APD (GM-APD). Such a Geiger breakdown is a self-sustainable process, i.e. the

discharge needs to be interrupted via an external quenching mechanism. The quenching can be realized by active or passive methods. However, as the most common quenching method in modern SiPM, only the passive quenching is described here.

Passive quenching If a Geiger discharge is triggered, the discharge current will cause a voltage drop over the quenching resistor R_q and reduces the available voltage at the APD. The operational voltage V_{OP} of the diode falls below the breakdown point. Hence, the field strength inside the depleted region falls below the threshold required for holes to generate secondary e^- -h pairs and the Geiger discharge is interrupted and the micro-cell can recharge via R_q . This operational circuit of a GM-APD is illustrated in Fig. 3.4 [Engelmann 2018].

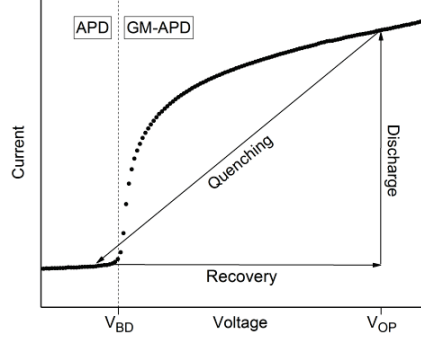


Fig. 3.4: Quenching scheme of a GM-APD. Image reprinted from [Engelmann 2018].

The SiPM's output signal The SiPM's output signal is the summed charge created by all discharged (fired) micro-cells. The charge of a single micro-cell released during a Geiger breakdown is given by

$$Q = (C_q + C_d) \cdot (V_{OP} - V_{BD}) = (C_q + C_d) \cdot \Delta V \quad (3.6)$$

with C_q the capacitance of the polysilicon quenching resistor and C_d the capacitance of the pn-junction of the micro-cell as modelled in Fig. 3.5(right).

To describe the timing characteristics, the signal needs to be decomposed in three components:

1. the rise time τ_{rise} can be approximated by

$$\tau_{rise} = R_d \cdot (C_q + C_g) \quad (3.7)$$

with C_g the grid capacitance [Engelmann 2018].

2. a fast component of the falling edge which is strongly influenced by the load resistance R_{load} of the front-end electronics

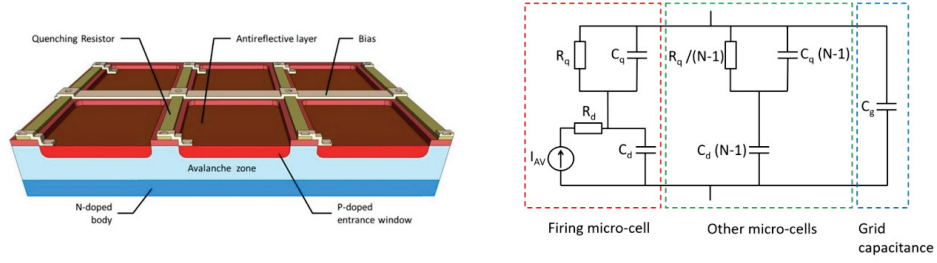


Fig. 3.5: Scheme of a SiPM (left, reprinted from [Ketek 2021b]) and electrical equivalent circuit of a SiPM (right, reprinted from [Engelmann 2018]).

$$\tau_{fast} = R_{load} \cdot (C_{eq} + C_g) \quad (3.8)$$

with C_{eq} defined as $(N-1) \cdot C_d$ (see Fig. 3.5(right)) [Engelmann 2018].

3. a slow component of the falling edge (defining the recovery time of the cell) which is strongly influenced by the quenching resistor R_q over which the micro-cell recharges

$$\tau_{slow} = R_q \cdot (C_q + C_g) \quad (3.9)$$

[Engelmann 2018].

Photon detection efficiency (PDE) The **Photon detection efficiency (PDE)** is not only the central parameter of a SiPM, it is also decisive in the context of spectroscopy for an improvement of a scintillation detector's energy resolution. According to

$$PDE = \epsilon \cdot QE \cdot P_{trigg} \quad (3.10)$$

the PDE is a product of a) the **geometrical efficiency** ϵ , b) the **quantum efficiency** **QE** and c) the probability for a photon to trigger an avalanche breakdown P_{trigg} [Saveliev 2010, Engelmann 2018].

The **geometrical efficiency** ϵ is the ratio between the SiPM area that is able to detect photons and the total SiPM area. The area that is insensitive to photon detection is composed of structures like the grid lines and the quenching resistors of each micro-cell. From this definition the trend of higher PDE for SiPMs with larger micro-cells is directly

concluded [Engelmann 2018].

The **quantum efficiency** QE of a SiPM can be defined as the ratio between the number of generated e⁻-h-pairs to the incoming photon flux [Tsang 1985, Saveliev 2010]. Besides potential photon reflection on the SiPM surface², the defining law of a semiconductor's QE is the Lambert-Beer law

$$I(x, \lambda) = I(\lambda)e^{-\alpha(\lambda)x} \quad (3.11)$$

with $I(\lambda)$ the initial photon flux of wavelengths λ , $I(x, \lambda)$ the photon flux at a distance x from the Si surface and α the absorption coefficient of Si [Saveliev 2010, Engelmann 2018].

The probability of an e⁻-h-pair to trigger a Geiger breakdown \mathbf{P}_{trigg_e} and \mathbf{P}_{trigg_h} is a function of the respective ionization coefficient $\alpha_{e^-,h}$ [McIntyre 1999] and is given by

$$\frac{dP_e}{dx} = (1 - P_e) \cdot \alpha_e(P_e + P_h - P_e P_h) \quad (3.12)$$

$$\frac{dP_h}{dx} = -(1 - P_h) \cdot \alpha_h(P_e + P_h - P_e P_h) \quad (3.13)$$

The total probability to trigger an avalanche \mathbf{P}_{trigg} is then given as

$$P_{trigg} = P_e + P_h - P_e P_h \quad (3.14)$$

In general, the probability to trigger an avalanche by electrons (P_e) is much higher and tends to saturate at smaller values of the overvoltage. From these observations it can be concluded that the SiPM design should account for electrons to trigger the avalanche [Engelmann 2018].

Spectral response The **spectral response** of a SiPM is determined a) for long wavelengths by the minimum energy required to excite an electron over the Si bandgap (1.12 eV) and is at $\lambda \approx 1100$ nm) and b) for short wavelengths by surface features of the SiPM that cause photoabsorption and prevent the photons to reach the depletion region of the SiPM [Saveliev 2010].

²Photon reflection can be reduced and transmittance increased by anti reflective coatings optimized for the desired spectral range of photons to be detected [Engelmann 2018].

SiPM noise considerations A photosensor's noise potentially influences a radiation detector's performance. For SiPM the noise is correlated with one of the following three phenomena:

1. **Dark counts:** SiPM dark counts are signals generated by thermally generated e^- - h -pairs in the depletion region and represent the main noise source of SiPM. The amplitude of such a SiPM dark count is identical to the 1 photoelectron (p.e.) level, since it is generated by the Geiger discharge of one single micro-cell. The **dark count rate (DCR)** is the average frequency of these thermal Geiger breakdowns of all micro-cells of a SiPM. The acceptable DCR is one of the limiting factors for SiPM areas in low photon applications [Saveliev 2010].
2. **Optical crosstalk:** The emission of optical photons during an avalanche discharge in reversely biased diodes has been already described in the mid 1950s [Newman 1955a, Newman 1955b] and the occurrence has been spatially correlated to the discharging regions [Chynoweth and McKay 1956]. The optical photons released during such an avalanche breakdown can subsequently be detected by a neighboring micro-cell, which is considered a noise contribution to the actual signal
3. **Afterpulses:** An afterpulse is a SiPM pulse generated by a charge carrier that has been trapped in a crystal impurity during an avalanche breakdown and triggers an avalanche after it had been released after a delay time Δt .

In the context of this thesis, SiPM noise has negligible impact on the achievable energy resolution of the radiation detectors due to the brilliance of the used scintillators. However, the influence of SiPM dark counts can be seen in the arrival-time-difference spectra when the detectors' time resolutions are measured (see. Sec. 7.2.6) and the phenomenon is described in [Schug 2019].

3.3. Scintillation detectors: photosensor's readout configurations

Scintillation detectors consist of both aforementioned components, a scintillator and a photosensor. There are two basic choices on how to read out a scintillation crystal: a) by 1-to-1 coupling, i.e. an individual crystal is read out by its own dedicated photosensor and b) a light sharing readout where the light from one scintillation crystal is distributed over several photosensor channels. The light sharing can be further subdivided into the readout of pixelated crystal arrays or monolithic crystals.

Each method has advantages and disadvantages and the ideal scintillator readout configuration is determined by the specific application.

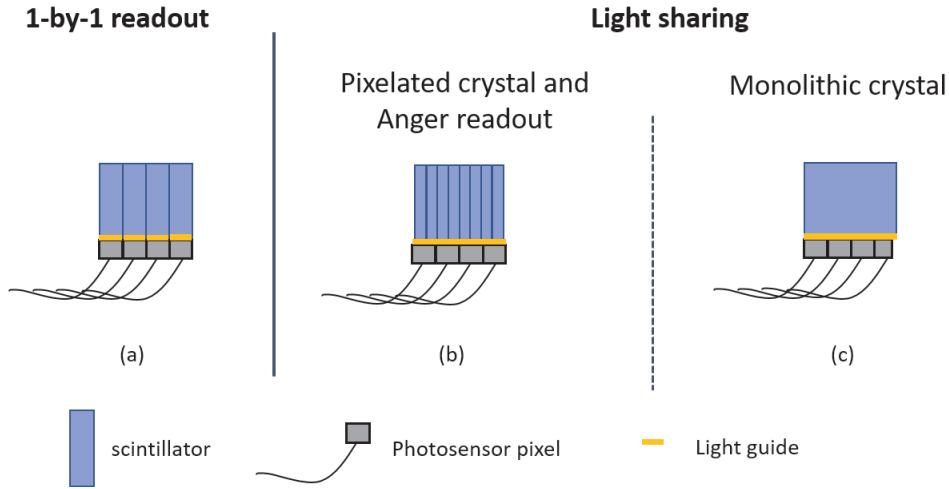


Fig. 3.6: Illustration of three configurations to read out a scintillator: (a) a 1-by-1 coupling where one crystal is read out by one photosensor channel/pixel, (b) an light sharing approach where one scintillator crystal is read out by multiple photosensor channels/pixels and (c) a monolithic scintillator with a multichannel readout.

1-by-1 readout In a 1-by-1 readout configuration a γ interaction is a priori directly known and no further position reconstruction is required in scintillation arrays involving this readout type. A potential downside are saturation effects of the photosensor for bright scintillators and/or at high γ energy or high costs for large area detector systems due to many electronic readout channels. Also the achievable spatial resolution is determined by the crystal and photosensor pixel size, e.g. using a pixelated scintillator with a KETEK PA3350WB-0808 64-channel SiPM array with $3 \times 3 \text{ mm}^2$ active channel area, the spatial resolution of the detector system will be of the same order.

Light sharing Using a light sharing readout approach of pixelated scintillator arrays, a spatial resolution of $\approx 1 \text{ mm}$ (see Sec. 6.1.2 and Sec. 7.2.2) can be achieved by an center-of-gravity calculation (Anger type calculation) [Lodge and Frey 2014] (see Eq. (6.2)). A potential downside, however, is a potential deterioration of the scintillator's energy resolution due to photosensor and electronics non-uniformities and light loss in potential insensitive areas between the photosensor channels.

A further reduction of readout channels or an increase of the detector area while keeping the amount of readout channels (e.g. 64 channels) can be achieved using monolithic detector blocks. In these configurations, the γ interaction position within the crystal needs to be determined by dedicated methods like the k-Nearest Neighbor (kNN) or the Categorical Average Pattern (CAP) algorithms [vanDam 2011]. With these methods a spatial resolution of the order of 3 mm has been reported for a large $\text{LaBr}_3\text{:Ce}$ ($50 \times 50 \times 30 \text{ mm}^3$) crystal block with a 256 channel readout, but also for a 64-channel MA-PMT

readout [Miani 2016, Mayerhofer 2017, Viegas 2018]. Recently, further improvements have been made by implementing machine learning methods to the problem of finding the interaction position within large monolithic crystals. Kawula *et al.* reported a spatial resolution of ≈ 1 mm for large ($50 \times 50 \times 30$ mm³) LaBr₃:Ce and CeBr₃ crystals by using a convolutional neural network [Kawula 2021].

In the context of this thesis both presented light sharing configurations have been used to read out scintillation detectors. A 1-by-1 coupling was only used for reference detectors used to characterize other detector's time resolutions.

3.3. Scintillation detectors: photosensor's readout configurations

Signal Processing and Digitization

Contents

4.1. General concepts of signal processing for radiation detectors	50
4.2. TOFPET v2c ASIC by PETSys Electronics	51
4.3. Hybrid-ganging readout board (HGRB)	53

In the previous chapter, the basics of scintillation detectors were reviewed. Inorganic scintillators were presented and the scintillation process was described. Subsequently, an overview of photosensors, as the light-collection stage of a scintillation detector, was given. The chapter ended with a brief summary of ways to couple scintillators to photosensors and the differences between the respective readout methods.

The photosensor's current signals then need to be amplified, shaped and digitized in order to provide data that can be further processed. The read-out electronic's efficiency also strongly influences the system's overall performance. This chapter will briefly present electronic read-out concepts for scintillation detectors, followed by a description of the electronics utilized in the framework of this thesis, however, it is not intended to provide a detailed explanation about the functionality of individual parts, such as amplifiers or shapers and their contribution to an overall detector system performance.

For further reading about the individual electronic components required for adequate signal processing and radiation detector electronics development, the reader is referred to the literature. A good introduction to this topic is given in [Knoll 2010] and [Spieler 2020].

4.1. General concepts of signal processing for radiation detectors

After incident radiation has been detected in a scintillator with subsequent collection of scintillation photons by a photosensor, the analogue PMT/SiPM's current signal needs to be further processed. This process can typically be divided into three stages:

- The small photosensor's output signal is amplified by an **(integrating) preamplifier**. If required (typically for long pulses), the signal integration transforms a short current input to a long step pulse¹[Spieler 2020].
- A **shaper** (main amplifier) provides a second amplification stage and filters/manipulates the pulse shape² (e.g. unipolar or bipolar) such that it can be further processed according to the requirements defined by the specific application and the implemented subsequent stages. As an example, the requirements of analog-to-digital converters (ADC) can be stated: the finite processing time of ADCs require a certain minimum pulse duration. Also, gradually rounded peaks are advantageous for ADCs [Spieler 2021].
Furthermore, by limiting the signal's bandwidth by filtering³ the signal-to-noise ratio (S/N) is improved.
- The analog signal is finally digitized. An **analog-to-digital** converter (ADC) digitizes pulses according to their amplitudes. Charge integrating devices (QDC: charge-to-digital converter) or digitization via time-over-threshold (ToT) measurements (using a time-to-digital converter (TDC)) are examples for further methods.⁴

The basic steps, from the detection of ionizing radiation (Sec. 2) in a radiation detector (Sec. 3) and the three stages of signal processing are depicted in Fig. 4.1. Furthermore, an additional stage, a discriminator, is shown.

For a further reading about the design and implementation of electronic readout for radiation detectors, the working principles and methods of individual components and their noise contributions, the reader is referred to the literature, e.g. [Knoll 2010, Spieler 2020, Spieler 2021, Kolanoski and Wermes 2016]. In the further course of this chapter, the signal processing electronics utilized in the measurements and evaluations within this thesis will be presented.

¹This is of practical relevance. It allows to implement subsequent components with smaller bandwidths, which again reduces electronic noise [Spieler 2020, Kolanoski and Wermes 2020]

²The easiest type of shaping circuits are CR ("differentiator") and RC ("integrator") components, built from a resistor R and a capacitor C. Also combinations, i.e. sequences of both or more sophisticated circuits are possible.

³each shaper is also a filter

⁴The later presented PETsys TOFPET v2c ASIC allows to either use a QDC or the ToT method via a TDC for signal digitization.

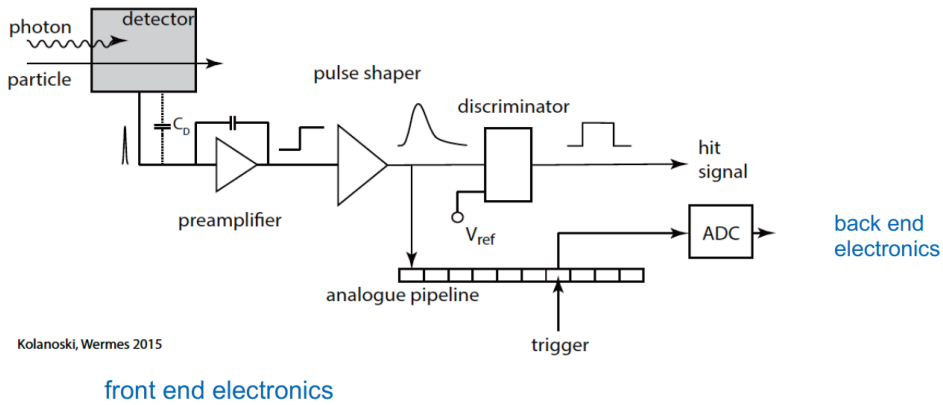


Fig. 4.1: Schematic of the individual steps performed to during the detection of radiation from the initial detection of the incident radiation to the digitization of detected signals. The block diagram shows the conventional analogue signal processing with subsequent digitization. Image reprinted from [Wermes 2020] (Initially published with german labels in [Kolanoski and Wermes 2016])

4.2. TOFPET v2c ASIC by PETSys Electronics

The central signal processing electronics components utilized for the detector characterizations and camera prototype assembly presented in this thesis work, is the TOFPET ASIC of PETSys Electronics S.A, Portugal. This ASIC was initially developed for signal processing of time-of-flight positron-emission tomography (TOF-PET) detectors for the EndoTOFPET-US [Aubry 2013] system [Bughalo 2013, Rolo 2013]. It was optimized to provide excellent coincidence-resolving-times (CRT) for a detector configuration comprising LYSO scintillation crystals one-to-one coupled to SiPMs.

PETSys Electronics released a new version (version 2b) of its TOFPET ASIC in 2017, followed by a version 2c in 2018. The ASIC is a 64 channel chip that performs signal digitization of signals of fast photon detectors with a maximum event rate of 600 kevents per channel [Petsys 2019]. Compared to version 1, the TOFPET 2c ASIC has a Wilkinson ADC implemented on board that allows for signal charge integration in addition to energy measurements via a time-over-threshold method using only a TDC. Furthermore, the dynamic range was increased from 300 pC to 1500 pC [Petsys 2019].

Signal triggering, processing and digitization on the TOFPET ASIC 2c is performed on an individual channel basis, i.e., each channel has its own dedicated amplifier discriminator and amplifier and an input signal is only further processed if the trigger logic of the respective channel has been set to an active status by the input signal. Although the trigger logic can be configured by the user, the nominal trigger logic mode (as used within the framework of this thesis) is based on three discriminators D_{T1} , D_{T2} and D_E , which allows for dark count rejection and is described in the following: The input signal current is replicated and fed into three independent branches (T, E and Q). A transimpedance amplifier (TIA) with selectable gain G_T (3000 Ω , 1500 Ω , 750 Ω or 375 Ω) and G_E (300 Ω , 150 Ω , 75 Ω or 38 Ω) converts the input currents of the T and

tion window and the applied settings for the individual thresholds are controlled via a *config* file from software side.

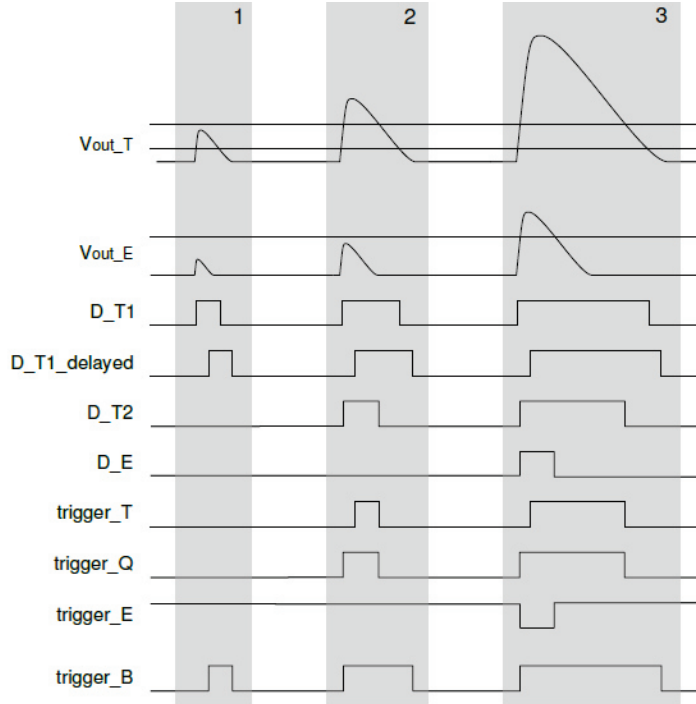


Fig. 4.3: Illustration of the trigger generation for three events (1, 2 and 3) with different amplitudes. The amplitude of event 1 is just sufficiently high to trigger D_T1 . Event 2 exceeds both timing thresholds V_{th_T1} and V_{th_T2} thus activating $trigger_T$ and $trigger_Q$, however, it cannot $trigger_E$. Only event 3 exceeds all three thresholds V_{th_T1} , V_{th_T2} and V_{th_E} and consequently triggers $trigger_T$, $trigger_Q$ and $trigger_E$, which leads to the digitization of this event [Petsys 2019].

Typically one 64 channel ASIC is soldered to one front-end board (FEB/A_v2). Two FEB/A_v2 build, together with two further boards (FEB/S and FEB/I) one front-end-module with a total of 128 channels (FEM128). The FEM128 is connected to the PETsys Electronics Evaluations kit's FEB/D board (via SAMTEC HQCD-030-20.00-TTL-SBL-1N cables (≈ 50 cm length or SAMTEC HQCD-030-40.00-TTL-SBL-1N (≈ 100 cm)) which houses, amongst other components, an FPGA and a GBE ethernet link to communicate with the DAQ PC.

4.3. Hybrid-ganging readout board (HGRB)

The energy resolution of a scintillation detector is of big importance for Compton imaging. Other than considering the sum dynode signal in multianode PMTs for this purpose, the fact that SiPM arrays are composed of individual, separated SiPM pixels explains the absence of such a sum signal output for SiPM arrays. The PETsys TOFPET v2c

4.3. Hybrid-ganging readout board (HGRB)

ASIC offers the option to generate a sum signal software-wise by clustering triggered SiPM/ASIC channels and adding the integrated charge of each channel. This method has a potential disadvantage, which is that the charge information of each channel's signal before exceeding the trigger thresholds and opening the integration window is lost. Therefore, a hardware sum signal is desirable. The various types of electronic circuits that allow to generate an output signal as the sum signal of several individual SiPM signals can be categorized in either active or passive, the method itself is referred to as "ganging". While active ganging generally provides superior signal-to-noise ratios compared to passive ganging methods, it is also more cost intensive and complex such that for many applications passive ganging methods are sufficient.

The method described in the following section belongs to the passive ganging methods, amongst which there are two basic methods: *parallel* ganging, where the individual SiPMs are interconnected in a parallel circuit and *serial* ganging with the SiPM being interconnected in series.

Parallel ganging allows to preserve the signal charge and provides a superior signal-to-noise ratio (S/N) compared to a series connection of SiPM. However, the signal amplitude is reduced and the parallel circuit of SiPM capacitance causes a large overall capacity resulting in both, long rise and decay time constants [Ootani 2018]. Therefore, the latter causes very poor timing and rate characteristics. For applications with fast timing requirements, a serial ganging is beneficial. Potential draw-backs, however, are a reduced signal charge and amplitude and the need for much higher bias voltages [Ootani 2018].

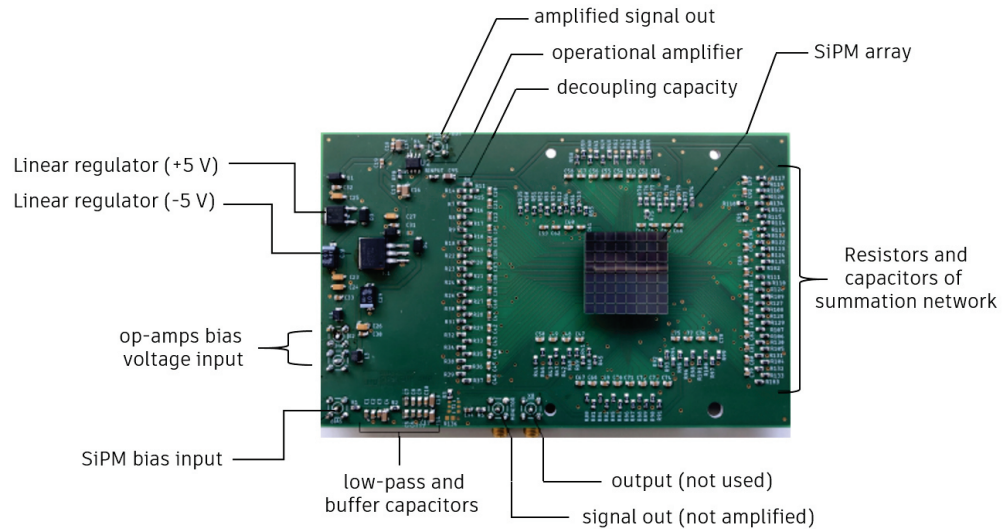


Fig. 4.4: Picture of the final hybrid-ganging readout board developed within the framework of this thesis and used to generate a signal as SUM of 64 individual SiPM array channels (image adapted from [Holthoff 2020]).

The effort to obtain the advantages of both, a parallel and serial ganging, results in a so called hybrid-ganging, which allows to sum the charge generated at several SiPMs on an array without directly adding also the individual diode capacities⁵. Here, the individual SiPMs are connected in series with each SiPM decoupled from its neighboring SiPM by a capacitor. The bias voltage is applied in a parallel circuit (common cathode). This method allows to preserve the signal charge (which results in a good energy resolution) and reduces the circuit capacity compared to a simple parallel ganging, resulting in good timing characteristics and therefore also in high rate capabilities of the circuit.

Within the B.Sc. thesis of Georg Holthoff, such a hybrid-ganging was implemented at the LMU Chair for Medical Physics partially within the context of this thesis work and the BFS MultiSiP project [Holthoff 2020]. Fig. 4.4 shows the hybrid-ganging readout board and a 64 channel SiPM array (KETEK PA3325WB-0808) plugged into it. Besides the actual hybrid ganging, the HGRB contains a transimpedance amplifier (can be bypassed) and linear regulators to provide the required ± 5 V supply voltage to the operational amplifiers (from a 12 V input voltage). A more detailed description of the HGRB and its electrical circuits can be found in [Holthoff 2020].

For the subsequently described evaluations of the energy resolution with direct sum signal generation via the HGRB, an Amptek multichannel analyzer (MCA 8000A [Amptek 2021]) has been used for signal digitization. The signal shaping of the analog signals was performed using an ORTEC 452 spectroscopy amplifier with 250 ns shaping time and a gain of 300.

⁵For a series connection of capacitors, the capacities add reciprocally.

4.3. Hybrid-ganging readout board (HGRB)

Electronically Collimated Medical (γ ray) Imaging Systems

Contents

5.1. Positron-emission-tomography (PET)	58
5.2. The Compton camera	62
5.3. γ -PET imaging	65

The first chapter gave an introduction to particle therapy as tumor treatment modality and its underlying motivation. Furthermore, it dealt with current challenges and limitations, especially the concept of range uncertainties. Among the various indirect and direct approaches to determine the particle beam range in human tissue, PET and prompt- γ imaging were presented in greater detail. Both methods rely on radiation detector systems. Therefore, the basic concepts of γ -ray detectors were described in the previous chapters.

In the following, electronically collimated detector systems (PET, Compton camera and γ -PET) will be presented, since the aim of this thesis' project was a component evaluation with subsequent commissioning of a Compton camera/ γ -PET prototype. The underlying concepts will be discussed and potential limits and improvements will be stated.

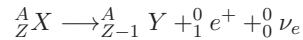
5.1. Positron-emission-tomography (PET)

Although the perspective of this thesis is mainly the commissioning of a Compton camera prototype, there are similarities between the utilized detectors. Furthermore, PET detectors might as well be used as individual components of a Compton camera in specific configurations. This is particularly the case when a PET scanner is combined with one (ore more) Compton cameras, forming a so called γ -PET device (see Sec. 5.3). Such a device was commissioned within this thesis' scope. Consequently, a PET scintillation detector was investigated to be used as PET and Compton camera absorber detector (Sec. 7). Therefore, this section will give a brief overview about PET imaging and approaches to further improve image resolutions by hardware developments¹.

Since the first positron-emission-tomography (PET) scanner was built in 1975 [Phelps 1975, Ter-Pogossian 1975], PET has become a commonly utilized metabolic imaging technique, but is also a powerful tool for *in situ* range control in hadron therapy, providing high imaging resolution [Maisey 2005, Parodi 2002].

Positron emitters in PET PET is based on the coincident detection of two photons from a positron annihilation.

For such a coincidence detection, isotopes that undergo a β^+ -decay



are required. In nuclear medicine, typically fluorodesoxyglucose (^{18}F) (**FDG**) is used as radiotracer, with the β^+ emitter ^{18}F [Maisey 2005]. In radiotherapy for dose delivery control in ion beam irradiation, the radioisotopes are produced during the irradiation by nuclear fragmentation (of either the target² or the projectile³) [Parodi 2002, Durante and Parodi 2020, BARB 2021]. Even **radioactive ion beams** (RIB) have been proposed for image-guided particle therapy to increase the signal intensity for on-line PET imaging [Urakabe 2001, Durante and Parodi 2020, BARB 2021].

The physics of PET Once a positron has been generated, it needs to slow down until it reaches a thermal equilibrium with surrounding bound electrons before it can annihilate. The range it can travel until it has thermalized contributes to the physical limit of the resolution of PET. The radius, spanned by a positron's range around

¹Potential improvements by efforts in image reconstruction methods and algorithms exceed the scope of this thesis and will not be discussed.

²The most commonly generated isotopes (that undergo β^+ -decay) in human tissue are ^{11}C , ^{14}N and ^{15}O (see Sec. 2.2.3)[Parodi 2002].

³for heavy ion irradiation [Durante and Parodi 2020]

the emission center, is determined by the electron density and the positron's energy [Derenzo 1982, Yamamoto 1984]. For the ^{18}F -decay⁴ 50% of the positrons stop within a radius of 0.31 mm and a point spread function in water (FWHM) of 0.13 mm. For ^{11}C and its decay positron' maximum energy of 0.96 MeV, the radius (50 %) is 0.6 mm and the FWHM of the point spread function is 0.13 mm [Derenzo 1982].

Once having reached thermal velocities, the positron may annihilate with an electron via an intermediate bound system, the **positronium**. Due to the momentum of the positronium the two annihilation γ rays are not emitted exactly back-to-back, but show a small acollinearity. From momentum conservation, deviations of $180^\circ \pm 0.25^\circ$ (in water) can be derived, but are found to be larger in experimental assessments due to the intermediate positronium state [Humm 2003, Berko and Hereford 1956, Shibuya 2007]. The two aforementioned characteristics of the β^+ decay in media (like liquids and solids) set physical constraints to the achievable image resolution of PET images [Humm 2003, Shibuya 2007].

An image of the emission source can be derived by the coincident detection of both annihilation γ rays in a ring(-like) detector system⁵. The distance between the two detectors that have detected the two photons spans a so-called **line-of-response** (LOR). By intersecting multiple LORs (calculated from multiple annihilations), the emission center becomes visible as the volume where the majority of the LORs intersect. This coincidence method surpasses the performance of passive collimation systems and exhibits a superior sensitivity of PET devices compared to single photon detection systems such as single photon emission tomography (SPECT) [Humm 2003].

While the two aforementioned limits to a PET system's spatial resolution are of physical nature, also technical limitations are conceivable. As an example, a coarse energy resolution of the involved detectors may result in a weak capability to identify Compton scattered γ rays, since scattering prior to the detection results in a change of the photons trajectory's direction and therefore in a wrong reconstruction of the LOR. Also, a coarse detector pixelation will result in a reduced image resolution.

Time-of-flight (TOF) PET In recent years the effort to improve the spatial resolution and quality of PET imaging systems has steadily increased. The most commonly pursued approach is using time-of-flight (TOF) PET, which was already suggested by Brownell et al. in 1969 [Brownell and Burham 1969]. Here, the positron emission can be confined to only a part of the LOR, due to a measurement of the detection time of the two respective annihilation photons. The first commercially used TOF PET scintillators (CsF and BaF2 crystals, 1-to-1 coupled to PMTs) could achieve CRTs between

⁴with a maximum energy of 0.64 MeV [Derenzo 1982].

⁵The diameters are between 80 and 90 cm for human body scanners and between 10 and 15 cm in preclinical small-animal systems [Schlegel 2018].

470 ps and 750 ps. However, they were still suffering from low light yield and low material densities, resulting in limited detection efficiency and spatial resolution, the latter due to the large crystal sizes required [Conti and Bendriem 2019, Saint Gobain 2020a, Melcher 2000, Surti and Karp 2016]. Nowadays, modern scintillation crystals such as LSO and LYSO, in combination with silicon photomultipliers (SiPMs) and dedicated signal processing electronics, allow for coincidence resolving times (CRT) of commercial systems reaching down to 200 ps [Conti and Bendriem 2019, Reddin 2018, vanSluis 2019, Surti 2015], while providing high detection efficiencies due to their high Z and density [Saint Gobain 2020b] and high spatial resolution (e.g. by using an Anger-type detector readout). For non-commercial laboratory setups CRT values around 100 ps could already be demonstrated by using LSO:Ce,Ca scintillation crystals [Grundacker 2020] or more novel scintillation crystals such as LaBr₃:Ce and CeBr₃ [Glodo 2006, Schaart 2010]. The continuous improvement of the CRT results in an improved image contrast due to an improved signal-to-noise ratio (SNR) [Surti 2007, Surti 2015]. However, the ultimate goal targets a CRT of about 10 ps [Grundacker 2019], which would allow to directly obtain the β^+ -annihilation position by measuring the detection time difference with an accuracy that is similar to the current reconstruction methods that rely on the intersection of the lines-of-response (LOR) of multiple detected positron annihilation photon pairs [Lecoq et al 2021].

Depth-of-Interaction (DOI) detectors While large radius PET systems, such as human body scanners, strongly benefit from an improved TOF capability and its improvements on the SNR, for smaller scanner radii (such as small-animal-PET scanners) a high detector spatial resolution becomes more important. The spatial resolution of the reconstructed PET images relies on the cross section of the scintillation crystal. For the commercially available preclinical PET scanners, the scintillation crystal cross sections range from to $1.5 \times 1.5 \text{ mm}^2$ to $1.0 \times 1.0 \text{ mm}^2$ depending on the manufacturers [Kuntner and Stout 2014]. The spatial resolution of PET scanners could be further improved by using a fine pitch of scintillation crystals, however, the optimal crystal pitch is a trade-off with the geometric efficiency given by the solid angle coverage that reduces with smaller crystal sizes, due to the optical insulation layers between individual crystals. The spatial resolution of small animal PET scanners is significantly deteriorated at the periphery of the PET field-of-view (FOV) caused by parallax errors introduced by the crystal thickness, due to which the true LOR deviates from the reconstructed one if one or both γ rays interact between the crystal surface and the photosensor surface [Ito 2010, Pomper and Lee 2005, Hoffman 1989].

This effect is illustrated in Fig. 5.1 and the improvement of image quality using DOI information is shown in Fig. 5.2.

However, a certain crystal thickness is required to provide a sufficient detection efficiency (system sensitivity) for 511 keV γ rays. The optimum detector thickness depends on the crystal material and ranges typically between 20 mm and 30 mm. In order to

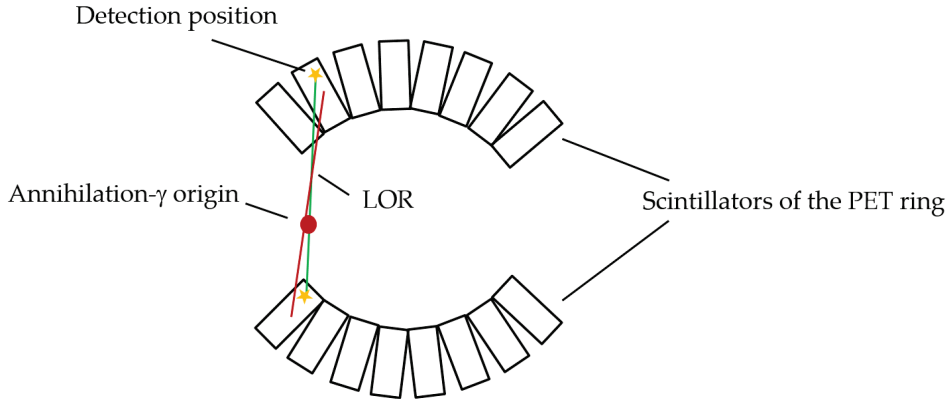


Fig. 5.1: Schematic PET detector with an off-center γ source (red). The yellow stars indicate the actual detection depth of the 511 keV annihilation γ rays and the green line denotes the corresponding LOR. The red line indicates the LOR if no DOI information is available and therefore the crystal center is assumed to be the interaction depth.

minimize the parallax error and to preserve the spatial resolution also in the periphery of the FOV, various types of depth-of-interaction (DOI) detectors have been proposed [Mohammadi 2019].

One type of DOI detector concept uses a multi-layer staggered crystal block with crystals of the layers shifted with respect to each other. Studies of such detectors have been presented by Takyu et al. [Takyu 2018] and Kang et al. [Kang 2019]. In Chap. 7 a three-layered DOI LYSO PET detector based on such a geometry will be presented and later be used as absorber detector of a γ -PET prototype, combining PET and Compton camera imaging (Sec. 8.1).

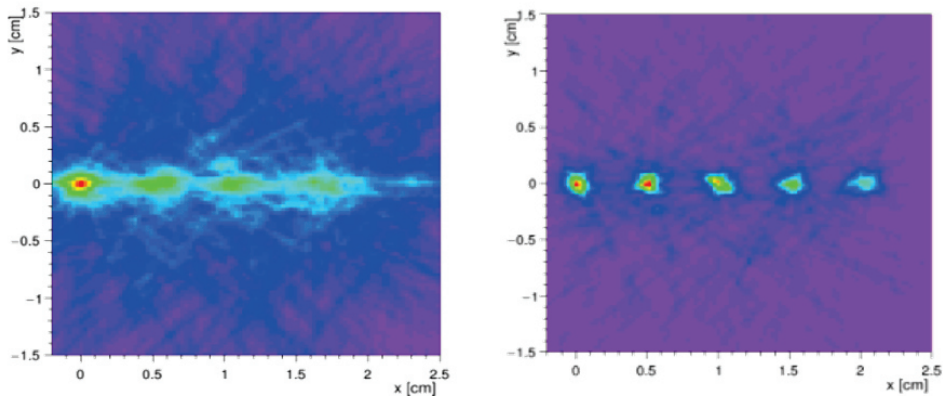


Fig. 5.2: Simulated PET image of five point sources in a PET ring with increasing distance from the center (from left to right) without (left) and with DOI information (right). Image provided by G. Lovatti.

5.2. The Compton camera

Mechanically collimated (Anger-)cameras suffer from low detection efficiencies, due to the absorbing nature⁶ of the collimator. In contrast, PET, as an electronically collimated device, relies on the coincident detection of two γ rays.

In 1974 Todd *et al.* proposed (and later demonstrated) another type of γ camera for medical imaging that relies on the kinematics of Compton scattering to localize γ rays' origins [Todd 1974, Everett 1977].

Such Compton cameras can image individual γ emitting isotopes and provide superior detection efficiencies compared to mechanically collimated systems [Krimmer 2015a, Fontana 2017]. Based on the detection of two successive interactions (Compton scattering with subsequent photoelectric absorption of the scattered γ ray), their general layout consists of two detector stages:

First, a thin scatterer component that aims to maximize the interaction probability for Compton scattering. The second stage, the absorber, is typically built from a high Z material with a thickness optimized for the targeted energy range in order to maximize the probability for photoelectric absorption [Fontana 2017].

The targeted application determines the exact configuration of a potential Compton camera. For range verification in hadron therapy mainly scintillators, semiconductors and gaseous detectors have been investigated [Krimmer 2015a]. Purely scintillator based cameras were, e.g., developed by Llosá *et al.* using three layers of monolithic $\text{LaBr}_3:\text{Ce}$ crystals with SiPM array readout (the MACACO prototype) [Llosa 2012, Llosa 2016] and a capability to resolve Bragg peak shifts of 10 mm [Solevi 2016]. Recently, Munoz *et al.* reported to be able to resolve Bragg peak shifts of only 3 mm using the MACACO II camera, an upgrade of the initial prototype used by Llosa [Munoz 2021]. Kishimoto *et al.* developed a Compton camera using pixelated GAGG scintillators and ran tests using a 70 MeV proton irradiation of water, PMMA and $\text{Ca}(\text{OH})_2$ [Kishimoto 2015, Taya 2016].

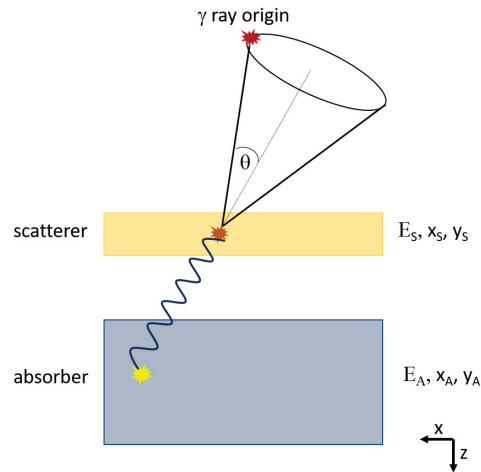


Fig. 5.3: Schematics of a Compton camera's working principle. An incident photon scatters in the scatterer and the energy deposit E_S as well as the interaction position x_S and y_S (and z_S) are measured. The scattered photon is subsequently fully absorbed in the absorber component. Again the energy and the interaction positions are measured. From the Compton kinematics the scattering angle θ can be derived, which spans a Compton cone.

⁶for all photons with oblique incident angles

Combinations of semiconductors, namely several layers of silicon strip detectors, were studied by Krimmer *et al.* using a BGO crystal block as absorber [Roellinghoff 2011, Krimmer 2015a, Krimmer 2015b] and by our group using a monolithic LaBr₃:Ce absorber [Thirolf 2014]. Evaluations of individual components are presented in [Lang 2015, Aldawood 2016, Liprandi 2018] including Compton images of ¹³⁷Cs and ⁶⁰Co point sources (measured in an alternative camera configuration comprising a pixelated GAGG scatterer) in [Liprandi 2018]. A good summary about ongoing investigations of other detector combinations such as Cadmium Zinc Telluride (CZT) scatterers and LSO/BGO absorbers, or fully semiconductor-based cameras of high purity Germanium (HPGe) or CZT is given in [Krimmer 2015b]. However, no further details are given in this thesis since these prototypes are only remotely related to the investigations given in this work.

Independent of the exact camera setup, the vertex of the γ -ray emission can be localized as described in the following: an incident photon scatters on a shell electron of the scatterer material's constituents. The energy deposit E_S and the interaction position x_S and y_S in the scatterer are measured⁷. In an ideal scenario, the residual photon leaves and passes the scatterer without any further interaction and is fully absorbed in the second stage. Here, the residual photon's energy E_A and the interaction positions x_A and y_A are measured. Ideally, the absorber also provides depth-of-interaction (DOI) information so that also the z coordinate of the absorption can be determined. Using E_S and E_A , Compton kinematics allows to derive the scattering angle θ according to

$$\cos\theta = 1 - m_e c^2 \left(\frac{1}{E_A} - \frac{1}{E_S + E_A} \right) \quad (5.1)$$

with θ as the Compton scattering angle, m_e the electron rest mass and c the speed of light. From the scattering angle and the interaction positions, a cone (**Compton cone**) can be drawn. The Compton cone's surface represents all possible γ -ray origins for the given values of $E_{S/A}$ and $x/y/z_{S/A}$.

Similar to the LORs in PET, superimposing multiple Compton cones will eventually yield the γ ray's origin. The method is exemplarily shown for one, two and ten detected photons (emitted from a source located at the center of the field-of-view; indicated by a black cross) with subsequent reconstruction (and intersection) of the Compton cones in Fig. 5.4.

For localizing a γ ray's emission vertex by two interactions, a complete absorption of the scattered photon is necessary, since in ion therapy the initial photon's energy is *a priori* unknown. By requiring at least three interactions⁸, the Compton kinematics

⁷Ideally the z coordinate of the interaction can also be determined. For thin detectors, however, the interaction is assumed to take place in the detector's center.

⁸To do so, multi-layer scatter components are required.

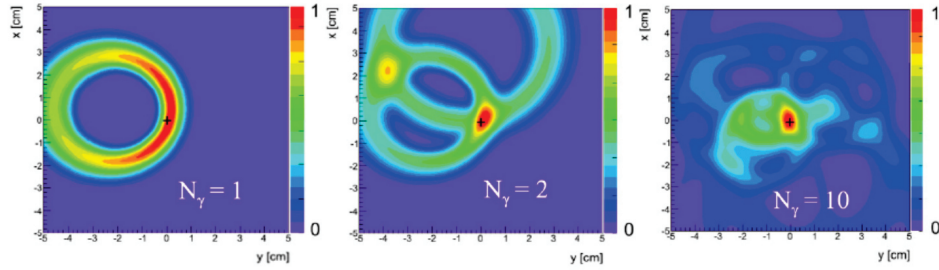


Fig. 5.4: Illustration of the intersection of multiple Compton cones resulting in defining a γ ray's origin. Left: single Compton cone. Center: intersection of two Compton cones. Right: Intersection of ten Compton cones. The γ ray origin is indicated by the black cross [Lang 2015].

of the incident photon is completely defined [Krimmer 2015b]. Alternatively, the recoil electron's trajectory can be measured (electron tracking). Electron tracking allows to also determine the γ ray's emission vertex for incompletely absorbed events, thus improving the efficiency of the Compton camera [Liprandi 2018]. Moreover, the additional kinematical information allows to reduce the Compton cone to an arc, which results (similar to the restriction of the LOR by TOF information) in an increased S/N ratio of the Compton image and, therefore, in a sensitivity improvement of the camera.

The angular resolution measure (ARM) To characterize a Compton camera's imaging quality typically the angular resolution measure (ARM) is stated. Illustratively speaking, the ARM represents the width of a reconstructed Compton cone (see Fig. 5.5).

Under the assumption that Doppler broadening can be neglected (see. Sec. 2.3.2), the uncertainties resulting of a finite width of the Compton cone are due to inaccuracies in the energy determination and finite spatial resolution of the detectors.

Hence, mathematically, the ARM is defined as the difference between (a) the scattering angle θ_{Int} determined by the interaction positions ($x/y_{S/A}$) (accounting for the finite spatial resolution of the detector components)

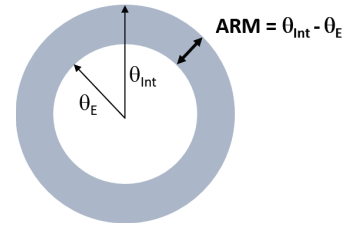


Fig. 5.5: Sketch of a Compton cone to explain the angular resolution measure (ARM) defined as the difference of $\theta_{Int} - \theta_E$

$$\cos\theta_{Int} = \frac{(r_S - r_0) \cdot (r_A - r_S)}{|r_S - r_0| \cdot |r_A - r_S|} \quad (5.2)$$

with r_0 as the emission vertex of the γ rays, r_S and r_A the respective coordinates of the interaction in the scatterer and the absorber and (b) by the energy deposits in the two camera stages θ_E (according to Eq. (2.9); accounting for the camera system's energy

resolution). From Eqs. (2.9) and (5.2) the influence of the spatial and energy resolution of the individual detectors becomes evident and motivates the detailed analysis of and effort to improve the detectors' energy resolution presented in the following chapters [Liprandi 2018].

5.3. γ -PET imaging

Combining the two previously described γ ray detection devices, a Compton camera and a PET scanner, results in a so-called γ -PET device⁹. Such a combined Compton- and PET scanner is capable to detect annihilation photons in a PET-only mode, photons from a single γ ray emitting nucleus (Compton-mode) or, if suitable radioisotopes are used, a triple coincidence (β^+ - γ coincidence) between two annihilation photons and a third gamma (γ -PET)¹⁰[Yoshida 2020]. Especially ^{10}C and ^{14}O are promising candidates for γ -PET in the context of online dose delivery control and range verification, since these isotopes are, like others, products of beam induced fragmentation processes in human tissue.

The limitations of PET, which requires β^+ emitters, and Compton cameras, which suffer from low sensitivity and spatial resolution¹¹, especially when the source-to-detectors distances increase, may be overcome by the detection of triple coincidences [Yoshida 2020, Nakano 2020]. This allows to intersect a LOR with a Compton cone. Other than in the individual imaging methods, where emission centers can only be reconstructed using the intersection of multiple LORs and Compton cones, respectively, the triple coincidence allows to theoretically localize the emission on a single event basis, resulting in a sensitivity improvement compared to the individual imaging techniques. C. Lang could show that already 40 detected triple-coincidences are sufficient to reliably image a sub-millimeter point source [Lang 2014, Lang 2015]. The principle of the γ -PET technique is exemplarily shown in Fig. 5.6, where four arms of Compton cameras (with the absorber serving also as the PET detector) are indicated.

Based on numerical simulations various groups have studied the imaging techniques based on the detection of β^+ - γ coincidences [Grignon 2007, Garcia 2012, Thierolf 2015]. In 2020 Shimazoe *et al.* presented a system for simultaneous PET and Compton imaging. The system, however, did not rely on the detection of triple coincidences in a γ -PET mode, but instead a dual imaging mode to simultaneously monitor positron and individual γ ray emitters [Shimazoe 2020, Uenomachi 2021]. The experimental demonstration of imaging in a triple- γ mode was given by Yoshida *et al.* also in 2020 [Yoshida 2020]. In Sec. 8.1 a prototype based on the four-arm geometry proposed by C. Lang [Lang 2015]

⁹also referred to as Compton-PET or Whole-Gamma Imaging (WGI).

¹⁰The three γ rays originate from a nucleus that undergoes a β^+ decay (two 511 keV annihilation γ rays) followed by a deexcitation of the daughter nucleus under the emission of a third γ ray. Prominent examples of isotopes that provide such a decay characteristics are ^{44}Sc , ^{10}C and ^{14}O .

¹¹For energies below about 500 keV, Fontana *et al.* showed that mechanically collimated systems may outperform Compton cameras in terms of spatial resolution [Fontana 2017].

was commissioned and characterized, that is capable of detecting triple coincidences. Unlike suggested in [Lang 2015], the scatter detector was no Si strip detector, but a pixelated GAGG scintillation array, providing an improved scattering efficiency.

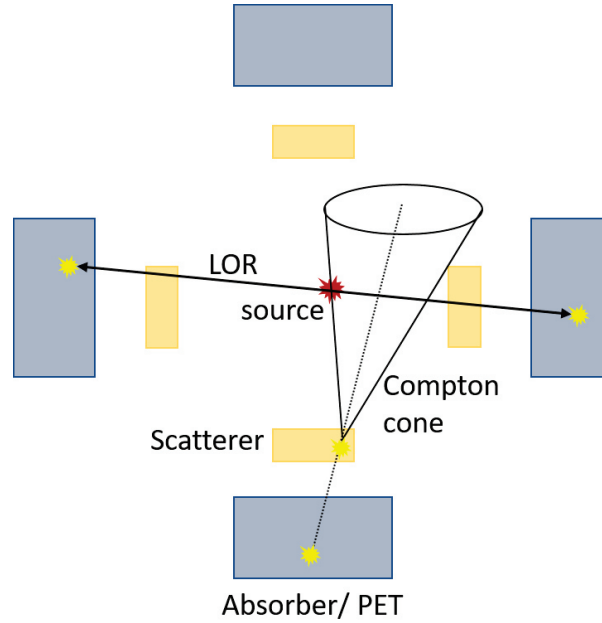


Fig. 5.6: Schematical illustration of the γ -PET technique. The intersection of a LOR and a Compton cone indicates the emission center of the three γ rays.

Part III.

Experimental Methods and Results

This part contains the insights, novelties and developments that have been achieved within the scope of the present thesis. The rationale behind all presented investigations was to build a Compton camera that can potentially also be extended to be used in a γ -PET configuration.

Starting with the scatterer component, a pixelated GAGG scintillation array, the crystal resolvability of all individual crystals of the array will be presented and a detailed comparison between a) a readout with SiPM arrays with 15 μm , 25 μm and 50 μm SPAD sizes and b) KETEK and HAMAMATSU SiPM arrays will be given. Also the energy resolution measured with the respective types of SiPM arrays will be reported and the contribution of the individual crystals to the overall energy resolution of the arrays will be correlated to the crystal's position in the scintillation array.

The absorber component's characterization will include a section about its time resolution in a readout configuration with a) a MA-PMT and b) a SiPM array. A detailed analysis of the energy resolution achieved with a) a SiPM array readout ($3 \times 3 \text{ mm}^2$ and $6 \times 6 \text{ mm}^2$ active channel area) and signal processing/digitization performed by the PETsys TOFPET v2c ASIC, b) a comparison between 25 μm and 50 μm SPAD SiPM arrays, c) a comparison between KETEK and HAMAMATSU SiPM arrays and d) a benchmark when using an individual channel signal processing approach (PETsys TOFPET v2c ASIC; software-wise sum) vs. a hardware-wise generated signal summation will be given. The energy range in which the aforementioned analysis was done spans from 100 keV up to 6.1 MeV, as this is the typical energy range of γ rays detected in the intended camera's applications for γ -PET and prompt- γ imaging. Furthermore, all performed studies were conducted with a) a $\text{LaBr}_3\text{:Ce}$ and b) a CeBr_3 scintillation crystal and the respective performances are compared to each other.

The final section is dedicated to an alternative radiation detector which was initially intended to be used in high-resolution PET, but could as well serve as Compton camera absorber detector. This staggered 3-layer LYSO crystal array provides Depth-of-Interaction information through its layered structure and is therefore capable of improving the Compton camera's image quality. This detector was characterized (as PET detector) by applying the information gained by the previous studies on how to adapt the PETsys TOFPET v2c ASIC's configuration to the properties to a specific detector configuration, differing from the one it has been designed for by the manufacturer. The characterization includes a proof of the crystal resolvability, the detector's energy resolution (including the energy resolution of each layer separately) and the achievable coincidence resolving time.

After the component characterization had been finalized, a first Compton camera prototype was commissioned via two Compton camera arrangements and tested online with carbon (^{10}C , ^{11}C , and ^{12}C) and oxygen (^{14}O , ^{15}O , and ^{16}O) beams at the GSI Helmholtz

III. Experimental Methods and Results

Centre for Heavy Ion Research in Darmstadt.

Compton Camera Components’ Characterization

Contents

6.1. Characterization of the scatterer component	72
6.1.1. Scintillators, photosensors and measurement configuration . . .	72
6.1.2. Crystal identification (flood maps) and spatial resolution . . .	73
6.1.3. Energy Resolution of the GAGG Scatterer	78
6.1.4. Summary	90
6.2. Characterization of the Compton camera absorber component 92	
6.2.1. Scintillators and photosensors	92
6.2.2. Time resolution of the absorber detectors components	95
6.2.3. Energy resolution of the absorber detector components	102
6.3. Conclusion	121

Within the next chapters, at many occasions a comparison between the detector performance in different SiPM photosensor readout configurations will be mentioned. A specific terminology to indicate the respective type of SiPM will be used. For the KETEK SiPM it is of the following form

PX yyzz WA-BBCC

where **X** stands for A:Photomultiplier Array or M:M for a single channel SiPM), yy represents the active area per channel (y [mm] \times y [mm]), zz the microcell size (in μm), A represents the series (e.g. B: blue sensitive or L: low noise) and the BBCC stands for the amount of channels along the x (BB) and y (CC) dimension of the array.

For example a KETEK PA3325WB-0808 is a SiPM array of the blue-sensitive series with 8×8 channels. Each channel has an active area of $3 \times 3 \text{ mm}^2$ and the microcell size is $25\mu\text{m}$.

6.1. Characterization of the scatterer component

In this first section, the characterization of the scatterer detector, a **Gadolinium Aluminium Gallium Garnet** ($\text{Ce}:\text{Gd}_3\text{Al}_2\text{Ga}_3\text{O}_{12}$) (GAGG) crystal array, will be presented. The evaluations will focus on the achievable spatial and energy resolution in various (with microcell sizes between $15\ \mu\text{m}$ and $50\ \mu\text{m}$) SiPM array readout configurations.

6.1.1. Scintillators, photosensors and measurement configuration

The specific Compton camera scatterer studied in this section is composed of a pixelated GAGG crystal array [C&A 2020a] comprising 16×16 individual crystals optically isolated by $150\ \mu\text{m}$ thick BaSO_4 . The crystal dimensions are $1.45 \times 1.45\ \text{mm}^2$ (front face; along the x and y dimension) and 6 mm height. The center-to-center crystal pitch is 1.6 mm (Fig. 6.1 (left)).

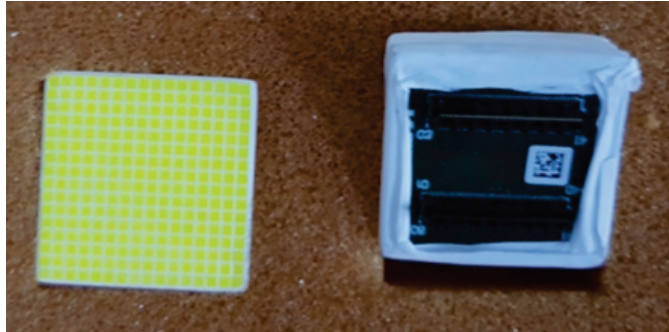


Fig. 6.1: Picture of a GAGG crystal array with optical reflector visible inbetween the individual crystals (left) and a GAGG array coupled to a SiPM array with teflon wrapping around the contact area to suppress light loss (right).

As photosensors, SiPM arrays of the two manufacturers KETEK and HAMAMATSU were investigated. All SiPM arrays had 8×8 channels and active channel areas of $3 \times 3\ \text{mm}^2$. SiPM microcell sizes ranged from $15\ \mu\text{m}$, $25\ \mu\text{m}$, $35\ \mu\text{m}$ to $50\ \mu\text{m}$ for the KETEK SiPM arrays [Ketek 2018, Ketek 2020a, Ketek 2020b, Ketek 2020c, Ketek 2021a]. Furthermore, in a configuration with artificially enlarged SiPM active areas (see Sec. 6.2.3) also a $47\ \mu\text{m}$ microcell size type array was used. Only one type of HAMAMATSU SiPM type (of the S14161 series) with $50\ \mu\text{m}$ microcells was used [Hamamatsu 2020].

In most cases, the scintillator arrays were coupled using optical grease (Saint Gobain BC-631 [Saint Gobain 2021b]/ Eljen technology EJ-550 [EJ 2021]). Furthermore, the detector performance of the $50\ \mu\text{m}$ SPAD SiPM arrays was investigated using a silicon rubber (RTV) sheet (Shin Etsu KE-42-T) with 1 mm thickness. The thicker light guide was motivated by a potential improvement of a GAGG scintillator array's energy resolution if the light spread over the SiPM array is improved and SiPM saturation is reduced. This influence of the light guide thickness on the flood map quality and the energy resolution was, e.g., studied by Takyu *et al.* [Takyu 2020]. The contact side

surface between the crystal arrays and the SiPM array was wrapped with several layers of teflon (see Fig. 6.1 (right)) and finally wrapped in black tape.

The electronic readout was performed using the PETsys Evaluation Kit comprising the TOFPET v2c ASIC [Petsys 2015]. The gain of the transimpedance amplifier (TIA) of the charge branch implemented in the ASIC was set to 3.65. The ASIC's trigger logic was operated in the nominal mode (see Sec. 4.2) using three discriminators to set the acquisition thresholds. Two thresholds in the timing branch (th_{T1} and th_{T2}) set the timestamp and trigger the acquisition of the signal digitization (via a time-over-threshold method) in the timing branch. For signals capable to exceed both timing thresholds and a third energy threshold (th_e) in the energy branch, also charge integration in the charge branch is triggered. Only events which exceed all three thresholds are considered as valid and further processed in the postprocessing. The minimal "steps" with which the thresholds can be set are given by the least significant bit (LSB). The value ($disc_lsb_x$) can be set individually for each threshold. The relation between digital value and mV units can be found in [Petsys 2019]. The respective used ASIC acquisition thresholds for the different detector assemblies are listed in Tab. 6.1. The event grouping time was set to 75 ns.

Parameter	PA3315WB -0808	PA3325WB -0808	PA3350WB -0808	S14161 -3050HS-08
OV (V)	5.0 V	5.0 V	5.0 V	2.7 V
disc lsb_{T1}	60 (\approx 3.5 mV)	60 (\approx 3.5 mV)	60 (\approx 3.5 mV)	60 (\approx 3.5 mV)
th_{T1}	5 (\approx 17.5 mV)	5 (\approx 17.5 mV)	5 (\approx 17.5 mV)	5 (\approx 17.5 mV)
disc lsb_{T2}	56 (\approx 8.0 mV)	56 (\approx 8.0 mV)	52 (\approx 11.0 mV)	54 (\approx 10.0 mV)
th_{T2}	10 (\approx 80.0 mV)	18 (\approx 144.0 mV)	26 (\approx 286.0 mV)	50 (\approx 500.0 mV)
disc lsb_{T2} (RTV)			56 (\approx 8.0 mV)	54 (\approx 10.0 mV)
th_{T2} (RTV)			40 (\approx 320.0 mV)	50 (\approx 500.0 mV)
disc lsb_E	52 (\approx 11.0 mV)	52 (\approx 11.0 mV)	46 (\approx 16.5 mV)	50 (\approx 13.0 mV)
th_E	8 (\approx 88.0 mV)	16 (\approx 165.0 mV)	5 (\approx 82.5 mV)	21 (\approx 273.0 mV)
disc lsb_E (RTV)			54 (\approx 10.0 mV)	50 (\approx 13.0 mV)
th_e (RTV)			8 (\approx 80.0 mV)	17 (\approx 221.0 mV)

Tab. 6.1.: ASIC LSB values and multiplication factor for the characterization measurements conducted with the indicated SiPM arrays (PA3315WB-0808, PA3325WB-0808, PA3350WB-0808 and S14161-3050HS-08). The used $disc_{lsb}$ and threshold values used for the two 50 μ m SPAD SiPM are shown in blue.

6.1.2. Crystal identification (flood maps) and spatial resolution

The spatial resolution of pixelated scintillator arrays using a light sharing readout approach can be determined by the acquisition of a "flood map", i.e. a 2D crystal response diagram where the calculated interaction positions of incident γ rays are accumulated. The irradiation is performed using an uncollimated radiation source (flood irradiation) thus motivating the term "flood map". If all individual crystals can be resolved in a detector, the spatial resolution is determined by the array's crystal pitch. The flood map can be generated by an event-wise Anger-type position calculation performed on

the digitized signals of all firing SiPM triggered within one initial γ -hit event. First, the total detected charge of each row and column of the SiPM array is calculated according to

$$\begin{aligned} Row_i &= \sum_{j=1}^8 C_{ij} \\ Col_j &= \sum_{i=1}^8 C_{ij} \end{aligned} \tag{6.1}$$

with i and j being the i^{th} row and j^{th} column on the SiPM array, respectively, and C_{ij} is the integrated charge measured at the SiPM pixel (i,j) .

The x and y position of the γ interaction is subsequently determined by calculating the weighted sum of all rows and columns, respectively, normalized to the total detected charge according to

$$\begin{aligned} x &= \frac{\sum_{j=1}^8 j \cdot Col_j}{E_\gamma} \\ y &= \frac{\sum_{i=1}^8 i \cdot Row_i}{E_\gamma} \end{aligned} \tag{6.2}$$

with x and y representing the position of a γ interaction in coordinates of the SiPM array channels and E_γ being the total energy deposit of the γ ray in the detector. The calculated hit positions of all detected γ rays are plotted in a 2D histogram, resulting in the flood map. The application of an energy window for event selection ensures that only fully absorbed γ rays (photo peak events) are considered to fill the flood map.

The flood maps of a GAGG array coupled (by optical silicon grease) to a KETEK PA3315WB-0808 (Fig. 6.2 (a)), PA3325WB-0808 (Fig. 6.2 (b)), PA3350WB-0808 (Fig. 6.2 (c)) and a HAMAMATSU S14161-3050HS-08 (Fig. 6.2 (d)) SiPM array are displayed in Fig. 6.2. Furthermore, the corresponding x - and y -projections of the flood maps are shown above and right of the flood map. For all measurements an acquisition time of 3600 s with a 219 kBq ^{137}Cs source was used. For event selection an energy window around the photo peak ($600 \text{ keV} < E_\gamma < 720 \text{ keV}$) was applied to the data¹. For the two SiPM arrays with 50 μm APDs (PA3350WB-0808 (Fig. 6.2 (e)) and S14161-3050HS-08 (Fig. 6.2 (f))) additionally the flood maps acquired with the crystal array coupled to the SiPM array are shown using an RTV silicon rubber sheet (1 mm thickness) as light guide. To ensure comparability between all shown flood maps (despite the different breakdown voltages and performance characteristics) the SiPM arrays were biased at the recommended overvoltage of 5.0 V (KETEK) and 2.7 V (HAMAMATSU).

¹All flood maps were generated from energy calibrated data.

6. Compton Camera Components' Characterization

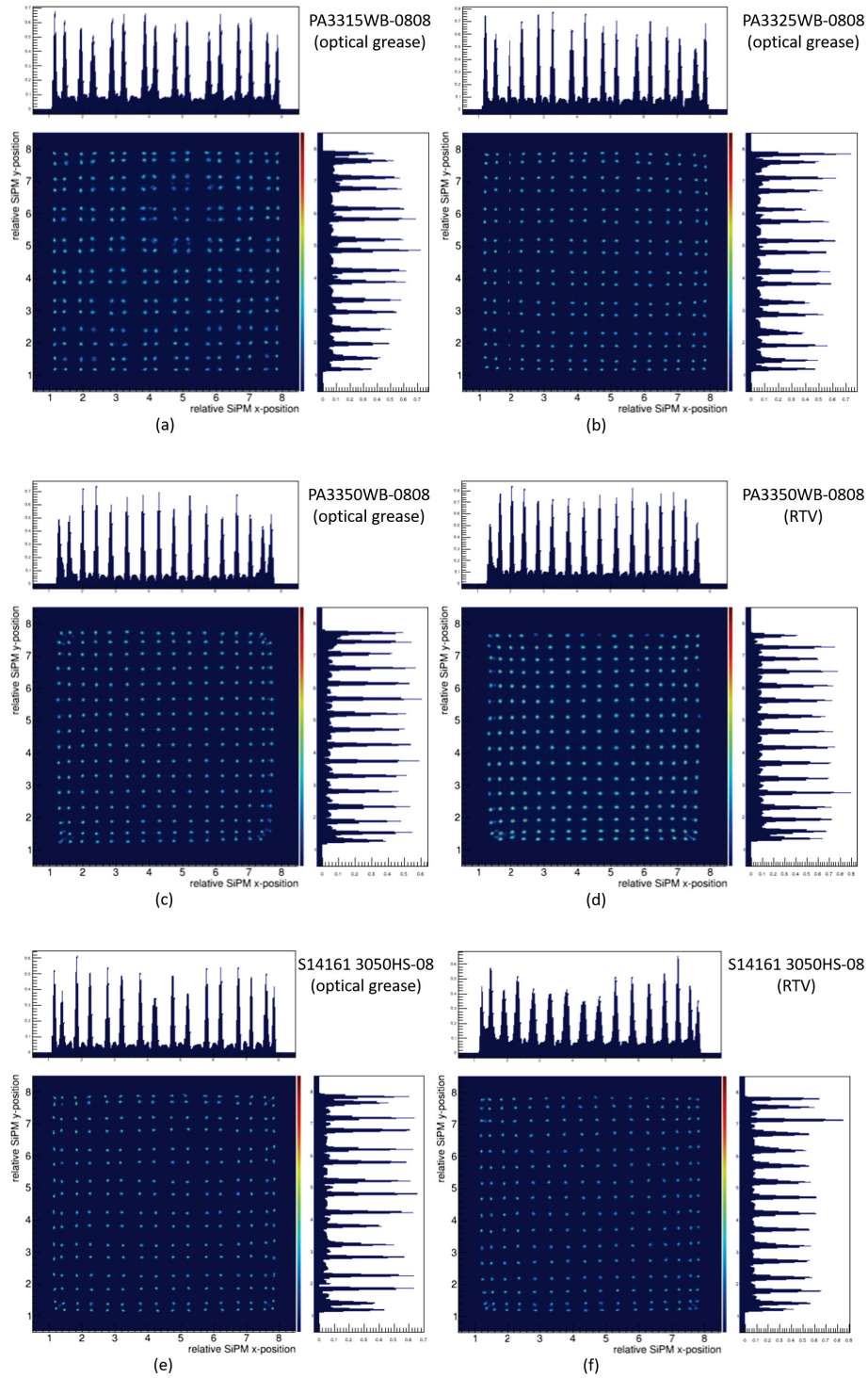


Fig. 6.2: Flood map and corresponding x- and y-projections of the crystal rows and columns acquired with a 16×16 GAGG array and a KETEK PA3315WB-0808 (a), PA3325WB-0808 (b), PA3350WB-0808 (c) all coupled using optical grease (Saint Gobain BC-631), while the crystal array coupling a KETEK PA3350WB-0808 used 1 mm of RTV silicon rubber sheet (Shin-Etsu KE-42-T) (d) (biased at 5.0 V overvoltage). Flood maps acquired using the HAMAMATSU S14161 3050HS-08 coupled to the crystal array using optical grease (e) and RTV sheet (f) are shown in the bottom row. Data were taken by a 1 h flood irradiation using a ^{137}Cs (219 kBq) radiation point source.

All flood maps of Fig. 6.2 (including their projections) show clearly identifiable crystal spots of all 256 individual crystals. Therefore, for the spatial resolution of all detector assemblies a value of 1.6 mm can be given.

Furthermore, there are two observations worth mentioning: a) the flood maps measured with the PA3315WB-0808, PA3325WB-0808 and S14161-3050HS arrays (coupled with optical grease) show sub-groups of 2×2 crystals and b) especially for the measurements conducted with the $50 \mu\text{m}$ APD SiPM arrays and coupling by optical grease, crystals of the outermost rows and columns appear to be shifted towards the more inner crystals (squeezed flood map). For the S14161-3050HS-0808 this effect is partially attributed the fact that the total SiPM array's area is slightly smaller than that of the scintillator array so that an increased light loss is expected for these edge crystals.

From further investigations, both effects can be correlated to the amount of triggered SiPMs per event:

Evidently, the clustering in sub-groups of 2×2 crystals is most prominent for the SiPM array with the smallest SPADs, while for the PA3350WB-0808 it cannot be observed at all. While the distribution of the scintillation photons is determined by the crystals' properties and light guide's thickness, the amount of triggered SiPM channels is mainly determined by the signal amplitude fed in the individual electronic channels.

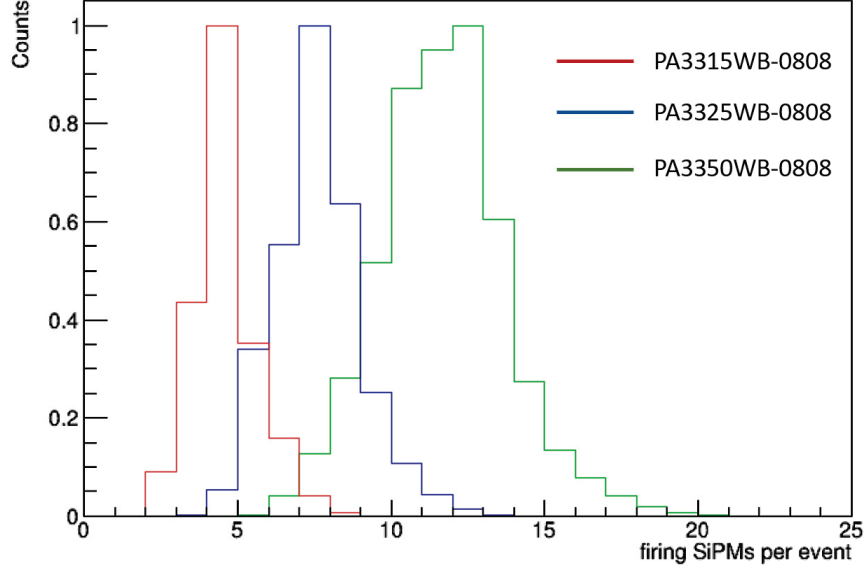


Fig. 6.3: Comparison of the number of firing SiPMs per fully absorbed 511 keV γ ray for a GAGG scintillator readout configuration using the KETEK PA3315WB-0808, PA3325WB-0808 and PA3350WB-0808 arrays.

If the signal amplitude is too low to exceed the ASIC thresholds, the signal digitization is not triggered and the photons detected in this respective channel will not

contribute to the overall event signal. Therefore, this channel is not considered for the Anger calculation. For a given light yield and point spread function, there are SiPM channels (at some distance from the crystal in which the γ interaction has occurred), for which the amount of photons reaching that SiPM channel is low. Hence, a high SiPM gain is required which determines whether the signal may exceed the trigger threshold and eventually will be digitized or not. For such scenarios, only a few SiPM channels contribute to the overall signal. The dominant fraction of the overall signal comes from the SiPM right below the crystal in which the interaction took place, hence, causing the structure of the SiPM array (8×8) to be visible in the flood map.

Fig. 6.3 shows the distribution of digitized SiPM signals from fully photoabsorbed 511 keV γ rays measured with a PA3315WB-0808, PA3325WB-0808 and PA3350WB-0808 array. As can be seen, a 511 keV photon triggers mainly between 3 and 5 SiPMs on the PA3315WB-0808, but between 9 and 13 for most interactions on the PA3350WB-0808 array.

Besides increasing the gain of the SiPM array, also the use of a thicker layer of light guide increases the number of digitized SiPM channels. This is due to a more uniform distribution of scintillation photons on the SiPM array surface. The effect can be seen by comparing Figs. 6.2 (d) and (f), where around 0.1 mm of optical grease and 1 mm of RTV silicon rubber have been used to couple the GAGG crystal array to the SiPM array. As the array with the highest gain of all four investigated types, the PA3350WB-0808 is the only one that does not show a clustering of the crystal response spots.

The second observation, the distortions of the edge crystals especially in measurements with the two $50 \mu\text{m}$ SiPM arrays, can also be related to the amount of firing SiPM. However, here the light can only distribute over fewer SiPM, because beyond the edge there no more SiPM channels. As a result, the SiPM structure becomes visible again. This effect is amplified by the loss of energy information (light loss). The light loss, however, is not only caused by the non-perfect reflectivity of the teflon cover at the crystal edges, but also by saturation of the few SiPMs detecting light due to the large fraction of scintillation photons that is indeed reflected from the teflon wrapping back onto the edge SiPMs. This effect also manifests in the photo peak being shifted towards smaller QDC channels in the uncorrected energy spectra of these edge crystals, compared to more central ones. As a consequence, the individual crystal spectra have to be corrected for non-linearities, inhomogeneities and saturation before applying a global energy window to draw the flood maps with best quality.

However, both aforementioned effects can be corrected in Compton and PET measurements, so that the data will not be negatively influenced by these effects.

A comparison of the flood maps between the two $50 \mu\text{m}$ APD SiPM arrays of the two manufacturers is given in Fig. 6.4. While the HAMAMATSU S14161-3050-08 shows

6.1. Characterization of the scatterer component

a minor clustering of the crystal response (due to the slightly reduced gain compared to the KETEK PA3350WB-0808 as can also be seen in the right panel Fig. 6.4), the flood maps acquired with both SiPM arrays show a clearly circular crystal response with well separated crystal spots. In addition to the flood maps, Fig. 6.4 shows the integral energy spectra of a ^{22}Na source acquired with the two SiPM arrays (left panel).

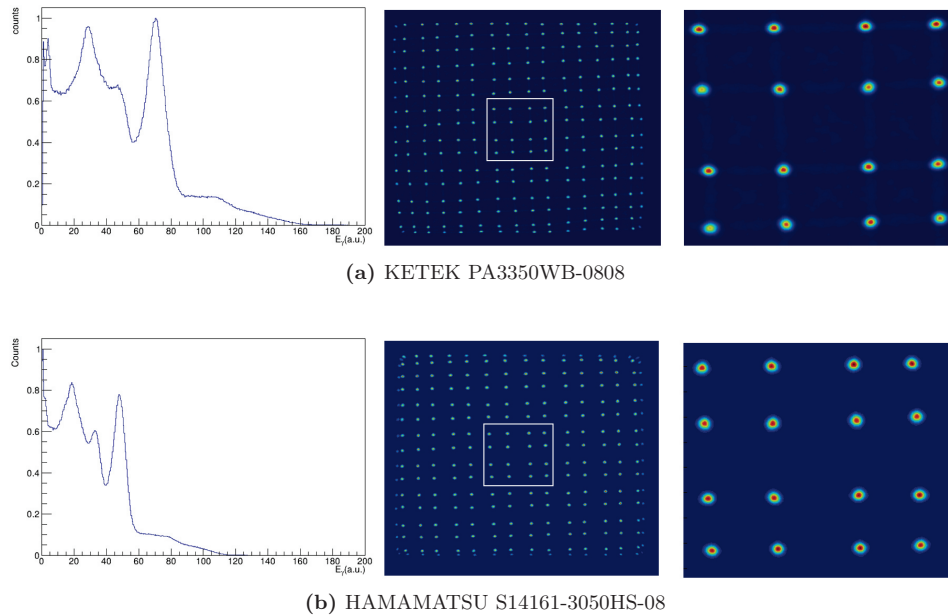


Fig. 6.4: Comparison of a GAGG array's integral energy spectra obtained from a ^{22}Na flood irradiation and the corresponding flood maps acquired with a KETEK PA3350WB-0808 (a) and a HAMAMATSU S14161-3050HS-08. The most right panel in each row is a zoom in the central region of the flood map within the region is indicated by the white square.

6.1.3. Energy Resolution of the GAGG Scatterer

Scintillation detectors provide the information about the energy deposit of an interacting γ ray by a conversion process. As described in Sec. 3.1, the response of a scintillator to a certain energy deposit within the crystal is determined by its light yield and results in the emission of a well defined amount of optical photons. These photons are subsequently collected by the photosensor whose output signal is further processed and finally digitized. The digitizer typically provides the energy information in digital units with the exact value being determined by the digitizer's dynamics (in bits) defining the achievable resolution and the initially detected energy. However, these digital values need to be converted into physically meaningful energy units. Moreover, potential non-linearities occurring during the detection process (e.g. by non-linear detector response, SiPM saturation, integrator non-linearities, etc.) need to be determined and the energy response needs to be calibrated. In contrast to single channel or monolithic detectors (one single signal channel), the energy response of the detector has to be calibrated sep-

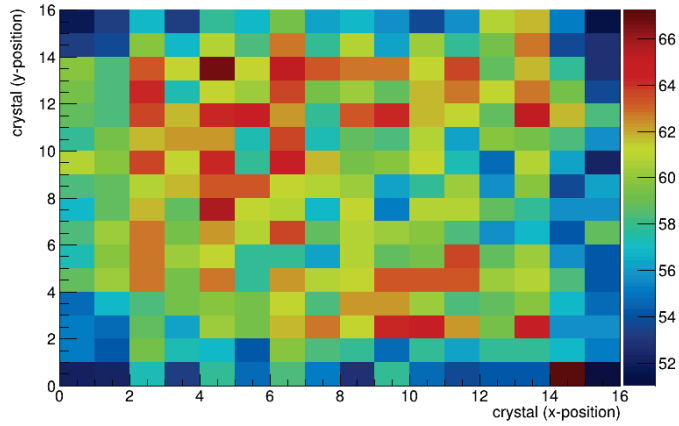


Fig. 6.5: Uniformity map of detected peak positions (662 keV photo peak of ^{137}Cs) of the 256 crystals of a GAGG scintillation array read out by a KETEK PA3315WB-0808 SiPM array biased at 5.0 V OV. The measured charge values (color coded) are displayed in arbitrary units and obtained by the summation of the charge of all firing and digitized SiPMs on the array.

arately for each contributing channel. This is the case no matter if the detector is built from an array of one-by-one coupled crystals or a light sharing approach is used, where the scintillation light distributes over several photosensor channels. The necessity of corrections (here gain matching) is illustrated in Fig. 6.5, which shows a 2D map of the 662 keV photo peak (of ^{137}Cs) positions (in a.u.) of a 16×16 GAGG array when read out by a KETEK PA3315WB-0808 SiPM array. The peak positions of the individual crystals show a variation of about 10 % around the mean value.

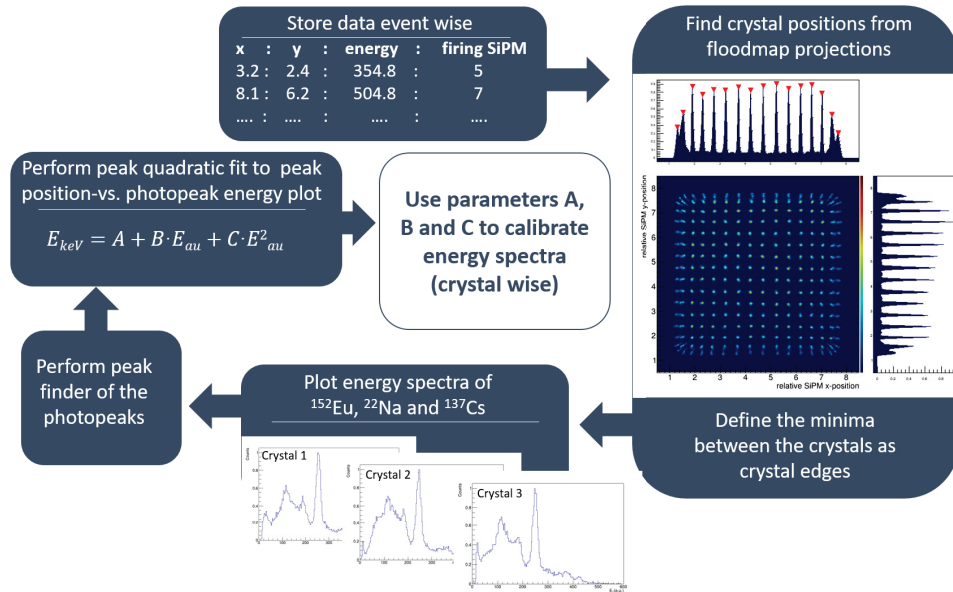


Fig. 6.6: Workflow chart to demonstrate the individual steps performed to linearize and calibrate the 256 GAGG crystal's energy response.

As a consequence, the overall energy resolution of a crystal array is not directly acces-

sible, or only in a blurred manner (by inhomogeneities). In order to perform a gain uniformity and non-linearity correction to the detector response, a semi-automatic method was developed, where the correction is performed automatically as a ROOT routine, but allows to access and potentially correct parameters manually at several points of the routine. The routine's workflow chart is pictured in Fig. 6.6 and executes the following steps sequentially:

1. The raw data containing all triggered SiPM channels (ordered eventwise) are processed, e.g., by calculating the photon interaction position (by an Anger-type calculation) and the full energy deposit of the initial γ ray hit in the crystal. Including the number of firing and digitized SiPMs, the data are stored in a ROOT NTuple. For each used γ source a separate data set (NTuple) is generated.
2. The data of a ^{22}Na source measurement are used to create a flood map including its x- and y-projections. From the two projection histograms, the centroid position of each crystal array rows and columns is searched. The mean value between two neighboring rows and columns, respectively, is taken as the position of the crystal rows' and columns' edges. *This step can alternatively be executed manually by retrieving the crystal position from the flood map using ROOT's graphical cut (TCutG functionality) [ROOT 2021]. At this point, the found crystal edges can manually be narrowed, in order suppress Compton scattered γ rays (that are subsequently fully absorbed in a neighboring crystal) in the measured energy spectra. This method is used to calculate the energy resolution of the detector.*
3. The measured energy spectra (with ^{152}Eu , ^{22}Na and ^{137}Cs) of each individual crystal are plotted and the photo peak positions of the 121 keV, 344 keV, 511 keV, and 662 keV transitions are searched by a peakfinder routine and stored for each crystal. *The found peak positions are written to an ASCII file, to allow for manual correction if necessary.*
4. A peak position vs. γ -ray energy graph is drawn and a quadratic fit (according to Eq. (6.3)) is applied for each individual crystal.
5. The obtained fit parameters (A, B and C) for each crystal are stored in a parameter file (ROOT format).
6. Optional: The parameters can be used to apply an event-wise quadratic correction to the measured energy and the resulting 256 energy spectra for each used radiation source are stored. Furthermore, another data set in ROOT (NTuple format) that contains the interaction position and calibrated energy can be stored according to

$$E_{keV} = A + B \times E_{a.u.} + C \times E_{a.u.}^2 \quad (6.3)$$

SiPM overvoltage dependency of the relative energy resolution For SiPMs, the performance characteristics strongly depends on the applied overvoltage. In general, there are effects causing the relative energy resolution to improve with higher overvoltages, such as a higher PDE and an increasing gain (in configurations where many individual SiPMs contribute to the total detected signal and therefore need to exceed a trigger threshold individually), but other effects have a deteriorating influence on the signal, such as an increased contribution of noise effects like dark count rate (DCR) and cross talk. These counteracting influences on the relative energy resolution make it a priori difficult to determine the best overvoltage for energy resolution measurements without a systematic investigation. Therefore, prior to a detailed investigation of the energy resolution, the best overvoltage for energy resolution measurements was determined for the KETEK standard SiPM array type (PA3325WB-0808). The relative energy resolution was determined by an integral spectrum measured at 511 keV and 662 keV obtained at SiPM overvoltages of 4.0 V, 4.5 V, 5.0 V, 5.5 V and 6.0 V, respectively. For both energies the minimum of the relative energy resolution was found at 5.0 V (Fig. 6.7), which is the recommended overvoltage by KETEK [Ketek 2020c].

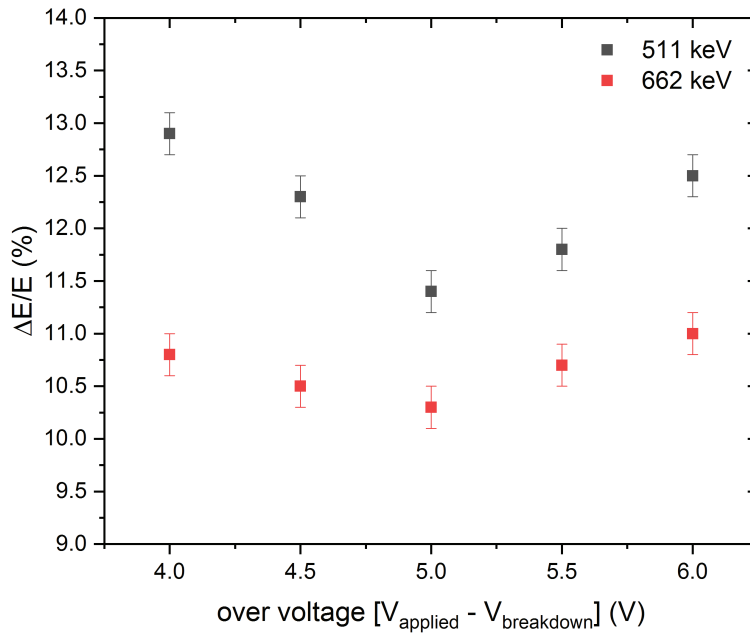


Fig. 6.7: Relative energy resolution of one GAGG scintillation array at 662 keV obtained from integral energy spectra². The shown energy resolution was obtained for a GAGG scintillation array read out by a PA3325WB-0808 SiPM array at varied overvoltages between 4.0 and 6.0 V in voltage steps of 0.5 V.

Energy Resolution at 511 keV and 662 keV In order to calculate the crystal array’s energy resolution, the 256 calibrated energy spectra are drawn into one histogram (integral energy spectrum) from which the relative energy resolution of the detector was obtained. The relative energy resolution of the GAGG array was determined at γ -ray energies of 511 keV and 662 keV, respectively. Furthermore, different SiPM types were investigated (KETEK PA3315WB-0808, PA3325WB-0808, PA3350WB-0808 and HAMAMATSU S14161-3050HS-08). All SiPM arrays were biased at the overvoltage that is recommended by the vendor (KETEK: 5.0 V OV; HAMAMATSU: 2.7 V OV). The obtained results are summarized in Tab. 6.2 (top part) for the γ energies of 511 keV and 662 keV. As for the flood maps, for the 50 μm APD SiPM arrays the energy resolution was also obtained when a 1 mm RTV sheet was used as light guide.

The best relative energy resolution was obtained with the PA3325WB-0808 (10.3 ± 0.1 %) and the S14161-3050HS-08 (10.2 ± 0.3 %) for the detector configurations with optical grease as light guide, and with the S14161-3050HS-08 (9.9 ± 0.3 %) when using 1 mm of RTV sheet as light guide.

	PA3315WB -0808	PA3325WB -0808	PA3350WB -0808	S14161 -3050HS-08
inclusive spectra [optical grease (BC-430)]				
at 511 keV	12.7 ± 0.1	10.5 ± 0.1	12.7 ± 0.1	11.3 ± 0.3
at 662 keV	11.1 ± 0.1	10.3 ± 0.1	11.2 ± 0.3	10.2 ± 0.3
inclusive spectra [1 mm RTV]				
at 662 keV			11.0 ± 0.1	9.9 ± 0.3
individual spectra [optical grease (BC-430)]				
at 662 keV	10.8 ± 1.1	10.0 ± 0.8	10.5 ± 0.8	10.4 ± 1.4
individual spectra [1 mm RTV]				
at 662 keV			10.7 ± 1.0	9.8 ± 0.9

Tab. 6.2.: Summary of the measured relative energy resolutions of the GAGG scintillation array at 511 keV and 662 keV for all investigated SiPM arrays (PA3315WB-0808, PA3325WB-0808, PA3350WB-0808 and S14161-3050HS-08) at the recommended overvoltage of 5.0 V (KETEK) and 2.7 V (HAMAMATSU). The measured energy resolution was determined by the inclusive spectra (top rows) and as an average value from all 256 individual crystals’ energy resolutions (bottom rows). For the 50 μm APD SiPM array under study the energy resolution was also determined when using 1 mm RTV as light guide to reduce SiPM saturation, which is displayed below the values obtained from measurements with optical grease coupling.

Spatial Dependency of the Energy Resolution *The results of the following paragraph were obtained partially in the framework of a BSc project [Zhou 2020] supervised by the author.*

¹All 256 individual spectra are filled into one common histogram. Linearity and saturation corrections, however, were still applied on individual channel basis.

²All 256 individual spectra are filled into one common histogram. Linearity and saturation corrections, however, were still applied on individual channel basis.

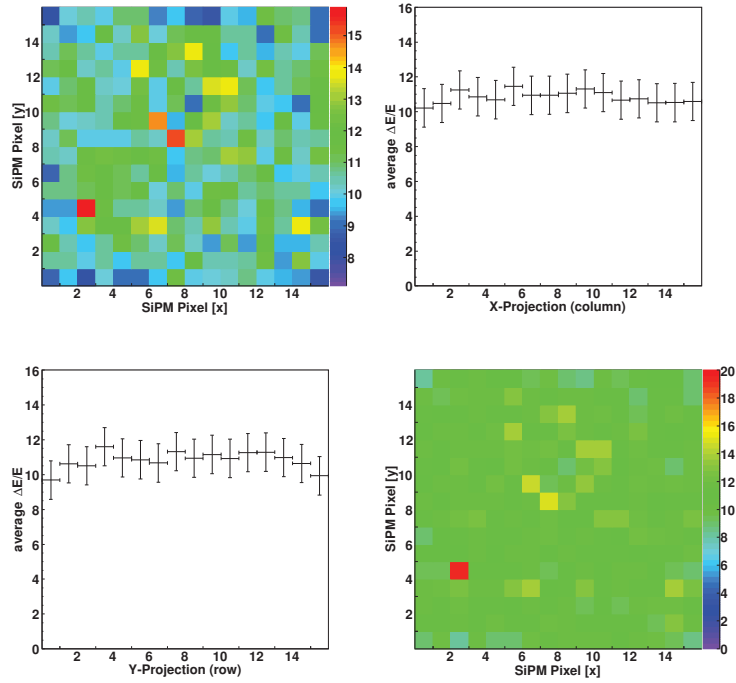
In addition to the integral energy resolution, also the spatially dependent relative energy resolution was measured, i.e., it was determined individually for each of the 256 crystals and plotted in a 2D map at the corresponding position. Fig. 6.8 shows the obtained 2D maps and the average value of each row and column as well as zoomed 2D maps (top left maps of each panel) of the GAGG crystal array with the PA3315WB-0808 (a), PA3315WB-0808 (b), PA3315WB-0808 (c,e) and 14161-3050HS-08 arrays (d,f). The data were obtained from 1.5 hour flood irradiations of the detectors with a ^{137}Cs source and the crystal selection was set such that only events found in the circular crystal response spot were selected, while the region inbetween the bright crystal spots was spared and these events (typically originating from multiple scattering) were rejected. Again, for the 50 μm SPAD SiPM arrays the energy resolution was also obtained when a 1 mm RTV silicon rubber sheet was used as light guide.

For all investigated detector configurations, a flat distribution of the average relative energy resolution of each column and row can be observed within the uncertainty. Except for the measurement conducted with the PA3325WB-0808 array, where the edge rows show a superior energy resolution compared to the center regions, no clear trend from center to edge crystals could be observed. Depending on the SiPM array under study, the inhomogeneity is of the order of 1.0 % (FWHM) for all SiPM arrays. From the fact that all six measured 2D energy resolution maps look very different in a detailed view, a strong influence of the SiPM array coupling on the specific energy resolution of an individual scintillation crystal can be concluded, since there is no other repeating pattern observable.

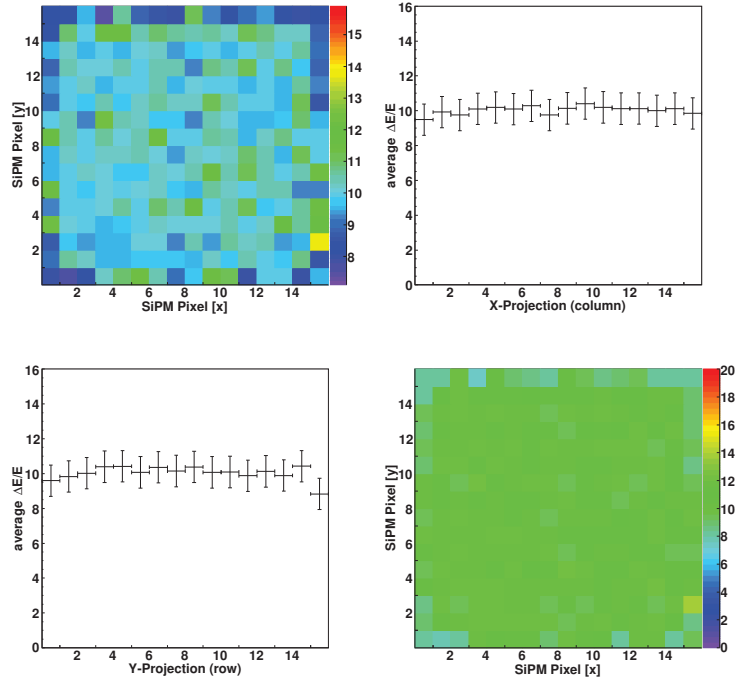
From the 256 individual relative energy resolution values, the overall energy resolution of the detector can also be calculated as the mean value of the distribution. The obtained values are superior compared to the ones obtained from an integral energy spectrum, as indicated by the variation of the individual values via their standard deviations. In contrast, this variation broadens the photopeak in the integral spectra, which causes the energy resolution to appear blurred. The GAGG array's energy resolution obtained at 662 keV from individual crystals is listed in Table 6.2 (bottom row). The best overall energy resolution obtained by this method was $10.0 \pm 0.8\%$ obtained with the PA3325WB-0808 when comparing the detector configurations where optical grease has been used and $9.8 \pm 0.9\%$ with the S14161-3050HS-08 (with 1 mm RTV as light guide) as overall best value.

Summary of the energy resolution A systematic investigation of the energy resolution of the 16×16 GAGG scintillator array intended to be used as Compton camera scatterer showed the best overvoltage to be applied to a PA3325WB-0808 array of 5.0 V (as recommended by the manufacturer KETEK). Using this voltage for all further investigations, it was found that the best energy resolution obtained from all KETEK arrays was reached with the PA3325WB-0808 ($10.0 \pm 0.8\%$) using the average value of the energy resolution derived from all 256 individual crystals. The overall best energy resolution of

6.1. Characterization of the scatterer component



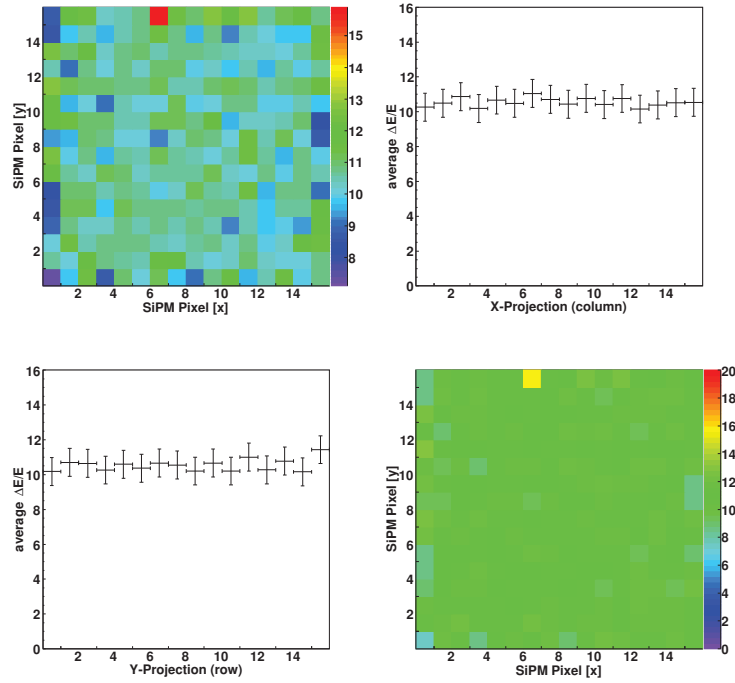
(a) PA3315WB-0808



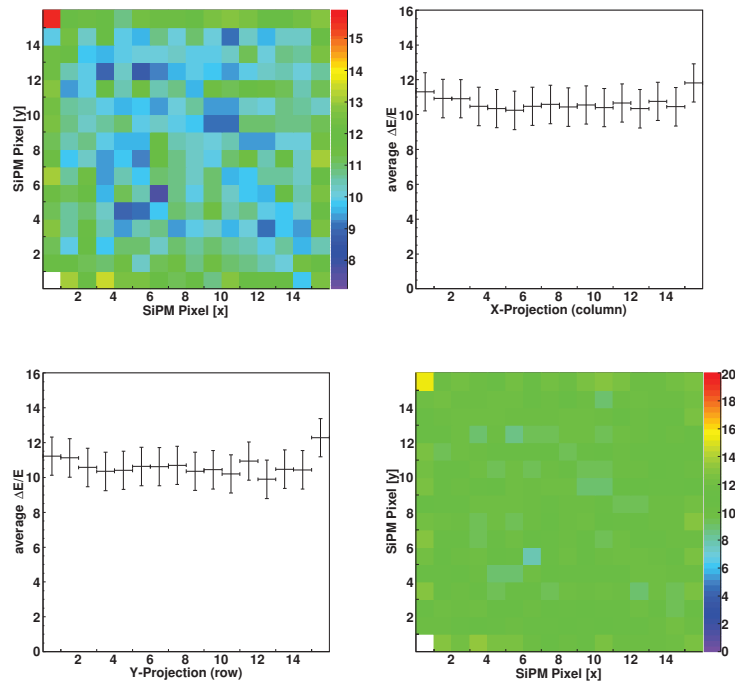
(b) PA3325WB-0808

Fig. 6.8: Measured relative energy resolution ($\Delta E/E$) of the 256 individual crystals of the GAGG scintillator array (color coded) and projections along the rows and columns acquired with a 16×16 GAGG array and a KETEK PA3315WB-0808 (a) and PA3325WB-0808 (b) (biased at 5.0 V overvoltage). Data were taken by a ^{22}Na flood irradiation for 1 hour. The plot in the top left corner shows the results with a more narrow color scale compared to the graphic in the bottom right.

6. Compton Camera Components' Characterization



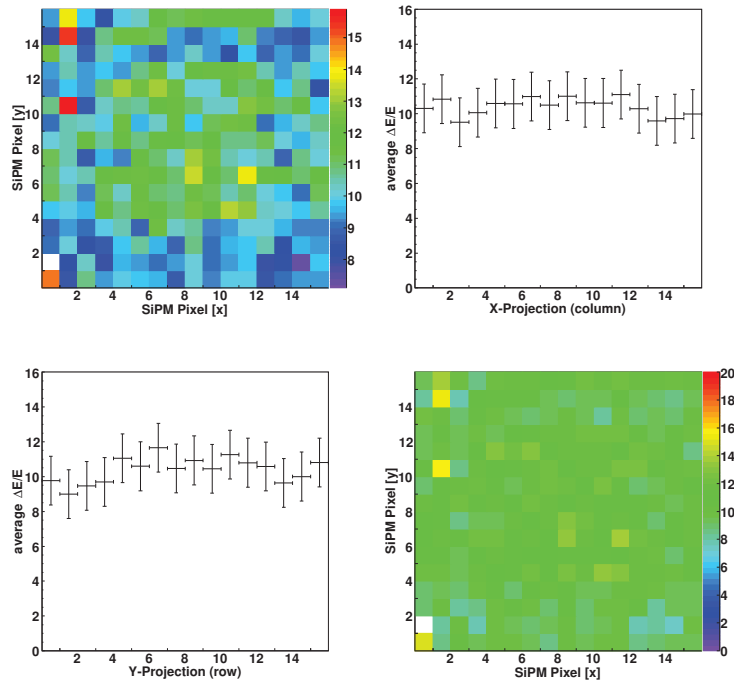
(a) PA3350WB-0808



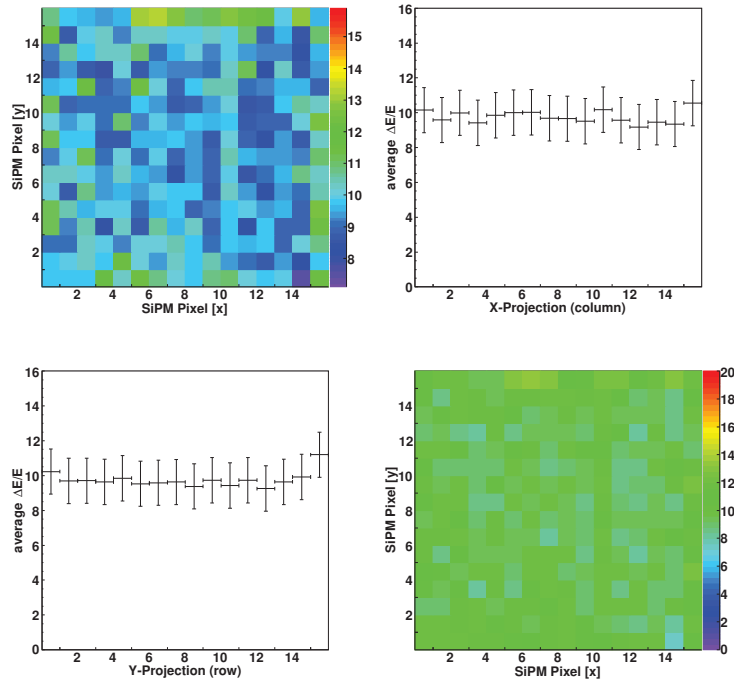
(b) PA3350WB-0808 (1 mm RTV)

Fig. 6.9: Measured relative energy resolution ($\Delta E/E$) of the 256 individual crystals of the GAGG scintillator array (color coded) and projections along the rows and columns acquired with a 16×16 GAGG array and a KETEK PA3350WB-0808 array coupled with optical grease (a) and 1mm of RTV silicon rubber sheet (b) (biased at 5.0 V overvoltage). Data were taken by a ^{22}Na flood irradiation for 1 hour. The plot in the top left corner shows the results with a more narrow color scale compared to the graphic in the bottom right.

6.1. Characterization of the scatterer component



(a) S14161-3050HS-08



(b) S14161-3050HS-08 (1 mm RTV)

Fig. 6.10: Measured relative energy resolution ($\Delta E/E$) of the 256 individual crystals of the GAGG scintillator array (color coded) and projections along the rows and columns acquired with a 16×16 GAGG array and a HAMAMATSU S14161-3050HS-08 MPPC array coupled with optical grease (a) and 1 mm of RTV silicon rubber sheet (b) (biased at 2.7 V overvoltage). Data were taken by a ^{22}Na flood irradiation for 1 hour. The plot in the top left corner shows the results with a more narrow color scale compared to the graphic in the bottom right.

$9.8 \pm 0.9\%$ was obtained with the S14161-3050HS-08, also using the average value from all 256 individual crystal energy resolutions. A comparison between the two methods of photosensor coupling (optical grease vs. RTV sheet) showed no clear tendency as for the S14161-3050HS-08 the energy resolution could be improved by using 1 mm of RTV sheet, while for the PA3350WB-0808 array the energy resolution deteriorated by doing so.

Upgrade to the latest KETEK low-noise SiPM series (PA3335WL-0808) and performance evaluation

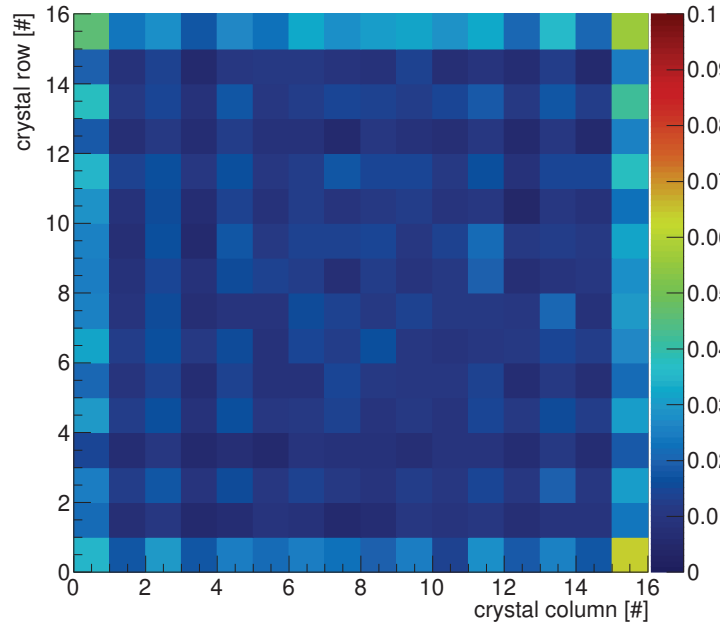
In April 2021, KETEK released a new low-noise SiPM series available in microcell sizes of $15\ \mu\text{m}$, $35\ \mu\text{m}$ and $47\ \mu\text{m}$. In Sec. 6.1.3 it could be shown that the best energy resolution of the GAGG crystal array was achieved using the HAMAMATSU S14161-3050HS-08 and a 1 mm RTV silicon rubber sheet light guide coupling or alternatively with the KETEK PA3325WB-0808 with optical grease coupling, respectively. This observation gave evidence that SiPM arrays with microcell sizes between $25\ \mu\text{m}$ and $50\ \mu\text{m}$ could provide a further improvement in terms of energy resolution due to an improved linear behavior compared to $50\ \mu\text{m}$ microcell size SiPMs, but increased PDE compared to $25\ \mu\text{m}$ microcell-size SiPMs. With the WL series, KETEK released a $35\ \mu\text{m}$ microcell size-type SiPM. Consequently, the GAGG array was also characterized using this new SiPM array (PA3335WL-0808) based on the $35\ \mu\text{m}$ microcell size.

The acquisition thresholds for all measurements involving the PA3335WL-0808 in this section were set to $v_{Th_T1} = 9\ \text{mV}$, $v_{Th_T2} = 218.5\ \text{mV}$ and $v_{Th_E} = 170\ \text{mV}$. The grouping window was set to 75 ns.

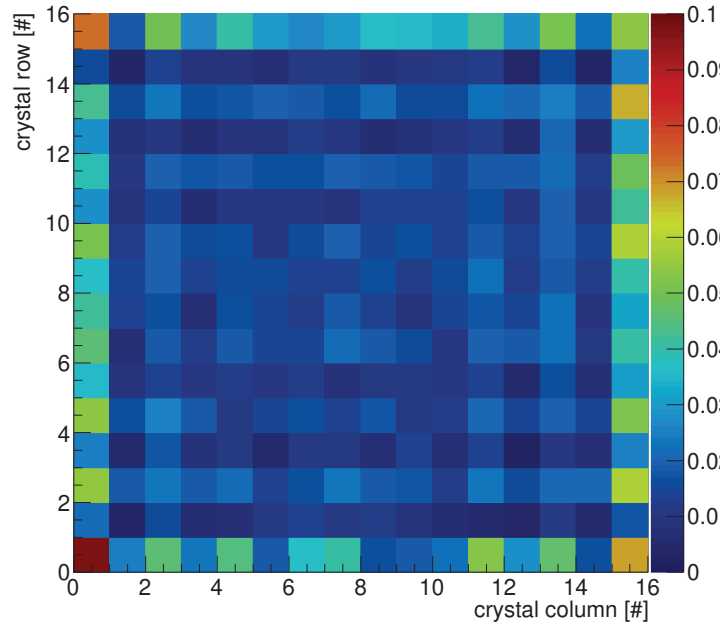
The GAGG scintillator array was optically coupled to the PA3335WL-0808 via a layer of $\approx 100\ \mu\text{m}$ optical grease.

As described earlier, all 256 individual crystal responses were corrected for gain non-uniformities of the crystal's light yield (LY) and for the SiPM/ASIC saturation using a quadratic correction function. The quadratic term serves as indicator for the saturation of the SiPMs/ASIC. Fig. 6.11 displays the quadratic term (color coded) of all 256 crystals as a position resolved map. The top map shows the correction parameter for a measurement with the PA3325WB-0808 and the bottom one with the new PA3335WL-0808, respectively. The comparison clearly shows an increase of saturation towards crystals at the edges of the PA3335WL-0808. The origin is the reflective teflon wrapping of the scintillator side surfaces. The photons emitted into such edge crystals, therefore, distribute over fewer SiPM pixels than it would be the case in central crystals, causing the SiPM to saturate if a large number of scintillation photons is reflected from the teflon layers. However, the amount of SiPM microcells available in case of the $25\ \mu\text{m}$ SiPMs appears to be sufficient, so that no increase of saturation can be observed.

The flood map obtained from a 3600 s long flood irradiation of the GAGG+PA3335WL-0808 detector shows clear crystal response spots. All 256 crystals can clearly be identified with basically no distortion. However, the previously described effect of a 2×2 clustering and the resulting visibility of the SiPM array structure (8×8) can also be observed (see Fig. 6.12).



(a) S14161-3050HS-08



(b) S14161-3050HS-08 (1 mm RTV)

Fig. 6.11: Non-linearity maps of a GAGG scintillator array acquired using a KETEK PA3325WB-0808 (top) and a KETEK PA3335WL-0808 (bottom). The maps show the quadratic component (C) of the quadratic function (Eq. (6.3)) that is applied to the individual crystal spectra in order to correct them for gain non-uniformity and saturation effects. The quadratic term is mainly influenced by saturations and therefore a valid measure to demonstrate saturation behavior of different SiPM microcell sizes.

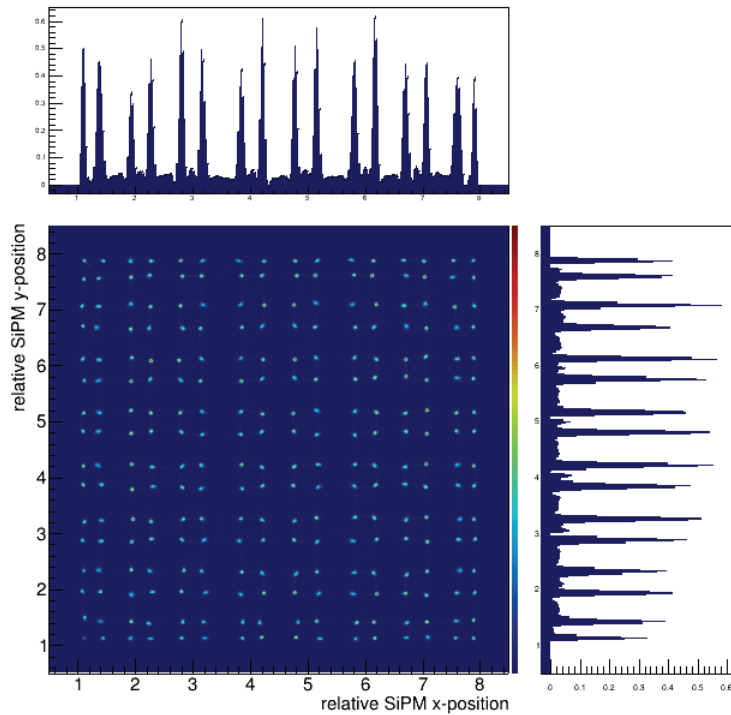


Fig. 6.12: Flood map acquired by irradiating a 16×16 GAGG scintillator array coupled to the PA3335WL-0808 SiPM array (at 5.0 V OV) for 3600 s with a ^{22}Na calibration source. The respective projections along the x- and y-directions are shown on top and left to the flood map. The crystal response was linearized and gain-corrected before plotting.

The energy resolution of the detector was evaluated using both, the integral and the individual crystal spectra. With both methods, an improvement between 0.8 % (vs. PA3325WB-0808 and inclusive method) and 1.7 % (vs. PA3350WB-0808 and inclusive method) could be achieved, when comparing measurements performed at 5.0 V OV (see Tab. 6.3)³. However, the best performance of the GAGG detector with the PA3335WL-0808 was achieved at an overvoltage of 6.0 V from an inclusive spectrum, reaching a relative energy resolution of 9.4% at 662 keV.

The energy resolution of all 256 individual crystals obtained at 662 keV measured with the PA3335WL-0808 is shown as a 2D map (including projections along the x-

³An overvoltage of 5.0 V was chosen for the comparison, because using SiPM arrays of the WB series, the best performance was obtained at 5.0 V.

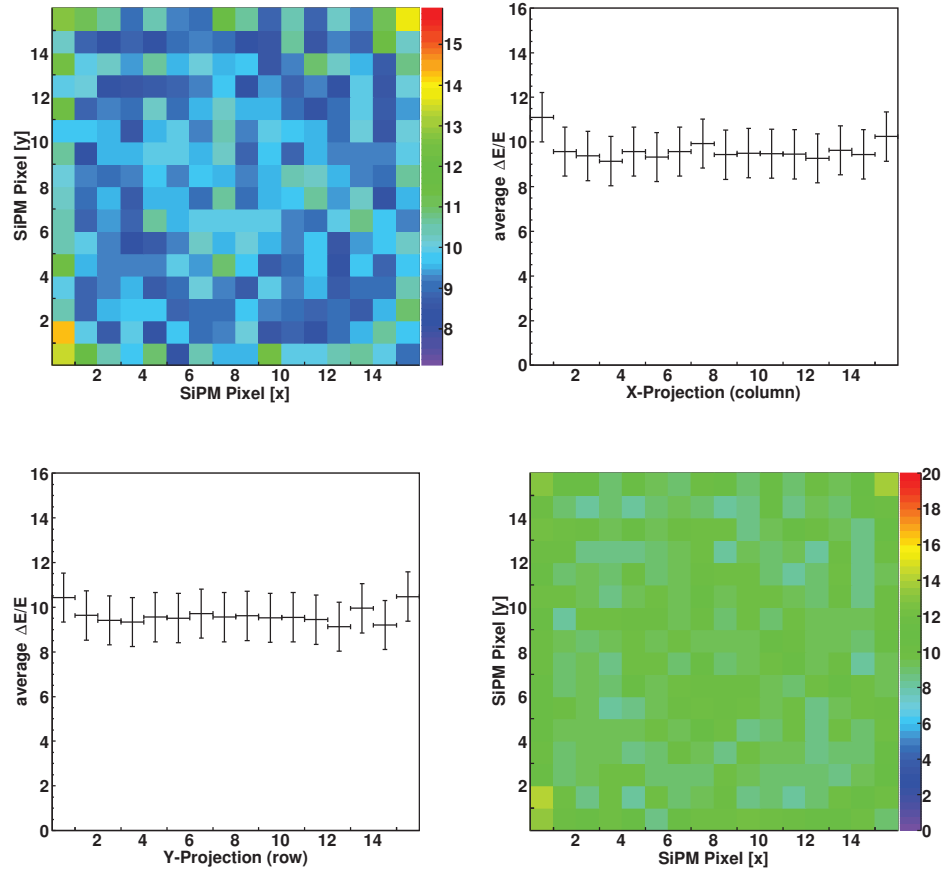


Fig. 6.13: Energy resolution map of the GAGG scintillator array coupled to a KETEK PA3335WL-0808 array biased at 5.0 V OV (again 5.0 V overvoltage were chosen to allow a comparison to the plots acquired using the SiPM arrays of the WB series). The energy resolution was measured at an energy of 662 keV by a 3600 s flood irradiation with a ^{137}Cs calibration source.

and y-dimensions) in Fig. 6.13. A high spatial homogeneity with a slight deterioration towards the edges and more prominent versus the corners could be observed.

6.1.4. Summary

A GAGG crystal array was investigated as potential scatterer component for a Compton camera or γ -PET prototype, respectively. Evaluations were performed using different types of SiPM arrays with $15\mu\text{m}$, $25\mu\text{m}$, $35\mu\text{m}$ and $50\mu\text{m}$ microcells of KETEK. The achievable energy resolution and the potential to identify all individual crystals was compared to results obtained using a HAMAMATSU arrays with $50\mu\text{m}$ microcell size. Furthermore, the influence of the light guide coupling between the detector and photo-sensor on the energy and spatial resolution was investigated.

$\Delta E/E$ [%]	PA3335WL -0808	PA3325WB -0808	PA3350WB -0808
inclusive spectra			
at 662 keV	9.5 ± 0.1	10.3 ± 0.1	11.2 ± 0.3
individual spectra			
at 662 keV	9.6 ± 0.9	10.0 ± 0.8	10.5 ± 0.8

Tab. 6.3.: Comparison of the relative energy resolution obtained using the new KETEK PA3335WL-0808 SiPM array series with the values obtained with the KETEK PA3325WB-0808 and PA3350WB-0808, respectively. All Shown values were obtained a γ -ray energy of 662 keV and an applied overvoltage of 5.0 V.

In all readout configurations it was possible to identify the individual crystal spots in the acquired flood maps, resulting in a spatial resolution determined by the crystal pitch of 1.6 mm. If the crystals were read out with SiPMs built from smaller microcell sizes ($< 50\mu\text{m}$), the array channel structure could be seen in the flood maps.

With regard to the energy resolution the best achieved value of $\Delta E/E = 9.4\%$ at an energy of 662 keV was observed using an SiPM array of the latest KETEK low-noise series with $35\mu\text{m}$ microcell size biased at 6.0 V OV. Generally, the energy resolution was found to be in the range between 9.5 % and 11.2% at 662 keV for all SiPM arrays under investigation and a good crystal-to-crystal homogeneity could be demonstrated.

The clearly identifiable crystals and the good energy resolution of the GAGG crystal array in a SiPM array readout configuration (for all investigated SiPM array types) makes it a suitable detector for the detection of γ rays in the few hundred keV and low MeV range, as required for Compton and PET imaging, respectively, in a medical environment.

6.2. Characterization of the Compton camera absorber component

An absorber detector of a Compton camera to be used for prompt- γ imaging for range verification in hadron therapy has to fulfill certain requirements. The type of absorber detector for the LMU Compton camera prototype was chosen with regard to a potential application in a clinical irradiation environment.

The scintillation crystals were not only chosen to provide an excellent energy resolution, but also excellent time resolution, high rate capability and high stopping power for γ rays specifically in the energy range between ≈ 2.5 MeV and 6.1 MeV. Therefore, a monolithic $\text{LaBr}_3\text{:Ce}$ crystal block with a reported energy resolution of 2.6 % (at 662 keV) and a decay time constant of 16 ns [Saint Gobain 2018] was chosen. Besides a high density of 5.08 g/cm^3 , a thickness of 30 mm is an appropriate choice to achieve a high detection efficiency for γ rays of the targeted energy of several MeV.

An excellent spatial resolution is achieved by using a light sharing approach with a pixelated photosensor as readout device. By applying a dedicated convolutional neural network algorithm to determine the 2D γ -interaction position within the crystal block, a spatial resolution at 1332 keV of only 0.96(2) mm has been achieved, which is well below the photosensor's granularity of 6 mm [Kawula 2021].

Alternatively to the $\text{LaBr}_3\text{:Ce}$ scintillator, a CeBr_3 crystal with identical dimensions was also investigated. CeBr_3 crystals provide similar characteristics as $\text{LaBr}_3\text{:Ce}$ scintillators (see Tab. 3.1), but do not exhibit any intrinsic background from internal radioactivity. Moreover, they are also less expensive, which is an advantage for the realization of largescale setups.

6.2.1. Scintillators and photosensors

The scintillators The scintillators investigated as potential candidates for a Compton camera absorber are monolithic crystal blocks with $50.8 \times 50.8 \times 30 \text{ mm}^3$ volume.

The initially chosen compound, $\text{LaBr}_3\text{:Ce}$, was selected due to its fast timing characteristics. With a reported decay time of 16 ns, it promises high count rate capability and excellent time resolution. Furthermore, the high brilliance with a light yield of 63 000 photons/MeV also promises an excellent energy resolution [Saint Gobain 2018].

Another compound investigated in the following sections is CeBr_3 [Scionix 2021]. These crystal's chemical structure is comparable to that of $\text{LaBr}_3\text{:Ce}$, the presence of Ce in the compound, however, makes a further doping obsolete. As for $\text{LaBr}_3\text{:Ce}$, also in CeBr_3 it is the $\text{Ce}^{3+} 5d \rightarrow 4f$ transition that characterizes the scintillation process, resulting in similar decay times for both materials. The light yield of CeBr_3 is reported to be of the order of 60 000 photons/MeV, but as stated by Quarati *et al.* this may be reduced by up to 25 % for encapsulated crystals [Quarati 2013].

Both crystals are hygroscopic, i.e., they must be encapsulated to avoid any kind of

contact with moisture. In terms of energy resolution, a superior performance by about 1 -2 % is reported for $\text{LaBr}_3\text{:Ce}$ compared to CeBr_3 [Quarati 2013]. On the other hand, $\text{LaBr}_3\text{:Ce}$ carries an intrinsic radioactivity of ca. (2 Bq/cm^3) due to the presence of the radioactive isotope ^{138}La in natural abundance [Kawula 2021, Saint Gobain 2018]. Another advantage of CeBr_3 compared to $\text{LaBr}_3\text{:Ce}$ is the reportedly higher resistance against high-dose gamma irradiation, which might be advantageous in clinical therapy environments [Drozdowski 2008, Kim 2021].

The photosensor All SiPM arrays that were used in the context of characterizing Compton camera absorber detectors are modules with 8×8 channels and $3 \times 3 \text{ mm}^2$ active channel area. Small differences of array dimensions between KETEK and HAMAMATSU SiPM modules arise from different packages (around the bare die (i.e. the silicon chip, that contains the SiPM structure)⁴.

KETEK specifies an overall area of $26.84 \times 26.84 \text{ mm}^2$, while HAMAMATSU arrays measure $25.8 \times 25.8 \text{ mm}^2$ [Ketek 2020a, Hamamatsu 2020]. To cover the full scintillator area, four SiPM arrays per crystal are used. During the measurement campaigns, however, a need for higher input charges per electronic ASIC channel was concluded (Sec. 6.2.3). Therefore, a "parallel ganging" adapter board (256-to-64 channels) was developed, that fits in surface area to four SiPM arrays and combines sub-matrices of 2×2 SiPM pixel to one signal output channel. This simple approach increases the input charge per ASIC channel approximately by a factor of 4, while the SiPM's decay time remains at acceptable values.⁵ Fig. 6.14 shows a picture of four

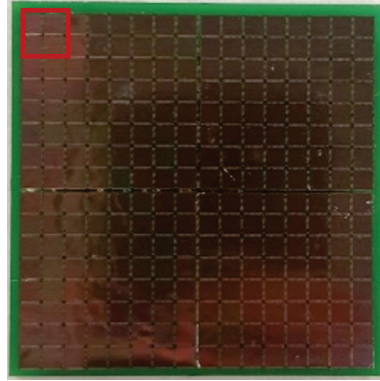


Fig. 6.14: Picture of four KETEK PA3350WB-0808 prototype arrays mounted onto the 256-to-64 channel adapter board. The red square in the top left corner illustrates how 2×2 individual SiPMs on the array are combined in parallel to one common readout channel.

KETEK arrays mounted to the adapter board. The red square in the top left corner indicates how 2×2 individual SiPMs are combined to one output channel. As can also be seen in Fig. 6.14, the adapter PCB is only minimally larger than the total SiPM area. Due to the different dimensions of KETEK and HAMAMATSU SiPM arrays, two types of boards were designed, with an identical electrical sketch, but different connector distances. The effective channel area of arrays in such a configuration is $6 \times 6 \text{ mm}^2$ with 64 output channels. In the following, arrays in such a configuration are named accord-

⁴The package includes the bonding of the bare die to some electrical connections of the package. Furthermore, it protects the die from scratches and other damages.

⁵The recovery time of parallelly combined SiPM pixels increases, due to the increased capacitance by adding the four individual capacities. Combining only four SiPM pixels, the recovery time is still within the acceptable input range (approx. 150 - 200 ns) for the ASIC. Furthermore, the signal is still fast enough not to cause pile-up effects.

6.2. Characterization of the Compton camera absorber component

ingly, e.g., four KETEK PA3350WB-0808 arrays on an adapter PCB are referred to as PA6650WB-0808, while four HAMAMATSU 3050HS-08 arrays mounted on an adapter PCB are referred to as 6050HS-08.

The monolithic absorber crystals were read out by different SiPM types. SiPM with microcell sizes of $15\ \mu\text{m}$ (PA3315WB-0808), $25\ \mu\text{m}$ (PA3325WB-0808) and $50\ \mu\text{m}$ (PA3350WB-0808) from KETEK were used. Among the three SiPM types, the PDE, but also the recovery time, increases with the microcell size. Consequently, the highest PDE is reached for the PA3350WB-0808 (50 % at 420 nm), which also has the longest recovery time with 80 ns over a $50\ \Omega$ load resistor. For detailed information of the SiPM properties, the reader is referred to the respective data sheets [Ketek 2018, Ketek 2020a, Ketek 2020b, Ketek 2020c]. Furthermore, characterization measurements have been performed with the recently released KETEK low-noise SiPM series (WL) using $47\ \mu\text{m}$ microcells (PA3347WL-0808) [Ketek 2021a]. All KETEK SiPM arrays reach a fill factor, i.e., the ratio between active to total area, of 82 % [Ketek 2020a].

Besides KETEK SiPM arrays, also arrays of a second vendor, HAMAMATSU, were investigated. The SiPMs of the S14161 series with $50\ \mu\text{m}$ SPADs were used. The S14161-3050HS-08 reaches a peak PDE of 50 % at 450 nm, the array fill factor, however, is with 74 % smaller than the one of KETEK arrays (82 %) [Hamamatsu 2020].

The optical coupling between the scintillators and the SiPM arrays was achieved using optical silicon grease (Saint Gobain BC-631 [Saint Gobain 2021b]/EJ-550 [EJ 2021]). The side surfaces of the contact surface between the crystals and the SiPM array were wrapped with several layers of teflon to minimize light loss on the crystal edges. Furthermore, black tape was used to prevent ambient light to reach the SiPM surface (Fig. 6.15).



Fig. 6.15: Picture of one of the monolithic CeBr_3 crystals (left) and of the coupled absorber detector (here: $\text{LaBr}_3:\text{Ce}$ and PA6625WB-0808) including black tape wrapping (right).

Signal processing For signal processing different kinds of electronics were used. The main focus of all evaluations was an ASIC-based readout based on the PETsys TOFPET v2c ASIC. For comparison, however, the time resolution (Sec. 6.2.2) as well as the energy resolution (Sec. 6.2.3) were also investigated with alternative signal processing electronics. More details about the specific electronics and readout configurations are given in the respective sections.

6.2.2. Time resolution of the absorber detectors components

The time resolution and coincidence resolving time (CRT), respectively, are not in the focus for Compton imaging as it is, e.g., used in γ -ray astronomy, since the final image is solely reconstructed by the calculation and intersection of Compton cones, obtained from the energy deposit and the interaction positions in the two camera components. However, for a Compton camera to be used to monitor a hadron beam's range, the excellent time resolution of $\text{LaBr}_3\text{:Ce}$ and CeBr_3 can be exploited for neutron- γ discrimination and, therefore, suppress the beam-induced neutron background during the hadron irradiation of matter. In this context, time resolutions below 1 ns are desirable [Biegun 2012].

This capability was demonstrated, e.g., in [Liprandi 2018], where time-of-flight spectra of secondary particles, that were created during a 20 MeV deuteron irradiation of a water target were registered and a clear separation between the emitted γ rays and fast neutrons could be observed.

6.2.2.1. Time resolution of the absorber detector with a PMT readout

The setup The time resolution of both crystal types, $\text{LaBr}_3\text{:Ce}$ and CeBr_3 , was investigated. The $\text{LaBr}_3\text{:Ce}$ was coupled to two different multianode photomultiplier tubes (MA-PMTs: HAMAMATSU H8500 and H9500), which are identical in their basic technology, however, differ in the amount of readout channels (64 vs. 256). Both MA-PMTs were biased at -950 V for the conducted measurements. The CeBr_3 crystal was coupled to the successor model of the H8500, the H12700A-10, which was biased at -900 V. As reference detectors (see next paragraph) a fast plastic scintillator (BC-418) coupled to a Photonis XP2020Q PMT (biased at -2000 V) was used.

In order to determine the time resolution of a specific detector of interest, this detector was placed such that it was facing the reference detector in a distance of ≈ 15 cm with a ^{22}Na point source (≈ 300 kBq) placed in the center inbetween both detectors.

The signals of both detectors' PMT outputs (Sig_1 and Sig_2) are fed into an Ortec 454 timing filter amplifier ($\tau_{\text{shaping}} = 200$ ns, Gain = 5) and the amplified signal is split into two signals (Sig_{1_1} , Sig_{1_2} , Sig_{2_1} and Sig_{2_2}) with identical amplitudes. The signals Sig_{1_2} and Sig_{2_2} are delayed by ≈ 12 ns by introducing a 2 m LEMO cable into the signal path. Subsequently, each of the four signals is fed into a four channel oscilloscope (LeCroy

6.2. Characterization of the Compton camera absorber component

Waverunner 640 Zi [Teledyne 2021]) (Fig. 6.16). Signals Sig_{1_1} and Sig_{2_2} are used to trigger the data acquisition in a coincidence mode, i.e., an acquisition is only triggered if the signals of both detectors are detected within a given time window and fulfill a selected energy condition. This energy condition was set such that the minimum energy threshold discriminates the noise peak (of the plastic scintillator), and only events with a minimum energy deposit of ≈ 430 keV (in the $\text{LaBr}_3\text{:Ce/CeBr}_3$) were triggering the data acquisition.

Once the acquisition was triggered, the acquisition timestamps generated (at the 8 % level of the maximum signal amplitude) of the respective second input signals (Sig_{1_2} and Sig_{2_2}) are registered. The arrival time difference was calculated and histogrammed.

The measurements were conducted without any active detector cooling at a typical room temperature of 21 °C.

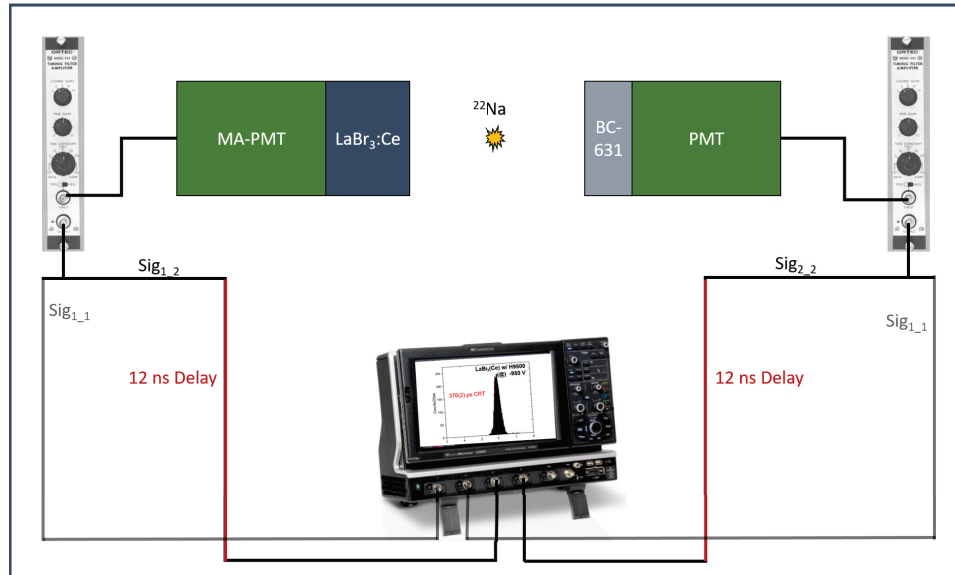


Fig. 6.16: Schematics of the setup used to determine the time resolution of the monolithic $\text{LaBr}_3\text{:Ce}$ crystals using a MA-PMT readout configuration.

The analysis procedure The CRT of the coincidence setup is determined as the FWHM of the arrival time distribution.

In a first step, the time resolution of the reference detector is determined. Therefore, an arrival time difference spectrum of two identical reference detectors is acquired. By performing a deconvolution of this arrival time difference spectrum according to Eq. (6.4), the time resolution ΔT_{ref} of an individual reference detector can be calculated under the assumption that the respective time resolutions are identical

$$\Delta T_{ref} = \sqrt{\frac{CRT_{ref}^2}{2}} \quad (6.4)$$

In a second step, one reference detector is replaced by one of the monolithic absorber detectors. The time resolution of the monolithic detector is determined from the FWHM of the Gaussian fit to the CRT of this specific setup according to

$$\Delta T_{monolith} = \sqrt{(CRT_{monolith-ref}^2 - \Delta T_{ref}^2)}. \quad (6.5)$$

The FWHM of the Gaussian fit applied to the time difference spectra is shown in Fig. 6.20 in red.

The time resolution Using the methods described in the previous paragraph, a time resolution ΔT (FWHM) of well below 300 ps was found for the LaBr₃:Ce (in both readout configurations) as well as for the CeBr₃ crystal. For the LaBr₃:Ce (with H9500 and H8500 readout) a time resolution of 250 ± 2 ps and 266 ± 2 ps, respectively, was found. The time resolution of the CeBr₃ crystal (with H12700A-10 readout) was measured to be 281 ± 3 ps.

The measured time resolution of the LaBr₃:Ce crystal with H9500 MA-PMT readout is in reasonable agreement with the previously reported value of 273 ± 6 ps [Aldawood 2016] using the same detector. The small deviations of the results reported in [Aldawood 2016] and in this work are most likely due to two general differences of the two measurements: a) the signal processing electronics was reduced in complexity in this work, i.e. the MA-PMT's signals were fed directly into an oscilloscope (compared to a Constant Fraction Discriminator (CFD) and a time-to-digital converter (TDC) in [Aldawood 2016]) and b) the time resolution in this work was evaluated at 511 keV (using a ²²Na source), whereas in [Aldawood 2016] a ⁶⁰Co source (1173 keV and 1332 keV) was used. The time resolution depends is expected to depend on the energy deposit in the scintillators. A large energy deposit causes a higher signal amplitude of the SiPM, which, due to the constant signal rise time, results in a steeper rising edge. Generally, a steep rising edge results in a small time jitter (= inaccuracy of the detection time between individual events), which improves the time resolution. In PET, for example, this motivates the desire for large SPAD SiPMs with high PDE and high gain compared to small SPAD SiPM.

6.2.2.2. CRT measured with the PETSys TOFPET v2c ASIC

In addition to the previously described absorber crystal timing characterization using a PMT-based readout, the achievable time resolution was also investigated for a fully ASIC-based readout scenario.

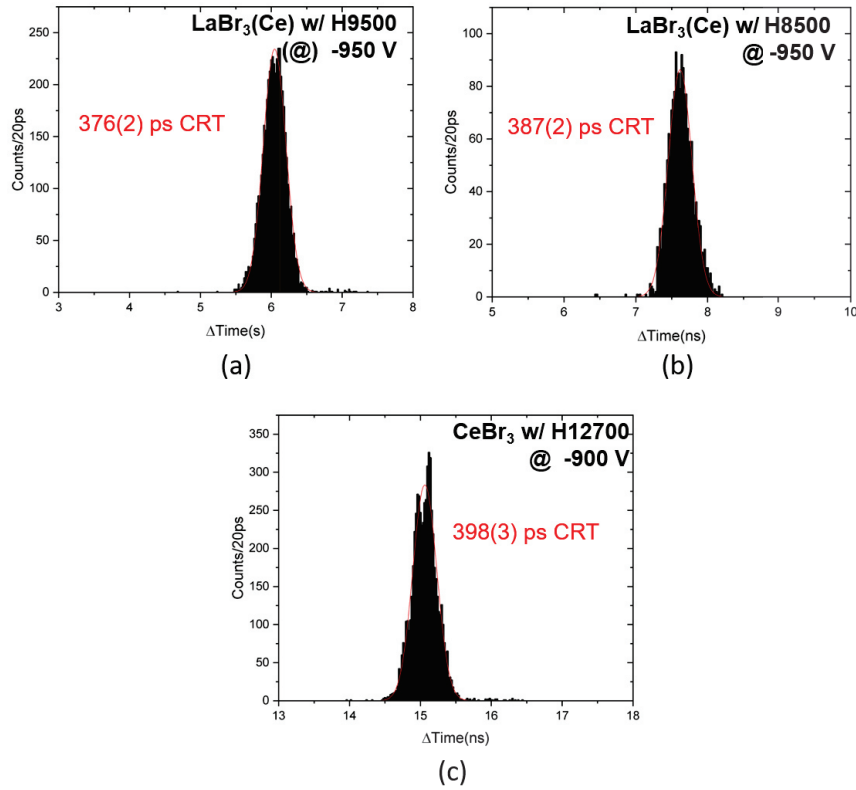


Fig. 6.17: Arrival time difference spectra of the LaBr₃:Ce (a) and (b) crystals and CeBr₃ (c), respectively, with MA-PMT read-out measured vs. a BC-418 plastic scintillator coupled to a Photonic XP2020Q PMT. The CeBr₃ crystal was coupled to a HAMAMATSU H12700A-10 MA-PMT biased at -900 V. The LaBr₃:Ce crystals were coupled to a HAMAMATSU H9500 and a H8500 MA-PMT, respectively, both biased at -950 V. The Gaussian fit that was applied to the time difference spectra is shown in red. The measured CRT values of the reference detector vs. the absorber modules is given as FWHM.

The ASIC/SiPM array time skew Before the measurements of the absorber's time resolution were conducted, the time skew had been determined. **Time skew** denotes the phenomenon that time stamps of simultaneously detected signals on multichannel systems may vary due to transit time differences of the signal between individual channels. The total time skew, i.e. the one of the SiPM array and the subsequent ASIC, was investigated using a homogeneous irradiation with a fast LED

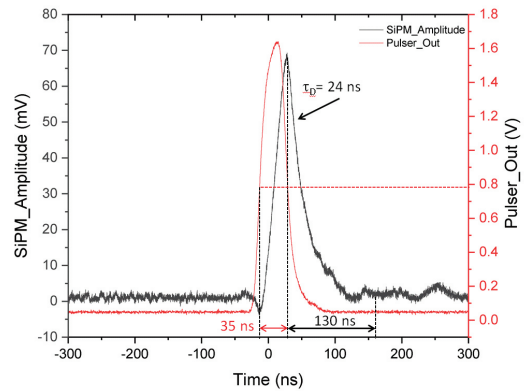


Fig. 6.18: Pulse generator voltage output (red) that drives an LED (Thorlabs LED450L) via a resistor together with the detected SiPM signal (black).

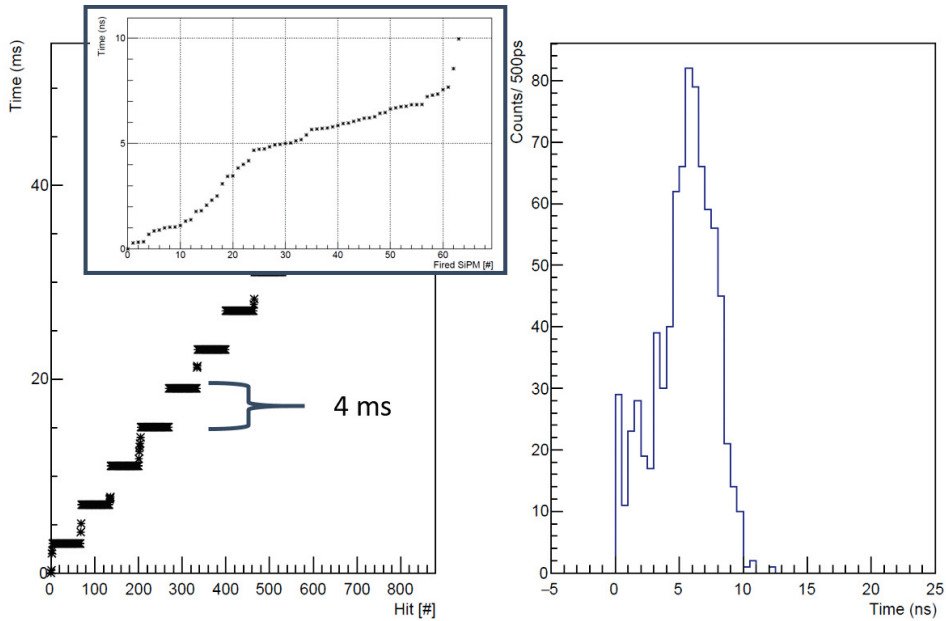


Fig. 6.19: Left: Arrival times of the LED pulses detected by a KETEK PA3325EB array and digitized using the ASIC (TOFPET v2b ASIC). The insert shows a zoom into the first pulse. Right: Arrival time distribution of the digitized signals of all 64 SiPM channels from 12 consecutive LED pulses.

pulse (Thorlabs LED450L/blue: 450 nm [Thorlabs 2018]). The measurements were conducted with the hardware available in August 2018, i.e. a KETEK PA3325EB-0808 array and the PETsys ASIC v2b on an evaluation board. The short LED pulse (with a repetition rate of 250 kHz; red histogram in Fig.6.18) superimposed to a SiPM (PM3325EB) signal generated by this pulse (black histogram) is displayed in Fig.6.18. Fig. 6.19 (left) shows the time stamps of the first 7 LED pulses. The pulses are detected in a temporal distance of 4 ms (250 kHz). The insert shows a zoom into the time distribution within one LED pulse. A delay of the last detected channel with respect to the first one of 10 ns was observed. The arrival time distribution of 12 detected events (Fig. 6.19 (right)) shows a time skew of the order of 10 ns for almost all hits. Only four hits were detected with a delay of more than 10 ns with respect to the first detected hit.

The coincidence time resolution The time resolution of a LaBr₃:Ce crystal coupled to four HAMAMATSU S14161-3050HS-08 arrays (in a 64 channel configuration) biased at 2.7 V OV was investigated. In this measurement configuration the reference detector is a LYSO crystal ($3 \times 3 \times 6 \text{ mm}^3$) read out by a single channel KETEK PM3325WB (single channel) SiPM biased at 2.5 V OV. The reduced bias voltage of the reference SiPM compared to the suggested one by the manufacturer is motivated by the strong non-linearity of the integrator for signals obtained by a one-to-one coupled LYSO in combination with a TIA gain of 2.5. In general, the specific ASIC configuration was

6.2. Characterization of the Compton camera absorber component

primarily determined by the requirements of the monolithic detectors rather than those of the reference detector.

The TIA gain was set to 2.65 and the three acquisition thresholds were set to $V_{th_1} = 12.5$ mV, $V_{th_2} = 110$ mV and $V_{th_e} = 124$ mV, respectively. The time stamps were generated when the signal exceeded v_{th_1} . The energy windows for all measurements were set to $\pm 1 \sigma$ around the 511 keV photo peak. The measured temperature at the two respective sensors (on the FEM128 board) right behind the SiPM was 24.6 °C and 24.7 °C, respectively. The ASIC temperatures were 19.9 °C and 20.4 °C. The measurement with the two reference detectors was run for 4 hours. The measurement time using a reference detector and the LaBr₃:Ce crystal amounted to 30 min, due to the much higher solid angle coverage of the monolithic detector compared to the reference detectors and the therefore higher coincidence rate. The CRT between the two reference detectors was measured to be 297 ± 4 ps in the previously described configuration. Using Eq. (6.4) a time resolution ΔT_{ref} of 210 ± 2 ps was derived.

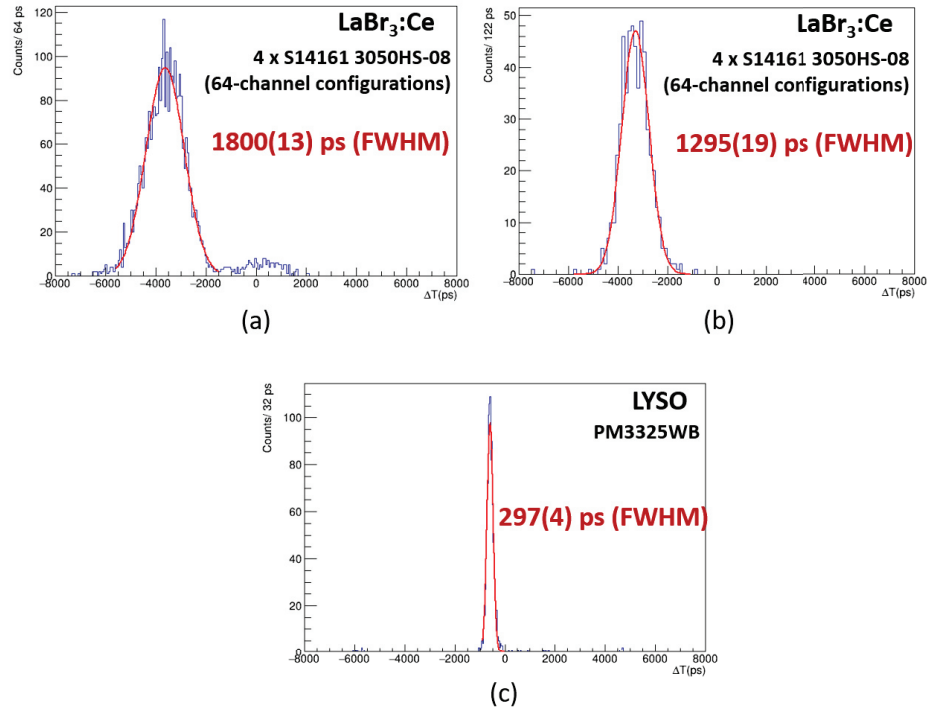


Fig. 6.20: Arrival time difference spectra of the LaBr₃:Ce read out by four HAMAMATSU S14161 3050HS-08 MPPC arrays (64 channel configuration) (a) and (b) and the arrival time difference spectrum of two LYSO crystals coupled to a KETEK PM3325WB SiPM (c). The red line in all three spectra represents the Gaussian fit applied to the distributions to obtain the measured CRT value of the respective setup.

The CRT of the setup comprising the LaBr₃:Ce crystal and the LYSO reference detector was not evaluated for all possible time stamp differences of (all up to 64) firing

Detector	Time resolution (ps)
LaBr ₃ :Ce H9500	250 ± 2
LaBr ₃ :Ce H8500	266 ± 2
CeBr ₃ H12700A-10	281 ± 3
LaBr ₃ :Ce S14161 3050HS-08	1279 ± 19

Tab. 6.4.: Summary of the time resolution of the monolithic absorber crystals with PMT and SiPM readout.

SiPM channels of the monolithic detector, but exemplarily for the specific channel of the SiPM array that appeared brightest for most acquired coincidence events. This SiPM channel is geometrically located on the line connecting the reference detector and the ²²Na source. By using only this single channel, the width of the arrival time spectrum is reduced, because the time skew between SiPM and/or ASIC channels is not contributing to the spectra any more. By only considering events with the same SiPM channel of the LaBr₃:Ce being the brightest, a CRT of 1800 ± 13 ps was measured.

By using further post-processing, the CRT could be reduced to 1295 ± 19 ps resulting in a time resolution of 1278 ± 19 ps. For this step, two further analysis conditions have been introduced before filling the time difference spectrum as described by Lamprou *et al.* [Lamprou 2020]: only coincidence events were considered for which the arrival time difference between the brightest 6 channels of the LaBr₃:Ce detector was less than 1 ns. Furthermore, instead of using the time stamp of the brightest SiPM channel, an energy weighted average t_{EA} of the first six timestamps was used to calculate the arrival time difference of the two detectors, according to

$$t_{EA} = \frac{\sum_{n=0}^5 t_n E_n}{\sum_{n=0}^5 E_n}. \quad (6.6)$$

Consequently, the cut to select only one (the brightest) SiPM channel is not required any more.

A calibration for the time skew, as also proposed in [Lamprou 2020], has not been done.

Conclusion Both investigated scintillation materials, LaBr₃:Ce and CeBr₃, provide an excellent time resolution of well below 300 ps, if read out by a MA-PMT, which is in good agreement with the values reported, e.g., by the manufacturer of the LaBr₃:Ce, Saint Gobain Crystals [Saint Gobain 2021a]. However, for smaller crystal volumes (cylindri-

cal; diameter: 1 inch, height: 1 inch), also superior values of the time resolution were reported for both, LaBr₃:Ce (148 ± 2 ps (at 511 keV)) and CeBr₃ crystals (164 ± 2 ps (at 511 keV)) [Fraile 2013, Vedia 2015].

Using the PETsys TOFPET v2c ASIC, the currently achievable time resolution resulting in values beyond 1 ns is clearly behind expectation. A possible principle way towards improvements has been shown by Lamprou *et al.* (time skew/ time walk calibrations, averaging of time stamps, position filtering). The authors used a LYSO crystal with the same area as the used detector within this work, but only half the thickness. Their best value for the time resolution of this crystal LYSO block was 497 ps (FWHM) [Lamprou 2020]. Using a LaBr₃:Ce ($25.8 \times 25.8 \times 5$ mm³) and a KETEK PA3325WB-0808 SiPM array, Viegas *et al.* could achieve a CRT of 1.66 ns using the TOFPET v2c ASIC [Viegas 2021].

Depending on the distance of a potential Compton camera prototype to the isocenter of the hadron beam in a treatment scenario, however, the time resolutions in both readout configurations might be sufficient to discriminate the prompt- γ signals from the neutron background. For example, for 20 MeV neutrons $\beta = 0.145^6$, which corresponds to a speed of 4.35 cm/ns [Liprandi 2018]. For such neutron energies even distances (camera to isocenter) as common for small animal irradiation (10 - 15 cm) would be sufficient to discriminate γ rays from fast neutrons. For faster higher energetic neutrons, e.g., 250 MeV⁷ β equals to 0.733, which corresponds to a neutron velocity of $v = 22$ cm/ns. In this case the distance of the Compton camera to the beam's isocenter must be several tens of cm in order to allow for discriminating the prompt γ rays from the (fast) neutron background.

In general, LaBr₃:Ce and CeBr₃ crystals are among the fastest known anorganic scintillation crystals resulting in an excellent time resolution, which could be confirmed in even for large crystal blocks ($51 \times 51 \times 30$ mm³) in the studies presented here for a MA-PMT readout configuration. For a readout configuration using a SiPM array and the PETsys TOFPET v2c ASIC further studies are necessary in order to improve the detector's time resolution.

6.2.3. Energy resolution of the absorber detector components

This section deals with a detailed evaluation of the relative energy resolution $\Delta E/E$ (given as the FWHM) of the monolithic Compton camera absorber detector, for an intended application in medical imaging devices such as γ -PET prompt- γ based range verification. Hence, the relative energy resolution in a wide range, from about 100 keV up to about 6.1 MeV, is of relevance. This section will be ordered in two parts. The first one deals with the energy resolution of the detectors in an energy regime below 1.5 MeV, which is accessible by radioactive sources. The second part is dedicated to the

⁶ $\beta = \frac{v}{c}$, with v the particles velocity and c the speed of light

⁷250 MeV/u is a typical energy for ion beam therapy

energy regime between 1.5 MeV and 6.1 MeV, which was investigated in measurements performed at the Maier-Leibnitz Laboratory (MLL) Tandem accelerator in Garching and the Marburger Ionentherapie Zentrum (MIT), Marburg. At accelerator facilities γ rays with energies in the MeV range can be obtained by irradiation of a target with a particle beam. By collisions between the projectile and the target nuclei, these nuclei may be excited with a subsequent deexcitation under the emission of a prompt γ ray⁸. For both energy regimes the main focus was put on the energy resolution obtained using the PETsys TOFPET v2c ASIC. However, also a hardware-based signal summation by "hybrid-ganging" (see Sec.4.3) with subsequent signal digitization performed by a pocket multi-channel analyzer (Amptek MCA8000A) (see Sec. 4.3) was investigated. The detector performance using both methods to generate a sum signal (software-wise and hardware-wise) was compared⁹.

The relative energy resolution of all detectors studied in this section was extracted from calibrated energy spectra. These spectra are obtained by applying a parabolic calibration function

$$E_{keV} = A + B \cdot E_{a.u.} + C \cdot E_{a.u.}^2 \quad (6.7)$$

to the registered and digitized γ ray's charge values ($E_{a.u.}$)¹⁰. The parameters A, B and C are determined by a) the determination of the photopeak positions (in a.u.) of several calibration sources (¹⁵²Eu, ²²Na, ¹³⁷Cs and ⁶⁰Co), b) plotting the found peak positions vs. the actual photo peak energy (in keV) and c) by applying a parabolic fit (according to Eq.(6.7)) to the data points.

6.2.3.1. Energy resolution below 1.5 MeV (offline characterization)

The following section presents a detailed investigation of the energy resolution of the monolithic absorber detectors at γ -ray energies that are accessible by radiation sources and therefore could be obtained by offline measurements.

Measurement configuration and hardware settings of the PETsys TOFPET v2c ASIC

The measurements presented in the following were conducted at temperatures between 21°C and 23°C, unless stated otherwise. The ASICs were actively cooled by fans to prevent local accumulation of warm air.

For the ASIC configuration, low threshold values and high gains had to be chosen due to

⁸T(p,p' γ)T* reactions, where T represents a target nucleus like oxygen or carbon.

⁹The scintillation photons distribute over several SiPM channels, due to the light-sharing readout. In a second step, the signals of all individual SiPM need to be summed i.o. to obtain the full information about the energy deposit in the scintillator.

¹⁰Note: These values are not provided in ADC channel units. There is an intermediate processing performed on the raw data performed by a PETsys Electronics routine. The output of this routine then can be further post-processed.

rather low photon levels detected on SiPM pixels far away from the interaction center. The TIA gain in the Q branch was set to the maximum value of 3.65¹¹. The applied threshold values for the measurements performed in the three different SiPM readout configurations are listed in Tab. 6.5.

	PA3325WB -0808	PA3350WB -0808	S14161 -3050HS-08
OV (V)	5.5 V	5.5 V	3.1 V
LaBr ₃ :Ce			
disc lsb _{T1}	62 (\approx 1.2 mV)	62 (\approx 1.2 mV)	62 (\approx 1.2 mV)
th _{T1}	5 (\approx 6.0 mV)	5 (\approx 6.0 mV)	10 (\approx 12.2 mV)
disc lsb _{T2}	54 (\approx 9.0 mV)	58 (\approx 5.5 mV)	51 (\approx 12.0 mV)
th _{T2}	12 (\approx 108.0 mV)	25 (\approx 137.5 mV)	13 (\approx 156.0 mV)
disc lsb _E	54 (\approx 9.0 mV)	59 (\approx 4.5 mV)	51 (\approx 12.0 mV)
th _E	13 (\approx 117.0 mV)	18 (\approx 81.0 mV)	21 (\approx 252.0 mV)
CeBr ₃			
disc lsb _{T1}	62 (\approx 1.2 mV)		62 (\approx 12.0 mV)
th _{T1}	5 (\approx 6.0 mV)	n.e.	5 (\approx 12.0 mV)
disc lsb _{T2}	54 (\approx 9.0 mV)	n.e.	51 (\approx 12.0 mV)
th _{T2}	12 (\approx 108.0 mV)	n.e.	18 (\approx 216.0 mV)
disc lsb _E	54 (\approx 9.0 mV)		51 (\approx 12.0 mV)
th _E	13 (\approx 117.0 mV)	n.e.	18 (\approx 216.0 mV)

Tab. 6.5.: ASIC least significant bit (LSB) values and multiplication factor for the characterization measurements performed with the indicated SiPM arrays (PA3325WB-0808, PA3350WB-0808 and S14161-3050HS-08) and monolithic LaBr₃:Ce and CeBr₃ crystals. The detector combination CeBr₃ and PA6650WB-0808 was not studied and therefore is labelled with "n.e." (not evaluated; this detector configuration could not be evaluated, after a broken SiPM array channel was discovered. Values obtained using a malfunctioning channel would not be comparable to values with all channel working). A detailed description of the ASIC's trigger logic is given in Sec. 4.2.

Energy resolution by software sum signal generation The energy resolution of the LaBr₃:Ce and the CeBr₃ absorber detector crystals was investigated for energies up to 1.5 MeV in various photosensor read-out configurations. While in previous setups with MA-PMTs used to read out the scintillators, advantage was taken from a direct access to the total energy deposit in the monolithic scintillator via its sum dynode output [Aldawood 2016, Binder 2017], SiPM arrays do not provide such a feature.

The overall energy deposit in the crystal, therefore, had to be obtained by a different method, which - for the setup used within this work - was realized by using the timestamps of the respective triggered SiPM channels. Similar to what has also been described in the previous chapter for the pixelated GAGG arrays, a time window (grouping window) was used to cluster all triggered SiPM channels, and followed by a summation of their detected charge in order to retrieve the full energy information. Here, the exact width of the grouping window is of less importance compared to the GAGG detectors, since typically (almost) all SiPM pixels detect some light after an interaction took place

¹¹Also TIA gain values of 1.7 and 2.5 were used. However, the best results were obtained with the maximum setting of 3.65.

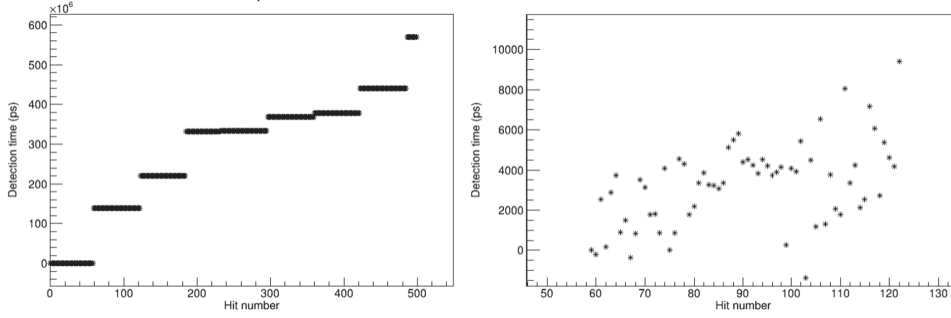


Fig. 6.21: Hit time distribution of all firing SiPM/ASIC channel triggered by nine initial γ events (left) and the detection time distribution relative to the timestamp of the brightest channel of one single γ interaction in the scintillator (right panel). Data were taken with a LaBr₃:Ce crystal coupled to four HAMAMATSU S14161 3050HS-08 array (64 channel configuration) using a 180 kBq ²²Na point source placed 5 cm in front of the detector.

in the scintillator. As a consequence, the probability that a dark count or background event that triggers an additional SiPM pixel is strongly reduced¹². Fig. 6.21 (right) shows that the arrival time stamps are detected within a time window of ≈ 12 ns. This time distribution determines the minimum length of the grouping window that is required to detect the full energy information. This observation is also consistent with observations obtained by evaluating the SiPM/ASIC time skew using an LED (see Fig. 6.19). Fig. 6.19 (left) shows the (arbitrary) time distribution of eight events.

In order to determine the energy resolution of the respective radiation source, measurement times between 180 s and 300 s are sufficient (for such large detector dimensions) to obtain good statistics in the energy spectra. From the (calibrated) energy spectrum of interest (e.g. the one of a ²²Na source) a fit window is set around the peak of interest such that the fit window includes the full peak, but not the Compton edge (e.g. for the 511 keV photo peak from ≈ 450 keV to 550 keV). The peak is fitted using ROOT's fit functionality. The chosen fit function is a Gaussian on top of a linear function, where the Gaussian represents to the photopeak and the linear component is used as a good estimate for the background distribution, provided the fit window is chosen sufficiently narrow. The peak's FWHM and centroid are taken to calculate the relative energy resolution at the given photon energy according to

$$E_{res} = \frac{\Delta E(FWHM)}{E_{centroid}} \quad (6.8)$$

3×3 mm³ active area SiPMs The energy resolutions at 511 keV, 662 keV and 1274 keV obtained for various detector configurations under investigation using the PETsys TOFPET v2c ASIC for signal processing are summarized in Tab. 6.6 (in black). The

¹²since (almost) all channels are active anyway

values shown in red were obtained by measurements using a MA-PMT and are given as a reference. The energy resolution with an alternative readout component - the "hybrid ganging readout board" (HGRB; Sec 4.3), that provides a direct summation of the individual SiPM charge signals on the hardware level (see next paragraph) - is shown in blue.

The first and direct approach to determine the relative energy resolution of the monolithic scintillators by using four tiled PA3325WB-0808 arrays (referred to as PA3325WB-1616), however, showed an energy resolution at 662 keV of only 14.0 % (15.2 %) for the LaBr₃:Ce (CeBr₃), which is about by a factor of four inferior compared to the values of 3.4 % (4.8 %) found in previous measurements conducted with a MA-PMT. The problem could be attributed to a high light loss on the SiPM array, due to the circumstance that only half of the SiPM channels could provide a charge signal that was high enough to exceed the trigger thresholds of the ASIC channel.

6×6 mm³ active area SiPMs To overcome this limitation, an adapter board was designed such that sub-groups of 2 × 2 SiPM pixels were combined in parallel, forming an overall SiPM array configuration with 8 × 8 channels and four times the active area as in the 16 × 16 pixel configuration (referred to as PA6625WB-0808) (see. also Fig. 6.14, where this configuration was already introduced). By using this method, all 64 ASIC input channels could be triggered and the light loss was minimized. The energy resolution of the LaBr₃:Ce (CeBr₃) crystals at 662 keV could be improved to 5.7 % (7.2 %), which, however, was still not reaching the MA-PMT results. Further improvement of the energy resolution could be achieved by using four KETEK prototype arrays with 50 μm microcell sizes (PA3350WB-0808) instead of the previously used 25 μm microcells to build a PA6650WB-0808 array (using the parallel ganging adapter PCB). Furthermore, for these four arrays, the homogeneity of the breakdown voltage was investigated to reduce gain fluctuations to a minimum. The mean breakdown voltage was found to be at 25.24 ± 0.06 V with the maximum value found to be at 25.35 V and the minimum at 25.00 V (Fig. 6.22).

Taking advantage of the improved PDE and higher gain of these 50 μm SPADs, an energy resolution of 4.1 % at 662 keV could be achieved, which is comparable to the performance of the MA-PMT, where values between 3.4 % and 4.0 % were achieved.¹³

Also, the detector and electronics were placed in a home-built¹⁴ cooling chamber and the energy resolution was measured (for the LaBr₃:Ce with the KETEK PA6650WB-0808) at 13.5 °C. However, the expected reduction in SiPM and ASIC thermal noise did not result in an improved energy resolution. Very similar values as achieved before of 5.2% (at 511 keV) and 4.2% (at 662 keV) were measured. This behavior indicates that the dominant factor that determines the energy resolution in this scintillator/photosen-

¹³depending on the type of MA-PMT [Binder 2019]

¹⁴by S. Liprandi [Liprandi 2018]

6. Compton Camera Components' Characterization

Detector/ photosensor	$\Delta E/E$ [%] @ 511 keV	$\Delta E/E$ [%] @ 662 keV	$\Delta E/E$ [%] @ 1274 keV	signal processing
LaBr₃(Ce)				
H12700A-10		3.4 ± 0.1	2.4 ± 0.1	mesytec (NIM/VME)
PA3325WB-1616	15.6 ± 0.2	14.0 ± 0.2	PETsys	
PA6625WB-0808	6.8 ± 0.1	5.7 ± 0.1	4.6 ± 0.1	PETsys
PA6625WB-0808	4.9 ± 0.2	4.1 ± 0.2	3.0 ± 0.2	MCA 8000A + HGRB
PA6650WB-0808	4.9 ± 0.2	4.1 ± 0.2	4.1 ± 0.2	PETsys
S14161-3050HS-08	5.7 ± 0.1	4.8 ± 0.1	4.7 ± 0.1	PETsys
S14161-3050HS-08	4.1 ± 0.1	3.6 ± 0.2	2.8 ± 0.2	MCA 8000A + HGRB
CeBr₃				
H12700A-10	5.6 ± 0.1	4.8 ± 0.1	3.4 ± 0.1	mesytec (NIM/VME)
PA3325WB-1616	17.4 ± 0.2	15.2 ± 0.2	8.4 ± 0.2	PETsys
PA6625WB-0808	8.6 ± 0.1	7.2 ± 0.1	5.5 ± 0.1	PETsys
PA6625WB-0808	5.7 ± 0.1	4.9 ± 0.1	3.8 ± 0.2	MCA 8000A + HGRB
S14161-3050HS-08	7.4 ± 0.1	6.1 ± 0.1	5.1 ± 0.1	PETsys
S14161-3050HS-08	5.9 ± 0.1	5.3 ± 0.2	3.9 ± 0.1	MCA 8000A + HGRB

Tab. 6.6.: Comparison of the relative energy resolution measured for various absorber detector combinations. The relative energy resolution is shown for a LaBr₃:Ce and a CeBr₃ crystal, respectively, each of them read out by one out of four SiPM array types (KETEK PA3325WB-1616, KETEK PA6625WB-0808, KETEK PA6650WB-0808 and HAMAMATSU S14161-3050HS-08) and is shown at 511 keV, 662 keV and 1274 keV. In blue: energy resolution measured using a hybrid ganging readout board ("HGRB") for sum signal generation and an Amptek MCA 8000A for signal digitization.

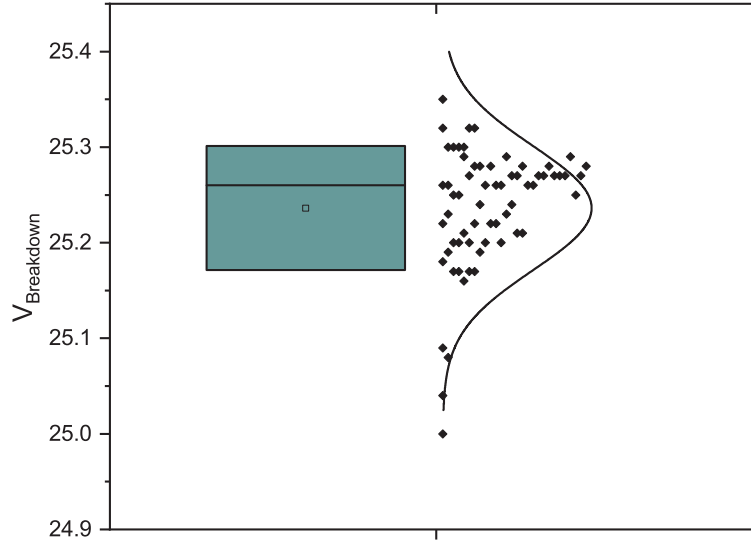


Fig. 6.22: Left: Box plot of the measured breakdown voltages of all 64 channels of a PA3350WB-0808 prototype array. The horizontal line indicates the median value (25.26 V), the black square the mean value of 25.24 ± 0.06 V. The size of the green box indicates the standard deviation of the distribution.

sor configuration is the light collection and not the photosensor's noise¹⁵. Therefore, it was concluded that no further active cooling in addition to the already implemented ventilation fans would be required.

The LaBr₃:Ce crystal's excellent energy resolution (with a KETEK PA6650WB-0808 readout) was exploited as coincidence detector to discriminate background events from actual Cherenkov photons generated in a PMMA radiator by 511 keV annihilation γ rays from a ²²Na point source in a joint measurement together with a group from the University of Siegen [Bäcker 2021].

HAMAMATSU MPPC arrays In addition, an absorber detector read out by four HAMAMATSU S14161-3050HS-08 arrays, again in an 8×8 channel configuration, was assembled. The measured energy resolution achieved using a $50 \mu\text{m}$ SPAD SiPM array was found to be 4.8% (at 662 keV), which is 0.7 % reduced compared to the values

¹⁵Other than in semiconductor radiation detectors such as high purity Germanium detectors or Si strip detectors, where the diode's leakage current is one of the main factors that deteriorates the energy resolution.

measured before with the PA6650WB-0808 configuration. The reason can most likely be attributed to the reduced gain of the S14616-3050HS compared to the PA3350WB-0808 SiPMs. As will be shown in the next paragraph, the fact that the peak PDE of the S14616-3050HS is found at longer wavelengths compared to the KETEK arrays (PDE_{max} at 450 nm [Hamamatsu 2020]), resulting in a lower effective PDE at the emission wavelength of the LaBr₃:Ce crystal ($\lambda_{peak} = 380$ nm [Saint Gobain 2018]) compared to the PA3350WB (PDE_{max} at 420 nm [Ketek 2018]), is only one contribution to the slightly degraded energy resolution. Furthermore, a smaller gain as also present for the 25 μ m microcell array PM3325WB can cause a deterioration of the energy resolution and would fit into the observed trend. The reason is related to the separate triggering on individual ASIC channels as it is done by the PETsys ASIC. This may result in a significant loss of signal charge information (scintillation photons) if a channel's signal only slightly exceeds the trigger threshold¹⁶. The lost fraction of the signal of such a channel decreases with an increasing the gain (and therefore the pulse's amplitude) of the SiPM. Therefore, a smaller gain, might result in a larger loss of energy information and therefore a deteriorated energy resolution.

A comparison between the relative energy resolution of all investigated detector configurations consistently shows the trend that a LaBr₃:Ce crystal provides an superior energy resolution superior by about 1 % to 1.5 % compared to a CeBr₃ crystal, which is in good agreement with literature [Fraile 2013, Quarati 2013, Kozyrev 2016, Vedia 2017].

The results of the following paragraph were obtained partially in the framework of a BSc project [Zhou 2020] supervised by the author.

Energy resolution measured with an alternative signal processing (charge (energy) summation via hybrid-ganging) The PETsys Electronics TOFPET Evaluation kit only provides charge integration and post signal processing for individual input signals from each SiPM array channel.

For light-sharing detector configurations, where the total detected energy distributes over several SiPM channels, the initial energy deposit in the scintillator can only be reconstructed during the post processing. A potential disadvantage of such a method is that each individual input channel has to exceed its own trigger threshold to start the signal integration. Therefore, a fraction of the signal (before the first timing threshold Th_{T1} is exceeded) is lost for each channel prior to the actual start of the integration. Even though this effect is small for a single channel, the sum of several channels has the potential to considerable deteriorate the energy resolution. A further disadvantage of individual channel integration is the higher level of electronic noise, since each individual electronics channel has its own noise contribution. Inhomogeneities in the amplifier

¹⁶which is especially the case for SiPM channels far away from the interaction position in the scintillator crystal

channels and non-linearities will further degrade the energy resolution.

Therefore, a signal summation on a hardware level is a promising alternative to the software-based energy sum generation. A hybrid-ganging readout board (HGRB, see Sec. 4.3) was developed at the Chair for Medical Physics in Garching [Holthoff 2020] in collaboration with the author and the KETEK GmbH.

The preamplified signal of the HGRB is fed into an ORTEC 452 spectroscopy amplifier with 250 ns shaping time and a gain set to 300. The amplified signal is subsequently digitized by an AMPTEC MCA 8000A multi-channel analyzer (MCA) [Amptek 2021].

Evaluations performed using this alternative detector readout method are intended to serve as benchmark test of the PETsys TOFPET v2c ASIC independently of the specific detector configuration.

Bias dependency of the energy resolution The energy resolution as a function of the PA6625WB-0808 overvoltage was evaluated by Y.J. Zhou in the framework of her B.Sc. thesis for two different CeBr₃ crystals. The results are consistent with the ones found by the author for the LaBr₃:Ce (using a PA6650WB-0808 and the PETsys TOFPET v2c ASIC). The minimum of the energy resolution was found for an OV of 5.5 V [Zhou 2020]. Further measurements were therefore conducted at this overvoltage. However, the energy resolution of the two crystals differs by about 3 %, with the newer crystal block (CeBr₃ # 2) showing the superior resolution. Comparing with studies performed in previous works, it could be concluded that the performance deteriorated over time and was not an initial issue of this specific crystal (see [Binder 2017, Viegas 2018]). A reliable explanation of the deterioration, however, cannot be given from the available information. A possible reason could be moisture leakage into the encapsulation of the hygroscopic scintillator material. Therefore, the energy resolution considered in the following was measured using the second, newer crystal with superior performance.

Comparison of SiPM types The excellent energy resolution achievable using the hybrid-ganging method is demonstrated in Fig. 6.24 (left), where an energy spectrum obtained

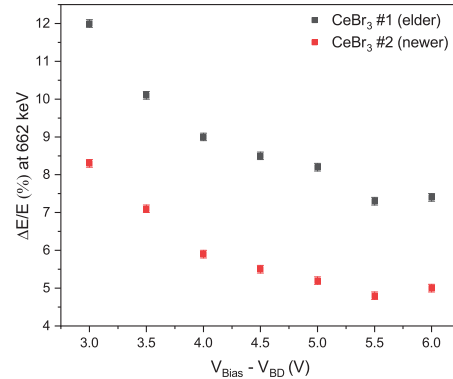


Fig. 6.23: Relative energy resolution of two CeBr₃ detector blocks as a function of the applied overvoltage when read out by the PA6625WB-0808. The overvoltage was incremented in 0.5 V steps from 3.0 V to 6.0 V. The data points in black belong to the measurement performed with the older, the data points in red belong to the measurements of the newer CeBr₃ crystal block. Graph adapted from [Zhou 2020].

with the CeBr₃ crystal coupled to a KETEK PA6625WB-0808 from a simultaneous irradiation with ¹⁵²Eu, ²²Na and ¹³⁷Cs is shown. The energy spectrum was obtained from an energy summation of all SiPM array channels using the HGRB as described before. Fig. 6.24 (right) shows the obtained energy resolution for this detector assembly plotted vs. the γ -ray energy (black data points) and a $1/\sqrt{E}$ fit to the data points (red dashed line)¹⁷. A more qualitative study of the energy resolution of the various absorber detector components is shown in Tab. 6.6. Generally, the energy resolution measured with the HGRB is between 1 % and 2 % superior compared to that measured with the TOFPET v2c ASIC. As visible from Tab. 6.6, the overall best energy resolution with $\Delta E/E = 3.6 \pm 0.2$ % at 662 keV was obtained with the LaBr₃:Ce crystal and the HAMAMATSU S14161-6050HS-08 SiPM array. This observation led to the previously stated conclusion that the reason for lower performance of the S14161-6050HS-08 compared to the PA6650WB-0808 with the TOFPET v2c ASIC is primarily due to the lower gain of the HAMAMATSU module and not the SiPM performance itself. Otherwise the best energy resolution would not have been measured with the S14161-6050HS-08 when read out using the HGRB.¹⁸

For the CeBr₃ crystal the energy resolution at 662 keV was found to be 5.3 % for the S14161-6050HS-08, whereas 4.9 % were measured using the KETEK PA3325WB.

Summary In summary, it can be stated that for both evaluated scintillation materials and all evaluated SiPM types the HGRB provides a superior energy resolution compared to the PETsys ASIC. Also, for both compounds, a SiPM type could be found that provides the same energy resolution (within the measurement accuracy) as could be achieved by using an MA-PMT readout.

Spatially resolved energy resolution The spatial homogeneity of the energy resolution of the two monolithic CeBr₃ detector blocks was evaluated by Y.J. Zhou using the hybrid-ganging board [Zhou 2020].

Data were collected by a 2D scan in (x,y) with a collimated 87 MBq ¹³⁷Cs radiation source. The collimation was realized by a $10 \times 10 \times 10$ cm³ Densimet block [DENSIMET 2021] with a 1 mm opening, resulting in a 1.1 mm photon irradiation spot size [Binder 2017]. The detector was irradiated at 64 positions (8×8), with a step size of 6.6 mm, such that the collimated γ ray source irradiated the crystal at the center of each of the 64 SiPM pixels. The measurement was conducted for 15 minutes at each

¹⁷The good agreement between the data points and the $1/\sqrt{E}$ fit function demonstrates that the relative energy resolution of this detector assembly is predominantly determined by Poisson statistics.

¹⁸Please note: The energy resolution with the PA3350WB-0808 is not given in Tab. 6.6, as two malfunctioning channels were found, which cause a deterioration of the measurable energy resolution and the outcomes would not be comparable any more. However, also in measurements with the KETEK PA6647WL-0808 (which showed a comparable energy resolution using the PETsys ASIC) with only a minimally superior energy resolution of 3.5 ± 0.1 % (at 662 keV; 5.0 V OV) was found using the HGRB (see Sec. 6.2.3.1).

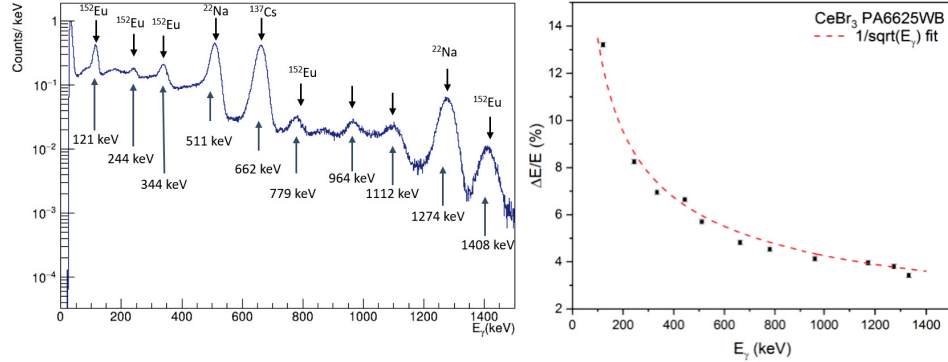


Fig. 6.24: Energy spectrum obtained with a CeBr₃ crystal read out with a KETEK PA6625WB-0808 by a simultaneous flood irradiation with three calibration sources (¹⁵²Eu, ²²Na and ¹³⁷Cs) (left) and the obtained relative energy resolution plotted vs. the initial γ -ray energy (black data squares) and a $1/\sqrt{E}$ fit (red dashed line) (right). The energy spectrum was obtained via a summation of all SiPM array channels using the hybrid-ganging readout board (HGRB; see main text). Reproduced from [Zhou 2020].

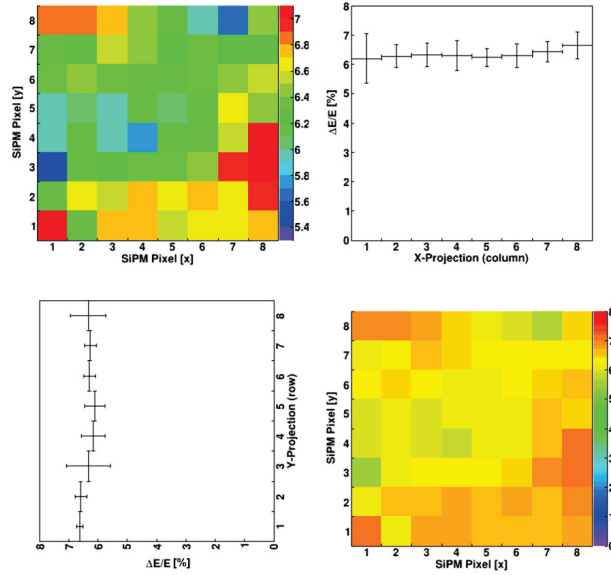
position. The calculated values of the energy resolution (including the projections along the x and y dimension) for both available CeBr₃ crystals are displayed in Fig. 6.25 [Zhou 2020].

The previously reported observation of a superior performance of the newer crystal (#2) could be confirmed by these detailed measurements.

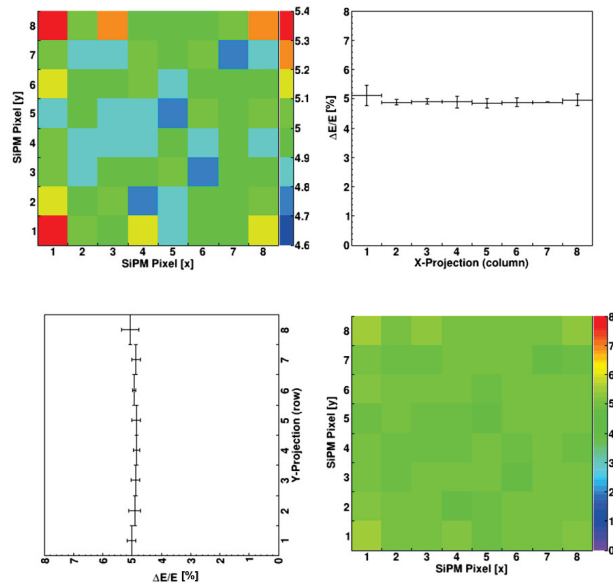
For the newer crystal a very uniform behavior of the energy resolution was observed, as can be seen from Fig. 6.25(b). The pixel-to-pixel fluctuations range from 4.7 % to 5.3 %, with a trend to observe the poorest energy resolution on the crystal edges. For the older crystal (Fig. 6.25(a)), also a poorer energy resolution in the bottom right edge of the crystal was observed. Compared to the other crystal, also the fluctuations are larger with a range from 5.4 % to 7.0 % ($\Delta_{min-max}$: 0.6% for crystal #2 vs. 1.6% for crystal #1).

Upgrade to the latest KETEK low-noise SiPM series (PA3347WL-0808) and performance evaluation As already mentioned in Sec. 6.1.3, a new KETEK low-noise SiPM array series was released in April 2021. Following the findings on the energy resolution of the LaBr₃:Ce and CeBr₃ crystals using the then available KETEK SiPM arrays from the WB series, also a potential performance improvement of the absorber detector in terms of its energy resolution using the new 47 μ m microcell SiPM types was investigated. Again the adapter mezzanine PCB to reduce the 256 channels to 64 channels was used for all further measurements and the resulting array will consistently be referred to as PA6647WL-0808.

The energy resolution was systematically evaluated at energies between 121 keV and 1274 keV at applied overvoltages to the SiPM arrays of 4.0 V to 7.0 V with an increment of 0.5 V. A comparison between the achievable energy resolution was furthermore done



(a) CeBr₃ #1 (older) crystal



(b) CeBr₃ #2 (newer) crystal

Fig. 6.25: Position dependent energy resolution map and corresponding projections from a 2D (x,y) scan (64 positions in ≈ 6 mm steps) of two monolithic CeBr₃ blocks read out by a PA6625WB-0808 SiPM array. The colour maps in bottom right corner of each panel shows the energy resolution for each of the 64 pixels in a range from 0% to 8%, whereas the plots in the top left show a zoomed view with a scale centered around the corresponding energy resolution.

by using the PETsys Electronics TOFPET v2c ASIC and the hybrid ganging (summation) board (HGRB). Using the PETsys ASIC the energy resolution obtained with the new PA6647WL-0808 array was found to be 4.1 % at 662 keV, which is identical to the previously reported performance of the PA6650WB-0808. Given the comparable PDE of both SiPM types, the finding is consistent with expectations. However, the reduced noise of the PA6647WL-0808 and the increased gain allowed to achieve this excellent energy resolution not only at one specific applied overvoltage of 5.5 V (as was done for the PA6650WB-0808), but over a range of overvoltages between 5.0 V to 6.0V. The practical benefit thereof is an easy gain adaptation via the SiPM overvoltage to fit a digitizer's (e.g. ADC or QDC) dynamic range.

Using the hybrid ganging readout board, an energy resolution of 3.6 ± 0.1 % at 662 keV was found (at 5.5 V OV). In terms of the overvoltage dependency of the energy resolution, the reported results are consistent with the ones obtained using the PETsys ASIC. The minimum of the energy resolution could be obtained at an overvoltage of 5.0 V with a value of $\Delta E/E = 3.5 \pm 0.1$ % at 662 keV. Fig. 6.26 (left) shows an energy spectrum of a simultaneous flood irradiation by three calibration sources (^{152}Eu , ^{22}Na and ^{137}Cs) of the $\text{LaBr}_3:\text{Ce}$ crystal (read out by the PA6647WL-0880) where the sum signal was generated via the HGRB. A comparison of this energy spectrum with the one obtained from the CeBr_3 (Fig. 6.24 (left)) clearly shows the superior energy resolution of the $\text{LaBr}_3:\text{Ce}$ in a readout configuration using the PA6647WL-0808. The measured values for the energy resolution of this detector is plotted in Fig. 6.26 (right) for energies between 121 keV and 1274 keV. A $1/\sqrt{E}$ fit curve (dashed red line) is overlaid to the data points. Again, the energy resolution of this detector assembly is predominantly determined by Poisson photon statistics.

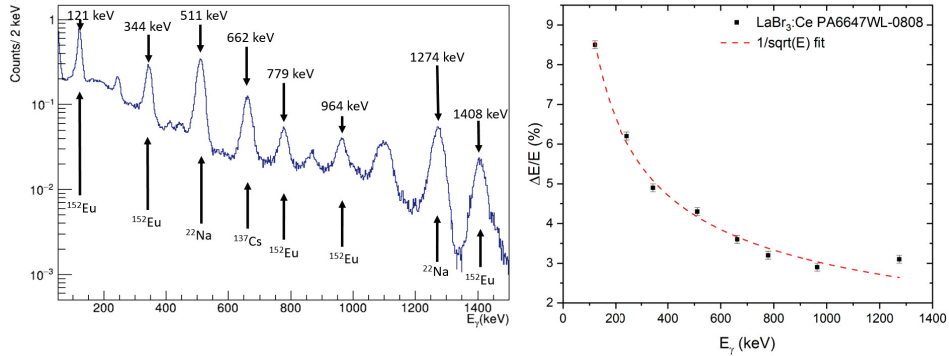


Fig. 6.26: Energy spectrum obtained with a $\text{LaBr}_3:\text{Ce}$ crystal read out by a KETEK PA6647WB-0808 array by a simultaneous flood irradiation with three calibration sources (^{152}Eu , ^{22}Na and ^{137}Cs) (left) and the obtained relative energy resolution (at 5.0 V OV) plotted vs. the initial γ -ray energy (black data squares) together with a $1/\sqrt{E}$ fit (red dashed line) (right).

Performance summary of the absorber detector below 1.5 MeV The relative energy resolution of monolithic scintillator blocks was investigated for photon energies up to 1.5 MeV. Among the two scintillation materials under investigation, the LaBr₃:Ce showed a superior energy resolution for all conducted measurements by about 1 % to 1.5 % compared to the CeBr₃ under study.

Using the PETsys TOFPET v2c ASIC, it was found to be beneficial to use a mezzanine board that generates $6 \times 6 \text{ mm}^2$ SiPM active channel areas by a parallel circuit of four (2×2) SiPMs to increase the input charge per ASIC channel. Furthermore, an improvement of the energy resolution with increasing SiPM gain was found¹⁹, resulting in $\Delta E/E = 4.1 \pm 0.2 \%$ at 662 keV measured with the KETEK arrays PA6650WB-0808 and PA3347WL-0808. Using the energy sum signal generation method by adding individually integrated SiPM signals of using their acquisition timestamps suffers from two main disadvantages: a) noise of each individual electronics channel is integrated and contributes to the overall sum signal and b) a small fraction of each individual signal is lost due to the fact that signal integration starts only after the acquisition threshold is exceeded in that specific channel.

Using the hybrid ganging method (HGRB) to generate a sum signal already on hardware level, these two effects can be avoided. For all measurements using this method the energy resolution could further be improved by up to 2.0 %. The values found for the HAMAMATSU S14161-6050-08 of $3.6 \pm 0.2 \%$ ($2.8 \pm 0.2 \%$) at 662 keV (1274 keV), KETEK PA3325WB-0808 ($4.1 \pm 0.2 \%$ ($3.0 \pm 0.2 \%$) at 662 keV (1274 keV)) and KETEK PA3347WL-0808 ($3.6 \pm 0.1 \%$ at 662 keV) are compatible with best results measured with a MA-PMT of $3.4 \pm 0.1 \%$ ($2.4 \pm 0.1 \%$). The overall best energy resolution of $3.5 \pm 0.1 \%$ at 662 keV was measured using the KETEK PA6647WL-0808 at 5.0 V OV and using the HGRB.

The excellent energy resolution of the both scintillator materials (LaBr₃:Ce and CeBr₃) in a SiPM array readout configuration (especially for the SiPM arrays built from larger microcells ($47 \mu\text{m}$ and $50 \mu\text{m}$)) makes it a suitable detector for the detection of γ rays in the few hundred of keV up to about 1.5 MeV, as required for a Compton camera in γ -PET imaging mode.

6.2.3.2. Energy resolution above 1.5 MeV

γ -ray energies relevant when applying the γ -PET triple coincidence imaging technique (100 keV - 1.5 MeV) are accessible by calibration sources. Therefore, detectors can be fully characterized with respect to their energy resolution in the laboratory. Higher energetic γ rays as they are of relevance in prompt- γ imaging (e.g. 6.1 MeV of ¹⁶O) require alternative sources, e.g. a nuclear excitation which subsequently deexcites to

¹⁹This statement is also valid for increased gain due to higher overvoltages. In this case, however, at around 6.0 V OV the negative effects of SiPM noise become more dominant, causing the energy resolution to deteriorate.

its ground state under the emission of such an energetic γ ray. Hence, characterization experiments need to be performed at accelerator facilities. The measurements described in this section were conducted at the Maier-Leibnitz-Laboratory's (MLL) Tandem accelerator in Garching, Germany, and the Marburger Ionentherapie Zentrum (MIT) in Marburg, Germany.

Experimental Setup The experimental setup for the detection of prompt γ rays at an accelerator facility is determined by the physical process of prompt γ generation. The ion beam (projectile; here: p^+ and ^{12}C) irradiates a target (here: water (H_2O) and PMMA ($(\text{C}_5\text{H}_8\text{O}_2)_n$)). The ions transfer their energy via inelastic scattering or fragmentation reactions to the target's nuclei, which are lifted into an excited state. The deexcitation occurs promptly under the emission of a γ ray (see Sec. 2.2.3). The prompt γ rays are emitted almost isotropically in 4π , while correlated fast neutrons are mainly emitted in forward direction relative to the beam direction. Consequently, in order to obtain a high S/B for prompt γ rays, it is beneficial to position the detector under an angle with respect to the beam axis. For practical reasons, for all measurements presented in this section, the detectors were placed under a 90° angle with respect to the beam axis. The distance between the detector surface and the isocenter was chosen to be 200 mm. Fig. 6.27 shows a picture taken during a measurement period at the MLL Tandem accelerator, where four absorbers were simultaneously operated (left), while the right panel shows a schematics of the setup.

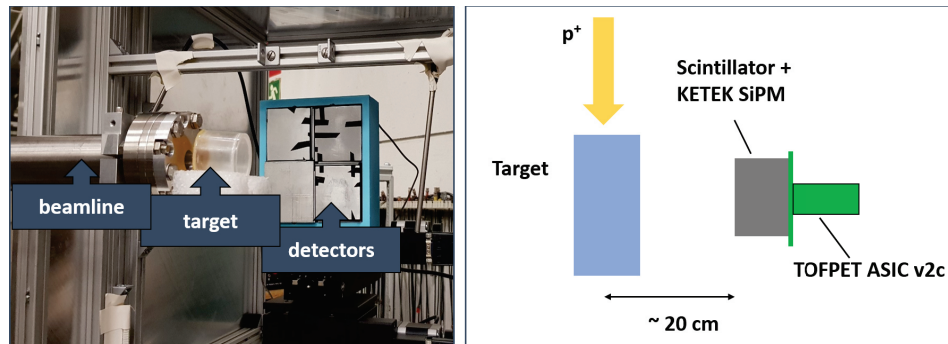


Fig. 6.27: Illustration of the setup used at the MLL Tandem accelerator to measure the energy resolution of monolithic absorbers to be used as absorber detector in a Compton camera setup. Left: The picture shows a detector configuration where four absorber detectors were placed in a 2×2 arrangement with the end of the beamline and the water target visible left of the detector assembly. Right: Schematics of the measurement setup with the detectors placed under an angle of 90° relative to the beam axis.

Measurement campaign at the MLL Tandem Accelerator The first measurement campaign at an accelerator facility was conducted at the MLL Tandem accelerator in Garching. The detectors under investigation were a $\text{LaBr}_3:\text{Ce}$ crystals alternatively coupled to the PA6650WB-0808 and PA6625WB-0808 arrays and the CeBr_3 crystal coupled to the PA6650WB-0808 array. The SiPM arrays were biased at 5.5 V overvoltage were

$\Delta E/E$ at	LaBr ₃ :Ce PA6650WB-0808	LaBr ₃ :Ce PA6625WB-0808	CeBr ₃ PA6650WB-0808
4.44 MeV	2.7 ± 0.1 %	3.7 ± 0.1 %	3.7 ± 0.1 %
6.13 MeV	1.8 ± 0.3 %	3.4 ± 0.3 %	3.0 ± 0.3 %

Tab. 6.7.: Summary of the measured energy resolution at the photo peak energy of excited ^{12}C and ^{16}O nuclei measured with the three investigated absorber detector assemblies.

read out by the PETsys TOFPET v2c ASIC. The ASIC settings are as given before (see Tab. 6.5)

Measurements were carried out using a 20 MeV proton beam with a proton current I_{p+} of around 5 and 15 pA²⁰ corresponding to $3 - 9 \times 10^7$ particles/s at the target that irradiated water and PMMA targets.

All measurements were conducted for 3600 seconds per detector configuration.

Fig. 6.28 shows the measured prompt- γ spectra from this first measurement campaign. From top to bottom, the detectors under study were a LaBr₃:Ce crystal read out by PA6650WB-0808 and PA6625WB-0808 SiPM arrays, respectively, and a CeBr₃ coupled to a PA6650WB-0808 array. The left column shows results obtained from a PMMA (rectangular block of $25 \times 20 \times 10$ mm³) irradiation, while the right one was obtained by irradiating a water target (water-filled cylinder of $h = 35$ mm, diameter = 35 mm with Kapton entrance window).

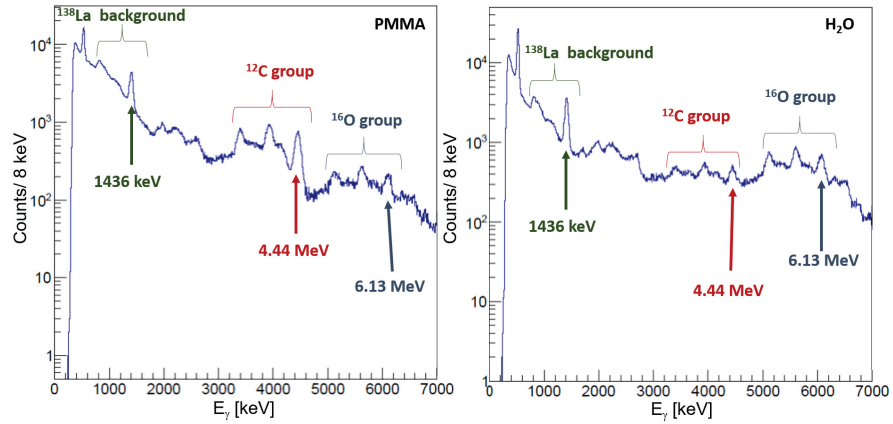
The 511 keV photo peak (from pair creation and fragmentation) is visible in all six spectra, indicating a dynamic energy range of at least 6.5 MeV (511 keV to 7000 keV). All spectra from the PMMA irradiation prominently show the peaks of the ^{12}C -group (photo peak, single (SE) and double escape (DE) peaks) and less prominently the peaks from the ^{16}O -group. In the spectra obtained by the irradiation of water, also the peaks of the ^{12}C - and ^{16}O -group are visible. However, here the oxygen group is more prominent due to stoichiometry of water, while the carbon group peaks are visible due to fragmentation reactions of oxygen nuclei with subsequent excitation and prompt deexcitation (see Tab. 2.2).

Evidently, the best energy resolution in this energy range was achieved with the LaBr₃:Ce coupled to the PA6650WB-0808 array, which is consistent with results obtained in the energy regime below 1.5 MeV. A more quantitative evaluation is shown in Fig. 6.29 and summarized in Tab. 6.7 for the photo peak energies of the deexcitation of the respective excited 2^+ states at 4.44 MeV of ^{12}C ($^{12}\text{C}(p,p')^{12}\text{C}^*$) and the 3^- state at 6.13 MeV of ^{16}O ($^{16}\text{O}(p,p')^{16}\text{O}^*$) nuclei [Kelly 1993, Kelly 2017].

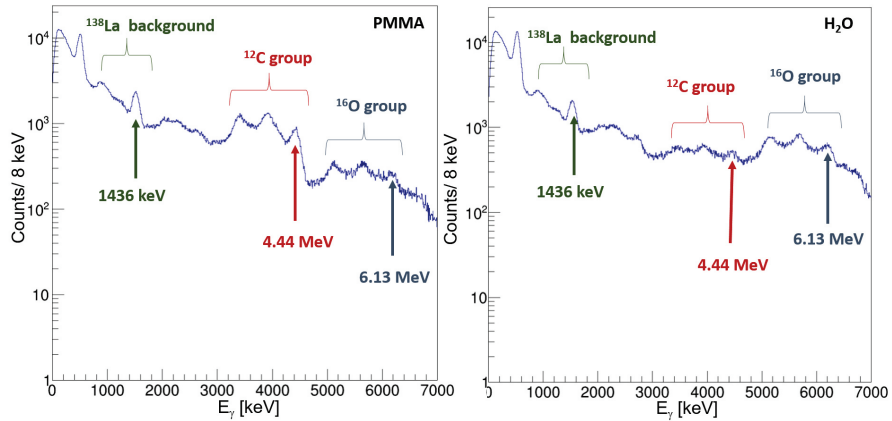
The detector assembly consisting of the LaBr₃:Ce crystal and the PA6650WB-0808 SiPM array shows with 1.8 % (2.7 %) at 6.13 MeV (4.44 MeV) a superior energy res-

²⁰due to current fluctuations at the accelerator

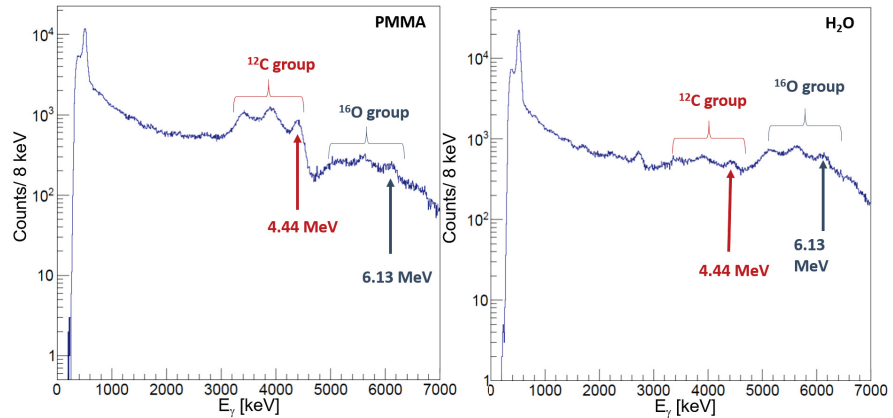
6.2. Characterization of the Compton camera absorber component



(a) LaBr₃:Ce read out with a PA6650WB-0808



(b) LaBr₃:Ce read out with a PA6625WB-0808



(c) CeBr₃ read out with a PA6650WB-0808

Fig. 6.28: Prompt γ energy spectra measured at the MLL Tandem accelerator obtained from a 20 MeV proton beam irradiation of water and PMMA targets for 3600 s. The shown spectra were measured with a LaBr₃:Ce crystal coupled to a KETEK PA6650WB-0808 and a PA6625WB-0808 SiPM array, respectively (top and middle panel) and a CeBr₃ crystal coupled to a PA6650WB-0808 array (bottom panel). The prompt γ spectra shown in the left column were obtained by irradiating a PMMA target, while the ones displayed in the right column were obtained by irradiating a water target.

olution by 1.2 % to 2 % compared to the two other detector assemblies. Only for this configuration the photo peak and single escape peak of the deexcitation of the 2^+ state (6.91 MeV) and the single escape peak of the deexcitation of the 1^- (7.11 MeV) state of ^{16}O are visible in the spectra, too. Fig. 6.29 also shows that the alternatively studied combinations of detector material with SiPM photosensor array, namely substituting the $\text{LaBr}_3:\text{Ce}$ by a CeBr_3 crystal and the PA6650WB-0808 by a PA6625WB-0808 array, result in comparable effects on the measured energy resolution. Within the measurement uncertainties the relative energy resolution at 4.44 MeV (6.13 MeV) of 3.7 % (3.0% and 3.4%, respectively) are of the same quality.

A further difference between the two used crystal compounds (besides the achievable energy resolution) becomes evident in the shown spectra (Fig. 6.28). While in the $\text{LaBr}_3:\text{Ce}$ crystal spectra the presence of ^{138}La manifests itself as a contribution to the spectra by a sharp γ line at 1436 keV (+ 32 keV X-ray) from the electron capture decay channel and in a continuous distribution starting at 798 keV followed by a beta continuum from the β^- decay channel, the CeBr_3 spectra are free of such radioactivity background contribution.

Measurement campaign at the Marburger Ionen Therapie Zentrum (MIT) A second measurement campaign could be conducted at the Marburger Ionen Therapie Zentrum (MIT) in Marburg. As this beam time was performed in parasitic mode jointly with the main user group from the University of Giessen, the beam parameters, especially the beam current, could not be set to our specific needs. As a consequence, the statistics of the measured energy spectra remained relatively low, resulting in a large uncertainty on the determined relative energy resolution values. Despite the low statistics, the capability to also measure prompt- γ spectra using the four HAMAMATSU S14161-3050HS-08 SiPM arrays (8×8 channel configuration) to read out the $\text{LaBr}_3:\text{Ce}$ crystal could be shown (Fig. 6.30 (right panel)). The measured spectra were obtained by a 1800 s irradiation of PMMA with ^{12}C ions at an energy of 200 MeV/u. As also the spectra shown in the previous section, the lines from ^{138}La are visible as well as three peaks (photo peak, SE and DE) originating from the deexcitation of ^{12}C from the 2^+ state at 4.44 MeV into the ground state. In contrast to the spectra obtained by proton irradiation, also a gamma line at 718 keV is visible. These γ rays are emitted by the transition of excited ^{10}B into the ground state. The $^{10}\text{B}^*$ is the result of fragmentation of the projectile ^{12}C ions into ^{10}C , which decays into $^{10}\text{B}^*$ via β^+ decay.

The statistics of this measurement was not large enough to provide a meaningful value for the relative energy resolution at 4.44 MeV for this readout configuration.

For comparison also the hybrid-gating readout board could be tested. In contrast to the signal processing performed by the PETsys TOFPET v2c ASIC, the energy spectra acquired using the hybrid-gating board show a linear behaviour up to 4.44 MeV²¹. This result indicates that already the detector assembly ($\text{LaBr}_3:\text{Ce}$ and SiPM array without

²¹Only a calibration that converts from ADC channels into keV plus an offset correction was performed on the energy spectra using a linear calibration function.

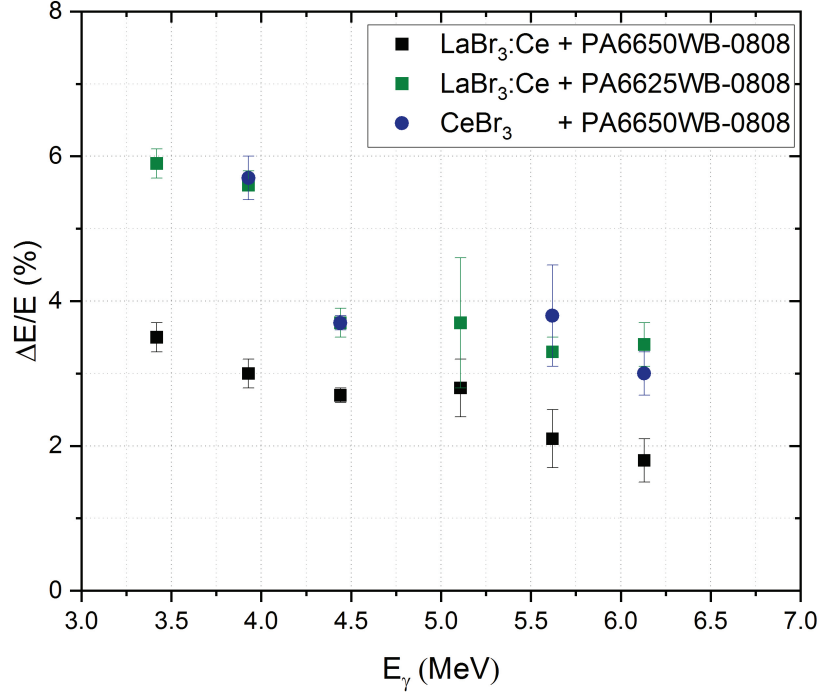


Fig. 6.29: Summary plot of the measured energy resolution of the LaBr₃:Ce crystal coupled to a PA6650WB-0808 and a PA6625WB-0808 SiPM array, respectively, and the CeBr₃ read out by the PA6650WB-0808 array at energies between 3 MeV and 6.1 MeV. The energy resolution was obtained from prompt γ photons obtained by a proton beam irradiation (20 MeV) of water and PMMA targets (each for 3600 s).

considering the specific readout configuration) provides a linear energy response (with only minimal saturation). Otherwise, the digitized signal would have also shown a non-linearity. The obtained prompt- γ spectrum is displayed in Fig. 6.30 (left panel). The measured energy resolution at 4.44 MeV was 3.5 ± 1.4 %. The large uncertainty on the given value arises from the large uncertainty on the fit due to the limited statistics of the photopeak.

Eventually, also the PA6625WB-0808 was tested to read out the CeBr₃ crystal using the hybrid-ganging readout board for detector signal summation. The obtained prompt γ spectrum is shown in Fig. 6.31. Also in this detector assembly configuration the triple-peak structure of the ¹²C deexcitation is clearly visible. However, again due to a lack of statistics, no meaningful value for the energy resolution at 4.44 MeV can be given.

Summary on the energy resolution above 1.5 MeV Both monolithic absorber crystal compounds were successfully tested at γ -ray energies up to 6.1 MeV obtained from exper-

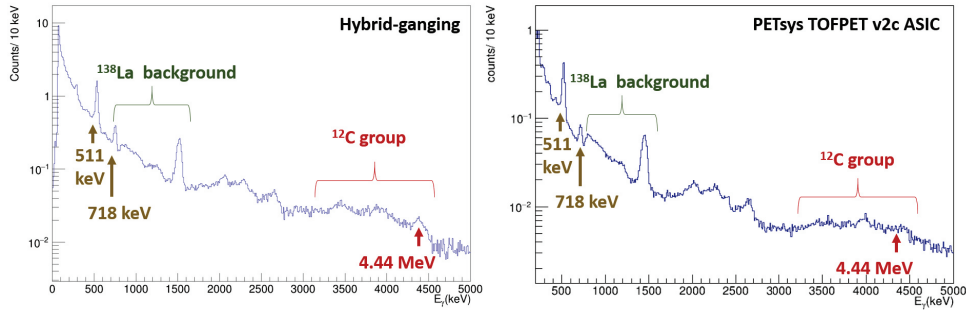


Fig. 6.30: Prompt γ spectra of a $\text{LaBr}_3:\text{Ce}$ crystal coupled to four S14616-30HS-08 arrays (using 64 ch. configuration) using the hybrid-gangang method to (hardware-wise) generate an energy sum signal (left panel) and the PETsys TOFPET v2c ASIC (right panel) as signal processing units. The prompt γ rays were obtained by the irradiation of PMMA with a ^{12}C ion beam (200MeV/u) for 1800 s at the Marburger Ionentherapie Zentrum.

imental campaigns at accelerator facilities. The prompt γ rays were obtained by an irradiation of water and PMMA targets with 20 MeV protons and 200 MeV/u carbon ions, respectively. Three different photosensor types were investigated (KETEK PA6650WB-0808 and PA6625WB-0808 arrays and the HAMAMATSU S14161-60*50HS-08 MPPC array) together with two types of signal processing electronics. The latter allowed to compare two different methods of energy sum signal generation. The best energy resolution at 6.1 MeV was obtained by the $\text{LaBr}_3:\text{Ce}$ crystal coupled to the PA6650WB-0808 SiPM array²². However, all investigated detector combinations allowed to resolve the prompt γ rays of the expected energies, proving the general capability of all configurations to be used as Compton camera absorbers for ion beam range verification in particle therapy.

The excellent energy resolution of the both scintillator materials ($\text{LaBr}_3:\text{Ce}$ and CeBr_3) in a SiPM array readout configuration (especially for the SiPM arrays built from larger microcells (47 μm and 50 μm)) at prompt γ energies up to 7 MeV and the wide energy ranges that are resolvable makes the absorber detector assemblies under investigation also a good choice as Compton camera absorber for prompt γ imaging for range verification in hadron therapy.

6.3. Conclusion

This chapter presented detailed evaluations of a scintillator-based scatter and absorber component for a Compton camera prototype with an SiPM array readout configuration with the focus on using the PETsys TOFPET v2c ASIC for signal processing and data acquisition.

The scatterer was characterized with respect to its energy resolution, and potential

²²Measurements from the Marburg beamtime are not taken into account here, due to the very limited statistics available.

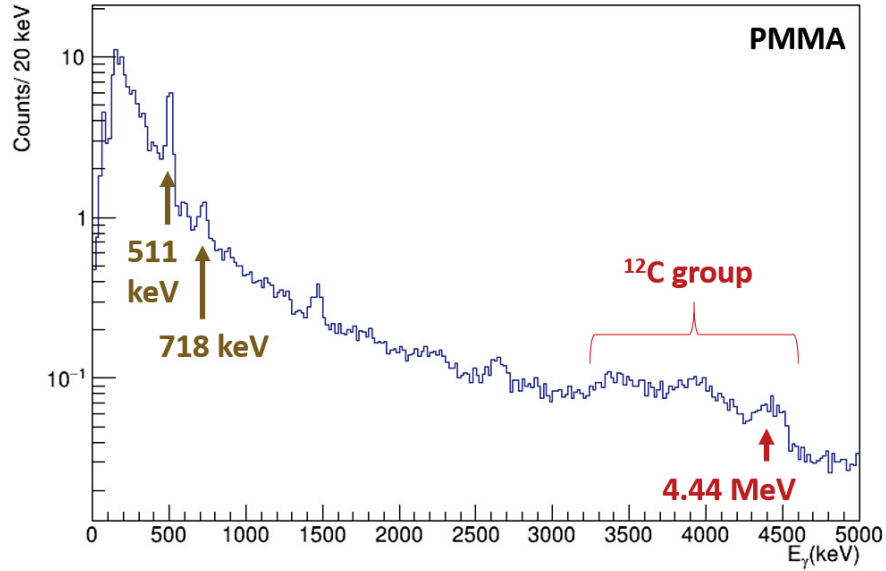


Fig. 6.31: Prompt γ -ray energy spectrum of a CeBr_3 crystal coupled a PA6625WB-0808 SiPM array using the hybrid-gating method for hardware-wise energy summation as signal processing unit. The prompt γ rays were obtained from the irradiation of a PMMA target with a ^{12}C ion beam (200 MeV/u) during an acquisition time of 1800 s at the Marburger Ionentherapie Zentrum.

to resolve all individual crystals in various SiPM readout configurations (KETEK vs. HAMAMATSU; different SPAD sizes; optical grease vs. RTV silicon rubber sheet). The achievable relative energy resolution ($\Delta E/E$) at 662 keV between 9.5 % and 11.2 % (depending on the exact detector assembly configuration) and clearly resolved individual crystals in all configurations under study, demonstrate the suitability of such detectors to be used as Compton camera scatterer component.

The energy resolution of the absorber with in a SiPM readout configuration was optimized until a comparable performance to PMT-readout configurations were achieved in a wide energy range between 100 keV and 7.0 MeV. The best value at 662 keV was $\Delta E/E = 4.1$ % obtained using the $\text{LaBr}_3:\text{Ce}$ crystal and SiPM arrays with 50 μm and 47 μm SPADs, respectively. At 6.13 MeV an energy resolution of 1.8 % could be achieved using the $\text{LaBr}_3:\text{Ce}$ crystal and the KETEK PA3350WB-0808 SiPM array. From the excellent energy resolution over such a wide energy range we concluded that the absorber detectors under investigations are suitable candidates as Compton camera absorber.

For the final Compton camera prototype the scatterer component will be set up using SiPM arrays of the KETEK PA3325WB-0808²³ series and will be upgraded in the near

²³Despite with the KETEK WL series, the best energy resolution was obtained using the 50 μm HAMA-

future to PA3335WL-0808, which provided the overall best measured energy resolution. The absorber component will be commissioned using KETEK's WL series with $47\mu\text{m}$, alternatively the HAMAMATSU S14161-3050HS-08 arrays will be used.

MATSU SiPM arrays. Those, however, will be applied for the absorber component, in a four-arm Compton camera/ γ -PET configuration, which is why the scatterers (before the upgrade) will be commissioned by KETEK's $25\mu\text{m}$ microcell arrays.

6.3. Conclusion

Characterization of a Trapezoidal Pixelated Detector with Intrinsic DOI Resolution as PET and Alternative Compton Camera Absorber for Energies Below 1.5 MeV

*This chapter was published in *Physics in Medicine and Biology* under the title 'Performance evaluation of a staggered 3-layer DOI PET detector using a 1 mm LYSO pitch with PETsys TOFPET2 ASIC: Comparison of HAMAMATSU and KETEK SiPMs' by Binder et al. [Binder 2021]. Some parts have been modified and details were added compared to the original publication. Furthermore, the sections 7.2.2 and 7.2.3 were supplemented by the investigation results of a second DOI LYSO crystal block with identical crystal total size, but a crystal pitch of 1.2 mm.*

Contents

7.1. Experimental setup and electronics settings	127
7.2. Measurements & results	131
7.2.1. SiPM arrival time distribution	131
7.2.2. Spatial information and crystal identification	132
7.2.3. Energy resolution	136
7.2.4. Inter crystal scattering (ICS)	139
7.2.5. Analysis of the time difference spectra	141
7.2.6. Coincidence resolving time	144
7.3. Discussion and conclusion	148

The information and experience gained in the previously described measurements can be used to read out other detector configurations, too. This chapter will show a characterization of a 3-layered stacked PET detector with intrinsic depth-of-interaction (DOI) resolution. This detector is planned to be used as PET detector in the SIRMIO project (Small animal proton Irradiator for Research in Molecular Image-guided radiation-Oncology; ERC Grant; PI: K. Parodi) [Parodi 2019]. This innovative, portable system for precision image-guided treatment combines in-beam PET with various other imaging

methods such as ionoacoustics and proton radiography. Furthermore, such a DOI LYSO crystal block can be used as an alternative absorber detector to the monolithic crystal blocks.

The focus of the PET detector will be on the improvement of the efficiency by using DOI information. For a given energy of 511 keV the detection efficiency depends on factors like the material density and the covered solid angle. For a given material, however, the efficiency can be improved by enlarging the thickness of the scintillation crystal. As a trade-off the image resolution will decrease, due to the uncertainty introduced on the reconstruction of the line-of-response (LOR). For an unknown depth of interaction an assumption has to be made (e.g. the interaction is assumed to occur in the center of the crystal). As shown in Fig. 5.1 the reconstructed LOR (red) will deviate from the actual LOR (green), if the depth of interaction is not taken into account. This effect becomes more dominant the thicker the crystal gets and influences the PET image resolution (see Fig. 5.2)

7.1. Experimental setup and electronics settings

The setup The detector used for this investigation is a trapezoidal three-layer stacked LYSO crystal block consisting of $0.9 \times 0.9 \times 6.6$ mm³ individual crystals, optically isolated by a layer of 0.1 mm thick BaSO₄ in between each crystal. The first layer consists of 23×22 crystals, the second layer comprises 23×23 crystals and the third layer is composed of 24×24 crystals. The crystals in the second layer are shifted by half a crystal pitch with respect to the first layer along the x-axis and the crystals in the third layer have an offset of half a crystal pitch along the y-axis with respect to the first and second layers. In order to couple the DOI scintillator block to the photosensor, optical grease (St. Gobain BC-631) was applied. A KETEK PA3350WB-0808 prototype SiPM array with a breakdown voltage of 25.2 V (5.0 V recommended overvoltage/ 30.2 V applied voltage) (as determined by the author) and a HAMAMATSU S14161-3050HS-08 MPPC array with a breakdown voltage of 38.6 V (2.7 V recommended overvoltage/ 41.3 V applied voltage) [Hamamatsu 2020] were used. Both arrays have 8×8 channels with an active area of 3×3 mm² and 50 μ m single-photon avalanche photodiodes (SPADs). The SiPM channel pitch is 3.36 mm (KETEK) and 3.2 mm (HAMAMATSU), respectively [Ketec 2021b, Hamamatsu 2020]. The PETSys Electronics Evaluation kit based on the TOFPET2 v2c ASIC was used as signal processing and data acquisition system. Two of these 64 channel ASICs are mounted on a front-end-module (FEM128) to which the detector is connected. Each ASIC channel is operated independently, i.e. has its individual amplifier, discriminator and digitizer (TDC/ADC) [Petsys 2019]. The working principle of the ASIC's trigger logic is described in Sec. 4.2. The setup is pictured in Fig. 7.1. On the left-hand side the DOI detector (wrapped with black tape) is connected to a FEM-128 front-end-module with the TOFPET v2c ASIC. On the right, a reference detector array ($3 \times 3 \times 5$ mm³ LYSO crystals coupled one-by-one to a KETEK PA3325WB-0808 SiPM array) is shown, which was used to measure the coincidence resolving time (CRT). The radioactive source (here: ²²Na with an activity of 180 kBq resulting in an accepted count rate in the low kHz range depending on the exact distance between the detector front surface and the radioactive source) is placed in the center between the two detectors. The blue ribbon cables transfer the digital signals to the FPGA. For the flood map acquisition and energy resolution measurements, the data were taken in single-mode in which the reference detector is not connected to the FPGA board and only the DOI detector is used. For measurements of the CRT, the data were taken in coincidence mode in which the reference detector is configured with the identical settings (e.g. thresholds, integration windows, etc.) as the DOI detector. As a reference to the initially investigated DOI LYSO with 0.9 mm crystal pitch, an alternative variant of DOI LYSO crystal block with a 1.2 mm crystal pitch and 16×17 crystals (first layer), 17×18 crystals (second layer) and 18×18 crystals in the third layer was investigated. This detector block was initially commissioned and characterized as a potential SIRMIO PET detector. Therefore, the crystal readout is identical to the one used within the SIRMIO configuration, i.e. the used photosensor is a HAMAMATSU

7.1. Experimental setup and electronics settings

S14161 3050HS-08 MPPS array biased at 2.7 V OV. The optical coupling between the crystal block and the MPPC array involved a 1 mm thick layer of silicon rubber sheet [Shin Etsu KE-42-T].

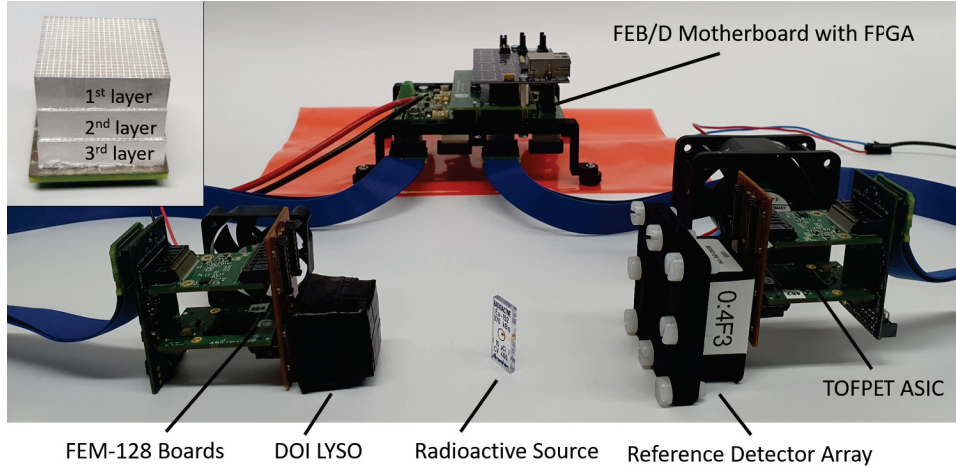


Fig. 7.1: The setup used for coincidence measurements is shown. The DOI detector is visible on the left connected to one FEM-128 frontend module containing the TOFPET v2c ASIC, while the reference detector used to determine the CRT is placed on the right side of the radioactive calibration source which is centered inbetween both detectors. The FEM-128 board are connected via the blue ribbon cables to the motherboard which contains the FPGA and is responsible for the communication to the acquisition computer via a gigabit ethernet link. The inset shows a picture of the DOI LYSO crystal placed on the KETEK PA3350WB-0808 array.

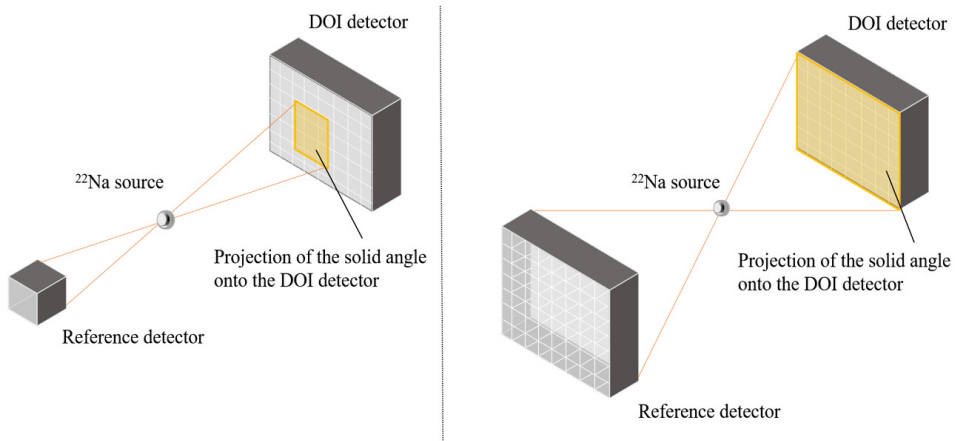


Fig. 7.2: Schematic of a coincidence setup for the DOI detector and a small reference detector (left) and a reference detector of larger active area in the same position (right). The orange squares represent the projection of the solid angle that can be covered by the reference detector for coincidences with the DOI detector.

The Reference detector array for CRT measurements When using a small reference detector compared to the total size of the DOI LYSO detector, geometrical constraints would allow for calculating the CRT only for a part of the DOI detector, if the setup is as compact as the used one with a distance between the DOI detector and the reference detector of only 60 mm. The reason is that the reference detector can only find opposing coincident channels within a solid angle spanned by all possible LORs and therefore depends on the detector’s surface area and the distance to the opposing coincident DOI detector crystal. Fig. 7.2 shows a schematic view of the coincidence setup consisting of a DOI detector and a small reference detector (left) and a larger reference detector (right). The orange lines represent the envelope of all possible LORs and the orange squares represent the projection of the solid angle spanned by all possible LORs onto the DOI detector. Fig. 7.2 shows that for a small reference detector compared to the DOI detector only for a subset of all DOI channels coincidences can be found due to geometrical constraints. To overcome this restriction either the distance between the two detectors can be increased, which reduces the coincidence rate and increases the measurement time. Alternatively, instead of the small single-channel reference detector, a full reference detector crystal array can be used to enlarge the solid angle coverage of the reference detector. The latter method was chosen in this work. The reference detector array was an 8 x 8 channel array (3 x 3 x 5 mm³ LYSO crystals) one-to-one coupled to a KETEK PA3325WB-0808 SiPM array, resulting in a reference detector active area of 27 mm × 27 mm. By using this reference detector array for the CRT measurements an opposite reference channel could be found for most of the 64 possible channels of the DOI detector. The bias voltage for the reference detector was lower than actually recommended by KETEK (set to 30.1 V). The reason is the large difference in signal amplitudes between a one-by-one coupling (reference detector array) and a light sharing approach (DOI detector). As consequence, the thresholds for optimum results are different. The focus was set to maximize the performance of the DOI detector. By reducing the bias voltage and consequently the gain of the reference detector, the performance with the low thresholds used for the DOI detector could be improved. Even though, in general, a higher bias voltage and the resulting steeper rising edge of the signal results in an improved CRT (until the deteriorating influence of noise such as dark counts become dominant), no deterioration on the measured CRT of the DOI detector is expected due to the low bias voltage of the reference detector array, since its time resolution, and therefore its contribution, is deconvolved from the DOI detector’s CRT.

The ASIC configuration All measurements were performed with the signal processing system set to the QDC mode, i.e. the charge integration stage (QDC) was used. As mentioned in the previous section, the full trigger logic (nominal mode) was used, including the timing threshold V_{th_T1} for dark count rejection and providing an accurate time stamp [Petsys 2019]. The thresholds V_{th_T1} and V_{th_E} were used for event validation and to start the actual signal integration [Petsys 2019]. The integration window length

is set dynamically between 20 ns and 900 ns and closes – on an individual channel basis – after the signal has dropped below the three respective threshold levels plus a delay of 6 ns (falling edge of `trigger_B`). The gain of the transimpedance amplifiers (TIAs) was set to the maximum value of 3000 Ω (G_T) for the time branch and 300 Ω (G_E) for the charge branch. The integrator gain was also set to the maximum value of 3.65. While the threshold starting the integration (v_{th_T2}) was set differently for the KETEK SiPM and HAMAMASTSU MPPC arrays, V_{th_T1} - defining the timestamps - was set to the minimum value of 2.8 mV [19] for the SiPM arrays of both manufacturers. For the flood maps the applied threshold settings were $V_{th_T2} = 12.6$ mV, $V_{th_E} = 9.8$ mV and $V_{th_T2} = 35.0$ mV, $V_{th_E} = 32.2$ mV for the KETEK and the HAMAMASTSU array, respectively. The relative energy resolution was measured with $V_{th_T1} = 2.8$ mV, $V_{th_T2} = 25.6$ mV and $V_{th_E} = 19.6$ mV (KETEK) and $V_{th_T1} = 2.8$ mV, $V_{th_T2} = 32.2$ mV and $V_{th_E} = 30.8$ mV (HAMAMASTSU). The system was actively cooled by a 12 V DC fan, which removes the warm air around the ASICs. While the temperature measured at the ASIC acquiring and processing the signals of the DOI detector was measured to be 28.4 ± 0.3 °C during the acquisition of the flood maps, the temperature was decreased to approx. 25.0 ± 0.3 °C by using a more powerful fan when measuring the CRT of the detector. In accordance with information from the manufacturer, the ASIC’s gain increases with decreasing temperature. Also the SiPM breakdown voltage decreases with rising temperature (22 mV/K (KETEK) [31] and 34 mV/K (HAMAMASTSU) [23]), which naturally leads to a higher applied overvoltage and therefore to an increase of the SiPM gain. The gain change of the system can only be given as entangled effect arising from a gain increase of both the SiPM and the ASIC and is approximated from previous experiments (in the temperature region between approx. 23 °C and 40 °C) to approx. 2.5 % per °C. As a consequence, the thresholds V_{th_T2} and V_{th_E} could be increased for the KETEK SiPM to determine the CRT and therefore for the SiPM arrays of both manufacturers identical thresholds could be used ($V_{th_T1} = 2.8$ mV, $V_{th_T2} = 39.2$ mV, $V_{th_E} = 28.8$ mV). This assured identical threshold settings for the reference detector during the CRT measurements of both SiPM/MPPCs.

The error analysis The errors given to the measured values presented in the next chapter are determined as follows: The statistical error given for all values of the energy resolution arises from the error on the Gaussian fit’s sigma value that is fitted to the photo peak. Since the fit error of the Gaussian’s centroid only contributes with about 1% to the statistical uncertainty it is neglected for the statistical error given in the following analysis. For the energy resolution of the individual layers, 12 crystals in a central region and 12 crystals in the edge region were evaluated for each layer. The obtained 12 values for each set of energy resolutions form a distribution. The 1σ standard deviation of this distribution is considered as the “inter-crystal variability” uncertainty (σ_{var}) of the energy resolution (represented by the length of the antennas in Fig. 7.7). The dependency, however, of the energy resolution’s mean value on the layer causes the distribution for the total energy resolution to be asymmetric and the concept of using the

7. Characterization of a Trapezoidal Pixelated Detector with Intrinsic DOI Resolution as PET and Alternative Compton Camera Absorber for Energies Below 1.5 MeV

mean value and 1σ standard deviation for the “inter-crystal variability” is not practical. Therefore, the resulting total energy resolution will be given as the median value and the “inter-crystal variability” uncertainty will be given as the median’s difference to the 10% and 90% levels of the range, representing the energy resolution intervals that contain 80% of the values. For the coincidence resolving time (CRT) three main sources contribute to the uncertainties. The statistical uncertainty originates from the fit uncertainty of the gaussian fit to the central peak in the time-difference spectra that were used to derive the CRT. Like for the error analysis of the energy resolution, there is also a contribution by the inter-crystal variability to the uncertainty of the CRT. However, for the CRT there on the individual layers, that is derived from the CRT of individual DOI crystal’s CRT, also a second contribution was evaluated and is included in the δ_{var} component of the error. This second contribution is the variability of the arrival time measurements between the channel combinations to the overall CRT, when measured versus all combinations of reference detector channels found in coincidence. This contribution to the error includes a geometrical factor. It could be shown that in some events not only one but two coincident reference detector array channels directly opposing the DOI detector channel of interest (relative to the ^{22}Na source) exhibit a minimum of the CRT. In contrast, the CRT increases when being measured against more distant reference channels until finally no coincidences are found any more. For the given values of the total CRT (by the first and brightest firing channel, respectively), the second component is not present, since only one opposing reference detector channel was used to derive the CRT of one specific SiPM/ASIC channel.

7.2. Measurements & results

This section will deal with the findings and detailed evaluations of characterization measurements of the DOI LYSO. Starting with a study of the arrival time distribution of SiPM/ASIC signals of a single γ interaction in the scintillator, from which the grouping time window for all further measurement is derived, a detailed evaluation of the flood maps, the layer-wise energy resolution and the layer-wise coincidence resolving time will be given. A comparison between the detector performance in the KETEK SiPM read-out configuration and the HAMAMATSU MPPC configuration will be given in each section.

7.2.1. SiPM arrival time distribution

As mentioned in the previous section the PETsys TOFPET v2b ASIC is designed for one-by-one crystal-to-SiPM coupling and therefore triggers each channel individually. In order to obtain data from a detector that involves light sharing, the individual SiPM/MPPC signals need to be grouped together in order to assign the multiplicity of SiPM/MPPC channels to one initial gamma event detected in one scintillation crystal. PETsys Electronics provides a post-processing script that clusters triggered ASIC

channels such that all channels firing within a (selectable) coincidence window (grouping window) around one triggered channel are assigned to a common event. For a channel to be considered inside the grouping window the arrival time stamp, set when V_{th_T1} is exceeded, is used. Furthermore, a geometrical constraint can be set such that only SiPM/MPPC channels within a given radius around the initially triggered channel are considered. Also, multiple hits of one channel are excluded. The grouping time window needs to be set such that all firing SiPM/MPPC channels of an initial gamma are grouped together, but ideally no noise and background events are added to the actual gamma event distribution. Fig. 7.3 shows the arrival time distribution with respect to the first firing channel and a zoom into the region from $t = 0$ to $t = 200$ ns (bottom row) for the KETEK PA3350WB-0808 array (left column) and the HAMAMATSU S14161-3050HS-08 (right column). The energy axis is normalized to the total detected charge. Fig. 7.3 shows that after approx. 70 ns no further SiPM pixels are caused to fire by the scintillation light of an initial photon. Using these results, the grouping window was set to 75 ns in order to ensure that all firing channels are grouped together.

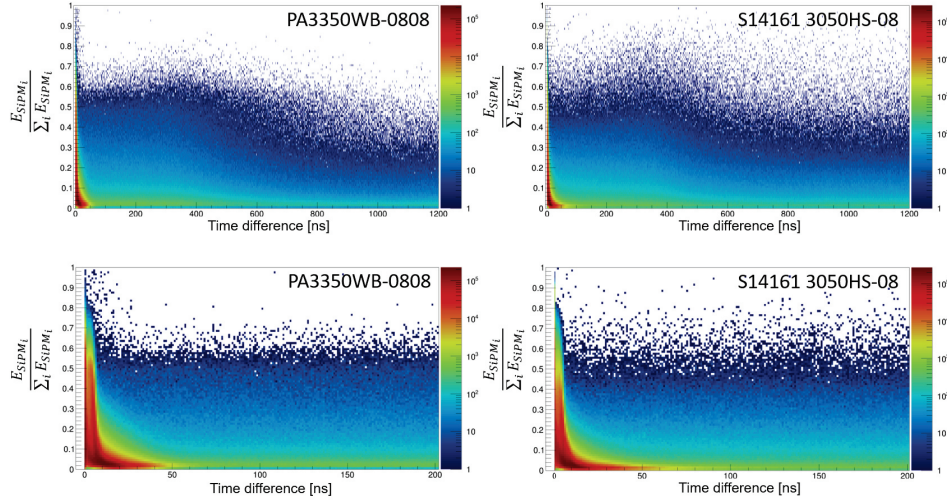


Fig. 7.3: Arrival time distribution (of several thousand events) of all firing SiPM channels within one gamma event with respect to the first firing SiPM pixel of the DOI detector block read out by the KETEK PA3350WB-0808 array (left column) and HAMAMATSU S14161-08 array (right column). On the y axis the fractional contribution of the energy registered in one event (normalized to its sum) is plotted. The maximum time evaluated corresponds to 1275 ns. The bottom row shows a zoom into the first 200 ns. The comparison between the 2D- histograms in the top and bottom row illustrates that by selecting a width of 75 ns for the grouping window to the distribution of the actual gamma event all SiPM triggered by the gamma event are taken into account, while fake coincidences are minimized.

7.2.2. Spatial information and crystal identification

The capability to spatially resolve each individual scintillation crystal of the DOI detector was shown by a flood irradiation of the detector with a ^{22}Na calibration source of 180 kBq activity. The radioactive source was placed in a distance of 2 cm (central position)

7. *Characterization of a Trapezoidal Pixelated Detector with Intrinsic DOI Resolution as PET and Alternative Compton Camera Absorber for Energies Below 1.5 MeV*

in front of the detector and data were taken for 600 s. The raw data were consecutively clustered into events belonging to one initial γ - hit in the detector by running a grouping routine provided by PETsys Electronics. The time window of this routine that defines the search range for quasi-coincident ASIC channels triggering after the first registered hit and thus determines what is considered to belong to the same γ event was set to 75 ns. The 2D interaction position within a detector layer was calculated via an Anger-type logic and an energy window from approx. -5σ to $+3\sigma$ around the photo peak of the inclusive energy spectrum was applied. For the Anger calculation the 64 channels of the SiPM array were clustered into 8 rows and columns (ROW_i and COL_i), respectively, with ROW_i (COL_i) being the total energy detected by the respective 8 SiPM of the i^{th} row (column). The interaction position in x (y) was calculated according to

$$x = \frac{\sum_{i=1}^n i \cdot COL_i}{\sum_{i=1}^n COL_i} \quad (7.1)$$

$$y = \frac{\sum_{i=1}^n i \cdot ROW_i}{\sum_{i=1}^n ROW_i} \quad (7.2)$$

The resulting (x,y) flood maps reveal that the individual crystals can clearly be resolved (Fig. 7.4 and Fig. 7.5 center rows). Most of the interactions are detected in the first layer (seen as brightest crystal response marked by a white triangle in the zoomed right-hand top panel of Fig. 7.4) due to the highest probability of 511 keV γ rays to be detected within the first 6.6 mm. Vertically shifted by half a crystal size, hits in the second layer appear with medium brightness in the flood map (marked with a white circle). The faintest spots, shifted horizontally by half a crystal size with respect to the first layer (highlighted by a white rectangle), belong to interactions in the third layer, being the least probable for interactions to occur. For both SiPM arrays under study from different manufacturers the flood maps exhibit clearly resolved crystal images with only minor distortions (see Fig. 7.4 (KETEK) and 7.5 (HAMAMATSU)). In order to confirm the assignment of photon interactions to their respective layers, also data were taken from a back-side irradiation of the detector block (i.e. placing the source in front of the SiPM array/frontend readout board). The bottom row of Fig. 7.4 shows a flood map obtained from such a back-side irradiation of the DOI detector read out by a KETEK PA3350WB-0808. The ordering of brightness of hits in the respective layers is reversed compared to the front-side irradiation. Due to geometrical constraints of this arrangement, imposed by the inhomogeneous matter distribution from the FEM-128 frontend boards carrying the ASIC chip and being plugged to the SiPM/MPPC arrays from the back-side, the ^{22}Na radiation source could not be placed in a central position for this irradiation scenario. This asymmetric irradiation explains why in the flood maps taken by back-side irradiations (Fig. 7.4 and Fig. 7.5 bottom rows) the crystal response appears brighter in the lower part of the flood map than in the top part.

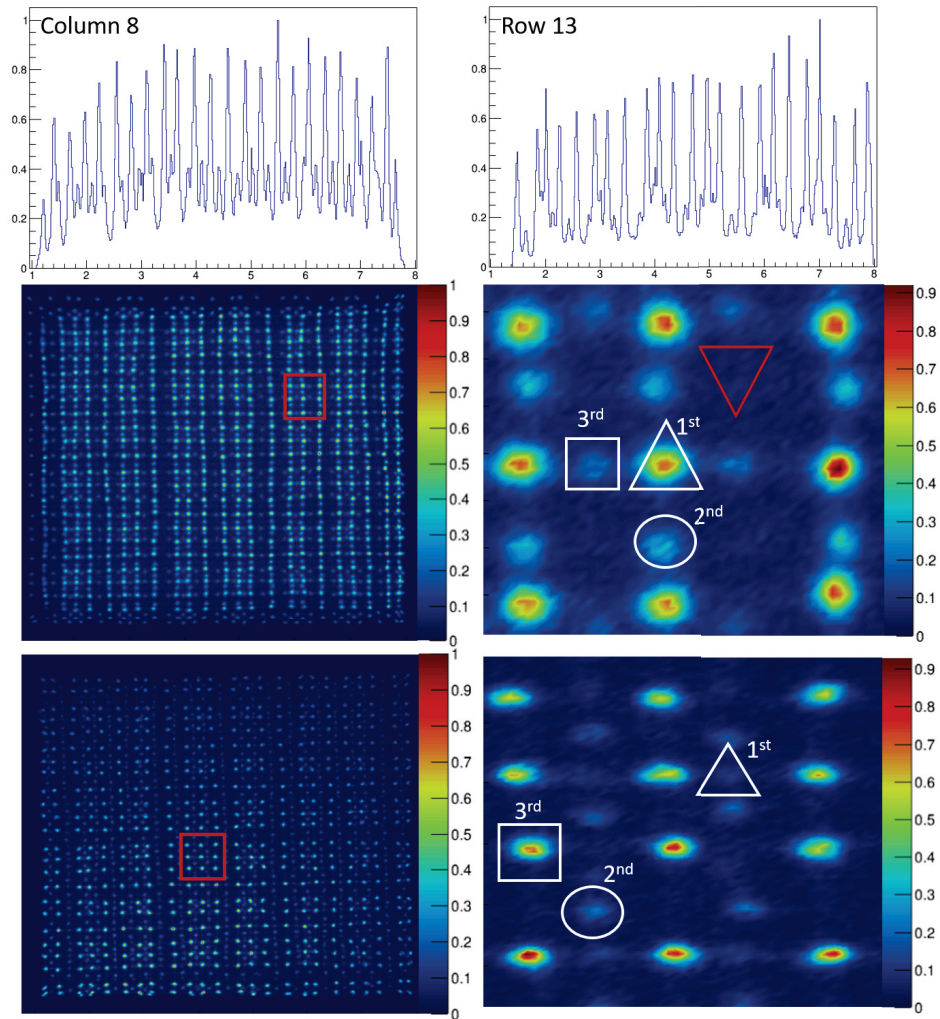


Fig. 7.4: Flood map acquired with the 3-layer DOI LYSO crystal block read out by a KETEK PA3350WB-0808 SiPM array operated at 5 V overvoltage (middle and bottom panels of left column), a zoom into the regions marked by the red rectangles (middle and bottom panels of right column) and the count rate profile of crystal column 8 and row 13 (top row). The middle panels show a flood map acquired in a 600 s front-side irradiation with a ^{22}Na source, while the data shown in the bottom panels were acquired during a 600 s back-side irradiation (see text). Crystals belonging to the first layer are indicated by a white triangle, crystals of the second layer by a circle and the squares indicate crystals of the third layer. The red triangle exemplarily highlights a region which only contains background and inter-crystal scattering events as will be described in section "Inter Crystal Scattering".

7. Characterization of a Trapezoidal Pixelated Detector with Intrinsic DOI Resolution as PET and Alternative Compton Camera Absorber for Energies Below 1.5 MeV

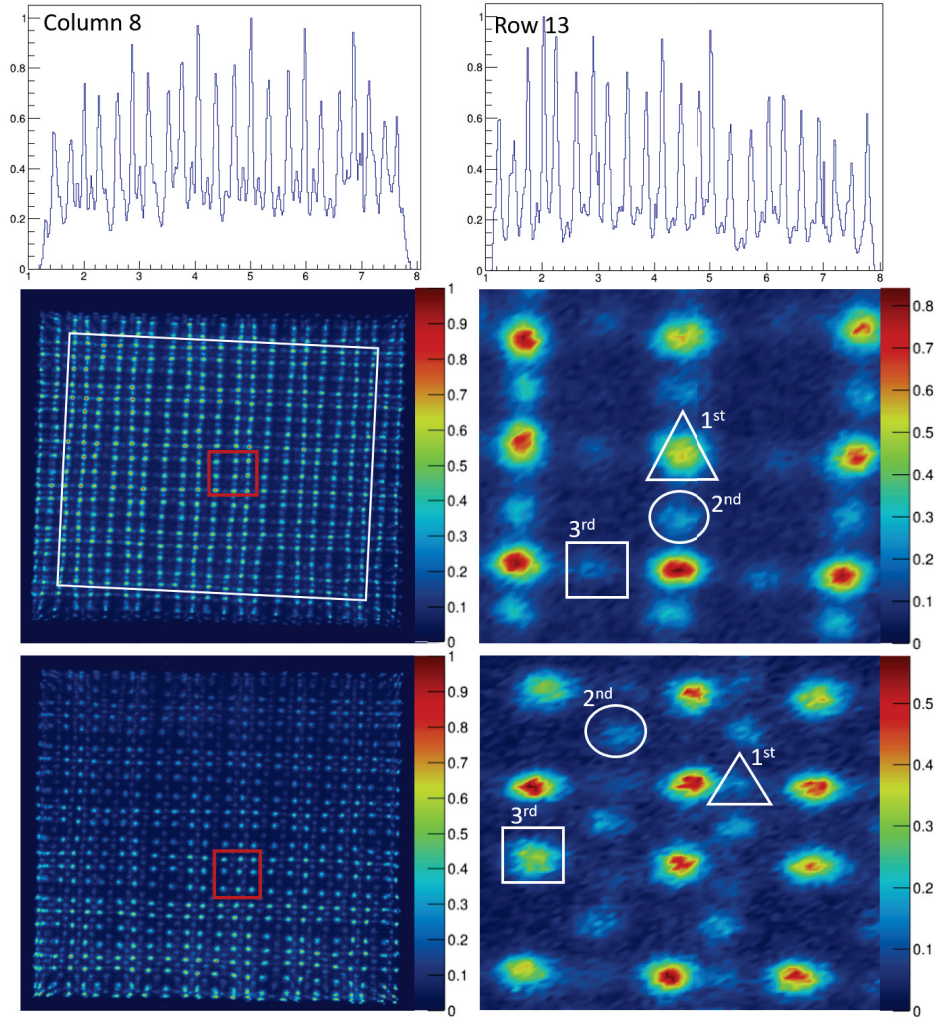


Fig. 7.5: Flood map acquired with the 3-layer DOI LYSO crystal block read out by a HAMAMATSU S14161-3050HS-08 MPPC array operated at 2.7 V overvoltage, irradiated with a 180 kBq ^{22}Na source (middle and bottom panels of left column), a zoom to the region marked by the red rectangle (middle and bottom panels of right column) and the count rate profile of crystal column 8 and row 13 (top row). The middle row shows a flood map acquired in a 600 s front-side irradiation with a ^{22}Na source, while the data shown in the bottom row were acquired during a 600 s back-side irradiation (see text). Crystals belonging to the first layer are indicated by a white triangle, crystals of the second layer by a circle and the square indicates crystals of the third layer. The white square in the middle left panel marks the two regions which were considered to contain “edge” and “central” crystals as discussed in the section “Energy Resolution”

For the sake of completeness, the flood map acquired with the 1.3 mm pitch DOI LYSO crystal block is shown in Fig. 7.6. All crystals can be identified and well separated from their respective neighbours for the central 13×15 pixels (counted via the first layer crystals). Towards the edges the flood map appears to be compressed. Consequently, only the first layer crystals can still be clearly resolved, while the second and third layer

crystals overlap and can not be distinguished from each others.

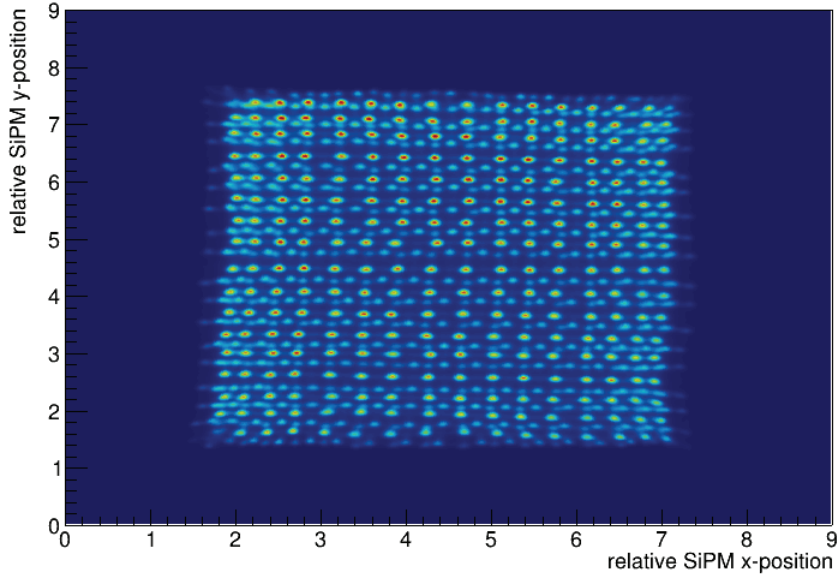


Fig. 7.6: Flood map acquired with an alternatively characterized 3-layer DOI LYSO crystal block with 1.3 mm crystal pitch read out by a HAMAMATSU S14161-3050HS-08 MPPC array operated at 2.7 V overvoltage, irradiated with a 180 kBq ^{22}Na source. The applied energy window was applied such that the photo peak of the uncorrected inclusive energy spectrum was fully included.

7.2.3. Energy resolution

The relative energy resolution ($\frac{\Delta E}{E}$) was determined using a 180 kBq ^{22}Na calibration source placed in a distance of about 5 cm centrally in front of the detector. The signal charge of any detected γ interaction within a selected crystal was filled in a histogram (energy spectrum). A calibration that takes into account non-linearities, such as SiPM saturation, was applied by using ^{152}Eu (121 keV, 244 keV and 344 keV), ^{22}Na (511 keV and 1274 keV) and ^{137}Cs sources (662 keV) to determine the photo-peak positions of their respective γ transitions and by fitting a quadratic calibration function

$$E_{\text{keV}} = A + B \cdot E_{\text{a.u.}} + C \cdot E_{\text{a.u.}}^2 \quad (7.3)$$

with E_{keV} and $E_{\text{a.u.}}$ being the measured energy in keV and arbitrary units, respectively, the parameters A, B and C being determined for each crystal separately by fitting and which was subsequently applied to the raw energy spectra. For a PET application the energy resolution of the two individual crystals that detect the two coincident 511

7. *Characterization of a Trapezoidal Pixelated Detector with Intrinsic DOI Resolution as PET and Alternative Compton Camera Absorber for Energies Below 1.5 MeV*

keV annihilation photons matters. Therefore, the energy resolution was exemplarily calculated for 24 individual crystals (12 at edge positions, 12 at a central position, see Fig. 7.5 center left panel) for all three layers. However, for the edge region of layer 3 measured with the KETEK SIPM array, only seven of the selected 12 crystals showed a spectrum that could be used to derive a spectrum. Crystal regions were defined manually and regions with less than approx. 8-12 % of the maximal amplitude were considered as background by best effort. The energy resolutions of the 1st, 2nd, and 3rd layers were 16.5 ($\pm 0.5_{stat} \pm 1.8_{var}$)%, 20.9 ($\pm 0.9_{stat} \pm 3.1_{var}$)% and 32.7 ($\pm 10.6_{stat} \pm 10.4_{var}$)%, respectively, with the KETEK array. For the DOI LYSO detector coupled to the HAMAMATSU S14161-3050HS-08 MPPC array energy resolutions of 19.3 ($\pm 1.2_{stat} \pm 2.3_{var}$)%, 21.2 ($\pm 1.6_{stat} \pm 2.5_{var}$)%, and 26.6 ($\pm 4.2_{stat} \pm 6.1_{var}$)% were measured for 1st, 2nd layers, respectively. We compared the measured energy resolution layer-wise and for the central and edge regions separately. For a confidence level of 0.05, the energy resolution of the first layer (central and edge region) was superior when measured with the KETEK SIPM array compared to the measurements performed with the HAMAMATSU MPPC array (p-value = 0.045 (central) and p-value = 0.045 (edge)). For the energy resolution of the second layer (central and edge region) with p-value = 0.994 (central) and p-value = 0.620 (edge) and the central region of the third layer (p-value = 0.072) no difference could be measured with statistical significance (p-value: 0.994). However, for the edge region of the third layer, the energy resolution measured with the HAMAMATSU MPPC array was superior compared to that measured with the KETEK SIPM array (p-value = 0.019). The error of the given values increases with deeper layers due to low statistic because of the very low probability for the low energy gamma rays (121, 244 and 344 keV from ¹⁵²Eu) to be detected in the deeper layers. Furthermore, an influence of the light loss at the edges can be observed. For the third layer, where the deterioration between the edges and the center is expected to be the strongest due to the coupling between the SiPM array and the crystal, a difference of around 6.3 % ($\frac{\Delta E}{E}$ [edge] = 29.7 ($\pm 5.9_{stat} \pm 6.6_{var}$) % and $\frac{\Delta E}{E}$ [center] = 23.6 ($\pm 5.9_{stat} \pm 3.8_{var}$)) % measured with the HAMAMATSU S14161-3050HS-08, and even 8.6 % ($\frac{\Delta E}{E}$ [edge] = 38.5 ($\pm 14.1_{stat} \pm 7.0_{var}$) % and $\frac{\Delta E}{E}$ [center] = 29.9 ($\pm 3.5_{stat} \pm 10.8_{var}$) %) could be observed for the KETEK PA3350WB-0808. The summarized energy resolution of the individual layers as well as the energy resolution of all layers calculated from the individual layers' energy resolution is listed in Tab. 7.1, while being partially illustrated in Fig. 7.7.

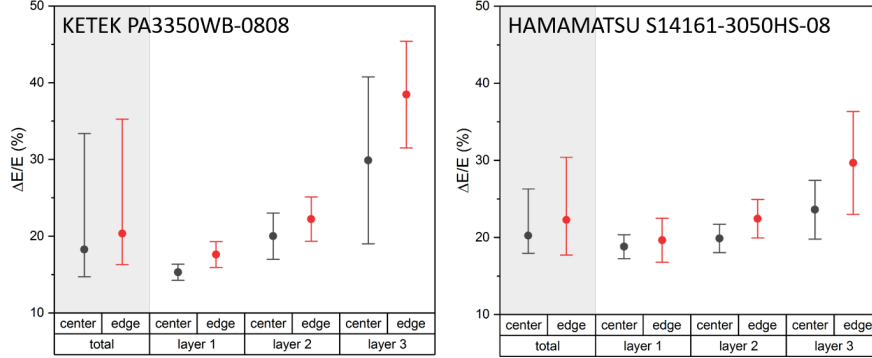


Fig. 7.7: Relative energy resolution measured at 511 keV with the KETEK PA3350WB-0808 (left) and HAMAMATSU S14161-3050HS-08 (right) shown for the three crystal layers and the total energy resolution of central and edge crystals given as the median value obtained by all evaluated individual crystals (light grey shaded column). The measured energy values are shown for crystals at the edges and the central region of the detector block. A deterioration of the relative energy resolution from the first to the third layer is observed, while no deterioration towards the edges is observed within the measurement uncertainties.

While for the first layer a superior energy resolution could be obtained with the KETEK array, the energy resolution of the third layer was observed to be superior when obtained by the HAMAMATSU MPPC array. As an explanation for the difference of the energy resolution of the first layer (where basically no influence of Inter-Crystal-Scattering (ICS) is present) for the two SiPM and MPPC arrays, respectively, can be given by i) a higher geometrical array fill factor (82 % vs. 74 %) of the KETEK PA3350WB-0808 that allows to detect a larger fraction of the scintillation light and ii) while a comparable photon detection efficiency (PDE) of both photosensor arrays of about 50 % at the peak sensitivity wavelength is reported [23, 26, 31], the KETEK SiPM array with a photon detection peak sensitivity at 430 nm matches almost exactly the peak emission wavelength of the LYSO crystal [20, 24, 26, 31], while the sensitivity of the HAMAMATSU MPPC array reaches its peak at 450 nm [20, 23], resulting in a reduced PDE at the peak emission wavelength of the LYSO crystals. For the strong deterioration of the energy resolution of third layer crystal when measured with the KETEK SiPM array, no straightforward explanation can be given. However, it seems that there is a contribution of light leakage. Due to the slightly larger area of the KETEK SiPM, it exceeds the crystal block. This causes the Teflon wrapping at the contact region between crystal and SiPM to be less efficient for the KETEK array than for the HAMAMATSU MPPC array. This might cause more scintillation photons to be lost at the edges.

At the time of the investigation of the energy resolution of the 1.2 mm crystal pitch DOI LYSO detector block, already the possibility to automatically generate inclusive corrected (linearisation and gain matching) energy spectra layer-wise was existent. For this reason the energy resolution of this detector is given as the inclusive energy resolution

7. Characterization of a Trapezoidal Pixelated Detector with Intrinsic DOI Resolution as PET and Alternative Compton Camera Absorber for Energies Below 1.5 MeV

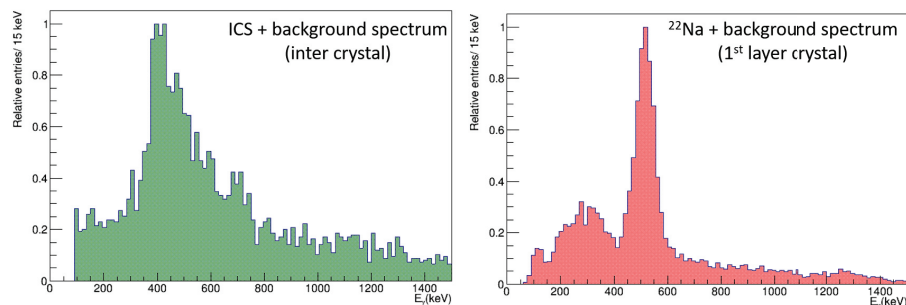


Fig. 7.8: ICS energy spectrum (from a ^{22}Na irradiation) with a non-Gaussian-shaped full absorption peak around 400 keV in a background region (however, this effect is also present as a background contribution of the spectra obtained from any other region) of the flood map (left panel) and ^{22}Na energy spectrum measured by a crystal in the first layer without ICS distortions, exhibiting a Gaussian-shaped 511 keV photopeak (right panel). The ^{176}Lu background is present in both spectra.

of individual layers (see Tab. 7.2). The measured inclusive energy resolution of the first, second and third layer at 511 keV was found to be $13.0 \pm 0.1 \%$, $13.1 \pm 0.1 \%$ and $15.6 \pm 0.1 \%$, respectively. Using this method to determine the energy resolution is not suitable to investigate the error contribution in such a detailed manner as previously presented for the 0.9 mm crystal pitch detector block. Therefore, only one value for the experimental uncertainty (dominated by the fit accuracy) can be given.

The superior energy resolution of the DOI LYSO with 1.3 mm crystal pitch compared to the one with 1.0 mm crystal pitch is due to the different method optical insulation (BaSO₄ [1.0 mm crystal pitch] vs. enhanced specular reflector (ESR) [1.3 mm crystal pitch]) between the individual crystals and explained by the superior light collection efficiency obtained using ESR [Kang 2021b].

7.2.4. Inter crystal scattering (ICS)

Intuitively, the best energy resolution is expected to be obtained from the third layer, since these crystals are coupled closely to the photosensor (i.e. with only a thin layer of optical grease inbetween) and experience the least scintillation light loss due to absorption when passing through the crystal. However, the energy resolution degrades

$\Delta E/E$ of	KETEK PA3350WB-0808	HAMAMATSU S13161-3050HS-08
first layer	$16.5 \pm 0.5_{stat} \pm 1.8_{var} \%$	$19.3 \pm 1.2_{stat} \pm 2.3_{var} \%$
second layer	$20.9 \pm 0.9_{stat} \pm 3.1_{var} \%$	$21.2 \pm 1.6_{stat} \pm 2.5_{var} \%$
third layer	$32.7 \pm 10.4_{stat} \pm 10.4_{var} \%$	$26.6 \pm 4.2_{stat} \pm 6.1_{var} \%$
all layers (averaged)	$19.1 \pm 1.7_{stat} - 3.8_{var} + 15.4_{var} \%$	$21.2 \pm 2.0_{stat} - 3.4_{var} + 8.4_{var} \%$

Tab. 7.1.: Summary of the measured relative energy resolution ($\Delta E/E$) of the three respective layers of the DOI detector block read out with the KETEK PA3350WB-0808 and the HAMAMATSU S14161-3050HS-08 SiPM arrays. The given values are the averaged values of crystals in the central and the edge regions.

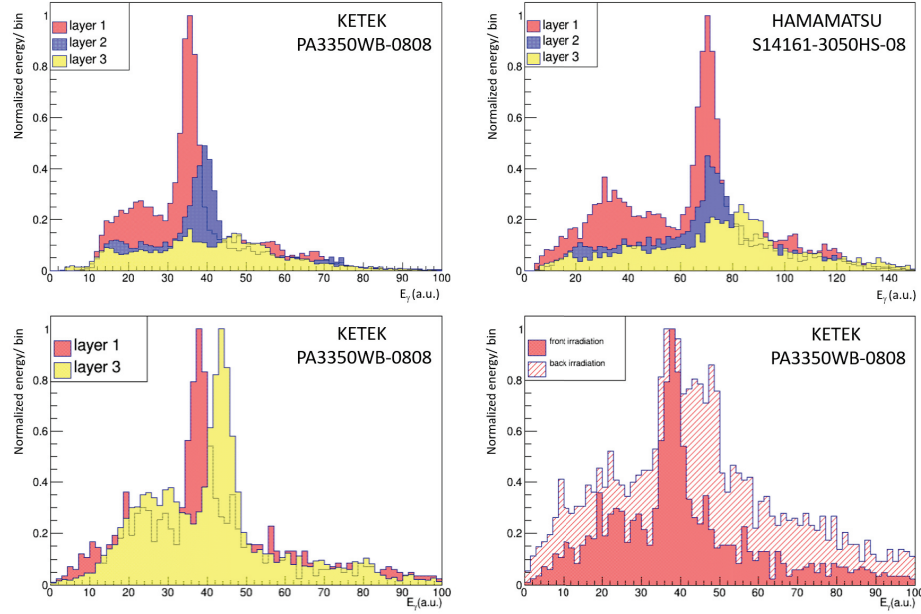


Fig. 7.9: Top row: Energy spectra of a ^{22}Na source placed in front of layer 1 and measured by a crystal in the first (red), second (blue) and third (yellow) layer of the DOI LYSO detector using the KETEK PA3350WB-0808 (left panel) and HAMAMATSU S14161-08 (right panel) SIPM arrays. Bottom row left: Energy spectra of a ^{22}Na source measured with the DOI detector read out by the KETEK PA3350WB-0808. The spectrum drawn in red was detected by one LYSO crystal in the first layer of the DOI detector when irradiated from the front side, while the yellow spectrum was registered by the crystal at the same position, but in the third layer, irradiated from the back side. Right: Energy spectra measured with one crystal in the first layer of the DOI LYSO detector and read out by the KETEK PA3350WB-0808 array from a front irradiation (solid color) and back irradiation (dashed histogram) with a ^{22}Na source.

from the first to the third layer, while also the inter-crystal variability increases. This phenomenon can be explained with Inter-Crystal-Scattering (ICS). The energy spectra of the second, and even more prominent the ones of the third layer, do not show a Gaussian shaped photopeak anymore. This phenomenon is dominant in the third layer (due to the poorest signal-to-background (S/B) ratio), therefore in the following the focus is set on the third layer. The arguments given in this section, however, are also valid for the second layer. A peak in the energy spectra of third layer crystals may have three potential origins. i) The trivial origin is a full photo absorption of an impinging γ ray resulting in the photopeak. ii) A second origin could be related to photo absorption occurring in one of the above crystal layers, while appearing as well in the energy spectrum of a 3rd layer crystal. However, this can be in practice excluded, due to the defined localization of such events (clear crystal response in the flood map) and the ability to assign photo absorption clearly to the corresponding crystal. iii) A third effect, however, results in generating a background contribution to the actual crystal energy spectra. Inter-crystal scattering (ICS) followed by full absorption of the scattered gamma in a different crystal results in a full absorption peak in the energy spectrum. Due to the

7. Characterization of a Trapezoidal Pixelated Detector with Intrinsic DOI Resolution as PET and Alternative Compton Camera Absorber for Energies Below 1.5 MeV

$\Delta E/E$ at	first layer	second layer	third layer
511 keV	$13.0 \pm 0.1 \%$	$13.1 \pm 0.1 \%$	$15.6 \pm 0.1 \%$
662 keV	$12.8 \pm 0.1 \%$	$12.4 \pm 0.1 \%$	$15.0 \pm 0.1 \%$

Tab. 7.2.: Summary of the energy resolution of the 1.2 mm crystal pitch DOI LYSO detector block at 511 keV and 662 keV. The given values are the average energy resolution in the given layer at the given energy.

light distribution measured at the photosensor, which corresponds to the response to the interactions in two crystals, the calculated interaction position cannot be assigned clearly to one specific crystal and thus forms a uniform background throughout the flood map. A region within the flood map that contains only ICS and background in the corresponding energy spectrum is exemplarily shown by the red triangle in the central right panel of Fig. 7.4. Such an energy spectrum exhibits a full absorption peak, as displayed by the ICS spectrum in Fig. 7.8 (left panel). The energy spectrum of the third layer consists of the actual gamma source spectrum plus the ICS spectrum. The photopeak and the full ICS absorption peak in these spectra are not found in the same ADC channel region, since the effectively registered amount of scintillation light originating from the full ICS absorption peak and detected by the photosensor is reduced compared to a primary photo absorption event due to absorption of the scattered photons along their trajectory through the crystals. Fig. 7.9 (top row) shows the peak positions of three neighboring crystals in the first, second and third layer of the DOI detector when read out by the KETEK PA3350WB-0808 array (left) and HAMAMATSU S14161-3050HS-08 array (right), respectively. The scintillation photon absorption can clearly be seen in the shift of the photopeak positions. Using a back-side irradiation, a clean energy spectrum with suppressed ICS can be observed in the third layer energy spectra, because in this scenario no preceding layers have to be traversed by the photon. However, a comparison of energy spectra measured in the first layer from a front-side irradiation and the third layer from back-side irradiation still shows a shift of the photopeak due to scintillation light loss by absorption of photons originating in the first layer (Fig. 7.9 (bottom row, left panel)). In order to consolidate this explanation, in a back-side irradiation the ICS full absorption peaks should be visible in the energy spectra of first layer crystals. However, in this scenario the photopeak corresponds to the leftmost peak (due to absorption) and the peak structure on the right if this peak corresponds to the full absorption of inter-crystal scattered photons. Fig. 7.9 (bottom row, right panel) shows a ^{22}Na energy spectrum detected in a first-layer crystal obtained from a front-side irradiation (solid red) superimposed to a ^{22}Na energy spectrum of the same crystal, but from a back-side irradiation including the ICS peaks (red dashed histogram).

7.2.5. Analysis of the time difference spectra

Due to the individual SiPM readout and signal processing provided by the PETsys ASIC, an arrival timestamp is assigned to each of the N firing SiPM channels, which is triggered

by an initial γ ray hit in one of the DOI LYSO detector crystals. In general, any of the N provided arrival timestamps belonging to a photon interaction can be used to determine the Coincidence Resolving Time (CRT). A reasonable choice which timestamp to use is either using the timestamp of the first registered firing SiPM channel or the timestamp of the brightest firing channel, respectively. Using the timestamp of the first firing channel is an obvious choice. However, using the timestamp of the brightest firing SiPM may also be beneficial, due to the steeper slope of the rising edge of the scintillator pulse for high amplitude signals and thus a smaller time walk for signals with non-identical amplitudes. Both methods have been investigated. The arrival time difference was calculated with respect to any channel of an 8×8 (64 channels) LYSO crystal array coupled to a PA3325WB-0808 SiPM array (one-by-one coupling) as described in Sec. 7.1 and illustrated in Fig. 7.2.

Fig. 7.10 (top row) shows the arrival time difference spectra measured with the KETEK PA3350WB-0808 (left) and HAMAMATSU S14161-3050HS-08 (right) with the timestamp of the first detected channel of the DOI LYSO detector used for the calculation. Displayed are inclusive spectra, which contain all arrival time differences from the different combinations between DOI LYSO detector channels and the channels of the reference detector. Three observations can be made: i) a central peak corresponding to the actual arriving time difference distribution and two satellite peaks at about ± 5000 ps are visible. ii) The satellite peak at the positive side of the time axis has a tail reaching at least down to the central peak. iii) The central peak is asymmetric, i.e. non-Gaussian shaped. The deviation from a Gaussian distribution is caused by small deviations between the signal transit times and data processing times of the contributing individual crystals. As a result, the centroids of the arrival time difference distributions of the individual channels are shifted with respect to each other and cause a non-Gaussian distribution in the inclusive spectrum. In Fig. 7.10 (bottom row) the inclusive arrival time difference spectra for the KETEK PA3350WB-0808 (left) and the HAMAMATSU S14161-3050HS-08 (right) are plotted with the timestamp of the DOI LYSO detector taken from the brightest firing channel. While the satellite peaks and the non-Gaussian shape of the central peak can still be observed, the tail of the satellite peak at the positive time axis disappears. The same difference between the respective arrival time difference spectra for the two timestamping methods can also be observed for individual channel pairs, i.e. one specific channel of the DOI LYSO detector versus a specific channel of the reference detector. The presence of the satellite peaks in the time-difference spectra was initially evaluated by D. Schug et al. [Schug 2019] using the TOFPET2 ASIC and a one-to-one coupling between a KETEK PM3325WB and a LYSO crystal. They could show that in particular for low values of the first timing threshold (V_{th_T1}), a dark count could trigger the corresponding discriminator. In cases where the trigger logic is configured such that a delay is applied to the logic signal do_T1 , the dark count would be responsible for the generation of a timestamp, even though it would not exceed the other two thresholds V_{th_T2} and V_{th_E} . If this ASIC channel subsequently detects a real

7. Characterization of a Trapezoidal Pixelated Detector with Intrinsic DOI Resolution as PET and Alternative Compton Camera Absorber for Energies Below 1.5 MeV

Timestamps provided by:	Coincidence Resolving Time (CRT)	Coincidence Resolving Time (CRT)
	KETEK PA3350WB-0808	HAMAMATSU S14161 3050HS-08
First firing SiPM	$678 \pm 13_{stat} \pm 124_{var}$ ps	$613 \pm 12_{stat} \pm 148_{var}$ ps
Brightest firing SiPM	$847 \pm 16_{stat} \pm 211_{var}$ ps	$637 \pm 10_{stat} \pm 97_{var}$ ps

Tab. 7.3.: Summary of the CRT values measured throughout this paper for the DOI LYSO detector read out by the two investigated SiPM arrays. The CRT was calculated by using the timestamp of the first firing DOI detector channel (first row) and by using the brightest channel (bottom row).

γ hit that triggers V_{th_T2} and V_{th_E} within the delay time of do_T1 , the time stamp of the previously dark count would be assigned to this γ hit. These events would cause the assigned time stamp to be wrong by $\Delta t = t_{delay_T1} - (t_{T2} - t_{T1})$, with the constant term t_{delay_T1} [35], resulting in satellite peaks at roughly ± 5.5 ns around the central peak for $t_{delay_T1} = 5.8$ ns (which is the default setting and was also used for the studies presented in this manuscript). However, both satellite peaks studied in [Schug 2019], had the same amplitude, whereas in the time-difference spectra presented in this study the satellite peak on the negative time axis exhibits only about roughly one tenth of the amplitude of the satellite peak on the positive time axis. This is a consequence of the light-sharing readout of the DOI LYSO crystal block. While for a one-to-one coupling configuration (as used for the reference detector) the dark count has to be detected in the same ASIC channel that also detects the subsequent γ hit, in the light-sharing approach the light emitted in one crystal triggers on average 10 – 11 ASIC channels. As a consequence, only in one of these ASIC channels a SiPM dark count needs to be detected in order to cause the satellite peak, resulting in about 10 times more events in the satellite peak corresponding to the assignment of a wrong timestamp in the DOI detector.

Furthermore, this observation also explains why the time-difference spectra obtained by the brightest firing channel show less entries in the satellite peaks compared to the one obtained by the first firing channel. While naturally for the first firing channel all of these wrongly assigned timestamps are included in the time-difference spectra, in the case of the brightest firing channel only channels which are the first and brightest firing channel can cause such a wrong timestamp to be used.

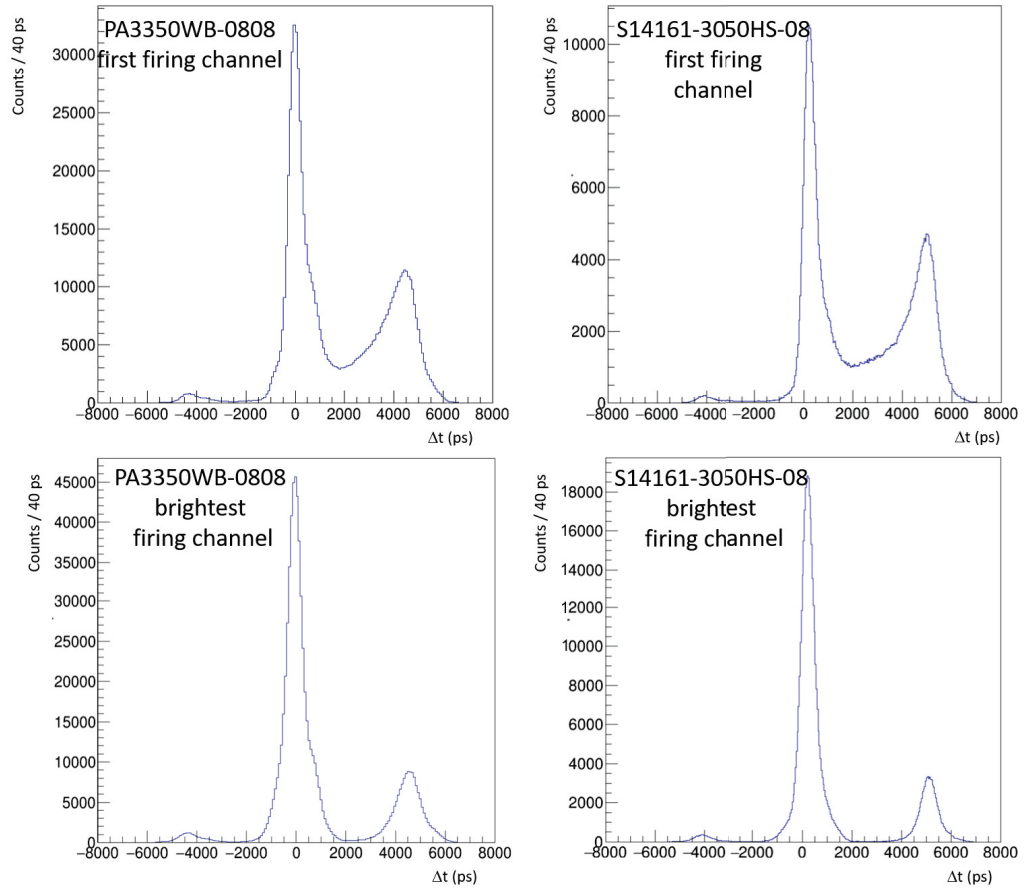


Fig. 7.10: Top row: Measured arrival time difference spectra of the DOI LYSO detector read out by the KETEK PA3350WB-0808 array (left) and the HAMAMATSU S14161-3050HS-08 MPPC array (right). The CRT was determined with respect to the first firing channel of the DOI detector. Bottom row: Measured arrival time difference spectra of the DOI LYSO detector read out by the KETEK PA3350WB-0808 array (left) and the HAMAMATSU S14161-3050HS-08 MPPC array (right). The CRT was determined with respect to the brightest firing channel of the DOI detector.

7.2.6. Coincidence resolving time

The coincidence resolving time (CRT) of the DOI detector depends on the detection time of individual gamma hits in the detector and therefore on the timestamps assigned to these hits. As already described in the previous section, the applied signal processing electronics operates all input channels individually, i.e. in case of an operation mode involving light sharing, one timestamp per electronic channel is provided. The first ASIC-generated timestamp was taken for the CRT calculation, but also a comparison to the obtained CRT using the timestamp of the brightest channel will be given. In order to determine the CRT of the DOI LYSO detector the procedure was as follows:

7. *Characterization of a Trapezoidal Pixelated Detector with Intrinsic DOI Resolution as PET and Alternative Compton Camera Absorber for Energies Below 1.5 MeV*

The CRT of two identical reference detector arrays ($3 \times 3 \times 5$ mm³ LYSO crystals one-by-one coupled to the (KETEK PA3325WB-0808 SiPM array, see Fig. 7.2, was measured and the time resolution (ΔT_{ref}) was calculated (under the assumption that the time resolution of the identical reference detectors (ΔT_{ref}) is also identical) according to

$$\Delta T_{ref} = \sqrt{\frac{CRT_{ref}^2}{2}} \quad (7.4)$$

similar to the procedure described in Sec. 6.2.2 and Eq. (6.4).

One reference detector was replaced by the DOI detector and the CRT between the remaining reference detector and the DOI detector was measured. The CRT of the DOI detector can subsequently be calculated according to

$$CRT_{DOI} = \sqrt{(CRT_{DOI-ref}^2 - \Delta T_{ref}^2) \times 2} \quad (7.5)$$

which is again the identical procedure as described in Sec. 6.2.2 and Eq. 6.5.

Since any of the 64 SiPM/MPPC channels can be the first one detecting photons, consequently providing the trigger timestamp, non-uniformities in the matching of the timestamps between different ASIC and/or photosensor channels lead to a deterioration of the CRT, due to a time jitter of the mean value of the Gaussian arrival-time-difference distributions of individual channels, resulting in a broadening of the overall Gaussian. The CRT measured with the KETEK PA3350WB-0808 array was determined as 678 ($\pm 13_{stat} \pm 124_{var}$) ps, while for the HAMAMATSU S14161-3050HS-08 array the measured CRT amounts to 613 ($\pm 12_{stat} \pm 148_{var}$) ps (Fig. 7.11). No significant deterioration of the CRT could be observed when comparing the CRT measured at central channels with channels being closer to the edges for the HAMAMATSU MPPC array, while for the KETEK SiPM array a deterioration at the edge channels can be observed.

Instead of using the timestamp provided by the first firing SiPM of the DOI LYSO detector, the timestamp of the brightest channel was also used to determine the CRT of the detector. A comparison of the obtained results of the two methods is given in Tab. 7.3. No statistically significant difference of the CRT can be seen between these two methods when the DOI crystal block is readout by the HAMAMATSU array (p-value = 0.299 at a significance level of 0.05). For the readout with the KETEK SiPM array, the two methods show a different result (p-value < 0.00002), with the method of using the first firing channel being the superior method. However, for the HAMAMATSU MPPC array the statistical uncertainty decreases by about 50 % when using the brightest channel as timestamp instead of the first channel. Also, the inter-crystal variability in

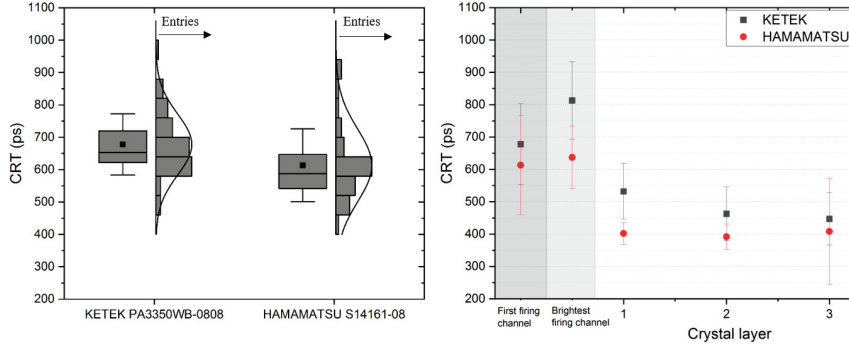


Fig. 7.11: Left: Measured CRT of the DOI LYSO detector with KETEK PA3350WB-0808 and HAMAMATSU S14161-3050HS-08 SiPM readout, respectively. The box charts belonging to the CRT distributions of the (up to) 64 channels indicate the interquartile range (25th percentile to 75th percentile) by the box size, the mean value (black square), the median (horizontal line), and the 1σ standard deviation (whisker) of the mean value. Right: Comparison of the CRT between KETEK and HAMAMATSU SiPM arrays. The values given for comparison are the combined CRT for all layers with the timestamps provided by the first firing channel (dark shaded grey)(as given in the left panel) and the brightest firing channel (light shaded grey shaded) and for the three individual DOI layers. The error bars correspond to 1σ standard deviation in the measured CRT values for all investigated crystals in the respective layer.

this case decreases by approx. 25%. In addition to the CRT with respect to the individual readout channels of the full detector block, the CRT was also determined for individual crystals of the three respective detector layers. In this case it was additionally required that for a specific crystal the first firing channel (providing the triggering timestamp) had also to be the brightest one within this photon event. This condition is fulfilled for 57.7 % (KETEK) and 49.6 % (HAMAMATSU) of all events. This requirement was applied to eliminate the connecting tail in the time difference distribution when using the first firing channel as timestamp (see Fig. 7.10). This tail may otherwise introduce a significant error to the Gaussian fit in cases where the statistics is low, which is especially the case when evaluating the CRT of crystals in the 3rd layer. Using this method, the overall CRT measured with the KETEK PA3350WB-0808 array was found to be $490 (\pm 44_{stat} \pm 82_{var})$ ps. However, when disentangled into the CRT values for the individual crystal layers, on average the CRT slightly improves from the first over the second to the third layer for the KETEK SiPM array. For the HAMAMATSU MPPC array no influence of the layer position on the CRT can be observed within the measurement uncertainties. However, the statistical uncertainty decreases with larger distance to the SiPM array, due to a higher detection probability in the first and second layers compared to the third layer. The CRT of crystals belonging to the three layers is $CRT_{1stlayer} = 532 (\pm 30_{stat} \pm 81_{var})$ ps, $CRT_{2ndlayer} = 463 (\pm 31_{stat} \pm 77_{var})$ ps and $CRT_{3rdlayer} = 447 (\pm 42_{stat} \pm 69_{var})$ ps, respectively. The measured CRT with the HAMAMATSU S14161-3050HS-08 is $CRT_{1stlayer} = 402 (\pm 18_{stat} \pm 28_{var})$ ps, $CRT_{2ndlayer} = 392 (\pm 22_{stat} \pm 32_{var})$ ps and $CRT_{3rdlayer} = 408 (\pm 36_{stat} \pm 160_{var})$ ps. These found results

7. Characterization of a Trapezoidal Pixelated Detector with Intrinsic DOI Resolution as PET and Alternative Compton Camera Absorber for Energies Below 1.5 MeV

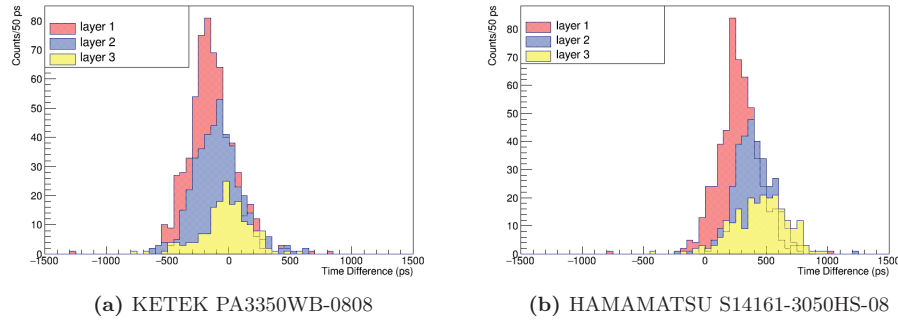


Fig. 7.12: Time difference spectra of neighboring single crystals from the first layer (red), second layer (blue) and third layer (yellow) of the DOI LYSO detector measured with the KETEK PA3350WB-0808 (left) and HAMAMATSU S14161-3050HS-08 (right) arrays. The shift of the mean value of the respective distributions is clearly visible. Furthermore, it is evident that the interaction probability for 511 keV γ rays is the highest in the first layer and decreases with further layers.

Timestamps provided by:	Coincidence Resolving Time (CRT)	Coincidence Resolving Time (CRT)
	KETEK PA3350WB-0808	HAMAMATSU S14161 3050HS-08
First layer	$532 \pm 30_{stat} \pm 81_{var}$ ps	$402 \pm 18_{stat} \pm 28_{var}$ ps
second layer	$463 \pm 31_{stat} \pm 77_{var}$ ps	$392 \pm 22_{stat} \pm 32_{var}$ ps
third layer	$447 \pm 42_{stat} \pm 69_{var}$ ps	$408 \pm 36_{stat} \pm 160_{var}$ ps
Total (by individual channels)	$489 \pm 34_{stat} \pm 82_{var}$ ps	$400 \pm 25_{stat} \pm 183_{var}$ ps

Tab. 7.4.: Summary of the CRT measured for the DOI LYSO detector read out by two alternative SiPM photosensor arrays. The CRT is shown individually for each of the three DOI layers as well as for the full detector block.

are summarized and compared to the values of the overall detector block without layer separation in Fig. 7.11 and listed in Tab. 7.4. For all three types of CRT determination (via first firing channel, brightest firing channel and individual layers), the CRT values determined for the two photosensors are in good agreement with each other within the 1σ uncertainties for the total CRT calculated by using the first firing channel, and for the CRT of the second and third layer crystals, respectively. Furthermore, the evaluation of the time difference spectra of individual crystals shows a shift of the mean value of the individual layers between 50 ps and 70 ps (varies for the LYSO detector from crystal to crystal) as shown in Fig. 7.12. For a refractive index of $n = 1.82$ (at the emission wavelength of 420 nm) [Epic-Crystal 2021a] this corresponds to a crystal thickness of 10 ± 2 mm, which is in reasonable agreement with the actual crystal thickness of 6.6 mm, taking into account that the scintillation light path is not straight from the interaction point to the photosensor, but is prolonged by various reflections.

7.3. Discussion and conclusion

The presented studies give a performance evaluation of a SiPM/MPPC array readout for a three-layer high resolution PET scintillation crystal block. For the studies presented in this work SiPM/MPPC arrays from two manufacturers (KETEK and HAMAMATSU) have been investigated and compared. For both photosensors a flood map with clearly resolved and distinguishable individual crystals could be acquired, also proving a spatial resolution of 1 mm in the x-y plane given by the crystal pitch and a DOI resolution of 6.6 mm (corresponding to the crystal layer thickness) of the DOI detector.

The overall relative energy resolution measured with the KETEK PA3350WB-0808 at 511 keV was 19.1 % and 21.2 % with the HAMAMATSU S14161-3050HS-08. By determining the relative energy resolution of individual crystals, the average energy resolution of the three layers of $16.5 (\pm 0.5_{stat} \pm 1.8_{var})$ %, $20.9 (\pm 0.9_{stat} \pm 3.1_{var})$ % and $32.7 (\pm 10.6_{stat} \pm 10.4_{var})$ % (KETEK) and $19.3 (\pm 1.2_{stat} \pm 2.3_{var})$ %, $21.2 (\pm 1.6_{stat} \pm 2.5_{var})$ % and $26.6 (\pm 4.2_{stat} \pm 6.1_{var})$ % (HAMAMATSU) for the first, second and third layer, respectively, could be achieved. While for the first and second layer the relative energy resolution is independent of the crystal position (i.e. edge or central crystals), in the third layer a strong deterioration towards the edges can be observed due to light losses at the contact region between SiPM and crystal.

With larger crystals (1.2 mm crystal pitch, same height) a superior energy resolution of the first, second and third layer of 13.0 ± 0.1 %, 13.1 ± 0.1 % and 15.6 ± 0.1 % could be achieved from an inclusive spectrum. However, it should be noticed that besides the crystal pitch and the coupling method (optical grease vs. rubber sheet), also the type of optical insulation between the individual crystals was different (BaSO₄ vs. enhanced specular reflector (ESR)), which is the reason for the difference in the achievable energy resolution.

The CRT was measured for each readout channel (SiPM/MPPC + ASIC) independently and stays below 1.1 ns for all measured 64 individual readout channels. By averaging over all responding signal channels a mean value of $678 (\pm 13_{stat} \pm 124_{var})$ ps (KETEK PA3350WB-0808) and $613 (\pm 12_{stat} \pm 148_{var})$ ps (HAMAMATSU S14161-3050HS-08), respectively, was found. For an evaluation of the CRT of individual crystals the values could be further improved to $532 (\pm 30_{stat} \pm 81_{var})$ ps, $463 (\pm 31_{stat} \pm 77_{var})$ ps and $447 (\pm 42_{stat} \pm 69_{var})$ ps for the 1st, 2nd and 3rd layer, respectively, measured with the KETEK SiPM array and $402 (\pm 18_{stat} \pm 28_{var})$ ps, $392 (\pm 22_{stat} \pm 32_{var})$ ps and $408 (\pm 36_{stat} \pm 160_{var})$ ps when read out by the HAMAMATSU MPPC array. All measurements and evaluations performed within the scope of this work were performed with SiPMs biased at the overvoltage recommended by the manufacturer. A performance evaluation of the DOI LYSO detector with respect to the applied SiPM overvoltage has not been done and is not in the scope of this paper. However, it could very well affect the relative comparison between the two different SiPM array types under study.

Throughout the studies presented in this chapter it was shown that the DOI LYSO

7. Characterization of a Trapezoidal Pixelated Detector with Intrinsic DOI Resolution as PET and Alternative Compton Camera Absorber for Energies Below 1.5 MeV

detector modules consisting of a staggered 3-layer LYSO detector block with 1 mm and 1.3 mm crystal pitch, SiPM readout and highly integrated ASIS-based signal processing fulfills all requirements demanded by modern high-resolution PET scanners, but also by Compton camera absorbers. Consequently, it can be concluded that the DOI LYSO detector is a very suitable alternative to the monolithic absorber crystals, especially with regard to the application of the Compton camera in a γ -PET imaging modality, where the absorber can also be used as a PET detector module. The tested SiPM arrays from KETEK and HAMAMATSU, respectively, generally show a comparable performance for the detector module. However, while the energy resolution measured with the KETEK SiPM array is slightly superior for the first layer to the one measured with the HAMAMATSU MPPC array, the latter shows a superior energy resolution for the third layer. Also, the CRT that was obtained with the HAMAMATSU MPPC array was superior to the one obtained with the KETEK SiPM array. Thus, there is not a superior and a minor choice in terms of the SiPM and both variants may very well be used to read out the crystal blocks. The PETsys TOFPET v2c ASIC and its accompanying front-end electronics boards provide a suitable signal processing and data acquisition for the SiPM arrays of both manufacturers.

The three-layered LYSO crystal arrays have been proven to fulfill the requirements for a Compton camera absorber component in terms of spatial, energy and time resolution. Especially for γ -ray energies of several hundred of keV it is a promising absorber candidate.

Compton Camera Commissioning and Characterization

Contents

8.1. Offline characterizations	153
8.1.1. A scintillator-based Compton camera with DOI capable LYSO absorber for γ -PET imaging (Prototype #1)	153
8.1.2. A LaBr ₃ :Ce/CeBr ₃ - and GAGG based Compton Camera for Prompt- γ Imaging (Prototype #2)	166
8.2. Online Camera Characterizations	171
8.2.1. Measurement campaign at GSI in February 2021	172
8.2.2. Measurement campaign at GSI in June 2021	176
8.3. LaBr₃:Ce- and GAGG based Compton Camera for Prompt-γ Imaging based on the latest KETEK low-noise SiPM series (Prototype #3)	185

The previous two chapters dealt with detailed evaluations of individual Compton camera components. As scatterer component the investigated GAGG crystal arrays provide a good energy resolution (1.6 mm) and a satisfying energy resolution of less than 10 % at an energy of 662 keV (if coupled to KETEK PA3325WB-0808/PA3335WL-0808 or HAMAMATSU S14141-3050HS-08 SiPM arrays).

For the absorber, both investigated concepts provided good results. The monolithic crystal blocks showed an excellent energy resolution with great spatial homogeneity over an energy range of more than 6 MeV (100 keV - 6130 keV). Furthermore, excellent time and spatial resolutions could be demonstrated.

The three-layered DOI LYSO crystal block cannot provide an energy resolution in the quality of LaBr₃:Ce and CeBr₃ crystals, but may benefit from its depth-of-interaction capability to reduce parallax errors. Also the achieved spatial resolution of 1 mm and 1.3 mm (depending on the crystal size) promises a good suitability for Compton imaging.

In this final chapter the benchmark tests of three different Compton camera prototypes, commissioned with these components, are presented. All prototype concepts used

a GAGG scatterer component and differ in the used absorber component or the attached photosensor. Both, a Compton camera built with a monolithic detector block and one with a three-layered DOI crystal block were assembled and evaluated. Starting with offline measurements using calibration point sources, camera properties such as the angular resolution measure (ARM), the spatial resolution and the reconstruction accuracy were investigated. For a detector assembly comprising a three-layered DOI absorber detector, also a γ -PET prototype was set up and tested. The final step was to commission a prototype consisting of four Compton camera arms and to run online measurements using carbon and oxygen ion beams (both stable and radioactive ion beams) at the GSI Helmholtz Centre for Heavy Ion Research in Darmstadt.

8.1. Offline characterizations

This first part is dedicated to offline characterizations of the developed Compton camera prototypes. The first prototype presented here comprises the GAGG crystal array coupled to a KETEK PA3325WB-0808 array as scatterer and a three-layered DOI LYSO crystal (1.3 mm crystal pitch). Both Compton camera components were read out using the PETsys TOFPET v2c ASIC. This Compton camera was also implemented in an extended setup together with two other GAGG crystal arrays that served as PET detectors, in order to allow for detecting triple-coincidences in a γ -PET prototype. A second prototype was built by substituting the segmented absorber component by a monolithic LaBr₃:Ce crystal block.

8.1.1. A scintillator-based Compton camera with DOI capable LYSO absorber for γ -PET imaging (Prototype #1)

The first Compton camera prototype presented was built from the pixelated GAGG scatterer detector (and PA3325WB-0808 photosensor) and the three-layered-stacked DOI LYSO crystal (1.3 mm crystal pitch, enhanced specular reflector (ESR) optical insulation) (and S14161-3050HS-08 SiPM array) as absorber component (Fig. 8.1). The distance between the scatterer and the absorber (front-to-front) was set to 43 mm equivalent to 55 mm from the scatterer's front surface and 98 mm from the absorber's front surface, respectively, to the setup's geometrical center (origin). Under an angle of 90° to the Compton camera two detectors serving as PET arrangement were placed. These PET detectors were identical to the modules used as Compton camera scatterers. The front-to-front distance of both detectors was 100 mm. A CAD schematic and a picture of the actual setup are shown in Fig. 8.1.

8.1.1.1. Component tests

Firstly, in order to prepare for measurements in the γ -PET mode, the individual detector performances were evaluated (Compton camera absorber and scatterer/ two PET detectors). By looking at the flood maps, the alignment of the GAGG scintillator arrays on the SiPM arrays was confirmed (Fig. 8.2).

Secondly, the energy resolution of the four detectors in this specific assembly was measured at a γ -ray energy of 662 keV (from a ¹³⁷Cs point source). The obtained relative energy resolution of the scatterer was $\Delta E/E = 10.4 \pm 0.2 \%$, while for the absorber $\Delta E/E = 12.8 \pm 0.1 \%$ ($12.4 \pm 0.1 \%$) [$15.0 \pm 0.1 \%$] were determined for the first (second) [third] layer. For the two PET detector assemblies an energy resolution of $10.0 \pm 0.1 \%$ (PET1) and $10.7 \pm 0.1 \%$ (PET2) was obtained. The corresponding ¹³⁷Cs energy spectra obtained using the three GAGG detector assemblies are shown in Fig. 8.3.

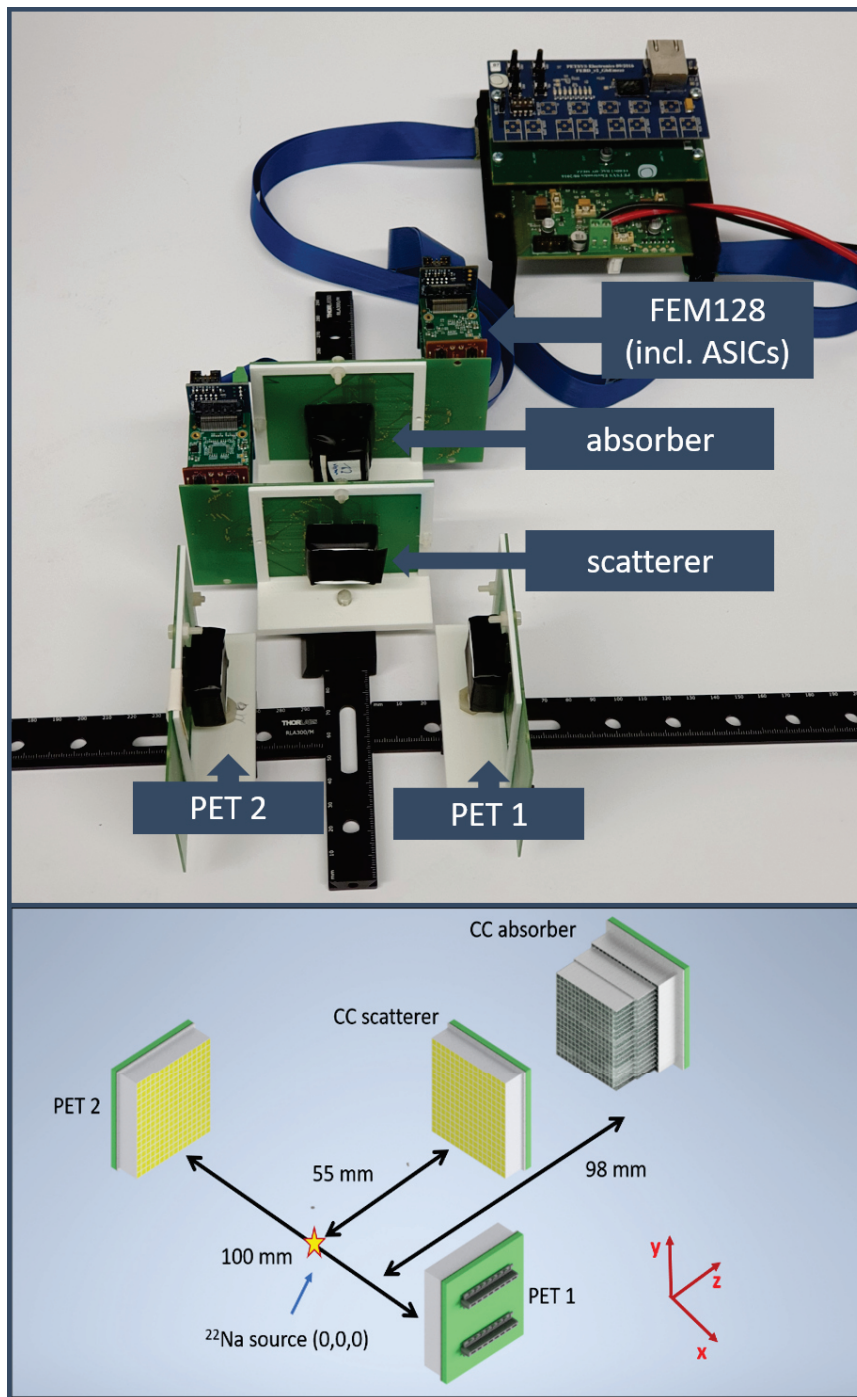


Fig. 8.1: Picture of the γ -PET prototype setup (top). For the sake of clarity, the electronic readout of the PET arrangement was not connected. CAD schematics of the Compton camera prototype and PET detectors used for offline camera characterization (bottom).

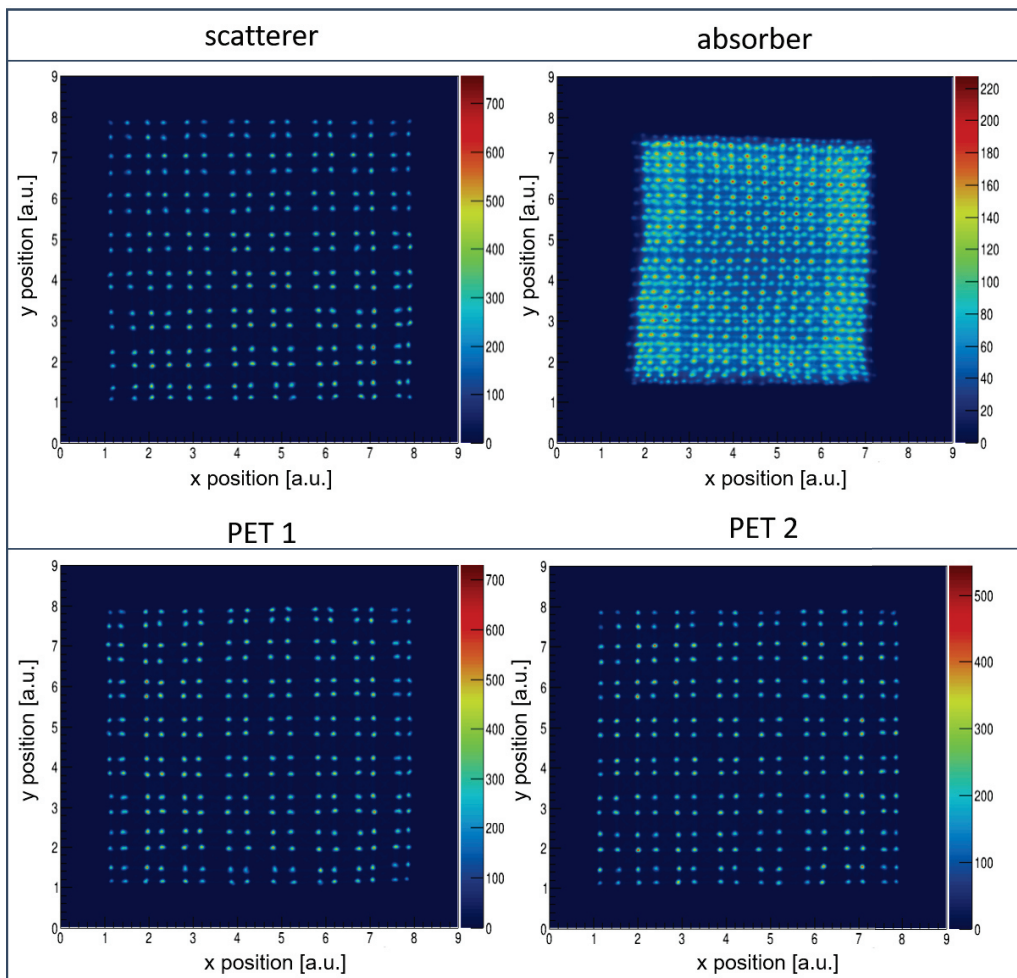


Fig. 8.2: Flood maps obtained from the four detectors of the γ -PET prototype by a ^{137}Cs irradiation.

8.1.1.2. Compton-only imaging mode

For an initial characterization of the Compton camera (Compton-only mode) measurements were conducted using a ^{22}Na point source (158 kBq activity¹) at three source-to-scatterer (z -dimension) distances ($z = 11$ mm, $z = 50$ mm and $z = 55$ mm)². Furthermore, for the distances $z = 11$ mm and $z = 50$ mm the radiation source was diagonally shifted to the positions ($x/y = 5$ mm and $x/y = 10$ mm) to acquire off-center images.

The data acquisition times were 1 hour for all measurements at $z = 11$ mm and the central source position at $z = 50$ mm, and 1.5 hours for both off-center source positions

¹at the time of the measurements

²11 mm was the closest distance possible without directly attaching the source to the scatterer. It was basically determined by the holder frames used to mount the detectors and the radiation source. 55 mm distance was used for a second measurement period

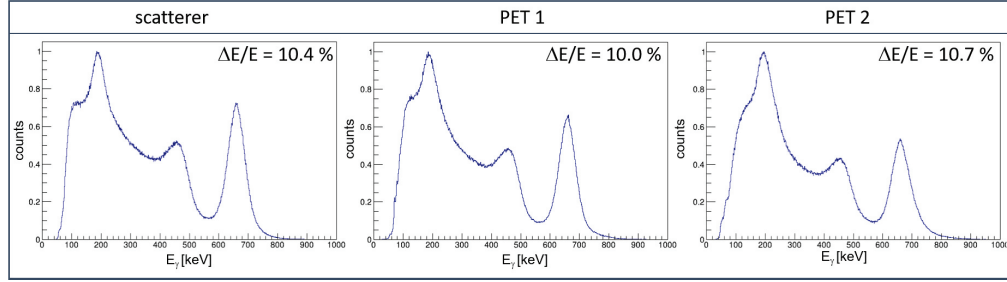


Fig. 8.3: Energy spectra of a ^{137}Cs point source measurement using the Compton camera (GAGG) scatterer (left), and the two PET detectors (center and right).

at $z = 50$ mm.

The image reconstruction was based on the Maximum-Likelihood Expectation Maximization (ML-EM) method and based on the Medium-Energy Gamma-ray Astronomy library (MEGALib) [Zoglauer 2005, Zoglauer 2008, Zoglauer 2021] and the presented values. Images of the point source measurements were obtained after 10 iterations.

Event selection Images were reconstructed for both available photopeak energies of the ^{22}Na source (511 keV and 1274 keV).

Incident γ rays that undergo Compton scattering in the scatterer and are subsequently fully absorbed in the absorber component can be visualized in a 2D energy correlation plot. These events must lie on a diagonal line that intersects both, the x- (energy deposit in the absorber) and the y-axis (energy deposit in the scatterer). Such an energy correlation plot is displayed in Fig. 8.4.

The top plot shows the energy deposition of events detected in coincidence (3 ns coincidence window) between scatterer and absorber in linear scale. The bottom shows a logarithmic scale and indicates the applied energy cuts for event selection by the yellow parallelograms. The prominent horizontal and vertical distributions intersecting the respective axes at 511

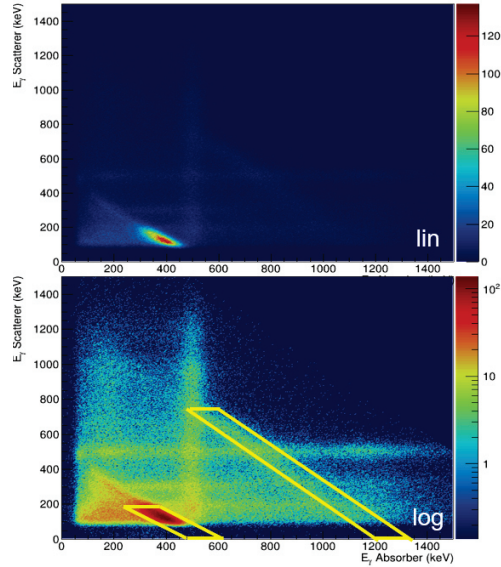


Fig. 8.4: Energy deposition in the scatterer and the absorber component of the first Compton camera prototype plotted in a linear (top) and logarithmic scale (bottom). The yellow rectangles indicate the regions-of-interest (ROIs) that have been chosen for event selection.

E_γ	$\Delta E/E$	1σ SD
511 keV	$13.6 \pm 0.2 \%$	35 keV
1274 keV	$9.7 \pm 0.2 \%$	62 keV

Tab. 8.1.: Energy resolution of the Compton camera prototype consisting of a GAGG scatterer (with PA3325WB-0808 photosensor) and a three-layered staggered LYSO detector block (with S14161-3050HS-08 readout). The energy resolution was determined from the coincident energy spectrum between both camera components. Also the 1σ standard deviation (SD) is shown as the value used for the energy cut for the event selection.

keV, correspond to "fake coincidences" of fully absorbed annihilation photons in one detector (horizontal distribution: in the scatterer; vertical distribution: in the absorber) with a background or noise³ event in the other camera component.

Two selection criteria were applied to the data in order to discriminate between signal and background:

- An energy gate: the width of the event selection energy gate was set to be the 1σ ($\pm 0.5\sigma$) of the coincidence energy resolution around the photopeak energy;
- An upper energy constraint to the maximum energy deposit in the scatterer, which was determined from a geometrical consideration. The energy deposit in the scatterer was limited by the covered solid angle of the absorber component.

The coincidence energy resolution of the Compton camera was determined from a one-dimensional histogram that contains all coincidence events (as contained in the coincidence energy spectrum). The measured energy resolution of the Compton camera prototype is 13.6 % (at 511 keV) and 9.7 % (at 1274 keV). This results in an energy gate width of $511 \text{ keV} \pm 35 \text{ keV}$ and $1274 \text{ keV} \pm 62 \text{ keV}$ for the two energies of 511 keV and 1274 keV, respectively (see Tab. 8.1).

Image reconstruction *The calculation of the ARM value and the image reconstruction was performed by V. Anagnostatou and M. Safari. The data to be reconstructed (after energy selection) were provided by the author in a list-mode format.*

The data (after energy selection) are subsequently written to an ASCII file (list-mode data) that is used as input for the 2D image reconstruction algorithm⁴. For the angular resolution measure (ARM) values of 14.9° , 14.0° and 14.2° were measured for 511 keV γ rays and the source placed at a distance of 11 mm to the scatterer for a central, $|x| = |y| = 5 \text{ mm}$ and $|x| = |y| = 10 \text{ mm}$ irradiation, respectively. By increasing the source-to-scatterer distance to 50 mm an ARM value of 11.0° at a central source position was

³E.g. dark count, cosmic γ ray, camera pile-up, etc.

⁴The spatial resolution for all three dimensions is obtained from 2D image reconstructions.

determined. For reconstructions using the 1274 keV γ rays of ^{22}Na ARM values of 15.7° ($z = 11$ mm) and 8.2° ($z = 50$ mm) were found for central source positions. In Fig. 8.5 the ARM distribution for a central source position and the closer source-to-scatterer distance is shown for 511 keV (left) and for 1274 keV at a source-to-scatterer distance of 50 mm (right). The blue line represents the Gaussian fit to the distribution used to obtain the ARM value as the FWHM of the fit curve. The ARM values for all performed measurements are summarized in Tab. 8.2.

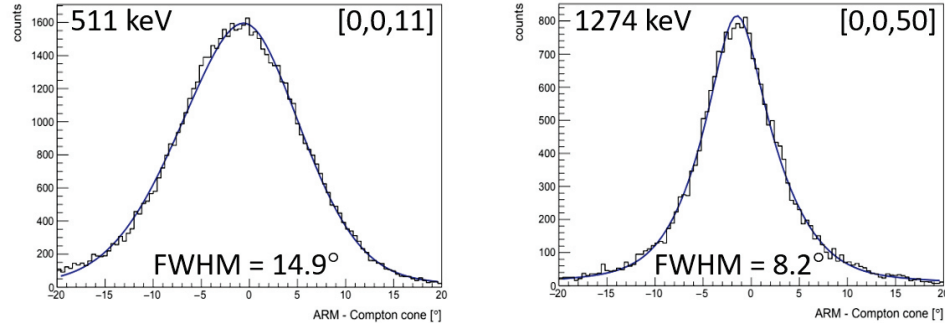


Fig. 8.5: Angular resolution measure (ARM) determined from an image reconstruction of a ^{22}Na point source at $x = y = 0$ mm and $z = 11$ mm at 511 keV and at $x = y = 0$ mm and $z = 50$ mm at 1274 keV, respectively.

The spatial resolution (SR) (given as the FWHM) at 511 keV was determined for the x , y and z coordinates from a fit to the projection along the respective axis (obtained from a 2D point spread reconstruction). At 11 mm source distance to the Compton camera prototype a spatial resolution (SR) of 3.7 mm (x) and 3.6 mm (y) was determined (using 69 058 events). Along the z -dimension the SR was found to be 4.1 mm. When the radiation source was shifted diagonally towards the edges of the camera's field-of-view (FoV), the spatial resolution deteriorated to 7.8 mm and 8.5 mm at $|x| = |y| = 10$ mm. These values, however, are hardly to compare with values obtained from central irradiation. Due to the fact that no sensitivity correction was applied during the image reconstruction, off-center source images show a tail that points towards the FoVs center⁵ (Fig. 8.6).

⁵This is consequence of the camera's sensitivity to be the highest in the center of the FoV.

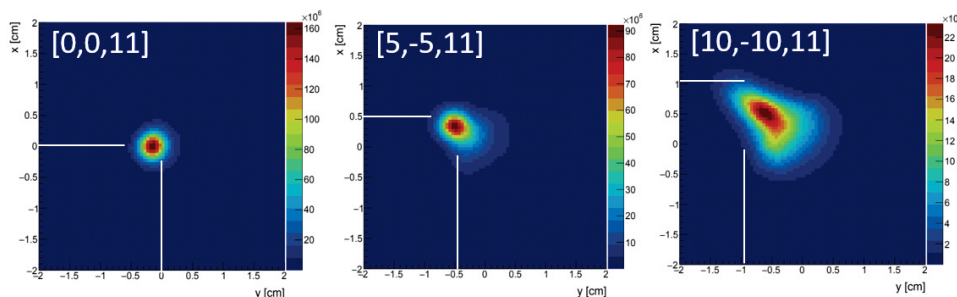


Fig. 8.6: Reconstructed images (at 511 keV) of a ^{22}Na point source (158 kBq) at a distance to the scatterer's front surface of 11 mm. The source was moved diagonally by 5 mm and 10 mm along both dimensions (x and y), respectively.

Consequently, concepts from optics that define the spatial resolution as the FWHM of a Gaussian-shaped point spread function do not apply anymore. In terms of reconstruction accuracy, i.e. the difference between the actual and the reconstructed source positions, values between 1 and 2 mm were found at central positions, but increase up to 5 mm towards the edges of the FoV.

At a γ -ray energy of 1274 keV (from a ^{22}Na source) the spatial resolution was measured to be 3.6 mm (x) and 3.7 mm (y) for a source-to-scatterer distance of 11 mm and 6.0 mm (x) and 6.1 mm (y) for a distance of 50 mm, respectively.

From evaluations at both studied photon energies, it can be seen that the spatial resolution deteriorates with increasing source-to scatterer distances (Fig. 8.7). This behavior is observed for both investigated γ -ray energies, however, it is less pronounced at 1274 keV than at 511 keV.

All found values of the spatial resolution (along all three dimensions) are summarized in Tab. 8.2.

In a second measurement period also images at a source-to-scatterer distance of 55 mm were taken, i.e. the configuration corresponds to the radiation source being placed at the origin of the γ -PET setup. With the radiation source placed at the coordinate origin an ARM of 7.6° and a spatial resolution of 9.0 mm along the x - and y -dimension was found. Both, the ARM and the SR confirm the trend found in the previous measurement series of an improvement of the ARM, but a deterioration of the SR for larger source-to-scatterer distances.

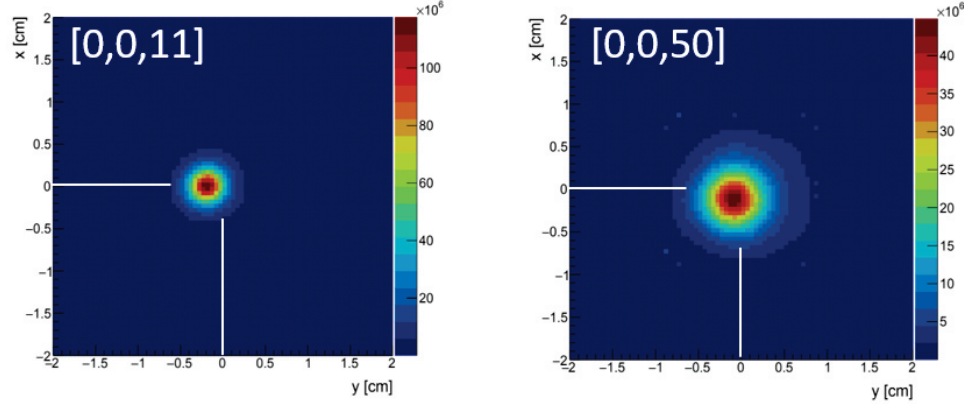


Fig. 8.7: Reconstructed images of a ^{22}Na point source at a distance to the scatterer's front surface of 11 mm (left) and 50 mm (right). The source was placed centrally along the x- and y-dimension (detector plane).

	511 keV				1274 keV	
	[0,0,11]	[5,-5,11]	[10,-10,11]	[0,0,50]	[0,0,11]	[0,0,50]
source position [x,y,z] (in mm)						
ARM [°]	14.9	14.0	14.2	11.0	15.7	8.2
SR_x [mm]	3.7	4.2	7.8	12.9	3.6	6.0
SR_y [mm]	3.6	4.7	8.5	12.3	3.7	6.1
SR_z [mm]	4.1	5.1	5.6	24.6	5.3	18.6

Tab. 8.2.: Summary of the performance characterization of Compton camera prototype #1.

Compton camera efficiency The efficiency of the Compton camera prototype was calculated based on the number of Compton events that could be reconstructed. The activity of the ^{22}Na point source at the time of the measurements was 158 kBq, resulting in an emission rate of 412 000 events/s of 511 keV annihilation γ rays and 158 000/s for 1274 keV γ rays in 4π .

The covered solid angle of the camera was 35.6 % ($z = 11$ mm) and 1.8 % ($z = 50$ mm), respectively⁶. For a source-to-scatterer distance of 11 mm, therefore, a detection efficiency of 1.70×10^{-4} and at 50 mm of 2.62×10^{-4} (both for central sources) is calculated for 511 keV γ rays. For 1274 keV photons the efficiency is 2.28×10^{-4} and 14.16×10^{-4} for $z = 11$ mm and $z = 50$ mm, respectively.

⁶the active camera area is calculated based on the scatterer obtained by the crystal's front surface of 1.45 mm \times 1.45 mm.

The reason for the improved detection efficiency for larger source-to-scatterer distances is that only a small energy band of energies can be detected in the scatterer, which is determined by the minimal energy that can be detected on one side (thus excluding small scattering angles to be detected) and a maximum energy on the other side (determined by the covered solid angle of the absorber).

The total Compton camera efficiency for 511 keV photons was calculated to 6.07×10^{-6} and 4.7×10^{-6} for central source positions at distances of 11 mm and 50 mm, respectively. At γ -ray energies of 1274 keV the determined efficiency is 81.30×10^{-6} ($z = 11$ mm) and 25.49×10^{-6} ($z = 50$ mm). The in general higher efficiency at 1274 keV compared to 511 keV is explained by the larger energy deposit of 1274 keV γ rays already at small scattering angles, so that these events are not lost due to the minimum energy threshold in the scatterer.

8.1.1.3. PET-only imaging mode

In addition to characterization measurements of the Compton camera, also the capability to take PET data and images was investigated. Therefore, the ^{22}Na point source was moved along the y coordinate of the γ -PET prototype and images were taken at $x = z = 0$ mm and $y \in [0, 1, 3, 6, 9, 12]$ (in mm). At each measurement point data were acquired for 600 seconds. Only coincidences between fully absorbed events (energy windows around the full photopeak's width) were taken into account.

The image reconstruction was performed using a simple back-projection method. From the reconstructed point source images (Figs. 8.8 and 8.9) a spatial resolution of 2 mm could be demonstrated and a reconstruction accuracy of a few hundred μm was achieved, which was determined by the positioning accuracy of the point source within the setup and not the reconstruction algorithm itself. Two sources placed next to each other in a center-to-center distance of 3 mm could clearly be distinguished. Fig. 8.8 shows reconstructed images of the ^{22}Na point source at $y = 0$ mm (top left), $y = 1$ mm (top right), $y = 3$ mm (bottom left) and $y = 9$ mm (bottom left). The nominal source position (along the x- and y-dimension) is indicated by the white lines. Fig. 8.9 shows the reconstructed image from the source being placed in the coordinate system's origin ($x = 0, y = 0$) together with the respective projections along the x- and y-dimension.

Eventually, an ML-EM method was used⁷ to reconstruct the point source images. Using 10 iterations, the spatial resolution could be improved to 1.0 mm. A total detection efficiency (in the systems center) of 2.36 % was calculated.

8.1.1.4. γ -PET imaging mode

After the demonstration of the general functionality of the individual γ -PET prototype parts (Compton camera and the PET detector pair) data were acquired for 2 hours to obtain $\beta^+\gamma$ coincidences. Therefore, a 140 kBq ^{22}Na point source was placed at an off-center position ($x = -5$ mm, $y = 5$ mm, $z = 5$ mm; coordinates according to Fig.

⁷by M. Safari

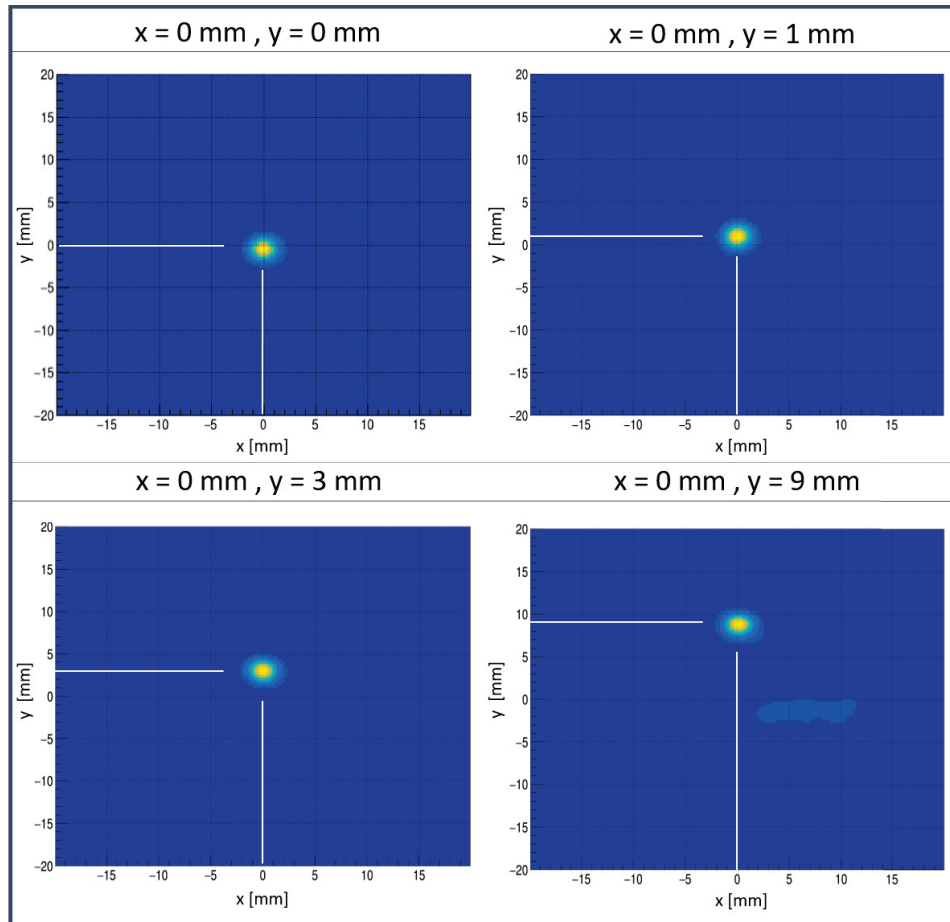


Fig. 8.8: Point spread function of a ^{22}Na point source at a central ($x = 0$ mm, $y = 0$ mm) (top left) and off-center positions ($x = 0$ mm, $y = 1$ mm) (top right), ($x = 0$ mm, $y = 3$ mm) (bottom left) and ($x = 0$ mm, $y = 9$ mm) (bottom right). The white lines indicate the nominal ^{22}Na source position.

8.1). To search for the triple coincidences between the two 511 keV annihilation γ rays and the 1274 keV photon, two trigger regions were defined. One contained the two PET detectors, the other the two components of the Compton camera. Within these two trigger regions the triggered ASIC channels were treated as a group of hits originating from a single γ -ray hit. Only events that triggered at least one detector in both trigger regions (3 ns coincidence window) were taken for a second post-processing step. This second step looped through all detected coincidences and used the ASIC channel identifier (channel-ID) to relate the triggered hits to one of the two detectors within the respective region. If an initial γ -hit was detected in both trigger regions and, furthermore, also registered on both detectors in each of the trigger regions, it was considered as a valid triple coincidence, on which, subsequently, an energy gate was applied such that only fully absorbed 511 keV annihilation photons were considered in the PET detector pair and the total detected photon energy in the Compton camera corresponded to 1274 keV.

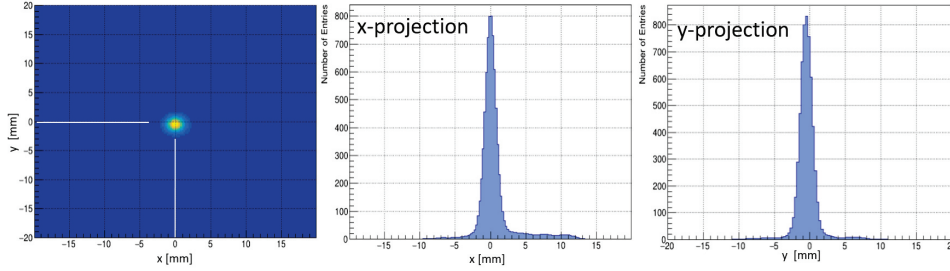


Fig. 8.9: Point spread function of a ^{22}Na point source at a central position ($x = 0$ mm, $y = 0$ mm) and the corresponding projections along the x- and y-dimension, respectively.

source position (x [mm], y [mm])	(0,0)	(0,1)	(0,3)	(0,6)
SR_x [mm]	1.9	2.0	1.9	2.0
SR_y [mm]	2.0	2.1	1.9	2.0
x_{recon} [mm]	0.0	0.1	0.0	0.1
y_{recon} [mm]	-0.5	0.9	3.0	5.9

Tab. 8.3.: Spatial resolution (SR) and reconstructed source position from four measurements performed with the radiation source placed at four y positions. The reconstruction accuracy is the difference between the actual source position and the reconstructed one.

From a two hour measurement only one event could be found after applying all post-processing conditions. Therefore, triple coincidences were formed by an event-wise combination of Compton and PET events for a proof-of-principle study⁸. Thus, the data set used for event reconstruction in γ -PET mode contained four energy values and 4×2 position values of γ -ray hits that originated from within the point source volume, but did not correlate in time (between PET and Compton events).

Point spread functions were reconstructed using PET-only, Compton-only and the γ -PET mode. The width (sigma) of the line-of-response (LOR) was set to 1.6 mm (crystal pitch) and the Compton cone’s width was set to 8.2° . All images were reconstructed using three iterations of the ML-EM method.

Using 419 events in PET-only mode a circular point spread function along the y- and z-dimension (PET plane) and a spatial resolution $\text{SR}_y = 3.5$ mm and $\text{SR}_z = 3.2$ mm (FWHM) was found. Along the x-dimension the PET detector pair is not capable to resolve the point source position due to its limited solid angle coverage and the resulting small angles with which the individual LORs intersect. Fig. 8.10 shows the reconstructed point spread function in the yz-plane and the xy-plane, respectively. Slices through the image along the individual dimensions are shown below. The red lines mark the bin

⁸This method is only valid for point-like radiation sources and it is ensured that the γ -ray vertices of all emitted photons are identical (within the range a positron can drift before it is thermalized and annihilates.)

which is plotted below as slice of the plane. The white lines indicate the actual point source position.

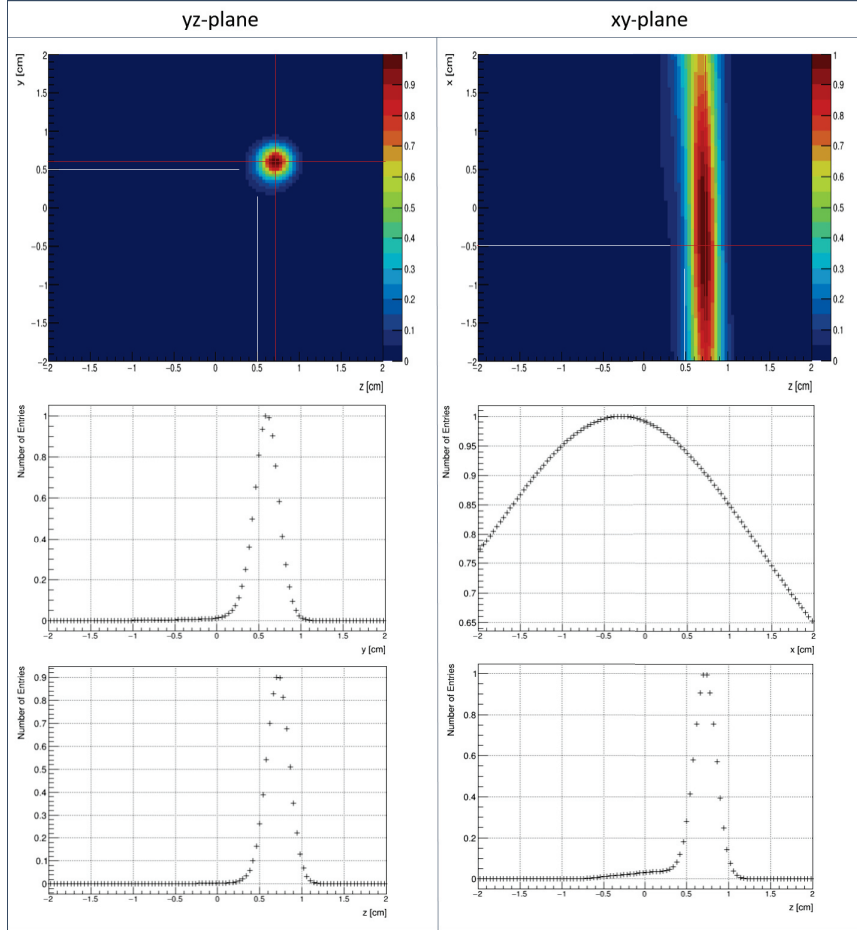


Fig. 8.10: Point spread functions of a ^{22}Na point source placed at $x = -5$ mm, $y = 5$ mm and $z = 5$ mm and reconstructed in PET-only mode (top row) and a slice through one bin (indicated by the red lines) along the two respective dimensions (central, bottom row). The white lines indicate the actual source position.

In Compton-only mode around 2000 events were used for the reconstruction (Fig. 8.11). Along the x - and y -dimension (Compton plane) a spatial resolution (FWHM) of $\text{SR}_x = 14.4$ mm and $\text{SR}_y = 19.3$ mm was obtained, respectively. Without detailed knowledge of the Compton camera's full system matrix no spatial resolution can be obtained along the z -dimension (that marks the distance of the source to the camera).

In γ -PET reconstruction mode, the point source could be localized in 3D using only 77 events. The obtained spatial resolution was 12.9 mm, 3.9 mm and 3.3 mm along the x -, y - and z -dimension, which indicates a similar spatial resolution as in PET-only mode (using 418 events) in the PET plane and an improvement of 1.5 mm in the x -dimension. The reconstruction accuracy was found to be 2.1 mm (x -dimension), 0.1 mm

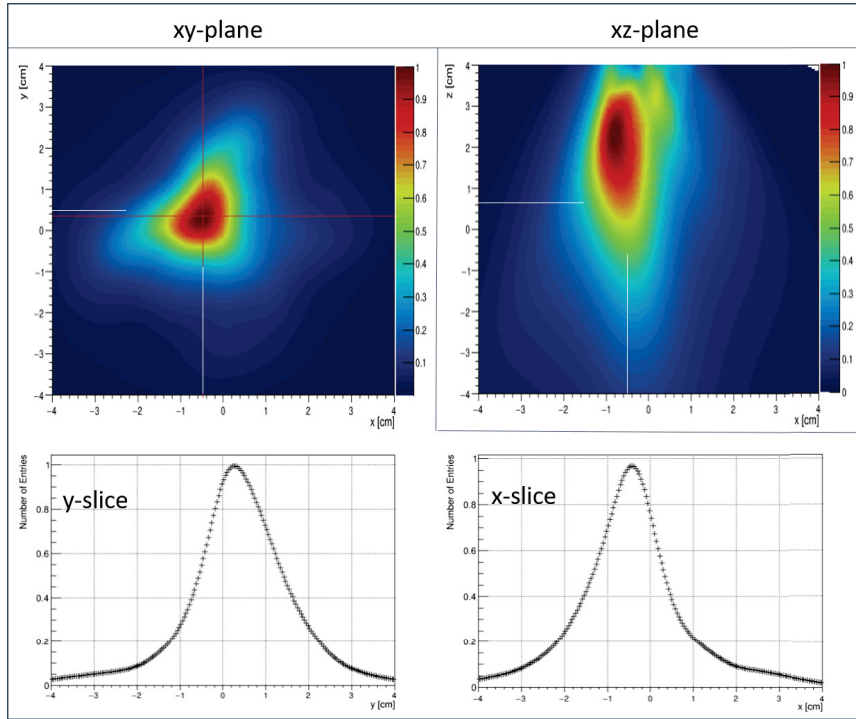


Fig. 8.11: Point spread functions of a ^{22}Na point source placed at $x = -5$ mm, $y = 5$ mm and $z = 5$ mm reconstructed in Compton-only mode (top row) and a slice through one bin (indicated by the red lines) along the two respective dimensions (central, bottom row). The white lines indicate the actual source position.

(y -dimension) and 1.2 mm (z -dimension). Fig. 8.12 shows the reconstructed images of the ^{22}Na point source in γ -PET mode in the xz - (left), xy - (center) and yz -plane (right). Below the 2D point spread functions, a cut through the bin that contains the distributions' maximum (indicated by the red lines) is shown for the two respective dimensions. Furthermore, in all image reconstructions in γ -PET mode an artefact at the exact inverse source position ($x = 5$ mm, $y = -5$ mm, $z = -5$ mm) can be observed (see Fig. 8.12), which does not reduce with an increasing number of events used for image reconstruction. Therefore, it is unlikely to originate from noise arising from a too high number of iterations of the ML-EM method, since such an image fragmentation would have to reduce with an increasing number of events. However, it is very likely to be caused by the second intersection of the LOR with the Compton cone. There is only a limited amount of detector combinations in this tight geometry of the prototype camera that can detect PET coincidences of a point source in an off-center position. Also the orientation of the Compton cones would be very similar. Consequently, a rather large amount of LOR-Compton cone intersections are found in a region which happens to be at $[x,y,z] = [5 \text{ mm}, -5 \text{ mm}, -5 \text{ mm}]$, corresponding to the inverse source position. Tab. 8.4 summarizes the findings on the image reconstruction in γ -PET mode.

Spatial resolution (SR)	PET-only	Compton-only	γ -PET
SR _x [mm]	-	14.4	12.9
SR _y [mm]	3.5	19.3	3.9
SR _z [mm]	3.2	-	3.3

Tab. 8.4.: Summary of the achieved spatial resolution along the x-, y- and z-dimension in PET-only, Compton-only and γ -PET imaging mode.

In conclusion, a proof-of-principle study of a γ -PET prototype was conducted and 3D point source images could be reconstructed using only 77 events. For the detection and reconstruction of "true" triple-coincidences the camera prototype setup has to be upgraded to at least four full Compton camera arms in order to obtain sufficient geometric efficiency.

8.1.2. A LaBr₃:Ce/CeBr₃- and GAGG based Compton Camera for Prompt- γ Imaging (Prototype #2)

A second Compton camera prototype was commissioned using the GAGG scatterer (as for prototype #1), but using a monolithic absorber crystal as absorber component. Prototypes with both available monolithic scintillator materials (available at the Chair for Medical Physics of LMU Munich), a LaBr₃:Ce and a CeBr₃ crystal, were commissioned. With regard to an application in a four-arm (cross-shaped) setup (see. Figs. 8.22 and 8.23) four HAMAMATSU S14161-3050HS-08 SiPM arrays (in a 64-channel configuration using an adapter PCB that combines four individual array channels into one) were chosen to read out the scintillator crystals. As for all Compton camera measurements within this thesis, the PETsys TOFPET v2c ASIC was used for charge integration and signal digitization.

The initial setup was designed with regard to the requirements set by measurement campaigns within the BARB project (an ERC project at GSI aiming at investigating the potential of radioactive ion beams for hadron therapy; PI: M. Durante) [BARB 2021], i.e. for first ion beam measurement campaigns it had to be operated simultaneously with the SIRMIO PET detector assembly [Parodi 2019]. Therefore, the Compton cameras were mounted to the (spherical) SIRMIO detector support structure that houses the PET detectors, such that these only blocked a minimum number of the SIRMIO PET detector positions. The scatterer was attached to a boomerang-shaped PCB (customized for the spherical shape of the detector support structure), which allows to be attached to the SIRMIO detector mount. The scatterer then occupies one of the slots that was initially intended to accommodate one of the SIRMIO PET detectors. The scatterer signals are transferred via three SAMTEC ribbon cables (HQCD-030-12.00-TEU-TED-

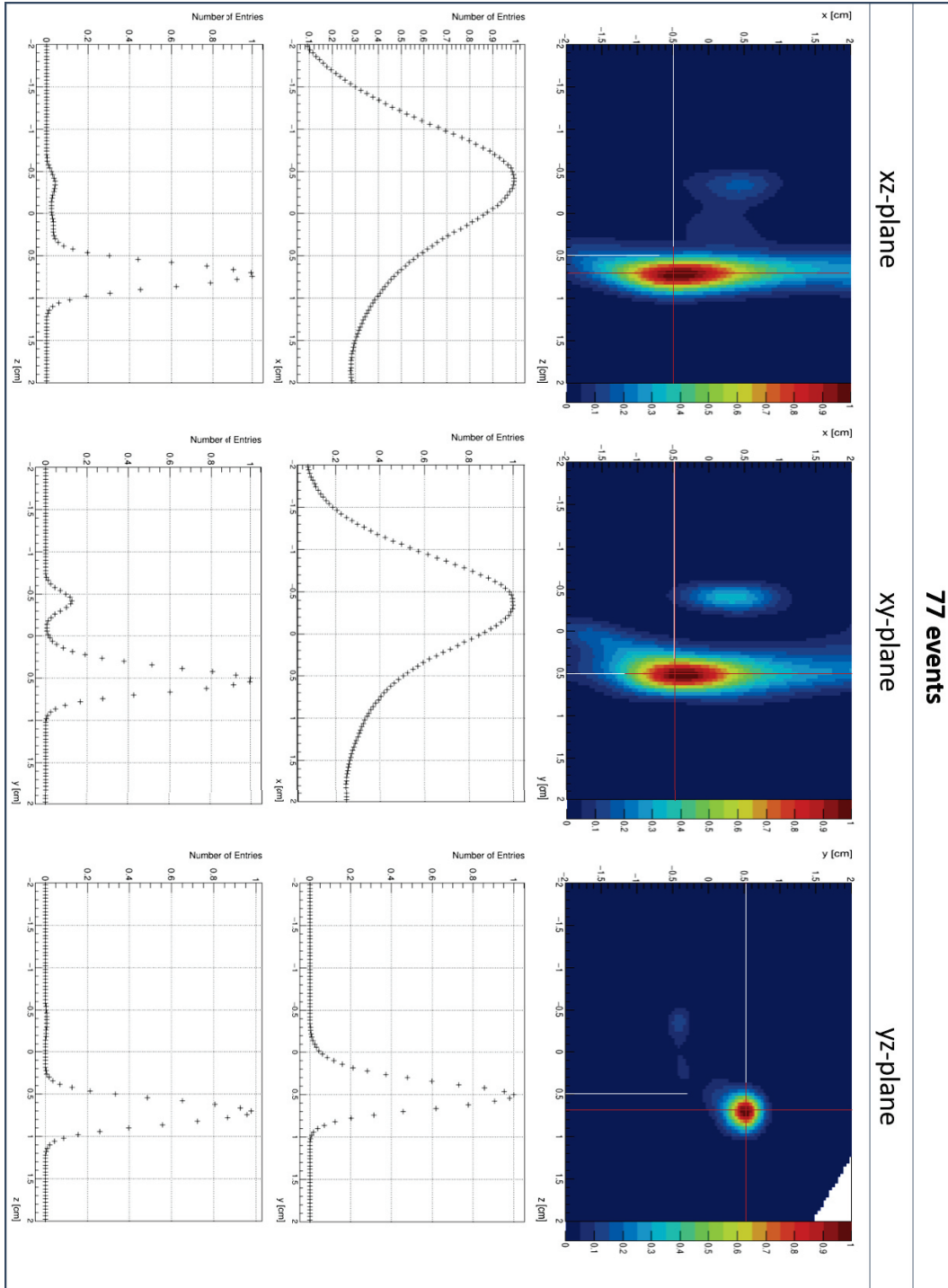


Fig. 8.12: Reconstructed image of a ^{22}Na point source at an off-center position ($x = 5 \text{ mm}$, $y = -5 \text{ mm}$, $z = -5 \text{ mm}$) in the xz - (left), xy - (center) and yz -plane (right). The white lines indicate the source position and the red lines represents the bin of which the 1D distribution is shown in the center and bottom row. Furthermore, an artefact that corresponds to the second intersection of the LOR and the Compton cone is visible at the inverse source position ($x = 5 \text{ mm}$, $y = -5 \text{ mm}$, $z = -5 \text{ mm}$) in all three 2D images.

1-N) to a mezzanine PCB that is plugged into the PETsys FEM128 ASIC board. The absorber, which is directly plugged into the FEM128 ASIC board, is enclosed in a 3D printed casing that consists of two individual parts. The front part contains the absorber detector, while the back part houses the FEM128 including the ASICs and allows for active cooling via an attached fan. A potentiometer within the fans bias circuit allows to regulate the supply voltage and, therefore, the fan's rotary speed. Consequently, the ASIC's temperature can be adjusted in a range from about 23 ° C to about 30 ° C, which allows to mimic conditions as they occur during the detector calibrations, even when the setup is later on brought to other facilities for measurement campaigns (e.g. at GSI).

The mechanical connection between the boomerang PCB and the camera casing was done via threaded rods, which also allowed to adjust the distance between the scatterer and the absorber component. For the following measurements a distance of 78 mm was chosen. The individual components of a single Compton camera arm are displayed inside the 3D printed housing in Fig. 8.13 (top) and individually in Fig. 8.13 (bottom).

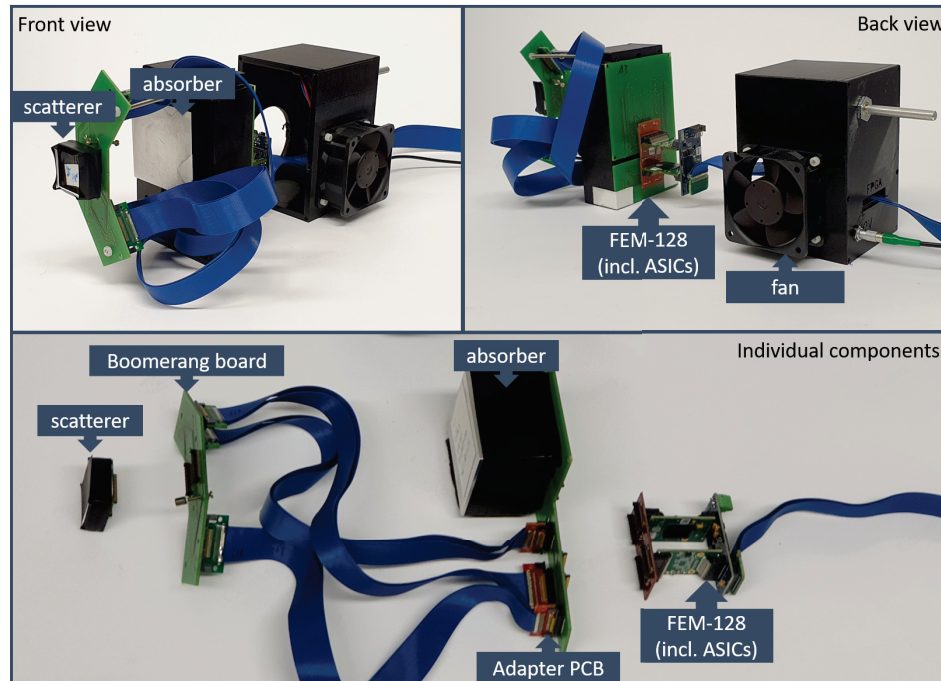


Fig. 8.13: Picture of the "Compton camera 2" prototype in front view (top left) and back view (top right). The GAGG scatterer is mounted onto a boomerang-shaped PCB that allows to mount the Compton camera to the SIRMIO detector mount structure. The absorber detector is placed in a 3D printed housing. The bottom picture shows the individual components without housing.

The SiPM overvoltage of the scatterer (PA3325WB-0808) was set to 5.0 V and the one for the absorber (S14161 3050HS-08) was set to 2.7 V .

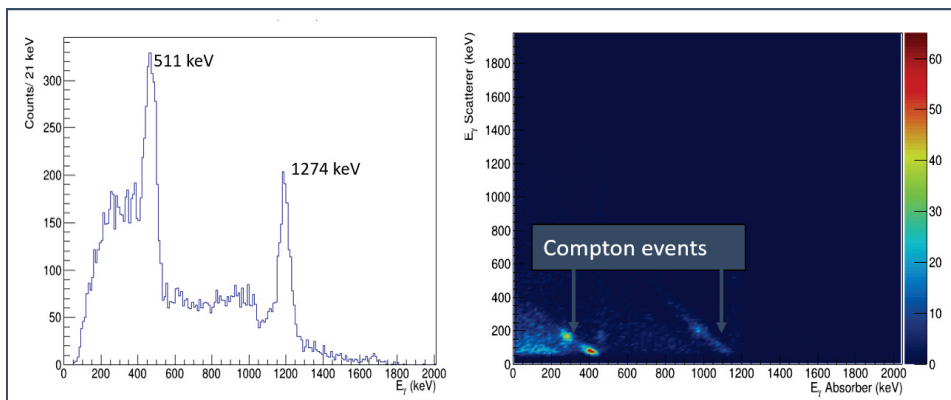


Fig. 8.14: Coincidence energy spectrum of a ^{22}Na point source measured at camera #1 and obtained from a 600 second measurement (left) and the corresponding 2D energy correlation between the energy deposits in the scatterer and the absorber detector (right).

A principle test to proof the functionality of this setup was performed within a calibration run using a 600 s irradiation using a ^{22}Na point source prior to the beamtime measurements at the GSI Helmholtz Centre for Heavy Ion Research in Darmstadt and applying the full four-arm Compton camera arrangement (Fig. 8.22 and 8.23). The ^{22}Na point source was placed in the center of the detector support structure resulting, in a distance to the four Compton camera scatterers of 100 mm. The evaluation of this calibration measurement is described within this section, whereas the results of the online measurements are given in a dedicated section (Sec. 8.2.2). The cameras were arranged such that each two opposite cameras were assembled using identical scintillator crystals. Cameras #1 and #3 were built using the $\text{LaBr}_3:\text{Ce}$ crystals, while cameras #2 and #4 were assembled using the CeBr_3 crystals.

Relative Energy Resolution The relative coincidence energy resolution of all four Compton cameras was measured at a photon energy of 511 keV and 1274 keV by triggering on the two respective components in coincidence (using a 3 ns coincidence window). For camera #1 a relative energy resolution of $\Delta E/E_{511\text{keV}} = 8.5 \pm 0.4 \%$ and $\Delta E/E_{1274\text{keV}} = 5.0 \pm 0.2 \%$ was measured. Camera #2 provided an energy resolution of $\Delta E/E_{511\text{keV}} = 10.3 \pm 1.8 \%$ and $\Delta E/E_{1274\text{keV}} = 4.8 \pm 0.5 \%$, respectively. $\Delta E/E_{511\text{keV}} = 11.7 \pm 0.8 \%$ and $\Delta E/E_{1274\text{keV}} = 5.7 \pm 0.3 \%$ was measured at camera #3 and $\Delta E/E_{511\text{keV}} = 11.4 \pm 0.9 \%$ and $\Delta E/E_{1274\text{keV}} = 6.4 \pm 0.4 \%$ at camera #4. These findings are listed in Tab. 8.5.

Image Reconstruction Image reconstruction was performed on a data set that contains data acquired from all four Compton cameras. Therefore, a listmode file that contains the camera identifier, as well as the calibrated energy values and the interaction positions

photon energy / energy resolution	511 keV	1274 keV
$\Delta E/E_{\text{camera}\#1}$ [%]	8.5 ± 0.4	5.0 ± 0.2
$\Delta E/E_{\text{camera}\#2}$ [%]	10.3 ± 1.8	4.8 ± 0.5
$\Delta E/E_{\text{camera}\#3}$ [%]	11.7 ± 0.8	5.7 ± 0.3
$\Delta E/E_{\text{camera}\#4}$ [%]	11.4 ± 0.9	6.4 ± 0.4

Tab. 8.5.: Relative energy resolution $\Delta E/E$ of four Compton cameras commissioned using the four monolithic absorber crystals. Cameras #1 and #3 were assembled using a LaBr₃:Ce absorber crystal, while camera #2 and #4 use a CeBr₃ crystal.

in the respective scatterer and absorber components was generated by a post-processing routine. An event pre-selection was performed to select only events with an initial energy of 1274 keV ($1100 \text{ keV} < E_{\text{total}} < 1400 \text{ keV}$).

The angular resolution measure (ARM), calculated from these events, was found to be 25° (obtained from histogramming data of all four cameras) as can be seen in Fig. 8.15. In a next step, the ^{22}Na point source data (nominal at a central position) were reconstructed (by M. Safari) using an ML-EM method and using 2 iterations, which was mainly determined by the low statistics obtained from only 600 s of measurement⁹. The reconstructed point spread function is shown in Fig. 8.16 including a cut through the bins indicated by the red lines along the x- and y-axis. The nominal source position ($x = 0 \text{ cm}$, $y = 0 \text{ mm}$) is indicated by the white lines. The maximum of the point spread function is found at $x = 15 \text{ mm}$ and $y = 4 \text{ mm}$, which results in an accuracy of 15 mm and 4 mm along the x- and y-dimension, respectively.

A likely reason for this poor accuracy is that the source initially was not perfectly aligned in the center of the detector support structure due to difficulties with accessing the inner part of the spherical structure when all detectors (also the PET detectors) and their electronics were mounted (as was the case during the beamtime campaigns). This could in principle be confirmed by a comparison of the Compton image with the one obtained by the SIRMIO PET arrangement. However, at the time of this thesis submission these data were not yet finally evaluated. The FWHM of the point spread function was found to be 7.6 cm and 6.6 cm along the x- and y-dimension, respectively. Furthermore, the cuts through a layer in the x- and y-dimension reveal an asymmetric point spread function along the x-dimension.

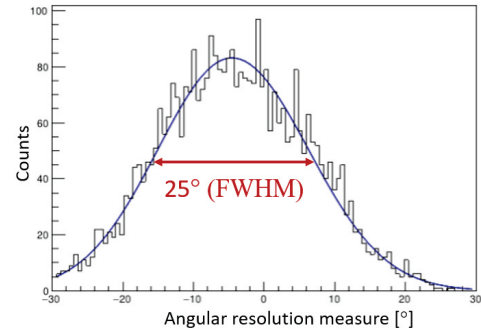


Fig. 8.15: Angular resolution measure (ARM) of all four individual Compton cameras arranged in a cross-shaped setup. The FWHM of distribution was found to be 25° .

⁹The rather short measurement time of 600 s was mainly determined by the tight beamtime schedule.

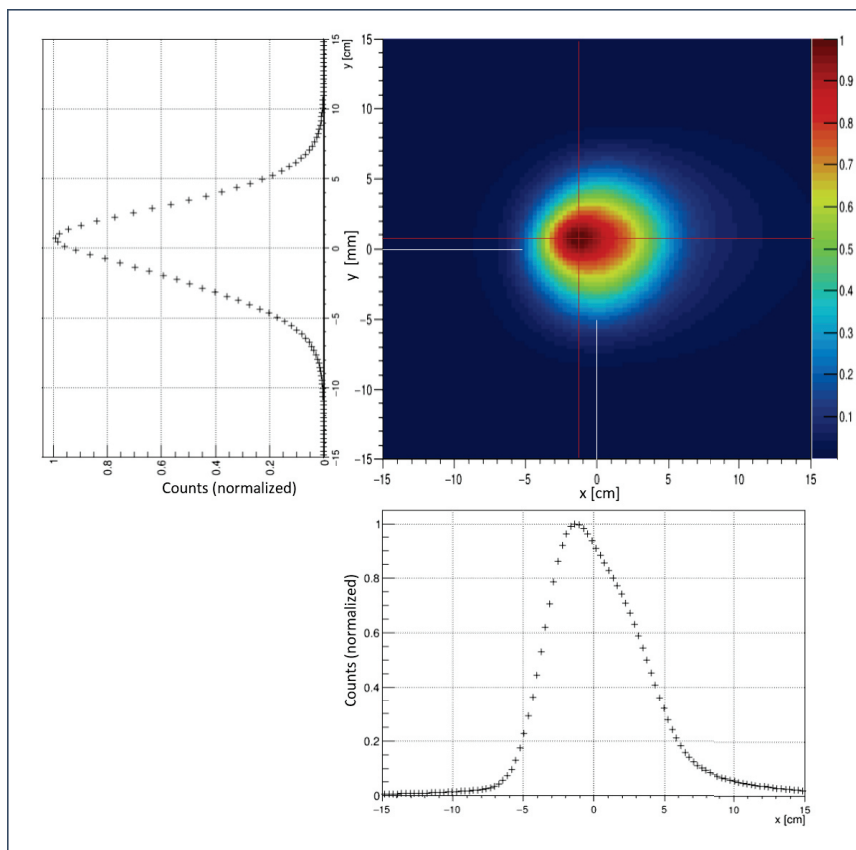


Fig. 8.16: Point spread function reconstructed from four Compton cameras arranged in a cross-shaped assembly. The coordinates of the individual cameras have been transformed into the later on used ion beam coordinate system, i.e., the x-dimension denotes the beam's direction. The panels to the left and below the point spread function show a cut through one bin (indicated by the red lines). The white lines indicate the ^{22}Na point source's nominal position.

8.2. Online Camera Characterizations

Based on the findings of the previous sections in which the general functionality of both Compton camera prototypes could be demonstrated, two online measurement campaigns at the GSI Helmholtz Centre for Heavy Ion Research in Darmstadt (FAIR Phase 0) were conducted. At GSI, research in hadron therapy and range verification (by means of PET) dates back to the early 1990s [Enghardt 1992]. In the following years also related studies like the fragmentation of light ions as a process that might potentially deteriorate the properties of ion beams in treatment, were conducted [Schall 1996].

Both measurement campaigns presented in this section were an integral part of the BARB project [BARB 2021] within which a γ -PET prototype for radioactive ion beam (RIB) range control is developed by LMU. The first beamtime in February 2021 was dedicated to carbon ion beam measurements (^{12}C , ^{11}C and ^{10}C), while the second one

(June 2021) was conducted using oxygen ion beams (^{16}O and ^{15}O)¹⁰.

The LMU contribution to both measurement campaigns was an in-beam PET prototype (SIRMIO) [Parodi 2019, Lovatti 2020, Nitta 2021a, Nitta 2021b] and four Compton cameras (the authors's contribution) in a cross-shaped arrangement that also allows to be used in γ -PET imaging mode.

8.2.1. Measurement campaign at GSI in February 2021

The measurements conducted during the first measurement campaign in February 2021 at GSI were an integral part of the BARB project. Consequently, the LMU γ -PET prototype was integrated into the overall measurement setup that consisted of a dual-head panel PET scanner (provided by the University Medical Center Groningen, P. Dendooven *et al.*), a water column (plus detector system provided by the GSI biophysics department), complemented with the LMU PET prototype¹¹ and the γ -PET prototype. The whole setup is schematically illustrated in Fig. 8.17. One side of the LMU detector arrangement is shown in more detail in Fig. 8.18. The top image shows a CAD drawing of two Compton cameras mounted to an optical breadboard that served as mounting table for the components. In between the two Compton cameras, a cross-like arrangement comprising four three-layered staggered LYSO crystal blocks was placed¹². Fig. 8.18 (bottom) shows a photograph taken after the arrangement was assembled at the GSI. One of these detector arrangements was mounted on both sides of the target phantom, resulting in four Compton cameras and a total of eight PET detectors.

The radioactive ion beam is delivered from the projectile fragment separator (FRS). Projectile fragmentation of the main ion beam produces radioactive isotopes, which are separated by the projectile fragment separator (FRS) from which the secondary radioactive ion beam can be guided towards the experiment (Fig. 8.17 (left side)) [Geissel 1992].

The Compton camera setup The setup for the first four-arm Compton camera (γ -PET) prototype consisted of two different kinds of Compton cameras. Each of the four scatterer was a 16×16 GAGG crystal matrix coupled to a KETEK PA3325WB-0808 SiPM array, as presented and characterized in Sec. 6.1. Two absorber detectors were assembled from $\text{LaBr}_3:\text{Ce}$ crystals read out by HAMAMAMATSU S14161 6050HS-08 SiPM arrays (as characterized in Sec. 6.2) and two absorbers were built using one DOI LYSO with 0.9 mm crystal and one with 1.2 mm crystals (see Ch. 7). The cameras were set up such that the two cameras with the monolithic detectors and the ones with the three-layered staggered DOI detectors were facing each other.

The alignment of the individual detector components was ensured by using adapter PCBs (onto which the detectors were plugged to centrally aligned connectors) and 3D printed frames mounted to an optical rail system.

¹⁰Approved beam time application SBio08 "Radioactive Ion Beams @ GSI".

¹¹at this time only eight (2×4) out of 56 detectors were used

¹²These detectors are part of the SIRMIO project [Parodi 2019, Nitta 2021b].

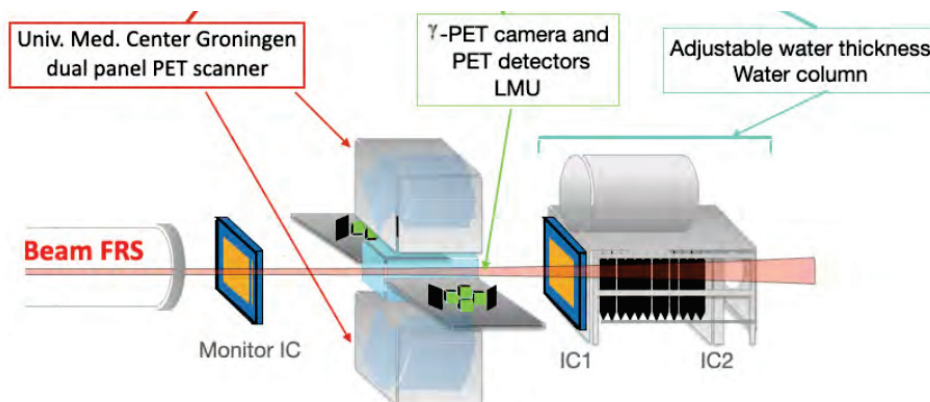


Fig. 8.17: Schematics of the setup used by the BARB collaboration during the measurement campaign in February 2021 at GSI [Boscolo 2021].

The cameras were integrated in a setup mounted to both sides of the PMMA phantom such that they form a cross-like arrangement. In between the two Compton cameras on each side, four SIRMIO PET detectors were placed.

The front-to-front distances between the scatterer and the absorber detectors was between ≈ 40 mm (for the DOI-LYSO-based cameras; 41.5 mm and 43.5 mm, respectively) and ≈ 65 mm for the ones using the monolithic absorbers (67.3 mm and 63.3 mm, respectively). The exact distances were mainly determined by the available space next to the beamline. The reason for the two different distances between the DOI-based and the monolithic absorber-based cameras was the larger surface area of the monolithic detectors compared to the DOI LYSO detectors. Since the spatial resolution of a Compton camera improves with larger scatterer-to-absorber distances, advantage was taken from the larger solid angle coverage of the monolithic detectors (in order to maintain a comparable detection efficiency for all four cameras).

The beam spill structure For all measurements conducted during the February campaign at GSI, Darmstadt, a spill structure of 2 s beam-on and 3 s beam-off was chosen. This structure was verified exploiting the good timing resolution of the PETsys TDC (30 ps binning/ 20 ps timing resolution (RMS) [Petsys 2019]), which allowed to monitor the structure of the delivered spills at the Compton camera’s scatterer. Fig 8.19 (top) shows the time structure of the delivered ^{11}C beam (2 s beam on/ 3 s beam off) monitored via the detected count rate at one of the Compton camera scatterers over the course of ≈ 3 min. Fig 8.19 (bottom) shows a zoom into three spills between 1114 s and 1125 s run time.

Prompt γ ray detection By triggering only on one of the monolithic $\text{LaBr}_3:\text{Ce}$ absorbers (of camera 3, which was placed under a backwards angle compared to the ion beam’s direction), prompt γ -ray spectra could be observed in the absorber from a 40

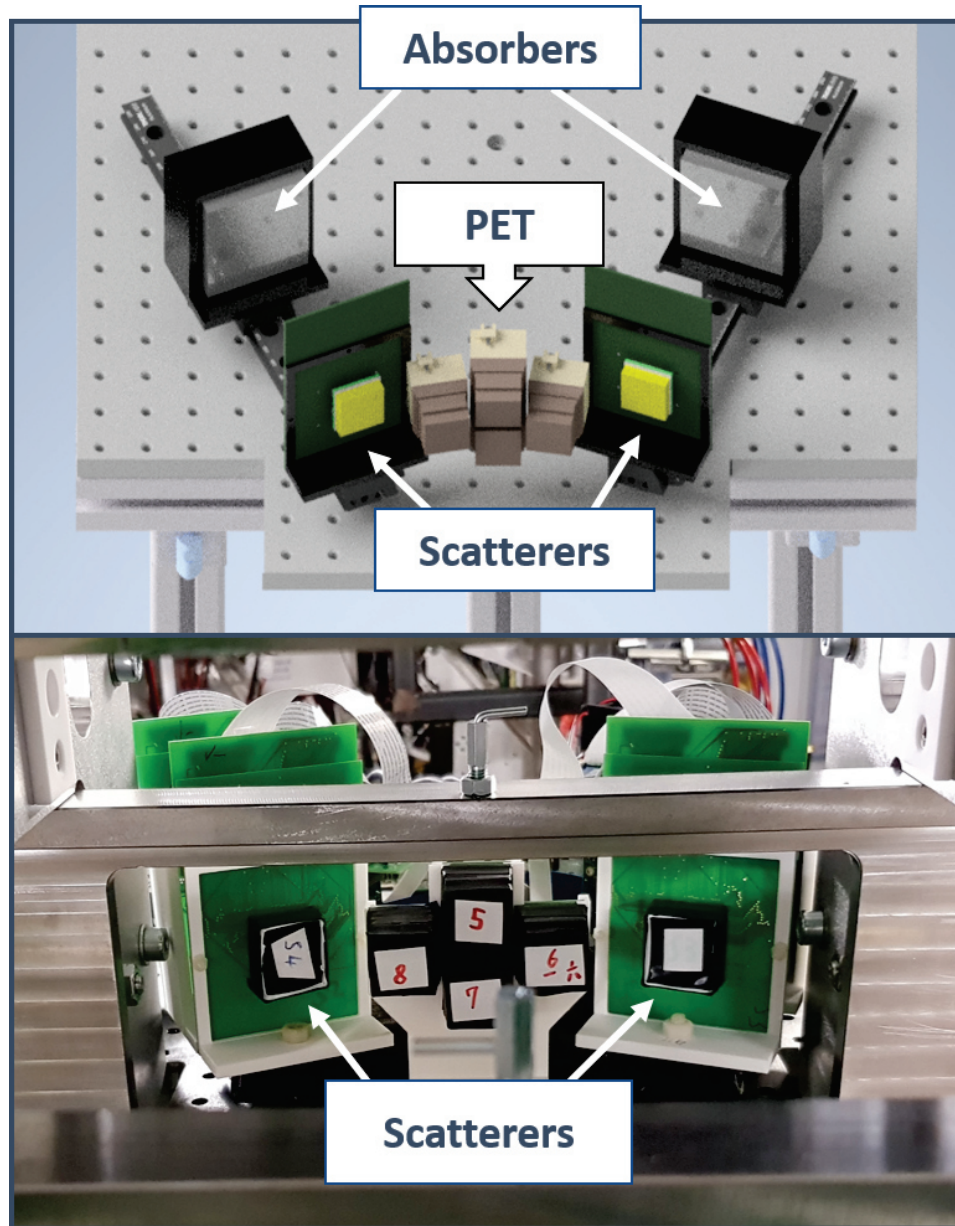


Fig. 8.18: Schematics (top) and picture (bottom) of one side of the February 2021 GSI beamtime setup. Four SIRMIO DOI PET modules (cross-like arrangement) are surrounded on both sides by Compton cameras.

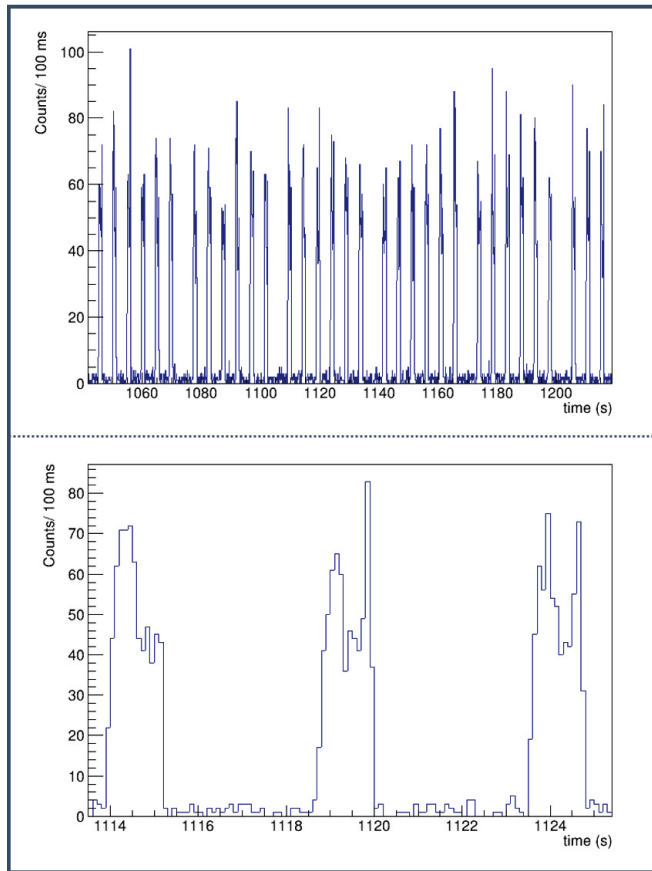


Fig. 8.19: Spill structure of a ^{11}C beam used for the measurement campaign at GSI and a zoom into three spills (bottom).

minutes PMMA irradiation with a ^{10}C beam (267 MeV/u; 1.1×10^6 particles per spill). The corresponding energy spectrum is shown in Fig. 8.20 (left panel). The right panel shows a zoom into the energy region from 2 MeV to 5 MeV on a linear scale. The three peaks of the ^{12}C group (photopeak, single and double escape peaks) can be identified. The signal-to-background ratio (S/B), however, is very poor.

In the energy spectra obtained from a ^{11}C beam (246 MeV/u; 2.1×10^7 particles per spill) no prompt γ peak structure is visible, but an increased background originating from beam generated secondary particle emissions can be seen (Fig. 8.21). This is likely not only correlated to the higher beam intensity, but also to the increase in the number of neutrons in the projectile nuclei (^{10}C vs. ^{11}C). Furthermore, the increased background level can also be derived from the fact that the structure of the intrinsic radioactivity in the LaBr₃ crystal is not observable anymore.

Triggering the Compton cameras in coincidence mode (between scatterer and absorber) would result in a better signal-to-background ratio, but would also reduce the

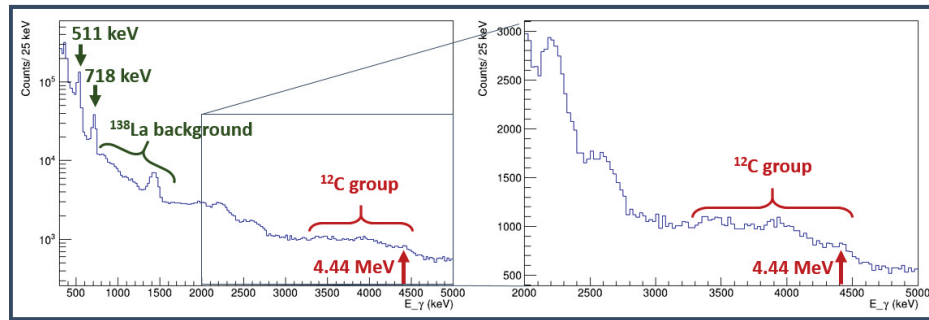


Fig. 8.20: Energy spectrum obtained from a 40 minutes irradiation of PMMA using a 267 MeV/u ^{10}C beam (1.1×10^6 particles per spill) (left). The right panel shows a zoom (in linear scale) into the region of the spectrum indicated by the blue rectangle.

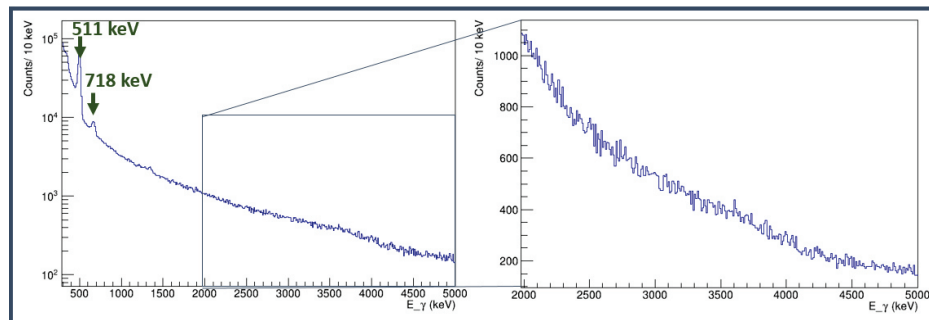


Fig. 8.21: Energy spectrum obtained from a 15 minutes irradiation of PMMA using a 246 MeV/u ^{11}C beam (2.1×10^7 particles per spill) (left). The right panel shows a zoom (in linear scale) into the region of the spectrum indicated by the blue rectangle.

efficiency to detect prompt γ rays by several orders of magnitude. Therefore, no sufficient number of Compton event originating from the prompt γ rays could be obtained. Consequently, no ion beam image reconstruction could be done on the data obtained from the February measurement campaign at GSI.

8.2.2. Measurement campaign at GSI in June 2021

A second measurement campaign in June 2021 at GSI, Darmstadt was dedicated to oxygen beams (^{16}O and ^{15}O).

The γ -PET setup The low statistics of the acquired data of the previous beamtime period motivated the use of four cameras that were using monolithic scintillators, due to their four times larger front surface compared to the three-layered DOI LYSO crystal blocks.

All four GAGG scatterers were read out using KETEK PA3325WB-0808 SiPM arrays. As absorbers two LaBr₃:Ce (camera #1 and camera #3) and two CeBr₃ (camera #2

and camera #4) crystals were used. All absorber crystals were read out by four HAMAMATSU S14141-3050HS-08 SiPM arrays mounted to an adapter board, such that the total number of signal channels was reduced to 64. The cameras were arranged such that two respective pairs with identical absorber scintillators were facing each others. During this measurement period, besides the four Compton cameras also online tests of 42 of the SIRMIO PET detectors mounted to the spherical detector support structure were performed. Therefore, the detector support could be used for an accurate alignment of the four Compton cameras. The exact position in the mounting structure, however, was determined by the occupation of 42 slots for the PET detector modules. For the scatterers, the already introduced boomerang-shaped mounting PCB (designed such that it allowed to attach the scatterer detector to the detector support frame without blocking open spots for other detectors) was used. Fig. 8.22 displays a CAD drawing of the described setup, comprised of the PET detector sphere, complemented by four pair-wise opposite Compton cameras. Also, the PCB allowed to transfer the individual signals¹³ to the ASIC without introducing high amounts of passive material to the scattered γ 's trajectory.

Fig 8.23 shows a picture of the setup as it was finally operated at GSI. The four Compton cameras are attached to the SIRMIO detector support frame forming a cross-like configuration.

The ASIC settings were set as determined in the previous chapters for the respective detector combinations.

²²Na calibration Before the online measurements started, an offline calibration run was performed using a ²²Na source placed in the center of the detector frame structure, i.e. the center of the FOV of all four Compton camera arms. Data acquisition was run for 600 s and the related analysis was discussed in Sec. 8.1.2.

Online: ¹⁶O and ¹⁵O beam spill structure As already described for the measurement campaign in February 2021, again the spill structure of the ion beam was monitored, in Fig. 8.24 shown for the ¹⁶O irradiation of a PMMA target (for 600 s). The top row shows the count rate¹⁴ of camera #1 (downstream), while the bottom row shows the count rate measured at camera #3 (upstream). From the zoom into the first minute of irradiation (right column) a spill structure of 2.5 s beam-on and 5.5 s beam-off can be deduced.

A comparison between the top and bottom rows of Fig. 8.24 shows a difference in the coincidence count rate of roughly a factor 50 between the cameras placed at forward and backward angles relative to the beam direction upstream (see also Par. 8.2.2). Furthermore, in the count rate histograms of camera #3 a continuous increase of background is visible (indicated by the red line). This is due to fragmentation of the

¹³and the SiPM bias

¹⁴in coincidence between scatterer and absorber

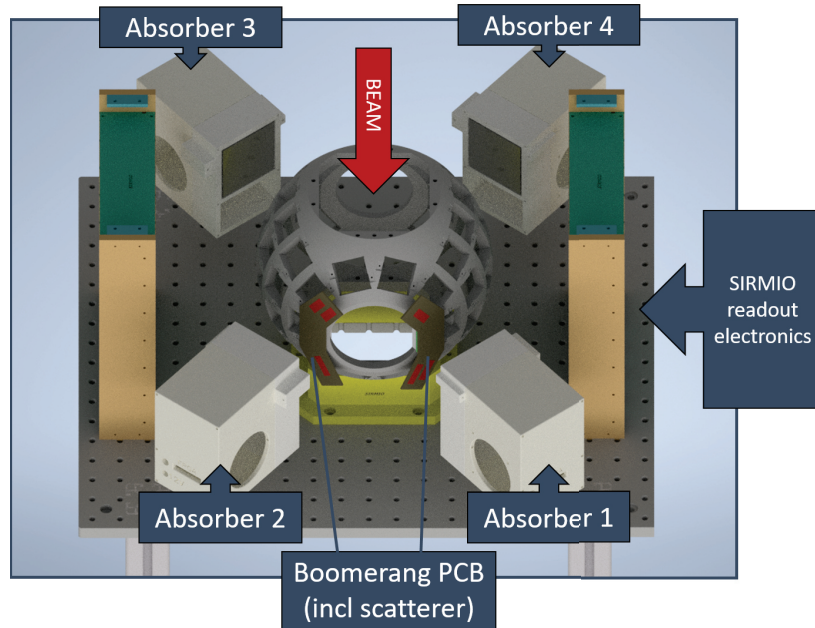


Fig. 8.22: Schematics of the setup used for the measurements in June 2021 at GSI. The SIRMIO detector support frame is shown in the center. The main components of the Compton camera (absorber detector in its housing and scatterer on the boomerang PCB) are displayed next to it. At the left and right of the spherical frame, the staggered electronics PCBs for the processing of the SIRMIO DOI PET detectors are shown. For clarity the schematics is drawn without these detectors, cables and further assembly material (such as screws).

projectiles as well as of the target nuclei, resulting in an accumulation of ^{15}O , ^{14}O , ^{11}C and ^{10}C in the target volume. While a significant part of the two (short-lived) radioactive isotopes of oxygen and ^{10}C will also decay during the ten minutes of irradiation, ^{11}C with a half-life of more than 20 minutes will strongly accumulate.

Online: ^{16}O and ^{15}O energy spectra First, a 600 s irradiation of a PMMA target using a ^{16}O beam ($8 \cdot 10^9$ particles per spill) was conducted. The data were processed for each of the four cameras individually. The coincidence window between the scatterer and the absorber was set to 1 ns, the grouping window for events within the same detector component was set to 75 ns.

A first comparison between the acquired energy spectra (coincidence spectra) between one camera placed downstream (camera #1) and another one upstream (camera #3) shows a factor of roughly 30 difference in the coincidence count rate (895 counts/s vs. 27 counts/s)¹⁵. Fig. 8.25 shows the corresponding spectra from 0 keV to 7000 keV on a linear scale (top row) and on a logarithmic scale (bottom).

The coincidence energy spectrum obtained with camera #1 shows that the higher

¹⁵Here, the factor is smaller compared to the one determined from the count rate histograms, since in the energy spectra further constraints like a minimum number of fired SiPM channels is applied.

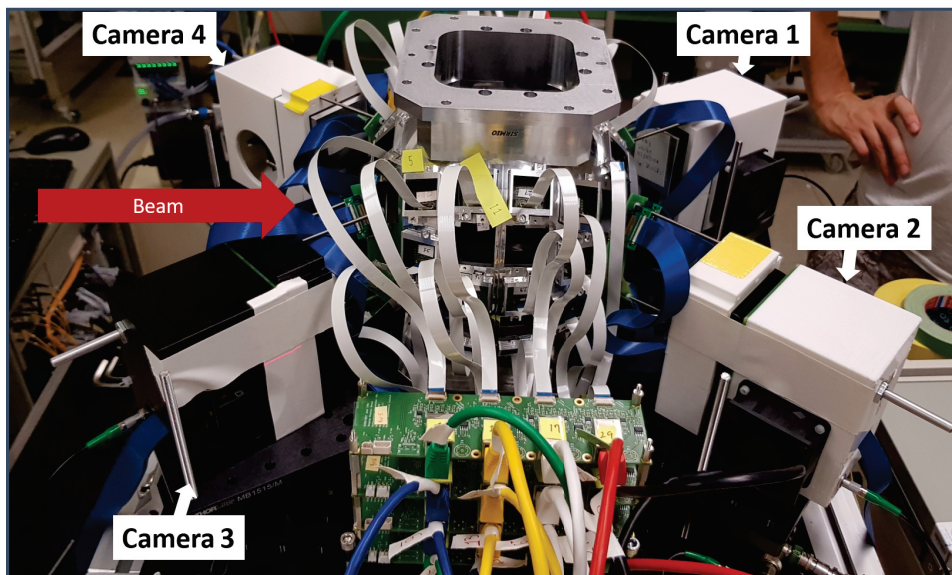


Fig. 8.23: Picture of the setup used for the measurement campaign at GSI in June 2021. In the center, the SIRMIO detector support frame can be seen with the outgoing signal cables. In the bottom center the amplifier board of the SIRMIO PET detectors are shown. To the left and right of the detector frame structure the four Compton cameras are displayed in their 3D-printed housings. The direction of the ion beam is indicated by the red arrow.

count rate is predominantly caused by a larger background contribution. The dominant background in an ^{16}O irradiation scenario emerges from fast neutrons and charged particles, which are primarily emitted in forward direction. Neutrons and heavy charged particles may lead to "fake coincidences" between a neutron/charged ion being detected in one camera component and a γ ray in the other or in true coincidences of two interactions in both Compton camera components. Furthermore, they potentially blur the energy spectra by causing pile-up in one of the detector components if they are detected within the 75 ns grouping window, applied to obtain the summed energy deposit in the Compton camera component.

In the coincidence energy spectrum of camera #3 (logarithmic scale), however, the 511 keV peak and the 718 keV transition (from the ^{10}C decay) can clearly be seen. Furthermore, a structure that might correspond to the three peaks (photopeak, single and double escape peak) of the 4.44 MeV prompt γ rays of the ^{12}C deexcitation can also be seen.

In order to verify this assumption, a method to enhance the signal to background ratio and to increase statistics in the spectrum was developed and applied. The original spectrum (from 2000 keV to 7000 keV) with a coarse binning is shown in Fig. 8.26 (top). For the mentioned contrast enhancement, in a first step the energy resolution of both detector components (absorber and scatterer) is determined as a function of the γ -ray energy. For each event the energy deposit in the respective detector is taken and

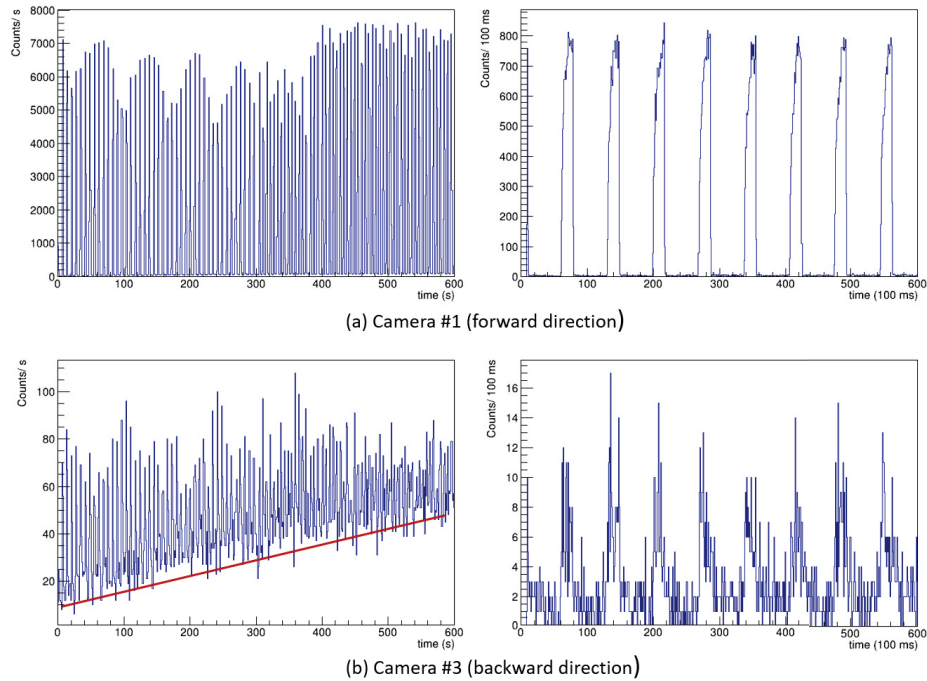


Fig. 8.24: Spill structure of an ^{16}O beam imaged for 600 seconds at camera #1 (a, left) and a zoom into the first 60 seconds (a, right). The beam-on phases lasted about 2.5 s followed by approximately 5.5 s beam-off. The bottom row shows the spill structure during the same irradiation measured with camera #3 (left panel) and a zoom into the first minute (right panel). The red line in the bottom left panel indicates the linearly increasing background due to the activation of the target with β^+ emitters.

a corresponding random number is generated. This random energy value is obtained by picking a value from a Gaussian distribution with its centroid at zero and a width that corresponds to the relative energy resolution of the detector at the measured energy¹⁶. Subsequently, the two new energy values, the one of the scatterer and the one of the absorber, are added and filled into the histogram that will contain the energy spectrum. After all data are filled into the histogram, this method is repeated using x iterations (e.g. 100 iterations in Fig. 8.26 (bottom)). Since each energy value is exchanged by a random value derived from its Gaussian width profile, energy values of one event but generated from different iterations will be filled in different bins.

Fig. 8.26 (bottom) shows the hereby "enhanced" spectrum of the ^{16}O ion irradiation measured at camera #3 after 100 iterations. It clearly shows the lines of the decay of the excited projectile ^{16}O nuclei. Important to note: this method can be used to prove the presence of Compton scattered prompt γ rays in the coincidence spectra. It cannot be used to determine the energy resolution at these energies since the shape of a γ -ray line is strongly determined by its shape in the original spectrum, which is most likely

¹⁶This is valid since the energy deposit can only be determined with an accuracy of the relative energy resolution.

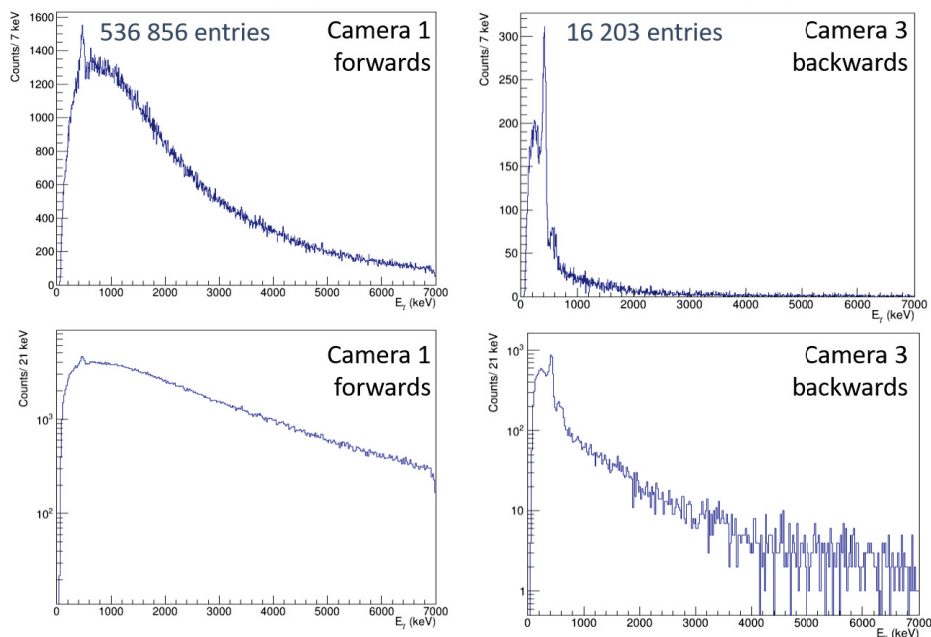


Fig. 8.25: Prompt γ spectra obtained from a 600 seconds ^{16}O irradiation of a PMMA target on a linear scale (top) and logarithmic scale (bottom). Camera #1 was placed downstream and camera #3 upstream of the oxygen beam direction.

non-Gaussian due to the low statistics. Also it does not allow to increase the amount of valid Compton events for later on image reconstruction of the ion beam.

Using ^{15}O beams, the beam intensity was between 1.0 and 0.7×10^7 particles per spill, which is about three orders of magnitude lower than what was reached using the ^{16}O beam (8×10^9). Consequently, also a prolonged measurement time of 40 minutes was not sufficient to obtain a comparable amount of statistics in the energy spectra obtained from these ^{15}O measurements and no lines that would correspond to prompt γ rays could be identified reliably (see Fig. 8.27).

The results of a very low detection efficiency on the one side and of high levels of background on the other side could later be confirmed in simulation studies performed by M. Safari. Currently there is an effort going on at the LMU Chair for Medical Physics to develop a machine learning based post-processing and image reconstruction method that is capable to discriminate between prompt γ -ray signals and background events. This could provide a way to image the ion beam based on the data obtained during this measurement campaign (even though it will still be dominated by low statistics). However, at the current point no Compton images from the two measurement campaigns at GSI could be obtained in Compton mode.

For a potential next measurement campaign an upgrade of the γ -PET prototype that

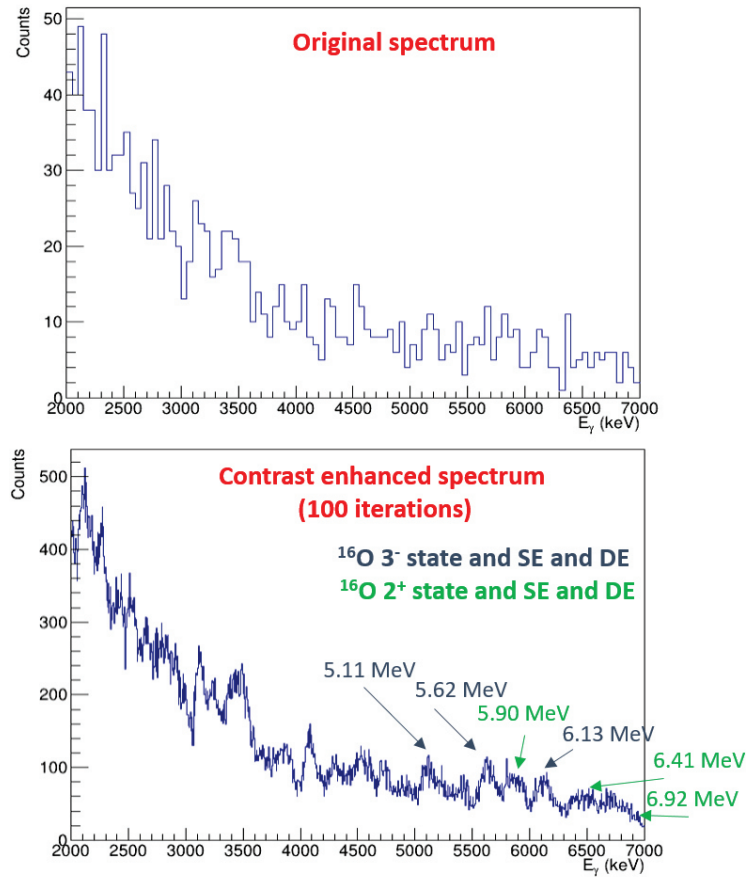


Fig. 8.26: Prompt γ spectrum plotted from 2000 keV to 7000 keV of a ^{16}O irradiation of PMMA for 600 seconds (top) and the same spectrum using the S/B and statistics 'enhancement' as described in the text (bottom).

covers larger solid angle, but also has an increased detection efficiency, is required. Simulation studies to find the optimum geometry and detector types are presently conducted.

Online: ^{16}O and ^{15}O PET imaging The LMU contribution to the BARB project is the development of a γ -PET detector system. Therefore, not only Compton imaging, but also the PET imaging capability of the prototype was investigated. Therefore, the two Compton camera scatterers that were opposing each other were triggered in coincidence. The 2D energy correlation between the two detectors is used to select valid PET events. Fig. 8.28 (left) shows this 2D correlation with an accumulation of events where the distributions corresponding to a 511 keV energy deposit in the respective detector intersect (obtained from scatterer #1 and scatterer #3). The right panel of Fig. 8.28 shows the summed energy deposit in the two detectors. The 511 keV annihilation photon coincidences appear as a peak at 1022 keV (2×511 keV) in the spectrum. The data were

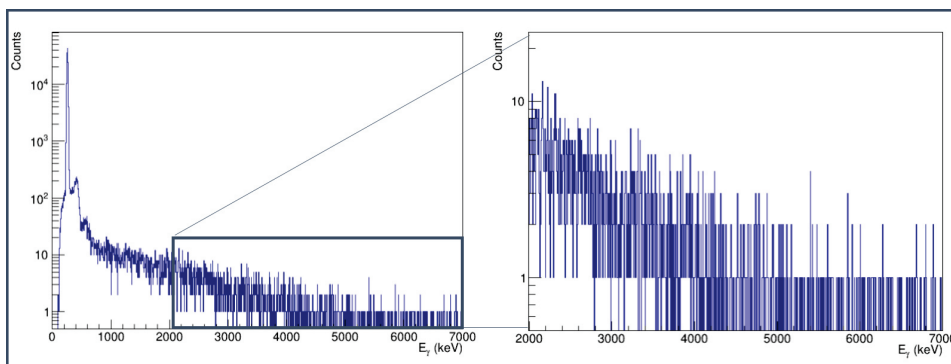


Fig. 8.27: Coincidence energy spectrum from a 36 minutes PMMA irradiation using a 15 beam.

acquired during a 600 seconds PMMA irradiation using a ^{16}O beam (8×10^9 particles per spill).

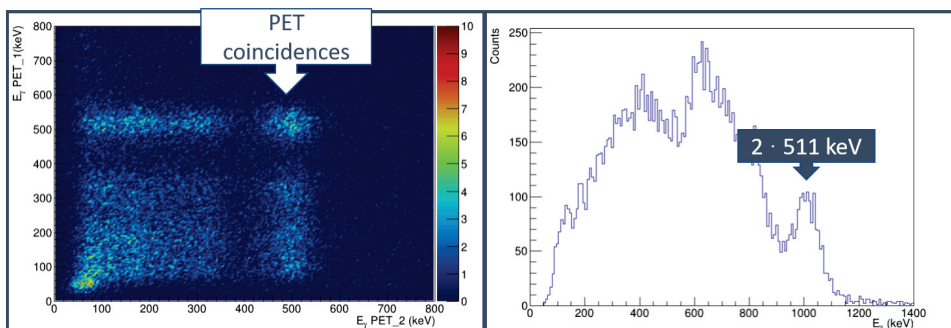


Fig. 8.28: 2D energy correlation of scatterer #1 and scatterer #3 triggered in PET mode (left) and the summed coincidence spectrum (right) obtained from a 600 s PMMA irradiation using a ^{16}O beam (8×10^9 particles per spill).

Before an image reconstruction is performed, the found hit positions are transferred into the beam coordinate system, with the beam trajectory directly from the negative towards the positive z -direction. The vertical dimension is labelled as y and the transversal one by x . Consequently, the y -dimension is the only one identical in both, the detector reference frame and the beam coordinate system. Along the x - and z - dimension, therefore, an elongation of the beam profile is expected to be visible due to the limited number of angles of intersecting LORs available from only four detectors.

For image reconstruction only data acquired from a ^{16}O irradiation of PMMA events obtained from the scatterer detector combination of camera #1 and camera #3 could be used (see Fig. 8.29). Approximately 1000 events could be used for the image reconstruction (using 3 iterations of ML-EM reconstruction)¹⁷. Along the y -dimension,

¹⁷Image reconstruction performed by. G. Lovatti

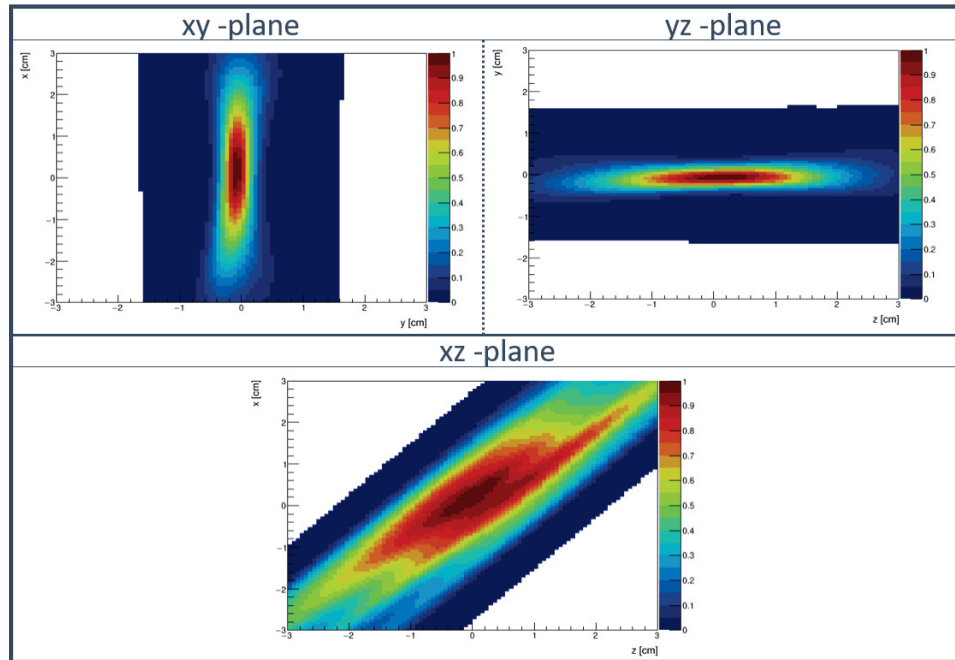


Fig. 8.29: ^{16}O ion beam β^+ activation reconstructed using the scatterer detectors of camera #1 and camera #3 as PET detectors.

which is the only axis identical in the detector internal reference frame and the global reference frame of the ion beam, the width of the profile is found to be 4.2 mm. Along the x- and y-dimension the image is dominated by the already stated limited number of intersecting angles of the LORs. Furthermore, the diagonal distortion of the image on the xz-plane shows the positioning of the two detectors from which the LORs emerge.

Summary A γ -PET prototype consisting of four Compton cameras was successfully developed and commissioned. Initial tests were conducted at GSI in Darmstadt. Compton scattered prompt γ rays could be detected and identified by using coincidence spectra between scatterer and absorber. However, the lack of statistics and a high beam-induced background (predominantly in forward direction with respect to the beam direction) did not allow for reconstruction of the prompt γ -ray emission vertices and therefore, online beam monitoring.

8.3. LaBr₃:Ce- and GAGG based Compton Camera for Prompt- γ Imaging based on the latest KETEK low-noise SiPM series (Prototype #3)

A third Compton camera prototype was commissioned to assess the performance of a Compton camera using the latest KETEK low-noise SiPM series. Characterized individually both Compton camera components provided the best energy resolution in a readout configuration using the KETEK WL series SiPM arrays.

The scatterer component consists of a GAGG scintillation array coupled to PA3335WL-0808 SiPM array. This detector combination was shown to provide the best relative energy resolution (9.5% at 662 keV) among all investigated detector assemblies (Sec. 6.1). According to

$$\Delta\theta = \frac{m_e c^2}{(E_{incident} - E_S)^2 \sin\theta} \Delta E_S \quad (8.1)$$

with $E_{incident}$ the energy of the incident γ ray, E_S the energy deposit in the scatterer and θ the Compton scattering angle, the energy resolution's contribution of the scatterer component can be estimated [Watanabe 2018, Katagiri 2021].

For the absorber, a LaBr₃:Ce crystal read out by a PA6647WL-0808 SiPM array was used. Again, this detector combination provided the best energy resolution (4.1% at 662 keV) using the PETsys TOFPET v2c ASIC (6.2.3). Both SiPM arrays were biased at 5.0 V overvoltage.

For the Compton camera prototype a scatterer-to-absorber distance (front-to-front) of 150 mm was chosen. Data were acquired using a ²²Na point source (140 kBq) at a distance of 50 mm to the front surface of the scatterer. The schematic and a picture of the setup is shown in Figs. 8.31 and 8.32. The mechanical setup was realized using 3D printed frames to which adapter PCBs were mounted. These adapters were used to allow the ASIC to be mounted without intersecting the photon trajectories. The detector assembly

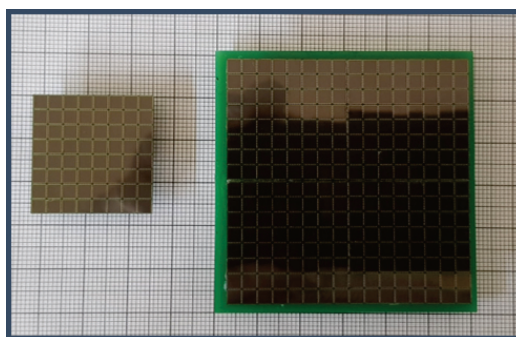


Fig. 8.30: Picture of the used SiPM arrays. The left array is a PA3335WL-0808 array as has been used to read-out the scatterer detector. On the right four PA3347WL-0808 SiPM arrays mounted to an adapter board to reduce the array's channels from 256 to 64 are shown.

mounted to the support frame was then attached to rail carriers connected to optical

8.3. *LaBr₃:Ce- and GAGG based Compton Camera for Prompt- γ Imaging based on the latest KETEK low-noise SiPM series (Prototype #3)*

rails, in order to allow for an exact positioning along the z-dimension. The alignment of the two detector components was ensured by using two identical adapter PCBs, with the connectors arranged to hold the SiPM array centrally positioned.

Three measurement runs were conducted with the source placed at $(x = 0 \text{ mm}, y = 0 \text{ mm})$, $(-2 \text{ mm}, 2 \text{ mm})$ and $(-4 \text{ mm}, 4 \text{ mm})$ for irradiations times of 5 hours per position.

Detector Energy Correlation and Event Selection The 2D energy correlation for coincidences between the scatterer and the absorber is shown in Fig. 8.33. Two prominent diagonal distributions are clearly visible intersecting both axes at 511 keV and 1274 keV, respectively. Furthermore, random coincidences with a full absorption of a 511 keV or a 1274 keV γ ray are visible as two vertical lines. Random coincidences with a full absorption of 511 keV γ rays detected in the scatterer are visible as faint horizontal distributions. By comparing Fig. 8.33 with the 2D energy correlation plot of prototype 1 (Fig. 8.4) the higher detection efficiency due to the larger covered solid angle and the thicker crystal is evident by the prominent structure correlated with the 1274 keV γ rays.

The coincidence spectrum (as the sum between the energy values detected in the two components) is shown in Fig. 8.34. The coincidence energy resolution is $6.9 \pm 0.2 \%$ and $4.3 \pm 0.2\%$ and, therefore, provides an energy resolution that is superior to many other scintillator-based detector systems, even for the individual components of such systems. For event selection two energy requirements must be fulfilled:

- An energy window around the photo peak. The width of the energy window was chosen to include the full photo peak [1180 – 1310 keV].
- The theoretically maximum energy deposit (from geometrical considerations) in the scatter detector is set as upper constraint ($E_{\text{max_scatterer}511} \approx 55 \text{ keV}$; $E_{\text{max_scatterer}1274} \approx 350 \text{ keV}$).

The latter in combination with a lower detection limit of γ -ray energies between 40 keV and 50 keV in the scatterer crystal¹⁸ causes a very low camera efficiency for 511 keV γ rays. Therefore, the Compton camera's imaging capabilities were only demonstrated for incident γ -ray energies of 1274 keV.

Event Reconstruction *The calculation of the ARM value and the event reconstruction was performed by M. Safari.*

Before the actual image reconstruction, the angular resolution measure (ARM) is determined for all three measured source positions. The calculated ARM values are 5.4°

¹⁸The lower energy cut-off varies from crystal to crystal

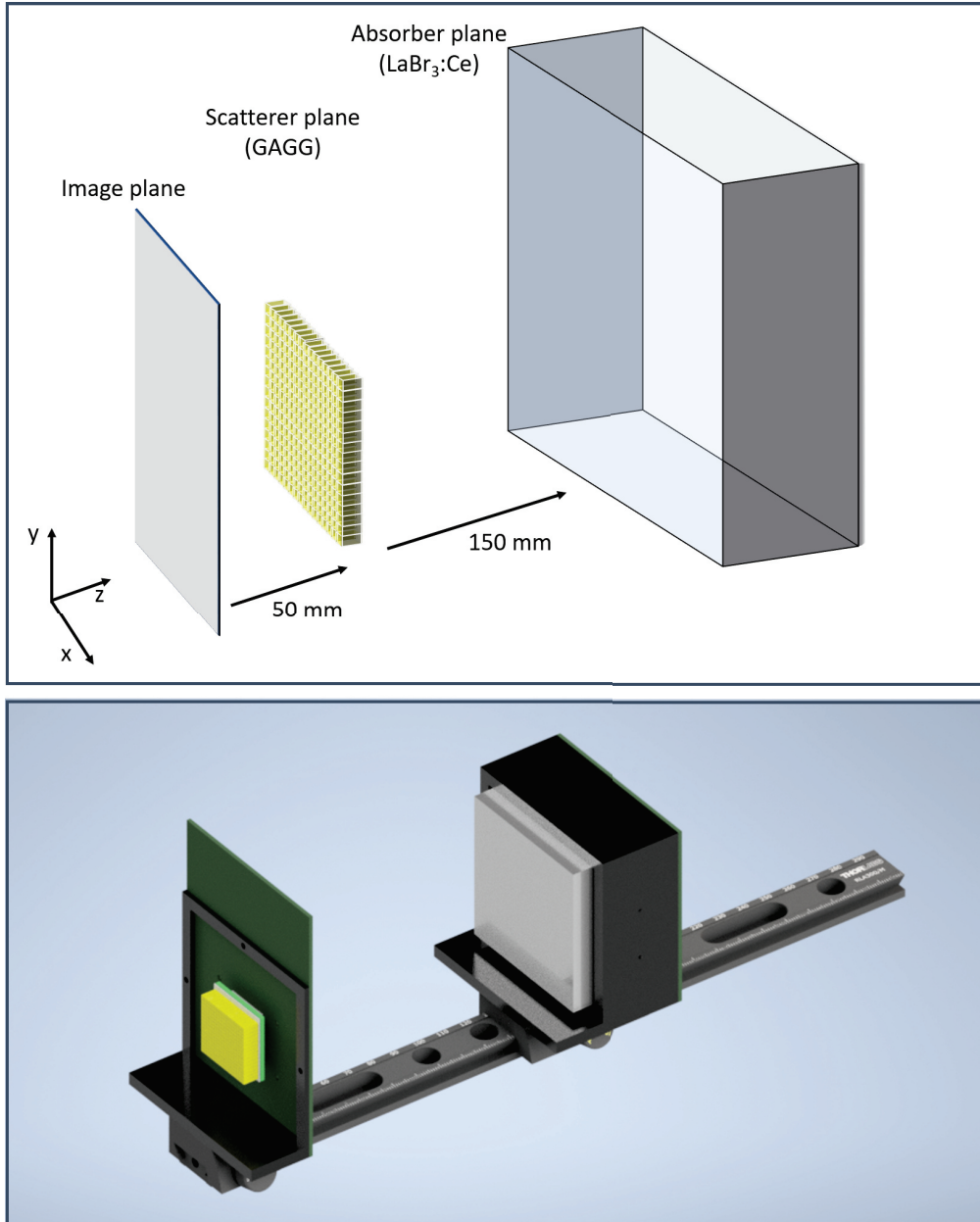


Fig. 8.31: Schematics of the setup used for the Compton camera prototype 3 (top) and 3D CAD image of the two detector components mounted to an optical rail system that is used to align the components along the z-dimension (bottom).

8.3. $\text{LaBr}_3\text{:Ce}$ - and GAGG based Compton Camera for Prompt- γ Imaging based on the latest KETEK low-noise SiPM series (Prototype #3)

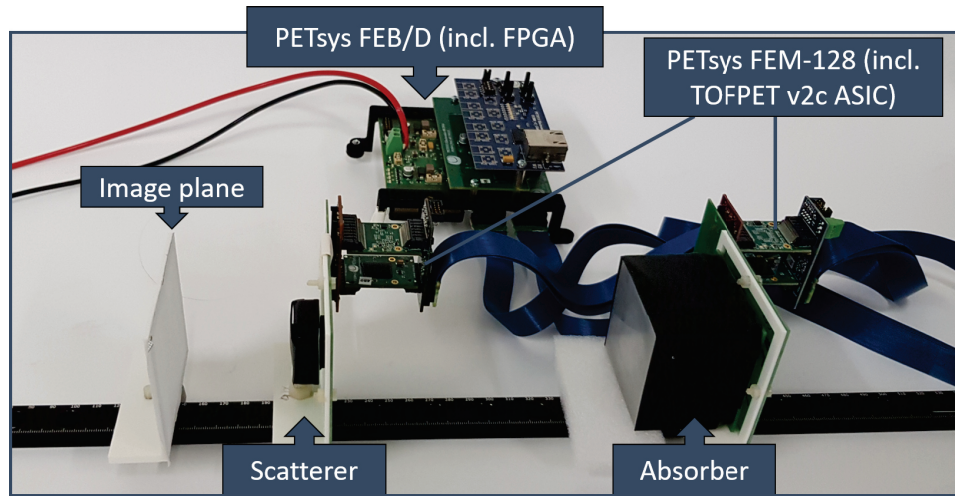


Fig. 8.32: Picture of the setup used for the Compton camera prototype 3. The detectors are mounted to adapter PCBs that allow to mount the FEM-128 readout boards (which contain the ASICs) to the side of the detectors in order to not place inactive material in the γ -ray trajectories. The PETsys FEB/D board that contains the FPGA and GBE ethernet link to communicate with the DAQ computer is visible in the background

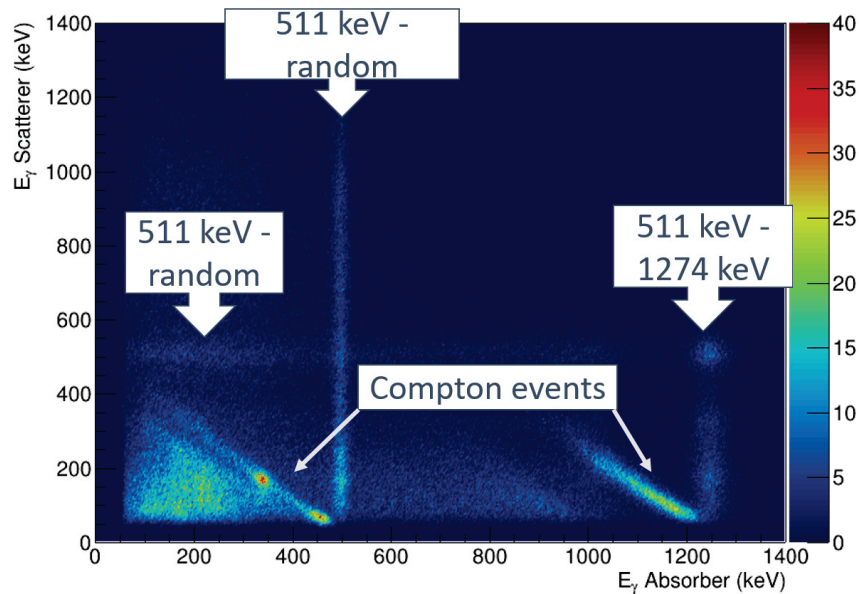


Fig. 8.33: 2D energy correlation between the energy deposit in the scatterer and the absorber for coincident events (3 ns coincidence window) obtained from a 5 h measurement with a ^{22}Na calibration point source placed centrally in the field-of-view.

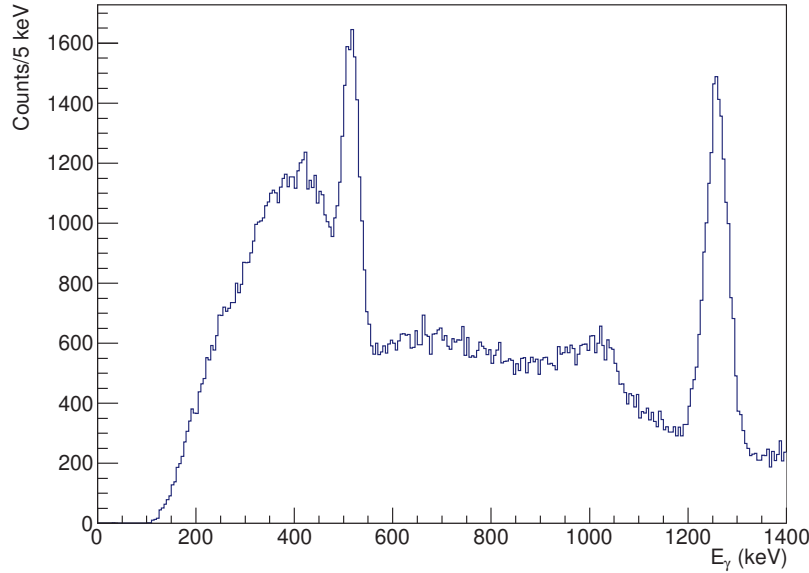


Fig. 8.34: Coincidence spectrum between the scatterer and the absorber components obtained from a 5 hours long ^{22}Na irradiation with the point source placed in the center of the field-of-view. The coincidence window was set to 3 ns.

(0 mm, 0 mm) (Fig. 8.35), 5.8° (-2 mm, 2 mm) and 5.4° (-4 mm, 4 mm), respectively.

2D Compton image reconstruction was performed using a ML-EM method (based on the MEGlib toolkit and libraries) with 10 iterations.

Fig. 8.36 (top row) shows the point spread function of the ^{22}Na point source placed at the three investigated positions. The accuracy with which the source could be localized ($\Delta x/y_{reconstructed} - \Delta x/y_{real}$) was found to be 0.8 mm for all three positions along the x-dimension and 0.4 mm, 0.4 and 2.3 mm along the y-dimension for $y = 0$ mm, $y = 2$ mm and $y = 4$ mm.

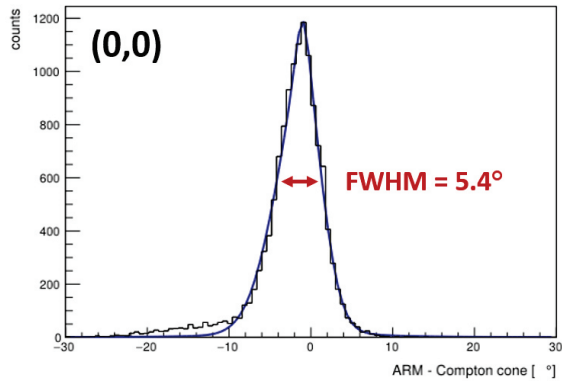


Fig. 8.35: Angular resolution measure (ARM) from a 5 h measurement with the radiation source at the central position (0 mm, 0 mm).

The FWHM of the point spread function, and therefore the spatial resolution of the Compton camera (in the imaging plane), was measured from the projec-

8.3. *LaBr₃:Ce- and GAGG based Compton Camera for Prompt- γ Imaging based on the latest KETEK low-noise SiPM series (Prototype #3)*

source position (x,y)	(0 mm, 0 mm)	(-2 mm, 2 mm)	(-4 mm, 4 mm)
ARM ($^{\circ}$)	5.4	5.8	6.2
SR _x (mm)	5.3	5.4	5.6
SR _y (mm)	5.2	5.3	5.6
Δ_x (mm)	0.8	0.8	0.8
Δ_y (mm)	0.4	0.4	2.3

Tab. 8.6.: Spatial resolution (SR) and reconstructed source positions from four measurements performed with the radiation source placed at four y positions. The reconstruction accuracy is the difference between the actual source position and the reconstructed one.

tions along the x- and y-dimension (Fig. 8.36 (center and bottom row)) and was found to be 5.3 mm (5.2 mm), 5.4 mm (5.3 mm) and 5.6 mm (5.6 mm) for the three positions along the x-dimension (y-dimension).

From the 5 h measurement at the central source position (0,0) 13 071 events could be identified to fulfill both energy requirements and were reconstructed as valid events, resulting in a Compton efficiency (with full photo absorption in the absorber) of 3.0×10^{-4} . For a covered solid angle of 1.71 % this results in a total efficiency of 5.2×10^{-6} .

The capability of the Compton camera prototype to resolve point source shifts is demonstrated by the software-wise superposition of the measurement data at (0 mm, 0 mm) and (-4 mm, 4 mm) resulting in a distance of 5.66 mm and a subsequent image reconstruction using an ML-EM method with 14 iterations. Fig. 8.37 shows the obtained image with two well separated maxima corresponding to the two point source positions. From these measurement the capability to resolve at least 5.66 mm shifts is concluded.

Summary In a Compton camera prototype arrangement, the relative coincidence energy resolution (as the sum of the energy deposit detected in the scatterer and the absorber) was measured to be 6.9 ± 0.1 % and 4.3 ± 0.1 % at energies of 511 keV and 1274 keV, respectively.

Compton images were reconstructed for incident γ -ray energies of 1274 keV using a ²²Na point source. Shifts of the radioactive source of 2 mm could be clearly resolved with a typical accuracy (x- and y-dimension) between 400 and 800 μ m. The spatial resolution, given as the FWHM of the point spread function, was found between 5.2 mm and 5.6 mm for all conducted measurements and point source shifts of 5.66 mm could be demonstrated.

The improvement in terms of the achievable energy resolution using the latest KETEK WL series SiPM arrays was shown in this study and the capability of these SiPMs to be used in a Compton camera setup was demonstrated.

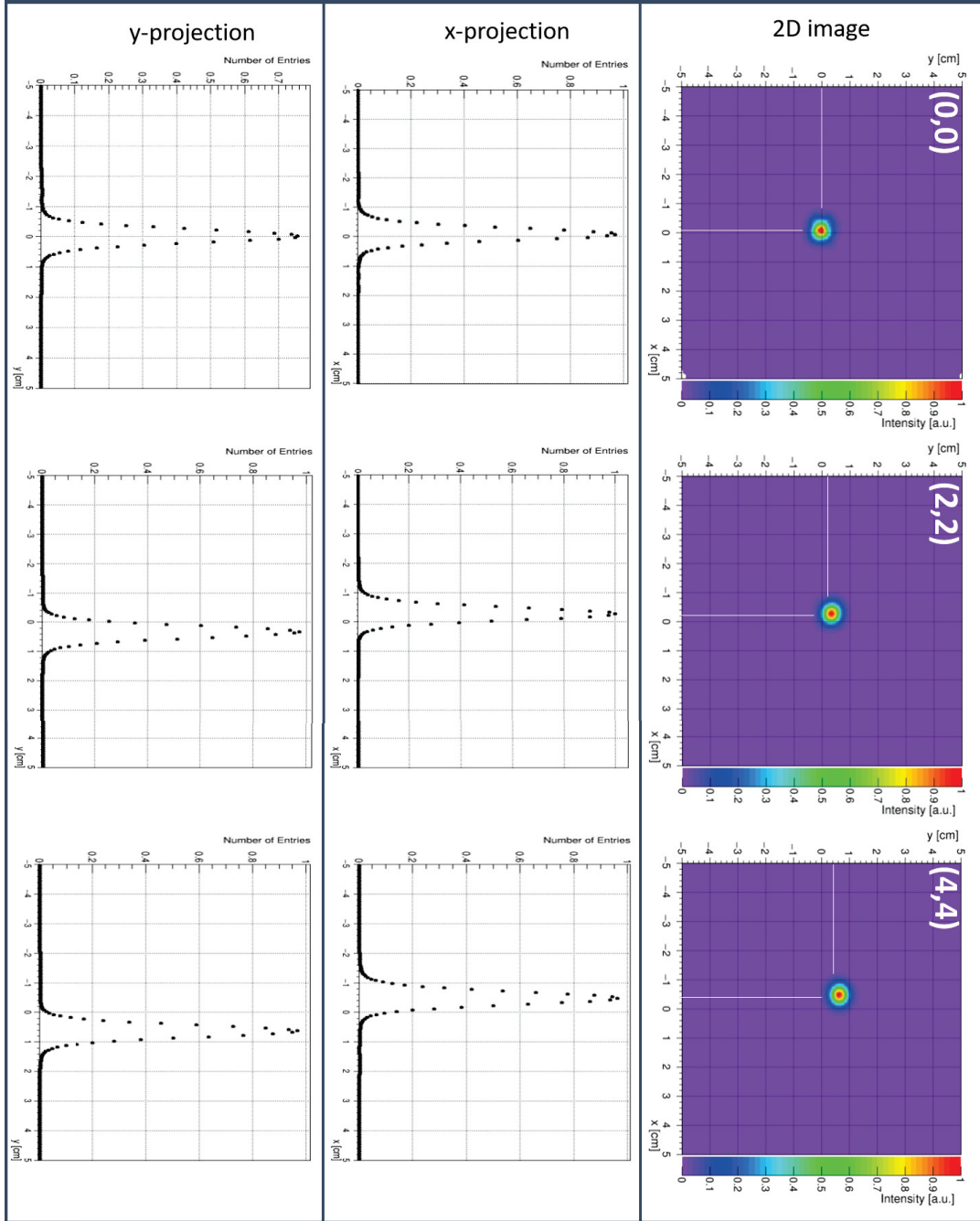


Fig. 8.36: Reconstructed images of three measurements (for 5 h) with a ^{22}Na point source at (0 mm, 0 mm), (-2 mm, 2 mm) and (-4 mm, 4 mm) (top row). The white lines indicate the actual source position. The projections along the x- and y-dimension are shown in the middle and bottom rows, respectively.

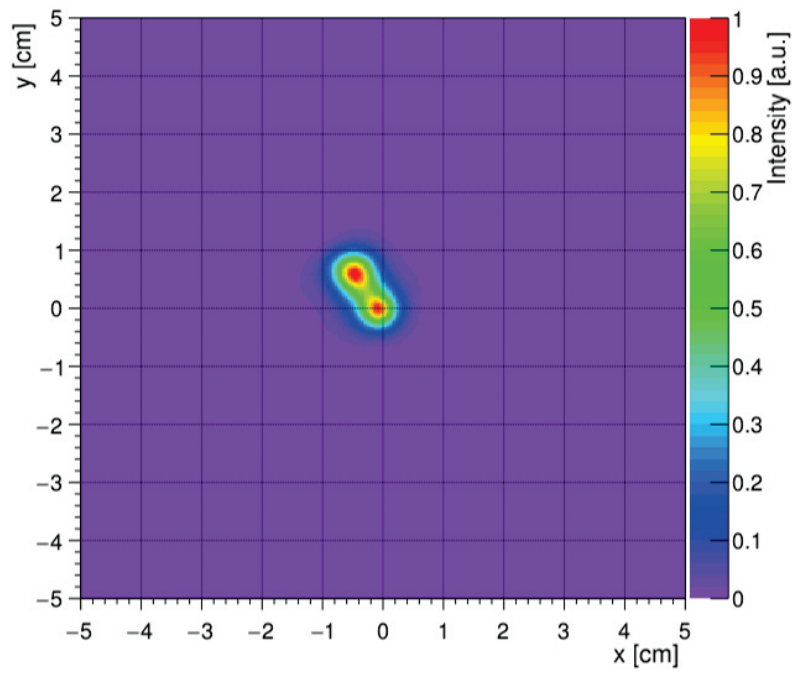


Fig. 8.37: Reconstructed image obtained from superimposed data of two separate measurements with the source placed at (0 mm, 0 mm) and (-4 mm, 4 mm). The image was obtained after 14 iterations of the ML-EM reconstruction algorithm.

Part IV.

**Summary, Future Perspectives and
Appendix**

Summary and Conclusions

The overarching rationale of this thesis work is the need for direct *in-vivo* range monitoring in ion beam therapy, to treat tumours more accurately with less damage caused to healthy tissue. Among various related approaches pursued at the LMU Chair for Medical Physics, this work is dedicated to the detection of beam induced secondary emissions (prompt- γ rays) by means of a Compton camera.

This thesis work was conducted in the framework of a joint research project between an LMU group and the KETEK GmbH. The project was funded by the Bayerische Forschungstiftung (BFS) under the name "MultiSIP: Development of a multi-channel readout for SiPM arrays" with the goal to introduce a SiPM readout with dedicated signal processing electronics to the LMU Compton camera prototype as alternative to the conventional MA-PMT readout. Hence, for all detector characterizations the influence of the SiPM properties (microcell size, PDE, etc.) was the core interest of the studies, together with a comparative study between KETEK and HAMAMATSU SiPM arrays. Furthermore, a scintillator-based alternative component for the Compton camera scatterer previously comprised of double-sided Si-strip detectors, was evaluated within the project.

The camera component evaluation was performed with regard those characteristics that directly translate into the Compton camera's imaging qualities, which is the energy and spatial resolution. In a clinical environment also the time resolution can be an important feature in order to enable discriminating the prompt photons from neutron (as well as other charged particle) background.

The scatterer Between 2017 and 2018, the general applicability of a GAGG based scatterer (with a SiPM readout) in combination with a monolithic $\text{LaBr}_3\text{:Ce}$ absorber (and MA-PMT readout) was demonstrated by a joint experimental campaign between the medical imaging group (Taiga Yamaya Lab) of the National Institutes for Quantum Science and Technology (QST) in Chiba, Japan and our group [Liprandi 2018]. While at that time the GAGG scatterer were the contributed by our Japanese collaborators, within the framework of this thesis, this technology was introduced and investigated in our group.

These crystal arrays consist of 16×16 individual crystals ($1.45 \times 1.45 \times 6 \text{ mm}^3$) optically decoupled by $150 \mu\text{m}$ of BaSO_4 . All SiPM arrays used to read out the scatterer

component provide 8×8 SiPM channels and an active channel area of 3×3 mm². As SiPM arrays, PA33**15**WB-0808¹, PA33**25**WB-0808, and PA33**50**WB-0808² arrays of KETEK's blue sensitive SiPM series (WB) and the PA33**35**WL-0808 of KETEK'S low noise (WL) were used. The performance was compared to that of a HAMAMATSU 305**0**HS-08 of the S14161-series.

Independent of the used SiPM type, all 256 individual crystals of the GAGG array could be clearly identified in all acquired flood maps. Hence, the achievable spatial resolution equals the crystal-crystal pitch of 1.6 mm.

The best energy resolution among all investigated SiPM arrays was achieved with the KETEK PA3335WL-0808 array of the (only recently introduced) low noise series with 9.5 % at 662 keV and an overvoltage of 5.0 V. Among the KETEK SiPM arrays of the WB-series, the one with 25 μm microcell size provided the best values (10.0% at 662 keV). 10.8 % and 10.5 % were measured with 15 μm and 50 μm microcell SiPM arrays, respectively, as average values from all 256 individual crystals. Despite the increase of the SiPMs PDE with increasing microcell sizes, for the bright GAGG crystals SiPM saturation appears to become the limiting factor which causes the energy resolution to deteriorate when using very large microcells (50 μm). The results obtained from a comparison measurement using a HAMAMATSU SiPM array with 50 μm microcell size fit into that trend. 10.4 % were measured at 662 keV.

It could be concluded that all investigated detector configurations are suitable as a Compton camera scatterer detector. The ideal photosensor would be the KETEK PA3335WL-0808 due to its superior energy resolution compared to all other investigated SiPM arrays.

The monolithic absorber As absorber detector monolithic LaBr₃:Ce and CeBr₃ crystal blocks were investigated. The front surface measures 51×51 mm² with a thickness of 30 mm, which was chosen to provide sufficient detection efficiency in the multi-MeV energy region of prompt- γ rays. For this detector type four SiPM types were investigated. As photon collection stage KETEK PA3325WB-0808, PA3350WB-0808, PA3347WL-0808 and HAMAMATSU S14161-3050HS-08 SiPM arrays were used. In each case four tiled SiPM arrays were used to cover the full surface of the monolithic crystals.

The energy resolution was determined using two different approaches to obtain the full energy deposit in the scintillator. The PETsys TOFPET v2c ASIC allows to use time-stamping to add the individually detected SiPM charges software-wise, while a hybrid-ganging method was implemented to directly generate a hardware-wise summed signal. The active channel area of the SiPM array channels were enlarged by a parallel ganging adapter board that combines submatrices of 2×2 SiPM pixel.

Two general observations were made: (i) the energy resolution of the LaBr₃:Ce was (as expected) by about 1 to 2 % superior to the CeBr₃ at all measured energies and (ii) the hybrid-ganging method provides about 1 % superior energy resolution than what was obtained using the TOFPET v2c ASIC. The overall best energy resolution at 662 keV

¹The microcell size is printed in bold letters

²Non-commercial prototype that was built within this thesis project as array from individual modules

was 3.5 % using the KETEK PA6647WL-0808 and the hybrid-ganging method. Using the TOFPET v2c ASIC, 4.1 % at 662 keV were achieved using the 47 μm and 50 μm microcell size arrays of KETEK. The HAMAMATSU readout provided 4.8 % and 3.6 % using the PETsys TOFPET v2c ASIC and the hybrid-ganging readout board, respectively.

During online ion beam tests, energy resolution values of down to 1.8 % at 6.13 MeV were achieved using the PA3350WB-0808 (and ASIC-based signal processing). In comparison to characterization measurements using a MA-PMT readout as used in previous works, the SiPM arrays provide a comparable performance. The time resolution was determined using a MA-PMT (with direct access to the full energy deposit in the crystal via a sum dynode output) and the TOFPET v2c ASIC. In case of the MA-PMT readout, the time resolution of both crystal compounds was determined to be well below 300 ps (250 ps (LaBr₃:Ce) and 281 ps (CeBr₃)). A detector arrangement consisting of a LaBr₃:Ce scintillator coupled to HAMAMATSU S14161-3050HS-08 SiPM arrays and read out the PETsys TOFPET v2c ASIC provided a considerably reduced time resolution of 1279 ps, which is behind expectation and requires further investigation in order to achieve a sub-ns timing as described to discriminate prompt- γ signals from neutron background [Biegun 2012]³.

The spatial resolution of the two monolithic scintillators was investigated by M. Kawula [Kawula 2021] (with contributions by the author in form of providing the measurement data) and is not part of this work. It could be shown that the interaction position of γ rays within the scintillators can be determined with a resolution of ≈ 1 mm (in a MA-PMT readout)⁴.

The findings obtained within this thesis, clearly demonstrate the general feasibility to build a Compton camera absorber using monolithic LaBr₃:Ce and CeBr₃ crystal blocks with a SiPM array readout. Ideally, SiPMs with microcell sizes of about 50 μm (or even larger) should be used.

The pixelated depth-of-interaction absorber Besides the monolithic crystal blocks, also a three-layer high resolution PET scintillation crystal block (LYSO) was under investigation. The underlying intention is to apply such a scintillator concept for Compton cameras in γ -PET configuration, where the highest energies do not exceed ≈ 1.5 MeV. For these studies SiPM arrays from both manufacturers (KETEK and HAMAMATSU) with 50 μm microcells were investigated and compared, all biased according to the recommendations given by the manufacturer [Ketek 2018, Hamamatsu 2020]. For both photosensors flood maps with clearly resolved and distinguishable individual crystals could be acquired, proving a spatial resolution of the crystal pitch of 1 mm in the

³The exact requirement is defined by the specific distance from the Compton camera to the ion beam's isocenter and the neutron energy.

⁴Measurements using a SiPM readout were conducted and point towards a comparable spatial resolution. However, these data need further investigations.

x-y plane and a depth-of-interaction (DOI) resolution of 6.6 mm (corresponding to the crystal layer thickness).

The overall relative energy resolution measured with the KETEK PA3350WB-0808 at 511 keV was 19.1 % and 21.2 % for the HAMAMATSU S14161-3050HS-08. The average energy resolution of the three layers was found to be $16.5 (\pm 0.5_{stat} \pm 1.8_{var})$ %, $20.9 (\pm 0.9_{stat} \pm 3.1_{var})$ % and $32.7 (\pm 10.6_{stat} \pm 10.4_{var})$ % (KETEK) and $19.3 (\pm 1.2_{stat} \pm 2.3_{var})$ %, $21.2 (\pm 1.6_{stat} \pm 2.5_{var})$ % and $26.6 (\pm 4.2_{stat} \pm 6.1_{var})$ % (HAMAMATSU) for the first, second and third layer, respectively. While for the first and second layer the relative energy resolution was independent of the crystal position (i.e. edge or central crystals), in the third layer a strong deterioration towards the edges was observed due to light losses at the contact region between SiPM and crystal.

With larger crystals (1.2 mm crystal pitch, same height) a superior energy resolution of the first, second and third layer of 13.0 ± 0.1 %, 13.1 ± 0.1 % and 15.6 ± 0.1 % could be achieved from an inclusive energy spectrum. However, it should be noticed that besides the crystal pitch, also the coupling method (optical grease vs. rubber sheet) was different.

The CRT was measured independently for each readout channel (SiPM/MPPC + ASIC) and stays below 1.1 ns for all measured 64 individual readout channels. The average CRT of individual crystals was measured to be $532 (\pm 30_{stat} \pm 81_{var})$ ps, $463 (\pm 31_{stat} \pm 77_{var})$ ps and $447 (\pm 42_{stat} \pm 69_{var})$ ps for the 1st, 2nd and 3rd layer, respectively, measured with the KETEK SiPM array and $402 (\pm 18_{stat} \pm 28_{var})$ ps, $392 (\pm 22_{stat} \pm 32_{var})$ ps and $408 (\pm 36_{stat} \pm 160_{var})$ ps when read out by the HAMAMATSU MPPC array, thus giving a slight advantage of the HAMAMATSU photosensor arrays with regard to the CRT.

Throughout the studies it was shown that the DOI LYSO detector module consisting of staggered 3-layer LYSO detector blocks with either 1 mm or 1.3 mm crystal pitch, respectively, SiPM readout and highly integrated ASIS-based signal processing provides a suitable Compton camera absorber, while but also fulfilling all requirements demanded by modern high-resolution PET scanners (as is interesting in the context of the γ -PET imaging modality). Consequently, it can be concluded that the DOI LYSO detector is an attractive alternative to monolithic absorber crystals, especially with regard to the application of the Compton camera in a γ -PET imaging modality, where the absorber can also be used as a PET detector module.

The Compton camera prototypes (using a three-layered staggered LYSO absorber)

A Compton camera prototype (with γ -PET imaging capability) was commissioned from a GAGG crystal array (read out by a KETEK PA3325WB-0808 SiPM array) as scatterer and a three-layer staggered LYSO crystal matrix (1.3 mm crystal pitch) using a HAMAMATSU S14161 3050HS-08 MPPC array as photosensor. Furthermore, the Compton camera setup was complimented by two GAGG detectors arrays perpendicular to the Compton camera's imaging plane to serve as PET assembly.

In a Compton-only imaging mode an angular resolution measure (ARM) of 15.7° and 8.2° was obtained for source-to-scatterer distances of 11 mm and 50 mm, respectively. The corresponding spatial resolution along the x- and y-dimensions was $SR_{x/y} = 3.7/3.6$ mm (for 11 mm distance) and $SR_{x/y} = 6.0/6.1$ mm (for 50 mm distance).

Using 511 keV annihilation photons (from a ^{22}Na source) the achievable spatial resolution of the PET detector arrangement was found to be 2.0 mm using a simple backprojection, and 1.0 mm using 10 iterations of an ML-EM method for image reconstruction.

The low solid angle coverage of the γ -PET system resulted in a triple-coincidence count rate (after energy selection) of only 1 - 2 count/s. Therefore, events obtained from a single measurement, but triggered in PET-only and Compton-only mode in the post processing, were combined to obtain a sufficient amount of triple-coincidence events. Using only 77 events reconstructed in γ -PET mode (via event-wise intersection of the line-of-response and the Compton cone) resulted in a full 3D imaging capability with a spatial resolution similar to the one obtained in PET-only mode (3.9 mm in y-dimension and 3.3 mm in z-dimension) when looking at the PET plane (y-z plane) and 12.9 mm along the x-dimension (i.e. dimension between the two PET detectors).

The Compton camera prototypes (using a monolithic absorber detector) A second Compton camera prototype was built using the GAGG scatterer and a monolithic $\text{LaBr}_3\text{:Ce}$ absorber detector. The photosensors were SiPM arrays of the latest KETEK low-noise series (WL) with $35\ \mu\text{m}$ SPADs for the scatterer and $47\ \mu\text{m}$ SPADs for the absorber. The front to front distance between the two respective components was chosen to be 150 mm.

The coincident relative energy resolution (as the sum of the energy deposit detected in the scatterer and the absorber) was measured to be $6.9 \pm 0.1\%$ and $4.3 \pm 0.1\%$ at energies of 511 keV and 1274 keV, respectively.

Compton images were reconstructed for incident γ -ray energies of 1274 keV using a ^{22}Na point source. Shifts of the radioactive source of 2 mm could be clearly resolved with a typical accuracy (along the x- and y-dimensions) between 400 and 800 μm . The spatial resolution, given as the FWHM of the point spread function, was found between 5.2 mm and 5.6 mm for all conducted measurements, which could be verified by the reconstruction of two point sources at a distance of 5.66 mm (4 mm distance along the x- and y-dimension between both sources).

The efficiency at a γ -ray energy of 1274 keV was measured to be 5.2×10^{-6} for an imaging plane at a distance of 50 mm in front of the scatterer detector.

Online tests at the GSI Helmholtz Centre for Heavy Ion Research, Darmstadt Both of the (offline) individually characterized Compton cameras were used in measurement campaigns at the GSI Helmholtz Centre for Heavy Ion Research in Darmstadt using carbon and oxygen radioactive ion beams. For the Compton camera based on the mono-

lithic absorber, the distance between the scatterer and the absorber was reduced to 78 mm in order to increase the camera's efficiency. Using a ^{10}C beam of rather low intensity (1.1×10^6 particles per spill) detector hits originating from the deexcitation of ^{12}C could be identified in the energy spectra of the absorber detectors. For all further measurements using carbon and oxygen ion beams, higher beam intensities were used. The resulting increased secondary particle emission (neutrons, protons, fragments) decreased the signal-to-background ratio to levels which did not allow for resolving prompt- γ line structures in the resulting spectra.

The signal-to-noise ratio was improved using Compton coincidence spectra for those cameras positioned upstream of the ion beam. Here, however, the low efficiency for Compton scattering hardly allowed to identify peak-like structures. For the cameras placed downstream of the beam, also the coincidence spectra were dominated by background. In general, the limited efficiency of the γ -PET prototype setup did not allow to reliably image the ion beam in Compton- or PET-mode.

In both measurement campaigns, the ion beam's spill structure (2 s beam on, 3 s beam off (February 2021) and 2.5 s beam-on and 5.5 s beam-off (June 2021)) could be verified using the timing information obtained by the scatterer detector.

Future Perspectives

This thesis work was dedicated to the development of a fully scintillator-based Compton camera with SiPM readout for ion beam range monitoring, commissioned at the LMU Chair for Medical Physics.

The component characterizations of the individual Compton camera components was completed within this thesis work. However, it is planned to look as well into the performance of a potential alternative scatterer crystal. Two options for such a scatterer are currently discussed: i) a high resolution GAGG (HR-GAGG) scatterer which promises 2 % - 4 % better energy resolution according to the manufacturers [C&A 2020a, C&A 2021, Epic-Crystal 2021b], with smaller crystal pitch than the currently used scintillator array (aiming at 1 mm). ii) a pixelated CeBr₃ crystal array, which would as well provide a considerably improved time resolution.

Two Compton camera prototypes were commissioned and first tests were performed in the laboratory and at accelerator facilities. Future steps will be focused on a deeper understanding of their properties as well as a performance improvement.

For the Compton camera with monolithic scintillator crystal there an ongoing M.Sc thesis project aims at systematic studies of the spatial resolution achievable with this the Compton camera prototype together with the achievable efficiency as a function of the scatterer-to-absorber distance, the source-to-scatterer distance and at different γ -ray energies (511 keV (²²Na), 662 keV (¹³⁷Cs), 779 keV (¹⁵²Eu), 1172 keV (⁶⁰Co), 1274 keV (²²Na) and 1332 keV (⁶⁰Co)).

Furthermore, it is planned to commission the setup used for the second measurement campaign at GSI (i.e. an arrangement of four Compton cameras) and to characterize it in γ -PET mode using a ²²Na point source.

For the γ -PET prototype using the three-layer staggered DOI LYSO crystal array an upgrade to four full Compton camera arms using a DOI LYSO detector with 1 mm crystal pitch as absorber would be desirable. Such an upgrade would result in an improved geometric efficiency, such that PET coincidences may not only be detected between two scatterers (as in the first prototype used for a proof-of-principle study), but also scatterer-absorber and absorber-absorber coincidences could be used as valid events. Especially the absorber-absorber coincidences used for the reconstruction of the LORs are expected to provide a significant improvement in terms of spatial resolution,

which was recently demonstrated in a study by Kang *et al.*, where a 0.8 mm pattern in a phantom could be resolved using a similar crystal geometry as intended in our case [Kang 2021a].

For future online measurement campaigns at GSI and for the final BARB γ -PET prototype two upgrades will be required: i) the geometric efficiency of the prototype needs to be improved, i.e. a larger solid angle needs to be covered by Compton cameras. Furthermore, simulation studies are currently going on in order to find the ideal components to be used to not only provide a high geometric efficiency, but also a good spatial resolution. Alternatives to the currently used monolithic detector blocks could also be multi-layered crystal arrays with DOI capability (such as used during the February measurement campaign), but using more than three layers, in order to also provide a higher stopping power for multi-MeV γ rays. ii) The background caused by neutrons and charged particles needs to be significantly reduced for Compton cameras placed under forward angles with respect to the beam direction. One way to go could be to use a fast plastic scintillator directly in the beam path, so that a timing and trigger signal could be provided on a single-ion base¹. In combination with an improved time resolution of the Compton cameras the prompt γ rays could be discriminated from the background by means of time-of-flight measurements. For the currently used 10 cm distance from the beam's isocenter to the scatterer detector, the required time resolution depends on the actual energy of the secondary particles, but would have to be at least in the region of only a few hundreds of ps, which is in reach of present technology.

¹This would, however, have the drawback that the beam profile would be widened due to the scattering in the fast plastic scintillator that is required to obtain a signal within these detectors.

Appendix

Contents

11.1. 6 mm ² active area SiPMs	204
11.2. Comparison of GAGG arrays of two batches	205
11.3. List of publications, conference contributions and submitted manuscripts	214

This chapter contains additional material to this thesis work. Sections 11.1 and 11.2 present further detector characterization studies that will provide further insights in and understanding of the performance of the GAGG scatterer detector. Both sections, however, were not essential to achieve the aim of this thesis, which was the commissioning of a Compton camera prototypes and are therefore, presented in the appendix. A list of publications and conference contributions is finally given.

11.1. 6 mm² active area SiPMs

For the intended application as a Compton camera scatterer component, an active detector front face area of $\approx 25 \times 25$ mm² provides a sufficiently high geometrical efficiency. However, when only using one Compton camera the geometrical efficiency can be increased by assembling larger scatterer modules from a combination of four GAGG arrays as used so far. In order to keep electronics costs reasonably low and to avoid occupying ASIC modules that might be required to also read out a larger sized absorber detector, the potential to read out four combined GAGG crystal arrays using a larger SiPM array with 6 mm² active channel area was investigated. This allows to accommodate four GAGGs crystal arrays, while still retaining only 64 readout channels.

Four KETEK PA3347WL-0808 arrays were combined to form a PA6647WL-0808 module as described in Sec. 6.2. The four GAGG crystal arrays were optically coupled to the SiPM array using optical grease.

A measurement was run for 300 s using a flood irradiation with a ¹³⁷Cs calibration point source. The acquisition thresholds were set exactly as in the measurements performed with the PA3350WB-0808 (see Tab. 6.1). The TIA gain, however, had to be reduced to 1.0, due to the higher initial gain of the KETEK PA3347WL-0808 compared to the PA3350WB-0808. The OV applied to the SiPM array was 5.0 V. An exact quantification of the energy cut, which selects only fully absorbed γ ray to be considered for plotting the flood map, cannot be given, since the inclusive energy spectrum contains 1024 ($4 \times (16 \times 16)$) individual energy spectra. Without applying a calibration to all of these individual crystals, the inclusive spectrum only shows a superposition of their individual spectra with several peak-like structures (see Fig. 11.2), while the 662 keV photopeak is smeared out by the jitter between the individual contributions. Fig. 11.1 shows the obtained flood map after applying an energy cut as indicated in Fig. 11.2.

The flood map shows a 2×2 structure (quadrants) that arises from the four individual GAGG arrays coupled to the SiPM array (white rectangles). Furthermore, another sub-structure of 4×4 crystal response spots can be seen in each of the four quadrants. As also observed with the readout configurations using SiPM arrays with 3×3 mm² active area, this structure is caused by the SiPM array's structure itself (channel size) and the amount of crystals being located directly above one SiPM channel.

Despite these minor distortions, 968 of 1024 crystals can be identified. The missing 56 crystals in the flood map are part of the crystal-array edges. These missing crystals are a consequence of the applied energy window and the relatively high light loss on the edges, resulting in most of the detected events to be discarded by the energy cut on the inclusive spectrum.

As also mentioned in the previous section, the distortions as well as the 2×2 clustering, representing the individual 16×16 GAGG crystal arrays, can be corrected in the post-processing of the Compton camera data. Consequently, it is concluded that this configuration is a viable alternative to the initial scatterer configuration, if low photon rates require a larger solid angle coverage of the camera area.

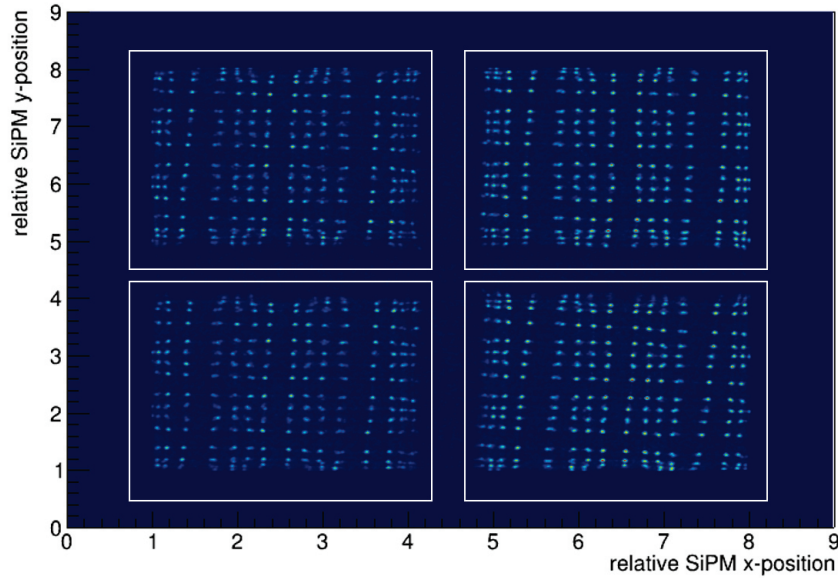


Fig. 11.1: Flood map of four GAGG scatterer array coupled to one KETEK PA6647WL-0808 module. The individual crystal arrays are marked by the four white rectangles.

11.2. Comparison of GAGG arrays of two batches

For a four arm γ -PET configuration a total of four GAGG scatter detectors is needed. Two of the available and investigated GAGG scintillation arrays were bought in 2019 (referred to as crystal array #1 and #2), while two more were bought in 2020 (referred to as crystal array #3 and #4). The performance of these arrays of the two orders were compared with each other and a considerably different behaviour in terms of their crystal response could be observed. From the measurements conducted and presented in the following section it could be concluded that the light yield of the older arrays shows a strong crystal-to-crystal inhomogeneity over the entire crystal array, while it appears to be significantly more uniform in the newer arrays.

While the crystal-dependent variation of the light yield in crystal array #1 and #2 is directly visible in the integral energy spectra's quality, it affects the flood map indirectly by the applied energy windows, where only photopeak events are selected.

Integral energy spectra In general, a radiation source's photopeak appears broadened in the uncalibrated integral energy spectrum of a pixelated scintillator, due to non-uniformities (e.g. gain, light yield) of each individual crystal's/ SiPM channel's contribution. These non-uniformities predominantly originate from three different sources. There might be gain non-uniformities arising from a) the photosensor and b) the electronics, respectively, and/or c) a variation in the light yield of the individual crystals

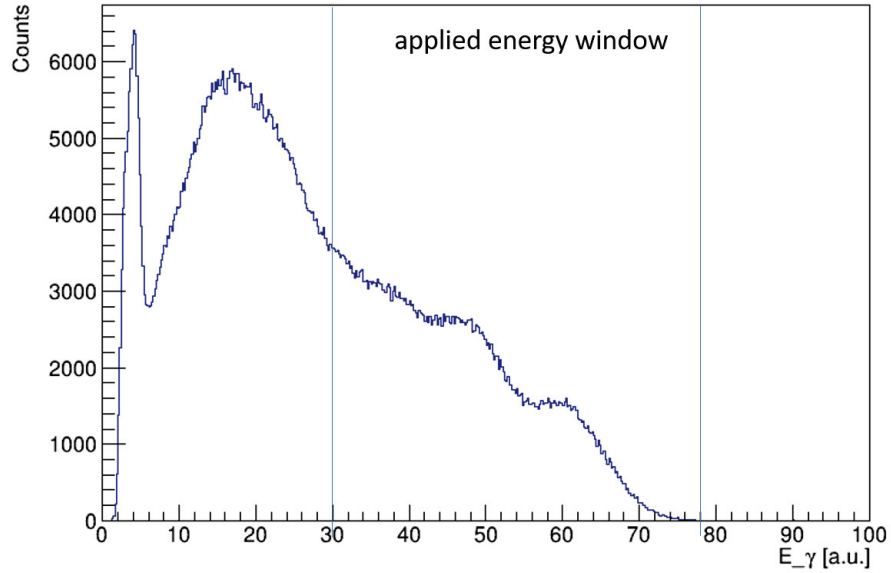


Fig. 11.2: Energy spectrum of ^{137}Cs acquired during a 300 s flood irradiation, using four combined GAGG scatterers mounted on one KETEK PA6647WL-0808 SiPM array. The energy window that was applied to generate the flood map is indicated by the two vertical lines.

(e.g. caused by a non-uniform doping profile or surface polishing).

Fig. 11.3a (Fig. 11.3b) shows the inclusive energy spectra (without linearity and saturation corrections) of a 200 kBq ^{22}Na calibration source measured with a crystal array of the old batch (crystal #2(black)) and the new batch (crystal #4(blue))coupled to a PA3325WB-0808 (PA3350WB-0808) SiPM array as readout sensor.

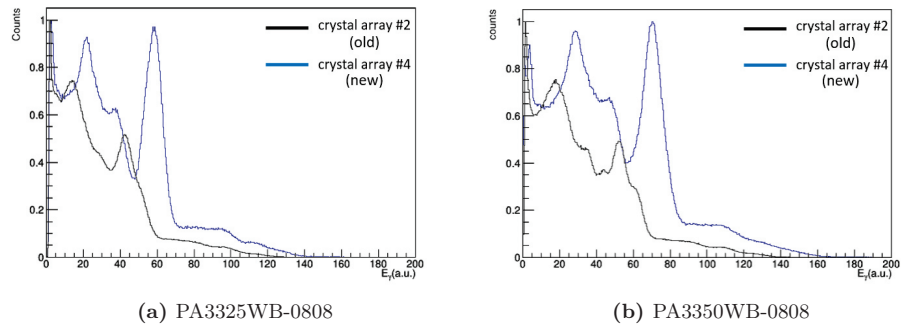


Fig. 11.3: Inclusive ^{22}Na energy spectra (without non-linearity/saturation calibration) obtained with the GAGG array #2 (red) and #4 (blue) read out by a KETEK PA3325WB-0808 (a) and PA3350WB-0808 (b) SiPM array.

For both types of SiPM arrays two observations can be made by comparing the energy spectra of crystal #2 and #4: a) crystal array #4 shows a Gaussian shaped 511 keV

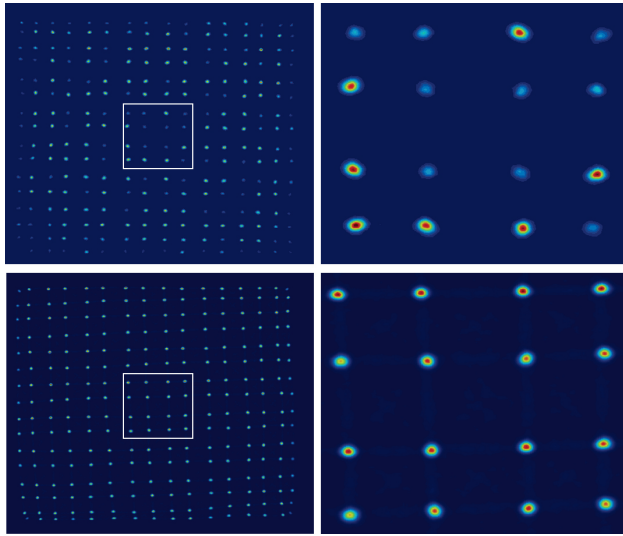


Fig. 11.4: Flood maps obtained from GAGG array #2 (top panel) and #4 (bottom panel) read out by a KETEK PA3350WB-0808 SiPM array. The full flood map with the individual 16×16 crystal responses is shown in the left column and a zoom in the central region (marked by the white square) is shown in the right column.

photo peak, whereas the photo peak measured with #2 shows a shoulder on the higher energy side and b) the 511 keV photopeak's centroid is found at higher digitizer values for crystal array #4.

Crystal resolvability and flood maps Subsequently, the flood maps of both crystals were compared. Fig. 11.4 (top left panel) shows the flood map obtained by crystal array #2 and a zoom into the central region (top right panel) read out by the PA3350WB-0808 SiPM array. The bottom panel of Fig. 11.4 shows the flood map acquired with crystal array #4 and the corresponding zoom into the central region. While crystal #4 shows a clear flood map with uniform crystal brightness (indicating the amount of events detected in the respective crystal are of the same order over the whole crystal array are), the flood map obtained by crystal #2 shows a crystal response with varying brightness. The origin of the faded spots in the flood map of crystal array #2 is found to be caused by the energy window applied for event selection. This energy selection is intended to ensure that only fully absorbed γ rays with well-defined energy deposits are shown in the flood map. However, in crystal array #2 it also rejects a large proportion of the detected events.

A comparison of the uncalibrated energy spectra of two neighboring crystals (one having a faded crystal response and one having a bright crystal response) shows that the photo peaks are not found at the same digitizer channels (Fig. 11.5 (right panel)) but differ by about 20 %. As consequence, the applied global energy window results for one crystal (crystal #1) in all photo peak events being considered for the flood map, while for crystal #2 only few events are considered and the crystal response appears faint in the flood map. Fig. 11.5 (bottom) shows a comparison of the energy spectra of two neighboring crystals of crystal array #3, where a flood map with equally bright crystal response was obtained. The 511 keV photo peaks are measured in the same

11.2. Comparison of GAGG arrays of two batches

region of QDC channels and, therefore, an approximately identical number of events is used to fill the flood map. The crystal to crystal variation of the photopeak positions in the arrays of the older batch becomes even more clear in Fig. 11.6, which shows the distribution of the 511 keV photopeak of all 256 crystals on crystal array #2 (left panel) with its variation of the photopeak clustering in three distinct regions and the more homogeneous distribution of crystal array #3 (right panel). The same observations could be made with GAGG array #1 (behaves as #2) and GAGG array #4 (behaves as #3).

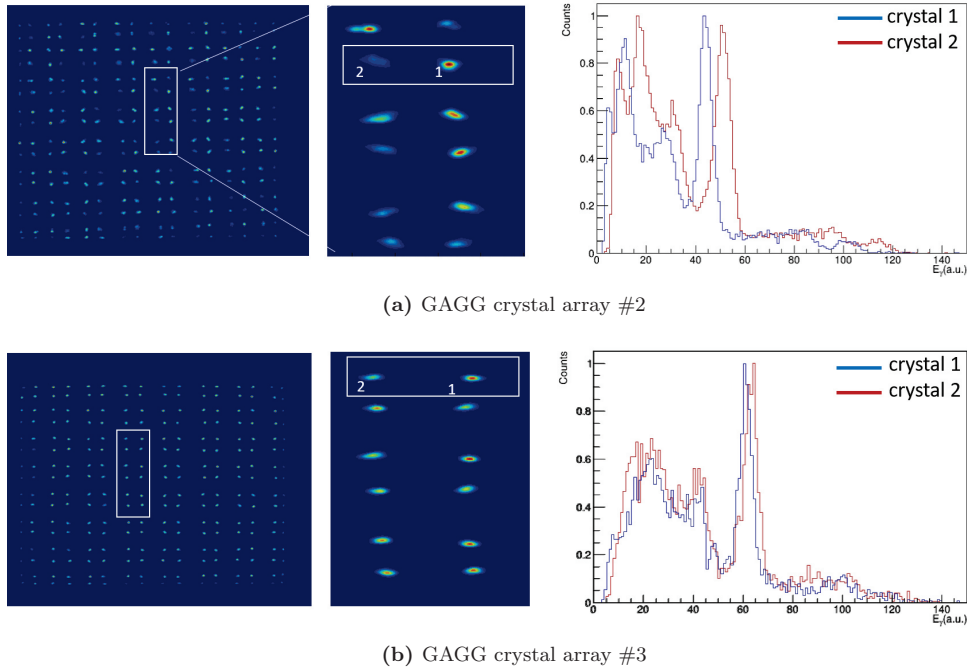


Fig. 11.5: Inclusive ^{22}Na energy spectra (without non-linearity/saturation calibration) obtained with the GAGG array #2 (red) and #4 (blue) read out by a KETEK PA3325WB-0808 (a) and PA3350WB-0808 (b) SiPM array.

A proof that the faint and bright spots are caused by the applied energy window due to a variation of individual crystal's photopeak positions is provided by using a ^{137}Cs flood irradiation (providing only a single γ line at 662 keV in the energy spectrum) and plotting two flood maps with two disjunct energy windows. The expectation that the two flood maps will show an inverse pattern of faint and bright crystal response spots can be verified. The corresponding flood maps are shown in Fig. 11.7. Comparing the two flood maps, the inverse pattern can be seen, which proves that there are basically two types of detector channels (GAGG scintillator + SiPM+ ASIC), which can be distinguished by their amount of detected and digitized charge for a given energy deposit in the scintillator.

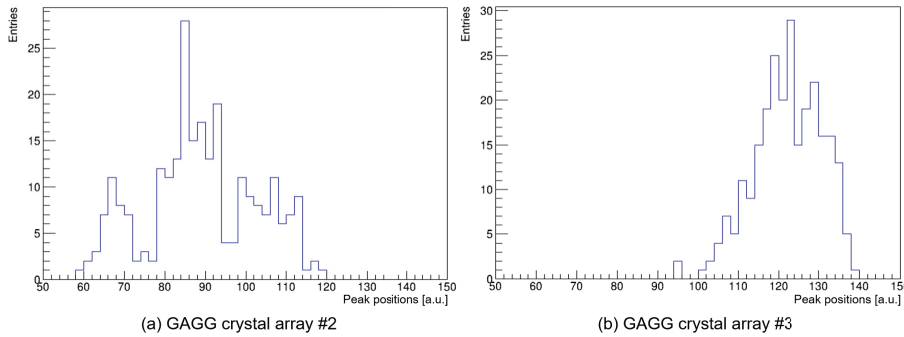


Fig. 11.6: Distribution of the 511 keV photopeak (in a.u.) of the 256 crystals of crystal array #2 (left) and #3 (right).

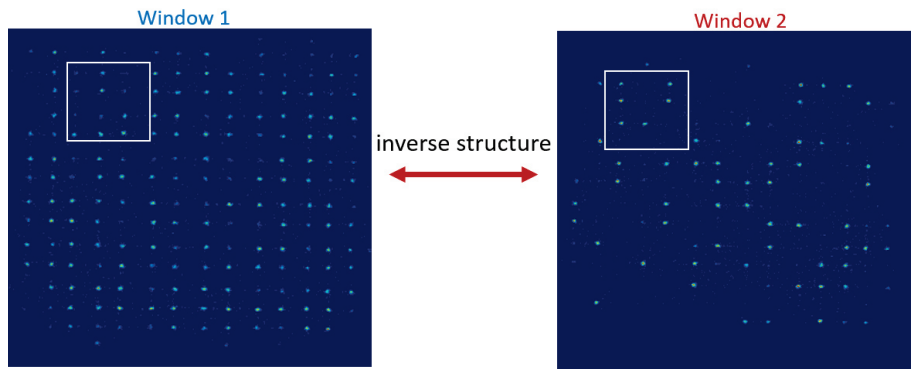


Fig. 11.7: Flood maps from a flood irradiation with a ^{137}Cs calibration source of GAGG crystal array #2 with disjunct energy windows set for event selection.

Origin of faint and bright crystal response As the origin of the faint and bright spots in the flood maps of crystal array #1 and #2 could be shown to be caused by a variation of the energy response of the individual detector channels, the reason for this inhomogeneity is further investigated in this section. Two potential causes have been investigated: a) a variation in the amount of detected scintillation photons, depending on the crystals position relative to the SiPM array and b) a variation of the light yield of the individual crystals themselves. A potential third cause - a non-uniformity of the ASIC channels - was assumed to be less likely, due to an implemented gain non-uniformity correction in the ASICs calibration procedure and the homogeneous breakdown voltage distribution of the SiPM arrays.

Two observations can be concluded: a) as can be seen in Fig. 11.8 the mean amount of firing SiPM channels for a detected 511 keV photo peak event is less for crystal #1 than for crystal #2 (as labelled in 11.5 (a)). This result is in accordance with the fact that the photopeak of crystal #1 is found at smaller QDC values, since the total detected energy

11.2. Comparison of GAGG arrays of two batches

is obtained by a summation of the individual firing SiPM channels that have been able to trigger an acquisition. One or two additional firing SiPM pixel for γ rays detected in crystal #2 naturally would result in a higher peak position. b) it can be shown that the number of firing SiPM channels for one specific crystal does not cause a significant shift of the photopeak's position. Furthermore, Fig.11.9 shows the energy distribution of detected γ events in crystal #1 and crystal #2 of GAGG array #2 for seven (a) and eight (b) firing SiPM. Especially in Fig. 11.9 (b) where predominantly the photopeaks are visible, it is obvious that their positions shift with respect to each other, which shows that even for an identical amount of firing SiPMs the photopeaks are not found at the same QDC channel values.

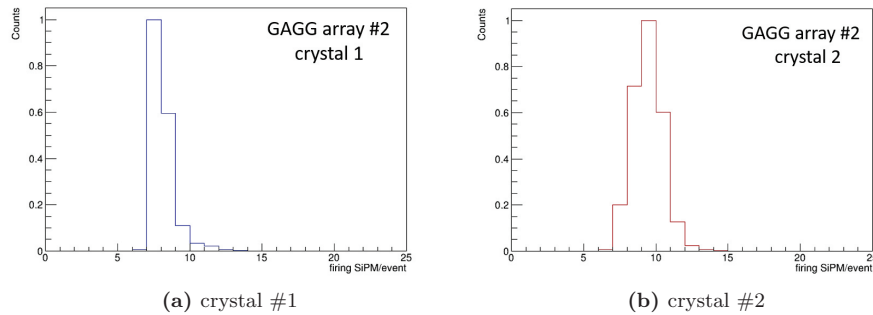


Fig. 11.8: Number of firing SiPMs triggered by a full absorption of 662 keV γ rays in two distinct crystals in GAGG crystal array #2.

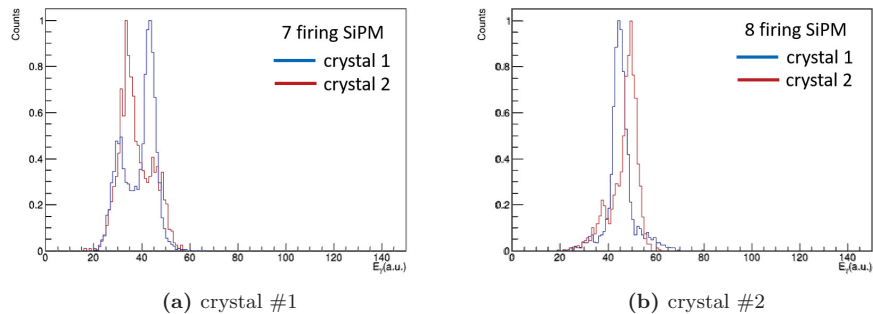


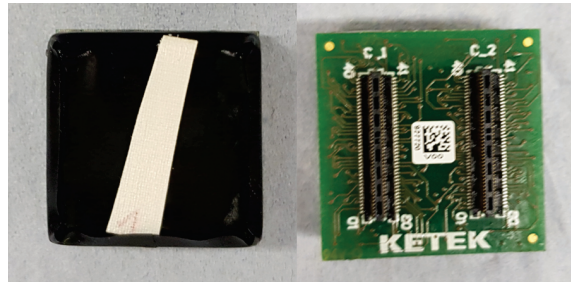
Fig. 11.9: Inclusive ^{22}Na energy spectra (without non-linearity/saturation correction) obtained with the GAGG arrays #2 (red) and #4 (blue) read out by a KETEK PA3325WB-0808 (a) and PA3350WB-0808 (b) SiPM array.

These two observations prove that the variation of the photopeak positions is related either to the gain of the SiPM/electronics or to the light yield of the crystal itself. The undefined distribution of faint spots in the flood map is a hint that the observations are not caused by a SiPM related feature, but rather are caused by the scintillation crystals themselves. This conclusion is also supported by the fact that faint and bright crystal responses are only observed in the two GAGG arrays of the first ordered batch and are visible independently of the used SiPM array type. Therefore, the results presented in

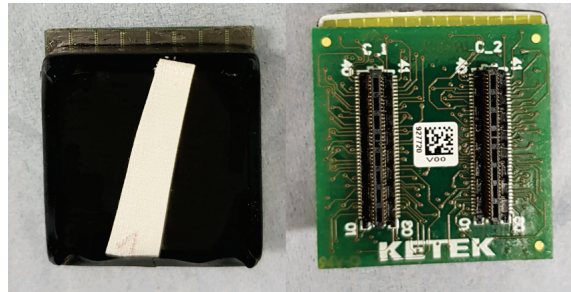
the following are dedicated to correlate the origin of faint and bright crystal response spots to the individual crystals in the GAGG array.

In order to do so, two measurements were conducted in which a flood map of GAGG array #2 was acquired with a KETEK PA3350WB-0808 SiPM array. A first measurement run was performed using a regular coupling of the SiPM array to the GAGG array, i.e. the GAGG array was placed symmetrically and centered onto the SiPM array (see Fig. 11.10 (top)). For a second measurement run the GAGG array was shifted by one crystal row with respect to the SiPM array (Fig. 11.10 (bottom)). The resulting flood maps are shown in Fig. 11.11. The left panel shows the flood map acquired with the aligned GAGG array, where all 16 crystal rows are visible (red labels). In the right panel (shifted GAGG array) only 15 crystal rows are visible, because crystal array row no. 16 is not covered by the SiPM array anymore. The red numbering in both panels indicate the absolute number of the crystal row, while the black numbers indicate the labelling of the rows for a centrally aligned array (such as the left panel shows). A comparison of both flood maps shows that the pattern of faint and bright crystal response spots shifts by one row as the crystal array shifts by the same distance. The red rectangles indicate GAGG crystal rows no. 10 and no. 11. A comparison of the individual patterns marked by these rectangles shows an identical pattern of faint and bright spots, which is shifted by one row with respect to the SiPM array. This comparison proves the origin of the pattern to be caused by a feature related to the individual crystals of the GAGG scintillation arrays and the light yield of its constituting crystals. Finally, Fig. 11.12 shows the inclusive energy spectra (left) of GAGG crystal array #1 (a) and #2 (b) from a ^{22}Na flood irradiation read out by a KETEK PA3350WB-0808 SiPM array. The right column shows the corresponding flood maps. A pattern of faint and bright spots could be observed with both crystals. The pattern, however, is not identical, which also shows that it must be caused by the GAGG arrays themselves and not by the readout (SiPM/ASIC).

11.2. Comparison of GAGG arrays of two batches



(a) crystal array #1 centrally aligned to the SiPM array



(b) crystal array #1 shifted by one crystal row compared to the SiPM array

Fig. 11.10: Top and bottom view of the GAGG scintillation array aligned centrally (a) and shifted by one crystal row with respect to the SiPM array (b).

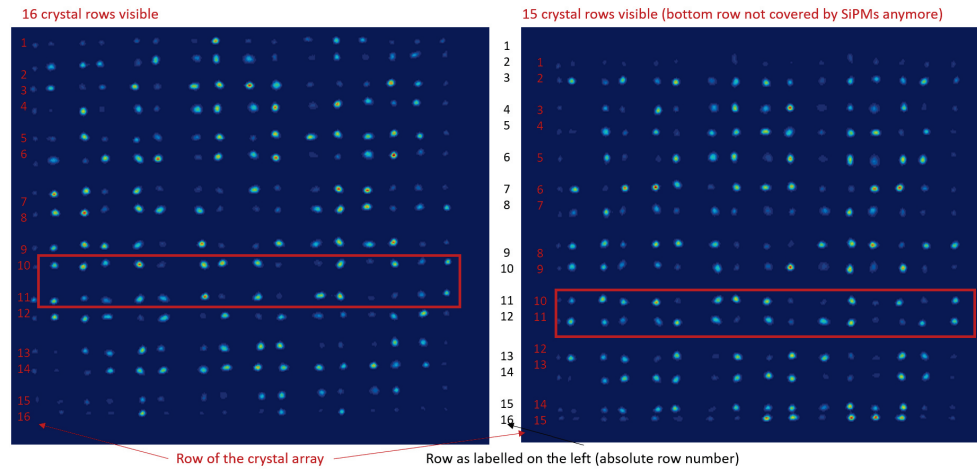
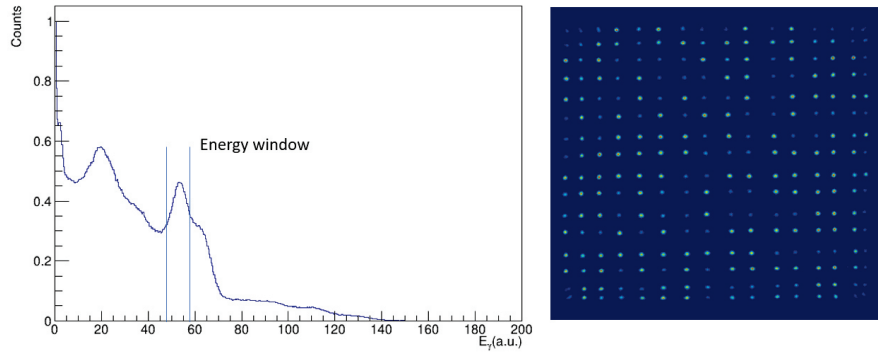
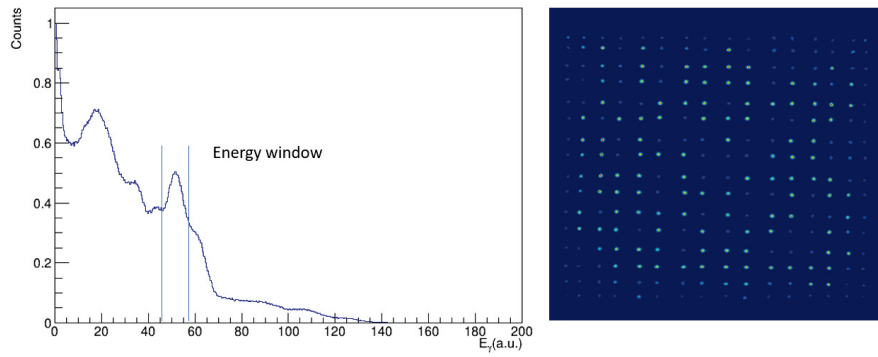


Fig. 11.11: Flood maps acquired with a centrally aligned GAGG scintillator array (left) and the GAGG array shifted by one row (right). The red rectangle marks crystal rows 10 and 11 counted from the top row.



(a) Inclusive energy spectrum (left) and flood map (right) of GAGG crystal array #1



(b) Inclusive energy spectrum (left) and flood map (right) of GAGG crystal array #2

Fig. 11.12: Inclusive energy spectra of GAGG crystal array #1 (a, panel, left) and #2 (b, left) with indicated energy window set to draw the corresponding flood maps shown in the right panel.

11.3. List of publications, conference contributions and submitted manuscripts

Papers:

1. **T. Binder** *et al.*, Performance evaluation of a staggered 3-layer DOI PET detector using a 1 mm LYSO pitch with PETsys TOFPET2 ASIC: Comparison of HAMAMATSU and KETEK SiPMs, *Phys. Med. Biol* 66, 125016, 2021.
2. **T. Binder** *et al.*, The performance of the new KETEK low-noise SiPM array series: Characterization in a Compton camera study, submitted to *IEEE Transactions on Nuclear Science*, October 2021, **currently under review**.
3. M. Kawula, **T. Binder**, S. Liprandi, R. Viegas, K. Parodi and P. G. Thirolf, Submillimeter precise photon interaction position determination in largemonolithic scintillators via convolutional neural network algorithms, *Phys. Med. Biol.* 66, 135017, 2021.
4. D. Boscolo, D. Kostyleva, M. Safari, V. Anagnostatou, J. Äystö, S. Bagchi, **T. Binder**, G. Dedes, P. Dendooven, T. Dickel, V. Drozd, B. Franczack, H. Geissel, C. Gianoli, C. Graeff, T. Grahn, F. Greiner, E. Haettner, R. Haghani, H. Harakeh, F. Horst, C. Hornung, J.-P. Hucka, N. Kalantar-Nayestanaki, E. Kazantseva, B. Kindler, R. Knöbel, N. Kuzminchuk-Feuerstein, B. Lommel, I. Mukha, C. Nociforo, S. Ishikawa, G. Lovatti, M. Nitta, I. Ozoemelum, S. Pietri, W. Plaß, A. Prochazka, S. Purushothaman, C.-A. Reidel, H. Roesch, F. Schirru, C. Schuy, O. Sokol, T. Steinsberger, Y. Tanaka, I. Tanihata, P.G. Thirolf, W. Tinganelli, B. Voss, U. Weber, H. Weick, J. Winfield, M. Winkler, J. Zhao, C. Scheidenberger, K. Parodi, M. Durante, the Super-FRS Experiment Collaboration, *Radioactive Beams for Image-Guided Particle Therapy: The BARB Experiment at GSI*, *Frontiers in Oncology* 11, 737050, 2021
DOI=10.3389/fonc.2021.737050
5. H. Bäcker, R. Bayerlein, **T. Binder**, S. Denker, I. Fleck and T. E. Peterson, "Gamma-Ray Imaging Using Coincident Detection of Cherenkov Photons for Medical Applications," in *IEEE Transactions on Radiation and Plasma Medical Sciences* (online), 2021,
DOI: 10.1109/TRPMS.2021.3101481

Oral Presentations:**DPG Frühjahrstagung 2019, Regensburg, Germany**

T. Binder *et al.*: Advances in a Silicon Photomultiplier Readout of a Compton Camera, Verhandl. DPG (VI), 54, HK 31.6 (2019).

DPG Frühjahrstagung 2019, Munich, Germany

T. Binder *et al.*: Advances in a Silicon Photomultiplier Readout of a Compton Camera, Verhandl. DPG (VI), 54, ST 3.2 (2019).

Young Investigators Workshop on Photon Detection in Medical Applications 2019, Siegen, Germany

T. Binder *et al.*: Energy resolution of a Compton camera absorber detector with SiPM readout

LMU-QST Workshop (online), 11.-13.1.2020

T. Binder *et al.*: Multichannel Readout for Scintillation Crystals via SiPM

Department Seminar: Chair of Medical Physics, LMU Munich (online), 7.2.2020

T. Binder *et al.*: Pixelated scintillators with SiPM readout for Compton Imaging at energies below 1.5 MeV

DGMP-Jahrestagung (online), 9.-11.9.2020

T. Binder *et al.*: Component evaluation of a scintillator/SiPM-based Compton camera prototype for Prompt- γ Imaging and γ -PET

Department Seminar (online): Department of Physics of Molecular Imaging (PMI), RWTH Aachen, 8.12.2020

T. Binder *et al.*: The PETsys TOFPET2 ASIC used in a light-sharing detector configuration

Joint Conference of the ÖGMP, DGMP and SGSMP - Dreiländertagung der Medizinischen Physik, 2021, Online

T. Binder *et al.*: Towards a γ -PET Prototype: Commissioning and first images in Compton and PET mode

IEEE-Nuclear Science Symposium and Medical Imaging Conference (IEEE-NSS MIC), Yokohama (Japan)/Online, 2021

T. Binder *et al.*: A γ -PET Prototype: Detector Characterization, Commissioning and first Imaging

Poster Presentations:

DPG Frühjahrstagung 2018, Würzburg, Germany

T. Binder *et al.*, Towards an alternative absorber detector for the Garching Compton Camera Prototype

MediNet Meeting 2018, Belgrad, Serbia

T. Binder *et al.*, Towards an alternative Absorber detector for the Garching Compton Camera Prototype

Jahrestagung der DGMP 2018, Nürnberg, Germany

T. Binder *et al.*: Characterization of a Compton Camera Absorber Detector

Jahrestagung der DGMP 2019, Stuttgart, Germany

T. Binder *et al.*: Comparison of monolithic Compton camera absorber scintillators with PMT and SiPM readout

IEEE Nuclear Science Symposium and Medical Imaging Conference (IEEE-NSS MIC) 2019, Manchester, UK

T. Binder *et al.*: Characterization of a second generation monolithic Compton camera absorber

IEEE-Nuclear Science Symposium and Medical Imaging Conference (IEEE-NSS MIC), Yokohama (Japan)/Online, 2021

T. Binder *et al.*: The performance of the new KETEK low-noise SiPM array series: Characterization in a Compton camera component study

Bibliography

- [Aldawood 2016] S. Aldawood, Commissioning of a Compton camera for medical imaging, Doctoral Dissertation, LMU Munich, 2016.
- [Albertini 2011] F. Albertini *et al.*, Is it necessary to plan with safety margins for actively scanned proton therapy?, *Phys. Med. Biol.* 56 4399, 2011.
- [Amptek 2021] Amptek Inc. Multichannel Analyzer 'Pocket MCA' - MCA8000A data sheet, downloaded from [https : //wwwusers.ts.infn.it/ rui/univ/Acquisizione_Dati /Manuals/AMPTEK%20MCA8000A.pdf](https://wwwusers.ts.infn.it/rui/univ/Acquisizione_Dati/Manuals/AMPTEK%20MCA8000A.pdf), September 2021.
- [Anderson 1969] H.H. Andersen *et al.*, An experimental investigation of charge-dependent deviations from the Bethe stopping power formula, *Nuclear Physics A* 125 1, 171-175, 1969.
[https : //doi.org/10.1016/0375 - 9474\(69\)90836 - 7](https://doi.org/10.1016/0375-9474(69)90836-7).
- [Aubry 2013] N. Aubry *et al.*, Endotofpet-us: a novel multimodal tool for endoscopy and positron emission tomography, *J. Instrum.* 8(04): C04002, 2013.
- [Auger 1925] P. Auger , Sur l'effet photoélectrique composé, *J. Phys. Radium* 5, 6 (6), 205-208, 1925.
[10.1051/jphysrad : 0192500606020500](https://doi.org/10.1051/jphysrad:0192500606020500) - [jpa - 00205207](https://doi.org/10.1051/jphysrad:0192500606020500)
- [Lodge and Frey 2014] M.A. Lodge and E. C. Frey, *Nuclear Medicine Physics - A Handbook for Teachers and Students*, Technical Editors: D.L. Bailey, J.L. Humm, A. Todd-Pokropek and A. van Aswegen, International Atomic Energy Agency, Vienna 2014.
ISBN: 978-92-0-143810-2
- [BARB 2021] D. Boscolo, K. Parodi, M. Durante, Ch. Scheidenberger *et al.*, Radioactive Beams for Image-Guided Particle Therapy: The BARB Experiment at GSI, *Frontiers in Oncology* 11, 2021.
DOI: 10.3389/fonc.2021.737050
- [Barkas 1956] W. H. Barkas *et al.*, Mass-Ratio Method Applied to the Measurement of L-Meson Masses and the Energy Balance in Pion Decay, *Phys. Rev.* 101, 778, 1956.

- [Barkas 1963] W. H. Barkas *et al.*, Resolution of the Σ^- -Mass Anomaly, *Phys. Rev. Lett.* 11 26, 1963.
- [Baskar 2014] R. Baskar *et al.*, Biological response of cancer cells to radiation treatment, *Front. Mol. Biosci.* 2014;1:24, 2014.
DOI: 10.3389/fmolb.2014.00024
- [Bäcker 2021] H. Bäcker *et al.*, Gamma-Ray Imaging Using Coincident Detection of Cherenkov Photons for Medical Applications, *IEEE Trans. Radiat Plasma Med. Sci.*, 2021.
DOI: 10.1109/TRPMS.2021.3101481
- [Beebe-Wang 2003] J. Beebe-Wang *et al.*, Simulation of Proton Therapy Treatment Verification via PET Imaging of Induced Positron-Emitters, *IEEE Proc. Nuc. Sci. Symp. Conf. Rec.* 4., 2496 - 2500 4, 2003.
DOI: 10.1109/NSSMIC.2003.1352399
- [Bennet 1975] G.W. Bennett *et al.*, Beam Localization via ^{15}C Activation in Proton-radiation Therapy, *Nucl. Inst. and Meth.*, volume 125(3) pp. 333–338, 1975.
DOI: 10.1016/0029-554X(75)90246-3
- [Berger 1964] M. J. Berger *et al.*, Tables of Energy Losses and Ranges of Electrons and Positrons, NASASP-3012, 1969.
- [Berko and Hereford 1956] S. Kerko and F.L. Hereford, Experimental Studies of Positron Interactions in Solids and Liquids, *Reviews of Modern Physics*, 28, 299–307, 1956.
<https://doi.org/10.1103/RevModPhys.28.299>
- [Bernier 2004] J. Bernier *et al.*, Radiation oncology: a century of achievements, *Nat. Rev. Cancer.* 4, 737–747, 2004.
<https://doi-org.emedien.ub.uni-muenchen.de/10.1038/nrc1451>
- [Bethe 1930] H. Bethe, Zur Theorie des Durchgangs schneller Korpuskularstrahlen durch Materie, *Annalen der Physik* 5, 325–400, 1930.
- [Bethe 1932] H. Bethe, Bremsformel für Elektronen relativistischer Geschwindigkeit, *Z. Physik* 76, 293–299, 1932,
<https://doi.org/10.1007/BF01342532>
- [BfG 2019] Bundesamt für Strahlenschutz, Strahlung und Strahlenschutz (in german), downloaded from
https://www.bfs.de/SharedDocs/Downloads/BfS/DE/broschueren/str-u-strschutz.pdf?__blob=publicationFile&v=12 (August 2021), 2019.
- [Biegun 2012] A.K. Biegun *et al.*, Time-of-flight neutron rejection to improve prompt gamma imaging for proton range verification: a simulation study. *Phys. Med. Biol.*

- 57 6429–44, 2012.
DOI: 10.1088/0031-9155/57/20/6429
- [Binder 2017] T. Binder, Evaluation of new Components for the Absorber Detector of the Garching Compton Camera Prototype, M.Sc. Thesis, LMU Munich, Munich, 2017.
- [Binder 2019] T. Binder, Characterization of a second generation monolithic Compton camera absorber , IEEE Medical Imaging Conference Poster Contribution, Poster Number: M-13-363, Paper ID: #1993, Manchester, 2019.
- [Binder 2021] T. Binder *et al.*, Performance evaluation of a staggered 3-layer DOI PET detector using a 1 mm LYSO pitch with PETsys TOFPET2 ASIC: Comparison of HAMAMATSU and KETEK SiPMs, Phys. Med. Biol 66, 125016, 2021.
- [Bloch 1933a] F. Bloch, Zur Bremsung rasch bewegter Teilchen beim Durchgang durch Materie, Ann. Physik 408 3, 285–320, 1933.
- [Bloch 1933b] F. Bloch, Bremsvermögen von Atomen mit mehreren Elektronen, Z. Phys. 81, 363 1933.
<https://doi.org/10.1007/BF01344553>
- [Bohr 1913] N. Bohr, On the theory of the decrease of velocity of moving electrified particles on passing through matter, In: The London, Edinburgh, and Dublin Philosophical Magazine and Journal of Science. 25:145, 10-31, 1913
DOI: 10.1080/14786440108634305,
- [Boscolo 2021] D. Boscolo on behalf of the BARB collaboration, First experiments with radioactive carbon beams at GSI for the BARB project (Biomedical Applications of Radioactive ion Beam), oral presentation at PTCOG conference, 2021.
available under:
<https://www.gsi.de/work/forschung/biophysik/ercarb/presentations#c53408>
- [Bragg and Kleeman 1904] W.H. Bragg M.A. and R. Kleeman, LXXIV. On the ionization curves of radium, The London, Edinburgh, and Dublin Philosophical Magazine and Journal of Science, 8:48, 726-738, 1904
DOI: 10.1080/14786440409463246
- [Britannica 2021a] Encyclopedia Britannica, *Discovery of radiation*,
<https://www.britannica.com/science/atom/Discovery-of-radioactivity> (visited August 2021), 2021.
- [Britannica 2021b] Encyclopedia Britannica, Radiation (physics),
<https://www.britannica.com/science/radiation> (visited August 2021), 2021.
- [Britannica 2021c] Encyclopedia Britannica, Delta ray,
<https://www.britannica.com/science/delta-ray> (visited August 2021), 2021.

- [Brownell and Burham 1969] G.L. Brownell and C.A. Burnham *et al.*, New developments in positron scintigraphy and the application of cyclotron produced positron emitters. In: Proceedings of a symposium medical radio-isotope scintigraphy, Salzburg, 1 163–176, 1969.
- [Bughalo 2013] R. Bughalo *et al.*, Design and Performance of an ASIC for TOF applications, 2013 IEEE Nuclear Science Symposium and Medical Imaging Conference (2013 NSS/MIC), pp. 1-4, 2013.
DOI: 10.1109/NSSMIC.2013.6829772.
- [C&A 2020a] C&A Corporation, GAGG Product Information, Downloaded from <http://www.c-and-a.jp/products.html>, July 2020.
- [C&A 2020b] C&A Corporation, Inspection report HG18A0211 (Report No. 20200629-1), 2020.
- [C&A 2020c] C&A Corporation, Inspection report Ga1930202 (Report No. 20200629-2), 2020.
- [C&A 2021] C&A Corporation, HR-GAGG Product Information, available under: <https://www.c-and-a.jp/assets/img/products/103210514HR-GAGG.pdf> (November 2021), 2021.
- [CDC 2021] Center for Disease Control and Prevention, picture taken from: <https://www.cdc.gov/nceh/radiation/spectrum.html>, August 2021.
- [Choi and Cho 2016] W. Choi, Wo and J. Cho, Evolving Clinical Cancer Radiotherapy: Concerns Regarding Normal Tissue Protection and Quality Assurance. Journal of Korean Medical Science 31, S75, 10.3346/jkms.2016.31.S1.S75, 2016.
- [Connell and Hellman 2009] P. P. Connell and S. Hellman, Advances in Radiotherapy and Implications for the Next Century: A Historical Perspective, Cancer Res. 69, 383-392, 2009.
DOI: 10.1158/0008-5472.CAN-07-6871
- [Chynoweth and McKay 1956] A.G. Chynoweth and K.G. McKay, Photon Emission from Avalanche Breakdown in Silicon, Phys. Rev. 102 2, 369-376, 1956.
- [Cerrito 2017] L. Cerrito, Radiation and Detectors - Introduction to the Physics of Radiation and Detection Devices, Springer International Publishing AG, ISBN 978-3-319-53179-3, 2017.
- [Compton 1923] A.H. Compton, A Quantum Theory of the Scattering of X-rays by Light Elements, Phys. Rev. 21 , 483 – 502, 1923.
- [Conti and Bendriem 2019] M. Conti and B. Bendriem, The new opportunities for high time resolution clinical TOF PET, Clin. Transl. Imaging 7, 139–147, 2019.

- [Cova 1996] S. Cova *et al.*, Avalanche photodiodes and quenching circuits for single photon-detection, *Appl. Opt.* 35, 1956–1976, 1996.
- [Dauvergne 2015] D. Dauvergne *et al.*, Prompt-Gamma Monitoring in Proton- and Carbon Therapy. Combined Development of Time-of-Flight Collimated- and Compton-Cameras, *Acta Physica Polonica A* 127, 1445-1448, 2015.
DOI: 10.12693/APhysPolA.127.1445
- [DENSIMET 2021] Plansee SE, Wolfram Schwermetalle website available at:
https : //www.plansee.com/de/werkstoffe/wolfram – schwermetall.html, accessed on 07.09.2021, 2021.
- [Derenzo 1982] S.E. Derenzo *et al.*, Dynamic Positron-emission tomography in man using small bismuth germanate crystals, *Proceedings of the sixth international conference on positron annihilation*, Forth Worth, Texas April 3-7, North Holland Publishing Company, 1982.
- [Dorenbas 2002] P. Dorenbas, Light output and energy resolution of Ce^{3+} -doped scintillators, *Nucl. Instr. Meth. A* 486, 208–213, 2002.
- [DuMond 1929] J. W. Du Mond, Compton modified line structure and its relation to the electron theory of solid bodies, *Physical Review* 33, 643–658, 1929.
- [Durante and Loeffler 2010] M Durante, J. Loeffler, Charged particles in radiation oncology, *Nat. Rev. Clin. Oncol.* 7, 37–43, 2010.
https : //doi.org/10.1038/nrclinonc.2009.183
- [Durante 2017] M. Durante, R. Orecchia and J. Loeffler, Charged-particle therapy in cancer: clinical uses and future perspectives. *Nat. Rev. Clin. Oncol.* 14, 483–495, 2017.
https : //doi.org/10.1038/nrclinonc.2017.30
- [Durante and Parodi 2020] M. Durante and K. Parodi, Radioactive Beams in Particle Therapy: Past, Present, and Future, *Frontiers in Physics* 8, 326, 2020.
DOI: 10.3389/fphy.2020.00326
- [Drozdowski 2008] W. Drozdowski *et al.*, CeBr_3 Scintillator Development for Possible Use in Space Missions, in *IEEE Transactions on Nuclear Science* 55, 1391-1396, June 2008.
DOI: 10.1109/TNS.2007.908579, 2008.
- [Einstein 1905] A. Einstein, Über einen die Erzeugung und Verwandlung des Lichtes betreffenden heuristischen Gesichtspunkt, *Annalen der Physik* 322, 132–148, 1905.
- [EJ 2021] Eljen Technologies, Silicone Grease EJ-550, EJ-552, 2021.
downloaded from :*https : //eljentechnology.com/images/products/data_sheets/EJ-550_EJ – 552.pdf* (6.8.2021)

- [Enghardt 1992] W. Enghardt *et al.*, The spatial distribution of positron-emitting nuclei generated by relativistic light ion beams in organic matter, *Phys. Med. Biol.* 37, 2127, 1992.
- [Enghardt 2004a] W. Enghardt *et al.*, Charged hadron tumour therapy monitoring by means of PET, *Nucl. Instr. Meth.* 525, 284-288, 2004.
<https://doi.org/10.1016/j.nima.2004.03.128>.
- [Enghardt 2004b] W. Enghardt *et al.*, Dose quantification from in-beam positron emission tomography, *Radiotherapy & Oncology* 73(Suppl 2), 96-98, 2004.
- [Engelmann 2018] E. Engelmann, Dark Count Rate of Silicon Photomultipliers - Metrological Characterization and Suppression, Dissertation (Universität der Bundeswehr München), 2018.
- [Epic-Crystal 2021a] Epic-Crystal, LYSO(Ce) Scintillator product data sheet, available at: <https://www.epic-crystal.com/download-center/>, 2021.
- [Epic-Crystal 2021b] , Epic-Crystal, GAGG-ce-scintillator product description, <https://www.epic-crystal.com/oxide-scintillators/gagg-ce-scintillator.html>, visited November 2021, 2021
- [Evans 1955] R.D. Evans, The Atomic Nucleus, Tata McGraw-Hill Publishing Company LTD, 1955.
- [Everett 1977] D. Everett *et al.*, Gamma-radiation imaging system based on the Compton effect, *Proc. Inst. Electr. Eng.* 124, 995-1000, 1977.
DOI: 10.1049/piee.1977.0203
- [Fano 1963] U. Fano, Penetration of protons, alpha particles, and mesons, *Annual Reviews Nuclear Science*, vol. 13, pp. 1-67, 1963.
- [Feng 2019] Y. Feng, Modeling and regularization in tomographic reconstruction for Compton camera imaging, *Signal and Image processing*. Université de Lyon. English, 2019.
available under: <https://tel.archives-ouvertes.fr/tel-02900652/document> (November 2021).
- [Ferlay 2019] J. Ferlay *et al.*, Global Cancer Observatory: cancer tomorrow. Lyon, International Agency for Research on Cancer, 2019.
- [Ferrero 2018] V. Ferrero *et al.*, Online proton therapy monitoring: clinical test of a Silicon-photodetector-based in-beam PET, *Sci. Rep.* 8, 4100, 2018.
<https://doi.org/10.1038/s41598-018-22325-6>
- [Fontana 2017] M. Fontana *et al.*, Compton camera study for high efficiency SPECT and benchmark with Anger system, *Phys. Med. Biol.* 628, 794-812, 2017.

-
- [Fontana 2018] M. Fontana, Tests and characterization of gamma cameras for medical applications, Doctoral Dissertation, L'Universite Claude Bernard Lyon 1, 2018.
- [Fraile 2013] L.M.Fraile *et al.*, Fast timing study of a CeBr₃ crystal: Time resolution below 120 ps at ⁶⁰Co energies. Nucl. Instr. Meth. 701. 235–242, 2013.
10.1016/j.nima.2012.11.009,
- [Frauenfelder 1999] H. Frauenfelder, E.M. Henley, Teilchen und Kerne - Die Welt der subatomaren Physik, R. Oldenbourg Verlag München Wien 1991, 4th ed., 1999.
- [Gasanov 1989] G. Gasanov, V. Golovin, Z. Sadygov, N. Yusipov, Russian patent #1702831, 1989.
- [Garcia 2012] A.D. Garcia *et al.*, PET-Compton system comparative evaluation with PET system using Monte Carlo simulation, Nucleus 51, 6–13, 2012.
- [Geissel 1992] H. Geissel *et al.*, The GSI projectile fragment separator (FRS): A versatile magnetic system for relativistic heavy ions, Nucl. Instr. Meth. B 70, 286, 1992.
- [Glodo 2006] J. Glodo *et al.*, CeBr₃ for time-of-flight PET, in: Proc. 2006 IEEE Nuclear Science Symposium Conference Record 3, 1570 – 1573, 2006.
- [Golnik 2014] C. Golnik *et al.*, Range assessment in particle therapy based on prompt γ -ray timing measurements, Phys. Med. Biol. 59, 5399-422, 2015.
DOI: 10.1088/0031-9155/59/18/5399.
- [Golovin 1989] V. Golovin, Z. Sadygov, M. Tarasov, N. Yusipov, Russian patent #1644708, 1989.
- [Golovin 1998] V. Golovin, Avalanche Photodetector, Russian Agency for Patents and Trademarks, Patent No. RU2142175, 1998.
- [Golovin and Saveliev 2004] V. Golovin and V. Saveliev, Novel type of avalanche photodetector with Geiger mode operation, Nucl. Instr. Meth. 518, 560-564, 2004.
- [Grau 2020] C. Grau *et al.*, Particle therapy in Europe, Molecular Oncology. 14, 1492-1499, 2020
DOI: 0.1002/1878-0261.12677.
- [Grignon 2007] C. Grignon *et al.*, Nuclear medical imaging using β^+ - γ coincidences from ⁴⁴Sc radio-nuclide with liquid xenon as detection medium, Nucl. Instr. Meth. A 571, 142–145, 2007.
DOI: 10.1016/j.nima.2006.10.048
- [Grubbe 1933] E.H. Grubbé, Priority in the therapeutic use of X-rays, Radiol. 21, 156–162, 1933.
- [Grundacker 2019] S. Grundacker *et al.*, High-frequency SiPM readout advances measured coincidence time resolution limits in TOF-PET, Phys. Med. Biol. 64, 055012, 2019.

- [Grundacker 2020] S. Grundacker *et al.*, *Experimental time resolution limits of modern SiPMs and TOF-PET detectors exploring different scintillators and Cherenkov emission*, Phys. Med. Biol. 65 025001, 2020.
- [Grundacker and Heering 2020] S. Gundacker and A. Heering, The silicon photomultiplier: fundamentals and applications of a modern solid-state photon detector, Phys. Med. Biol. 65 17TR01, 2020.
- [Hamamatsu 2014] Hamamatsu Photonics K.K., H12700 Datasheet, 2014.
available under:
https://www.hamamatsu.com/resources/pdf/etd/H12700_H14220_TPMH1379E.pdf,
(November 2021).
- [Hamamatsu 2015] Hamamatsu Photonics K.K., H9500 Datasheet, 2015.
available under:
<https://dtsheet.com/doc/749743/hamamatsu-h9500>, (November 2021).
- [Hamamatsu 2007] Hamamatsu Photonics K.K., Photomultiplier Tubes-Basics and Applications - Third Edition (Edition 3a), 2007.
available under:
https://www.hamamatsu.com/resources/pdf/etd/PMT_handbook_v3aE.pdf,
(November 2021).
- [Hamamatsu 2020] Hamamatsu Photonics K.K., MPPC (Multi-Pixel Photon Counter), S14160/14161 series datasheet, 2020.
available under:
https://www.hamamatsu.com/resources/pdf/ssd/s14160_s14161_series_kapd1064e.pdf,
(November 2021).
- [Henderson 1989] B. Henderson, G.F. Imbush, *Optical Spectroscopy of Inorganic Solids*, Clarendon Press, Oxford, 1989.
- [Hertz 1887] H. Hertz, Über einen Einfluss des ultravioletten Lichtes auf die elektrische Entladung, *Annalen der Physik* 267, 983–1000, 1887.
- [Hoffman 1989] E.J. Hoffman *et al.*, PET system calibrations and corrections for quantitative and spatially accurate images, *IEEE Trans. Nucl. Sci.* 36, 1108–1112, 1989.
- [Holthoff 2020] G. Holthoff, *Entwicklung eines Szintillationsdetektors fuer die Protonen-Computertomographie*, B.Sc. thesis, LMU Munich, 2020.
- [Humm 2003] J.L. Humm *et al.*, From PET detectors to PET scanners, *Eur. J. Nucl. Med. Mol. Imaging* 30, 1574-97, 2003.
DOI: 10.1007/s00259-003-1266-2.
- [Ito 2010] M. Ito *et al.*, A four-Layer DOI Detector With a Relative Offset for Use in an Animal PET System, *IEEE Trans. Nuc. Sc.* 57, 976 - 981, 2010.
DOI: 10.1109/TNS.2010.2044892

-
- [ICRU 2007] International Commission on Radiation Units and Measurements: Prescribing, recording, and reporting proton beam therapy. ICRU Report no. 78. Bethesda, MA, 2007.
- [Jensen 2013] A. D. Jensen *et al.*, Proton and Carbon Ion Therapy, CRC Press (C.-M. C. Ma, T. Lomax(ed.)) and W.R. Hendee (series ed.), 2013.
ISBN: 978-1-4398-1607-3 (Hardback)
- [Kanazawa 2002] M. Kanazawa *et al.*, Application of an RI-beam for cancer therapy: In-vivo verification of the ion-beam range by means of positron imaging, Nucl. Phys. A. 701, 244–52, 2002.
doi : 10.1016/S0375 – 9474(01)01592 – 5
- [Kang 2019] H.G. Kang *et al.*, Optimization of a 3-Layer DOI PET Detector with a 1 mm LYSO Pitch for High-Resolution Small Animal PET Imaging, IEEE NSS/MIC conference, Manchester, M-13-015, 2019.
- [Kang 2019b] H.G. Kang *et al.*, Optical imaging for the characterization of radioactive carbon and oxygen ion beams. Phys. Med. Biol. 64 115009, 2019.
doi : 10.1088/1361 – 6560/ab1ccf
- [Kang 2021a] H.G. Kang *et al.*, Initial results of a mouse brain PET insert with a staggered 3-layer DOI detector. Phys. Med. Biol. 66 215015, 2021.
DOI: 10.1088/1361-6560/ac311c
- [Kang 2021b] H.G. Kang *et al.*, A staggered 3-layer DOI PET detector using BaSO₄ reflector for enhanced crystal identification and inter-crystal scattering event discrimination capability, Biomed. Phys. Eng. Express. 7, 2021.
DOI: 10.1088/2057-1976/abf6a8
- [Karger 2018] C.P. Karger, Der Strahlentherapie-Prozess. In: Schlegel W., Karger C., Jäkel O. (eds) Medizinische Physik. Springer Spektrum, Berlin, Heidelberg, 2018.
https : //doi – org.emedien.ub.uni – muenchen.de/10.1007/978 – 3 – 662 – 54801 – 1_19
- [Kraan 2015] A.C. Kraan, Range verification methods in particle therapy: underlying physics and Monte Carlo modeling, Front. Oncol. 5, 150, 2015.
- [Katagiri 2021] H. Katagiri *et al.*, Development of an omnidirectional Compton camera using CaF₂(Eu) scintillators to visualize gamma rays with energy below 250 keV for radioactive environmental monitoring in nuclear medicine facilities, Nucl. Instrum. Meth. A 996, 165133, 2021.
https : //doi.org/10.1016/j.nima.2021.165133.
- [Kawula 2021] M. Kawula *et al.*, Sub-millimeter precise photon interaction position determination in large monolithic scintillators via convolutional neural network algorithms, Phys. Med. Biol. 66, 135017, 2021.

- [Kelly 1993] J. H. Kelly *et al.*, $^{16}\text{O}(\text{p},\text{p}')$, Nucl. Phys. 564 1, 1993. available on: <https://www.nndc.bnl.gov/ensdf>
- [Kelly 2017] J. H. Kelly *et al.*, $^{12}\text{C}(\text{p},\text{p}')$, Nucl. Phys A968, 71, 2017. available on: <https://www.nndc.bnl.gov/ensdf>
- [Ketek 2016] KETEK GmbH, Ketek SiPM Technology, Downloaded from: <http://www.ketek.net/products/sipm-technology/> (August 2016)
- [Ketek 2017] KETEK GmbH, Ketek SiPM Technology, Downloaded from: <https://www.ketek.net/sipm/technology/microcell-construction/> (August 2021)
- [Ketek 2018] KETEK GmbH, Preliminary Product Data Sheet, SiPM-Silicon Photomultiplier, PM3350-WB, 2018.
- [Ketek 2020a] KETEK GmbH, Product Data Sheet, SiPM-Silicon Photomultiplier, PA3325-WB-0808 (REV2020-A), 2020.
Downloaded from: <https://www.ketek.net/wp-content/uploads/2016/12/KETEK-PA3325-WB-0808-Datasheet.pdf> (November 2021).
- [Ketek 2020b] KETEK GmbH, Product Data Sheet, SiPM-Silicon Photomultiplier, PM3315-WB-0808 (REV2020-B), 2020.
- [Ketek 2020c] KETEK GmbH, Product Data Sheet, SiPM-Silicon Photomultiplier, PM3325-WB-0808 (REV2020-A), 2020.
Latest version available from Broadcom Inc. under: <https://www.broadcom.com/products/optical-sensors/silicon-photomultiplier-sipm/afbr-s4k33p6425b> (November 2021)
- [Ketek 2021a] KETEK GmbH, Product Data Sheet, SiPM-Silicon Photomultiplier, WL-series, 2021.
Latest version available from Broadcom Inc. under: <https://www.broadcom.com/products/optical-sensors/silicon-photomultiplier-sipm/afbr-s4k33p6447l> (November 2021)
- [Ketek 2021b] KETEK GmbH, Ketek SiPM Technology, downloaded from: <https://www.ketek.net/sipm/technology/microcell-construction/> (August 2021)
- [Kim 2021] C. Kim. *et al.*, A Review of Inorganic Scintillation Crystals for Extreme Environments, Crystals 11, 669, 2021.
<https://doi.org/10.3390/cryst11060669>
- [Kim 2007] C.-H. Kim *et al.*, Simulation Studies on the Correlation of Distal Dose Fall-off of a 70-MeV Proton Beam with a Prompt Gamma Distribution, Journal of the Korean Physical Society 50, 1510-1513, 2007.

-
- [Kim 2009] D. Kim *et al.*, Pinhole Camera Measurements of Prompt Gamma-rays for Detection of Beam Range Variation in Proton Therapy, Journal of the Korean Physical Society 55, 1673-1676, 2009.
- [Kishimoto 2015] A. Kishimoto *et al.*, Demonstration of three-dimensional imaging based on handheld Compton camera, Journal of Instrumentation 10 P11001, 2015.
DOI: 10.1088/15701748-0221/10/11/P11001
- [Klein Nishina 1929] O. Klein, Y. Nishina, Über die Streuung von Strahlung durch freie Elektronen nach der neuen relativistischen Quantendynamik von Dirac. Z. Physik 52, 853-868, 1929.
<https://doi-org.emedien.ub.uni-muenchen.de/10.1007/BF01366453>
- [Knoll 2010] G.F. Knoll, Radiation detection and measurement, John Wiley & Sons, fourth edition, 2010.
- [Knopf and Lomax 2013] A-C. Knopf and A. Lomax, In vivo proton range verification: a review. Phys. Med. Biol., 58(15):R131-60, 2013
DOI: 10.1088/0031-9155/58/15/R131
- [Kolanoski and Wermes 2016] H. Kolanoski, N. Wermes, Teilchendetektoren, Springer Spektrum, 2016.
DOI: 10.1007/978-3-662-45350-6
- [Kolanoski and Wermes 2020] H. Kolanoski, N. Wermes, Particle Detectors: Fundamentals and Applications, Oxford Scholarship Online, 2020.
DOI: 10.1093/oso/9780198858362.001.0001
- [Kozlovsky 2002] B. Kozlovsky *et al.*, Nuclear Deexcitation Gamma-ray Lines from accelerated particle interactions, Astrophys. Journal 141, 523, 2002.
- [Kozyrev 2016] A. Kozyrev *et al.*, A comparative study of LaBr₃(Ce³⁺) and CeBr₃ based gamma-ray spectrometers for planetary remote sensing applications, Review of Scientific Instruments 87, 085112, 2016.
DOI: 10.1063/1.4958897
- [Krimmer 2015a] J. Krimmer, Development of a Compton camera for medical applications based on silicon strip and scintillation detectors, Nucl. Instrum. Meth. A 787, 98 – 101, 2015.
doi : <http://dx.doi.org/10.1016/j.nima.2014.11.042>.
- [Krimmer 2015b] J. Krimmer, D. Dauvergne, J. Létang and E. Testa, Prompt-gamma monitoring in hadrontherapy: A review. Nucl. Instr. and Meth. A 878, 2017.
DOI: 10.1016/j.nima.2017.07.063
- [Kuntner and Stout 2014] C. Kuntner and D. Stout, Quantitative preclinical PET imaging - opportunities and challenge, Frontiers in Physics 2, 2014.
DOI: 10.3389/fphy.2014.00012

- [Lamprou 2020] E. Lamprou *et al.*, Exploring TOF capabilities of PET detector blocks based on large monolithic crystals and analog SiPMs, *Physica Medica*. 70, 10-18, 2020.
DOI: 10.1016/j.ejmp.2019.12.004
- [Lang 2014] C. Lang *et al.*, Sub-millimeter nuclear medical imaging with high sensitivity in positron emission tomography using $\beta^+\gamma$ coincidences, *Journal of Instrumentation* 9, P01008, 2014.
DOI: 10.1088/1748-0221/9/01/P01008.
- [Lang 2015] C. Lang, Design of a Compton Camera for Medical Imaging and Characterization of its components, Doctoral Dissertation, LMU Munich, 2015.
- [Lawrence 1958] J.H. Lawrence *et al.*, Pituitary irradiation with high-energy proton beams: a preliminary report, *Cancer Res.* 18, 121-34, 1958.
PMID: 13511365
- [Lecoq 2017] P. Lecoq *et al.*, *Inorganic Scintillators for Detector Systems*, Springer International Publishing, eBook ISBN 978-3-319-45522-8, 2019.
- [Lecoq et al 2021] P. Lecoq *et al.*, Roadmap toward the 10 ps time-of-flight PET challenge, *Phys. Med. Biol.* 65 21RM01, 2021
DOI: 10.1088/1361-6560/ab9500
- [Lee 1964] C.A. Lee *et al.*, Ionization Rates of Holes and Electrons in Silicon, *Phys. Rev.* 134 A761, 1964.
- [Lin 2016] H.-H. Lin *et al.*, A comparison of two prompt gamma imaging techniques with collimator-based cameras for range verification in proton therapy, *Radiation Physics and Chemistry* 137, 144-150, 2016.
doi : 10.1016/j.radphyschem.2016.04.020.
- [Liprandi 2018] S. Liprandi, Development and Performance Evaluation of Detectors in a Compton Camera Arrangement for Ion Beam Range Monitoring in Particle Therapy, Doctoral Dissertation, LMU Munich, 2018.
- [Liu and Chang 2011] H. Liu and J.Y. Chang, Proton therapy in clinical practice, *Chin. J. Cancer.* 30, 315-326, 2011.
DOI: 10.5732/cjc.010.10529
- [Litzenberg 1999] D.W. Litzenberg *et al.*, On-line monitoring of radio-therapy beams: experimental results with proton beams, *Med. Phys.* 26, 992-1006, 1999.
- [Llosá 2012] G. Llosá *et al.*, Detector characterization and first coincidence tests of a Compton telescope based on LaBr₃ crystals and SiPMs, *Nucl. Instr.Meth.A* 695, 105-108, 2012.
DOI: 10.1016/j.nima.2011.11.041.

-
- [Llosa 2016] G. Llosá *et al.*, First images of a three-layer Compton telescope prototype for treatment monitoring in hadron therapy, *Frontiers in Oncology* 6, 14, 2016.
DOI: 10.3389/fonc.2016.00014.
- [Lovatti 2020] G. Lovatti *et al.*, An advanced simulation and reconstruction framework for a novel in-beam PET scanner for clinical proton irradiation, Poster presented at the IEEE NSS/MIC conference 2020, M-08-275, 2020.
- [Lozano 2018] I.I.V. Lozano, Prompt gamma imaging based on Compton camera detector systems for range verification in proton therapy treatments, Doctoral Dissertation, LMU Munich, 2018.
- [Lubsandorzhev 2006] B.K. Lubsandorzhev, On the history of photomultiplier tube invention, *Nucl. Inst. Meth. A* 567, 236-238, 2006.
ISSN 0168-9002
- [Maisey 2005] M.N. Maisey, Positron Emission Tomography in Clinical Medicine. In: D.L. Bailey, D.W. Townsend., P.E. Valk, M.N. Maisey (eds) *Positron Emission Tomography*. Springer, London, 2005.
https://doi-org.emedien.ub.uni-muenchen.de/10.1007/1-84628-007-9_1
- [Martins 2021] M. Martins *et al.*, Towards real-time PGS range monitoring in proton therapy of prostate cancer, *Sci. Rep.* 11, 15331, 2021.
<https://doi.org/10.1038/s41598-021-93612-y>
- [Mayerhofer 2017] M. Mayerhofer, Optimizing the spatial resolution of the monolithic LaBr₃ absorbing scintillator of the Garching Compton-camera prototype, Master Thesis, University of Hamburg/LMU Munich, 2017.
- [Maxim 2016] V. Maxim *et al.*, Probabilistic models and numerical calculation of system matrix and sensitivity in list-mode MLEM 3D reconstruction of Compton camera images, *Phys. Med. Biol.* 61, 243, 2016.
- [McCleskey 2015] M. McCleskey *et al.*, Evaluation of a multistage CdZnTe Compton camera for prompt γ imaging for proton therapy, *Nucl. Inst. Meth. A* 785, 163-169, 2015.
<https://doi.org/10.1016/j.nima.2015.02.030>
- [McGowan 2013] S.E. McGowan *et al.*, Treatment planning optimisation in proton therapy, *Br. J. Radiol.* 86 (1021), 20120288, 2013.
- [McIntyre 1985] R.J. McIntyre, Recent developments in silicon avalanche photodiodes, *Measurement* 3, 146-52, 1985.
- [McIntyre 1999] R.J. McIntyre, A new look at impact ionization-Part I: A theory of gain, noise, breakdown probability, and frequency response, *IEEE Trans. Electron. Dev.* 46 1623, 1999.

- [McMaster 2021] McMasters University, Course resources (Mes Phys4R06/6R03): Radioisotopes and Radiation Methodology, Chapter 4: Scintillation Detectors, 2021. available under:
<https://www.science.mcmaster.ca/radgrad/images/6R06CourseResources/4R6Notes4scintillationDetectors.pdf> (November 2021).
- [Melcher 2000] C.L. Melcher, Scintillation Crystals for PET, J. Nucl. Med. 41, 1051-1055, 2000.
- [Miani 2016] A.M. Miani, Determination of the Spatial Resolution of a Monolithic scintillator in a Compton Camera system with MeV range Photons, Master Thesis, Univ. Milano/LMU Munich, 2016.
- [Min 2006] C.-H. Min *et al.*, Prompt Gamma Measurements for Locating the Dose Falloff Region in the Proton Therapy, Applied Physics Letters 89 183517, 2006.
DOI: 10.1063/1.2378561.
- [Min 2008] C.-H. Min *et al.*, Development of an Array-Type Prompt Gamma Detection System for the Online Measurement of the Range of the Proton Beam in a Patient: a Monte Carlo Feasibility Study. Journal of the Korean Physical Society. 52, 888-891, 2008.
DOI: 10.3938/jkps.52.888.
- [Min 2012] C.-H. Min *et al.*, Development of array-type prompt gamma measurement system for in vivo range verification in proton therapy, Med Phys. 39, 2100-7, 2012.
DOI: 10.1118/1.3694098.
- [Mohammadi 2019] I. Mohammadi *et al.*, Minimization of parallax error in positron emission tomography using depth of interaction capable detectors - methods and apparatus, Biomed. Phys. Eng. Express 5, 062001, 2019.
- [Mohan and Grosshans 2017] R. Mohan, D. Grosshans, Proton therapy – Present and future, Advanced Drug Delivery Reviews 109, 26-44, 2017.
<https://doi.org/10.1016/j.addr.2016.11.006>.
- [Moller 1933] Ch. Møller, Zur Theorie des Durchgangs schneller Elektronen durch Materie, Ann. d. Phys. 408, 285-320, 1932.
- [Munoz 2018] E. Muñoz *et al.*, Study and Comparison of different sensitivity models for a two-plane Compton camera, Phys. Med. Biol. 63, 135004, 2018.
- [Munoz 2021] E. Muñoz *et al.*, Proton range verification with MACACO II Compton camera enhanced by a neural network for event selection, Sci. Rep. 11, 9325, 2021.
<https://doi.org/10.1038/s41598-021-88812-5>

-
- [Nakano 2020] T. Nakano *et al.*, Imaging of ^{99m}Tc -DMSA and ^{18}F -FDG in humans using a Si/CdTe Compton camera, *Phys. Med. Biol.* 65, 05LT01, 2020.
- [NCI 2021] National Cancer Institute, 2021. information available at: <https://www.cancer.gov/about-cancer/treatment/types>
- [NIST 2021a] National Institute of Standards and Technologies, available at: <https://physics.nist.gov/PhysRefData/Xcom/html/xcom1.html>, 2021.
- [NIST 2021b] National Institute of Standards and Technologies, PSTAR: Stopping Power and Range Tables for Protons, available at: https://physics.nist.gov/cgi-bin/Star/ap_able.pl, 2021.
- [Nitta 2021a] M. Nitta *et al.*, Development of a depth of interaction PET Detector for Small Animal In-Beam PET Measurements, oral presentation at IEEE NSS/MIC conference 2021, M-09-02, 2021.
- [Nitta 2021b] M. Nitta *et al.*, First in-beam imaging test of a high resolution DOI detector system for the SIRMIO PET scanner, oral presentation at IEEE NSS/MIC conference 2021, M-17-05, 2021.
- [Nobel prize 2021] NobelPrize.org. Nobel Prize Outreach AB 2021. available on <https://www.nobelprize.org/prizes/lists/all-nobel-prizes>, 12 Aug 2021.
- [Newman 1955a] R. Newman, W.C. Dash, R.N. Hall, and W.E. Burch, *Phys.Rev.* 98, 1536(A), 1955.
- [Newman 1955b] R.Newman, Visible Light from a Silicon p-n Junction, *Phys. Rev.* 100, 700, 1955.
<https://doi.org/10.1103/PhysRev.100.700>
- [NRC 2021] United States Nuclear Regulatory Commission, Ionizing radiation, on <https://www.nrc.gov/reading-rm/basic-ref/glossary/ionizing-radiation.html>, 2021.
- [Ootani 2018] W. Ootani, Overview of Readout Techniques for Cryogenic SiPMs, International Conference on the Advancement of Silicon Photomultipliers (Schwetzingen, Germany), Jun 11th - 15th, 2018, downloaded from https://indico.gsi.de/event/6990/contributions/31545/attachments/22643/28404/ICASiPM_OverviewCryoReadout_Ootani.pdf
- [Paganetti 2012] H. Paganetti, Range uncertainties in proton therapy and the role of Monte Carlo simulations, *Phys. Med. Biol.* 57, R99, 2012.
- [Paganetti 2008] H. Paganetti *et al.*, Clinical implementation of full Monte Carlo dose calculation in proton beam therapy, *Phys. Med. Biol.* 53, 4825, 2008.

- [Parodi and Enghardt 2000] K. Parodi and W. Enghardt, Potential application of PET in quality assurance of proton therapy, *Phys. Med. Biol.* 45, N151, 2000.
- [Parodi 2002] K. Parodi *et al.*, In-beam PET measurements of β^+ radioactivity induced by proton beams, *Phys. Med. Biol.* 47 21-36 2002.
- [Parodi 2007] K. Parodi *et al.*, Patient study on in-vivo verification of beam delivery and range using PET/CT imaging after proton therapy, *Int. J. Radiat. Oncol. Biol. Phys.* 68, 920–934, 2007.
- [Parodi 2012] K. Parodi , PET monitoring of hadron therapy, *Nuclear Medicine Review* 15 Suppl. C, C37-42, 2012.
- [Parodi 2015a] K. Parodi, Vision 20/20: Positron emission tomography in radiation therapy planning, delivery, and monitoring, *Med. Phys.* 42, 7153–68, 2015.
DOI: 10.1118/1.4935869
- [Parodi and Assmann 2015] K. Parodi and W. Assmann, Ionoacoustics: A new direct method for range verification, *Modern Physics Letters A* 30, 1540025, 2015.
<https://doi.org/10.1142/S0217732315400258>
- [Parodi and Polf 2018] K. Parodi and J.C. Polf, In vivo range verification in particle therapy, *Med. Phys.* 45, e1036-e1050, 2018.
doi : 10.1002/mp.12960.
- [Parodi 2019] K. Parodi *et al.*, Towards a novel small animal proton irradiation platform: the SIRMIO project, *Acta Oncologica* 58, 1470-1475, 2019.
DOI: 10.1080/0284186X.2019.1630752
- [Pawelke 1997] J. Pawelke *et al.*, In-beam PET imaging for the control of heavy-ion tumour therapy, *IEEE Trans. Nucl. Sci.* 44,1492–1498, 1997.
- [PTCOG 2021] Particle therapy Co-operative group (PTCOG) website: <https://www.ptcog.ch/> (accessed September) 2021, 2021.
- [Peng 2017] Q. Peng *et al.*, Experimental assessments of the timing performances of detectors constructed with LaBr₃, CeBr₃, LFS, LSO, LYSO, GAGG scintillators, *IEEE Nuclear Science Symposium and Medical Imaging Conference (NSS/MIC) 2017*, 1-2, 2017.
DOI: 10.1109/NSSMIC.2017.8532651, .
- [Petsys 2015] PETsys Electronics SA, PETsys TOF ASIC Evaluation Kit, Information Sheet, 2015. available from:
https://www.petsyselectronics.com/web/website/docs/products/product2/Flyer%20E-kit2_V25.pdf (November 2021).

-
- [Petsys 2018] PETsys Electronics SA, High performance TOFPET2 ASIC, product flyer, 2018. available from:
https://www.petsyselectronics.com/web/website/docs/products/product1/Flyer_ASIC2_V18.pdf (November 2021).
- [Petsys 2019] PETsys Electronics SA, TOFPET 2c SiPM readout ASIC datasheet (Rev. 10), 2019.
latest version (Rev. 13) available under (registration required): [https://www.petsyselectronics.com/web/website/documentation/TOFPET2%20Downloads/Documentation/PETsys%20TOFPET%20C%20ASIC%20%20Datasheet%20\(rev%2013\).pdf](https://www.petsyselectronics.com/web/website/documentation/TOFPET2%20Downloads/Documentation/PETsys%20TOFPET%20C%20ASIC%20%20Datasheet%20(rev%2013).pdf)
- [Phelps 1975] M.E. Phelps *et al.*, Application of Annihilation Coincidence Detection to Transaxial Reconstruction Tomography, *Journal of Nuclear Medicine* 16, 210-224, 1975.
- [Pinto 2014] M. Pinto *et al.*, Design optimisation of a TOF-based collimated camera prototype for online hadrontherapy monitoring, *Phys. Med. Biol.* 59, 7653–7674, 2014.
DOI:10.1088/0031-9155/59/24/7653
- [Podgorsak 2010] E.B. Podgorsak, *Radiation Physics for Medical Physicists*, 2nd ed., Springer, 2010.
- [Podgorsak 2005] E.B. Podgorsak (ed), *Radiation Oncology Physics: A Handbook for Teachers and Students*, Vienna: International Atomic Energy Agency, 2005.
- [Polf 2009a] J.C. Polf *et al.*, Prompt gamma-ray emission from biological tissues during proton irradiation: a preliminary study, *Phys. Med. Biol.* 54, 731, 2009.
- [Polf 2009b] J.C. Polf *et al.*, Measurement and calculation of characteristic prompt gamma ray spectra emitted during proton irradiation, *Phys. Med. Biol.* 54, N519, 2009.
- [Pomper and Lee 2005] M.G. Pomper and J.S. Lee, Small animal imaging in drug development, *Curr. Pharm. Des.* 11, 3247–3272, 2005.
- [Quarati 2013] E.G.A. Quarati, Scintillation and detection characteristics of high-sensitivity CeBr₃ gamma-ray spectrometers, *Nucl. Inst. Meth. A* 729, 596-604, 2013.
- [Reddin 2018] J.S. Reddin *et al.*, Performance evaluation of the SiPM based Siemens Biograph vision PET/CT system, In: *IEEE nuclear science symposium and medical imaging conference record*, Sydney, Australia, 2018.
- [Renker 2005] D. Renker, Silicon Photomultipliers, Oral Presentation, slides available at: <http://ndip.in2p3.fr/beam05/cdrom/Sessions/renker.pdf>, 2005.

- [Renker 2006] D. Renker, Geiger-mode Avalanche Photodiodes, history, properties and problems, Nucl. Inst. Meth. A 567, 48-56, 2006.
- [Renker and Lorenz 2009] D. Renker and E. Lorenz, Advances in Solid State Photon Detectors, Journal of Instrumentation 04, P04004-P04004, 2009.
- [Ribberfors 1975] R. Ribberfors, Relationship of the relativistic Compton cross section to the momentum distribution of bound electron states, Physical Review B 12, 2067-2074, 1975.
- [Richter 2016] C. Richter *et. al*, First clinical application of a prompt gamma based in vivo proton range verification system, Radiotherapy and Oncology 118, 232 – 237, 2016.
doi : [http : //dx.doi.org/10.1016/j.radonc.2016.01.004](http://dx.doi.org/10.1016/j.radonc.2016.01.004)
- [Roellinghoff 2011] F. Roellinghoff *et al.*, Design of a Compton camera for 3D prompt-gamma imaging during ion beam therapy, Nucl. Inst. Meth. A, 648 (Supplement 1) S20-S23, 2011.
DOI: 16/j.nima.2011.01.069
- [Rolo 2013] M. D. Rolo *et al.*, TOFPET ASIC for PET applications, Journal of Instrumentation 8, C02050, 2013.
- [ROOT 2021] TCutG Class Reference (ROOT Reference guide), available at [https : //root.cern.ch/doc/master/classTCutG.html](https://root.cern.ch/doc/master/classTCutG.html), 2021.
- [Rutherford 1899] E. Rutherford, Uranium Radiation and the Electrical conduction Produced by it, Philos. Mag. 47, 109, 1899.
- [Sadygov 1998] Z. Sadygov, Avalanche Detector, Russian Agency for Patents and Trademarks, Patent No. RU2102820, 1998.
- [Sadygov 2006] Z. Sadygov *et al.*, Three advanced designs of micro-pixel avalanche photodiodes: Their present status, maximum possibilities and limitations, Nucl. Inst. Meth. A 567 ,70-73 , 2006.
- [Saveliev 1995] V. Saveliev, Avalanche Photodiode on Base of “Needle” Metal Resistor Semiconductor Structures, Proceedings of New Development on Radiation Detectors, 7th European Symposium on Semiconductor Detectors, Schloss Elmau, Germany, May 1995.
- [Saveliev and Golovin 2000] V. Saveliev and V. Golovin, Silicon avalanche photodiodes on the base of metal-resistor-semiconductor (MRS) structures, Nucl. Inst. Meth. Phys. Res. Sec. A, Vol. 442, Issues 1-3, pp. 223-229, 2000.
- [Saveliev 2010] V. Saveliev, Silicon Photomultiplier - New Era of Photon Detection, Advances in Optical and Photonic Devices (Intechopen), 2010.
DOI : 10.5772/7150

- [Saint Gobain 2018] Saint Gobain, Lanthanum Bromide and Enhanced Lanthanum Bromide product data sheet, 2018, downloaded from
<https://www.crystals.saint-gobain.com/sites/imdf.crystals.com/files/documents/lanthanum-material-data-sheet.pdf>
- [Saint Gobain 2020a] Saint-Gobain Crystals, BaF₂ Barium Fluoride Scintillation Materials, 2020.
available at:
<https://www.crystals.saint-gobain.com/sites/imdf.crystals.com/files/documents/barium-fluoride-data-sheet.pdf> (November 2021).
- [Saint Gobain 2020b] Saint-Gobain Crystals, LYSO Scintillation Material, 2020.
available on <https://www.crystals.saint-gobain.com/sites/imdf.crystals.com/files/documents/lyso-material-data-sheet1.pdf>
- [Saint Gobain 2021a] Saint Gobain, Scintillation Products Technical Note-Lanthanum Bromide Scintillators Performance Summary (Revision: June 2021), 2021.
available at:
<https://www.crystals.saint-gobain.com/sites/imdf.crystals.com/files/documents/labr-performance-summary-2021.pdf> (November 2021).
- [Saint Gobain 2021b] Saint-Gobain Webpage, Assembly Materials:
<https://www.crystals.saint-gobain.com/products/assembly-materials>, accessed 6.9.2021, 2021.
- [Schaart 2010] D. R. Schaart *et al.*, LaBr₃:Ce and SiPMs for time-of-flight PET: achieving 100 ps coincidence resolving time, *Phys. Med. Biol.* 55, N179, 2010.
- [Schaart 2021] D. R. Schaart, *Physics and technology of time-of-flight PET detectors*, *Phys. Med. Biol.* 66, 09TR01, 2021.
- [Schall 1996] I. Schall *et al.*, Charge-changing nuclear reactions of relativistic light-ion beams ($5 \leq Z \leq 10$) passing through thick absorbers, *Nucl. Instr. Meth. B* 117, 221, 1996.
- [Schlegel 2018] W. Schlegel, C. P. Karger, O. Jäkel, *Medizinische Physik, Springer Spektrum*, (2018).
ISBN (eBook): 978-3-662-54801-1
- [Schneider 2016] U. Schneider *et al.*, Neutrons in proton pencil beam scanning: parameterization of energy, quality factors and RBE, *Phys. Med. Biol.* 61, 6231–6242, 2016.
- [Schug 2019] D. Schug *et al.*, Initial Measurements with the PETsys TOFPET2 ASIC Evaluation Kit and a Characterization of the ASIC TDC, *IEEE Transactions on Radiation and Plasma Medical Sciences* 3 444-453, 2019.
DOI: 10.1109/TRPMS.2018.2884564.

- [Scionix 2021] Scionix, *High resolution low background CeBr₃ scintillators - application note*, <https://scionix.nl/wp-content/uploads/2017/07/CeBr3-scintillation-detectors.pdf>, 2021.
- [Shibuya 2007] K. Shibuya *et al.*, Annihilation photon acollinearity in PET: volunteer and phantom FDG studies, *Phys. Med. Biol.* 52, 5249, 2007.
- [Shimazoe 2020] K. Shimazoe *et al.*, *Development of simultaneous PET and Compton imaging using GAGG-SiPM based pixel detectors*, *Nucl. Inst. Meth. A* 954, 161499, 2020.
- [Sigmund 1975] P. Sigmund, *Radiation Damage Processes in Materials*, C. duPuy, ed., Noordhoff, Leiden, 3, 1975.
- [Sigmund and Schinner 2020] P. Sigmund and A. Schinner, *The Bloch correction, key to heavy-ion stoppings*, *Journal of Applied Physics* 128, 100903. 2020; <https://doi.org/10.1063/5.0015478>
- [Smeets 2012] J. Smeets *et al.*, Prompt gamma imaging with a slit camera for real-time range control in proton therapy, *Phys. Med. Biol.* 57, 3371, 2012.
- [Smeets 2016] J. Smeets *et al.*, Experimental Comparison of Knife-Edge and Multi-Parallel Slit Collimators for Prompt Gamma Imaging of Proton Pencil Beams, *Radiation Oncology* 6, 156, 2016.
doi : 10.3389/fonc.2016.177300156.
- [Solevi 2016] P. Solevi *et al.*, Performance of MACACO Compton telescope for ion-beam therapy monitoring: first test with proton beams, *Phys. Med. Biol.* 61 5149, 2016.
- [Sysoeva 2002] E. Sysoeva *et al.*, Comparison of the methods for determination of scintillation light yield, *Nucl. Inst. Meth. A* 486, 67–73, 2002.
- [Spieler 2020] H. Spieler, *Electronics Part II*. In: Fleck I., Titov M., Grupen C., Buvat I. (eds), *Handbook of Particle Detection and Imaging*, Springer, Cham. https://doi-org.emedien.ub.uni-muenchen.de/10.1007/978-3-319-47999-6_3-2, 2020.
- [Spieler 2021] H. Spieler, *Analog and Digital Electronics for Detectors*, Physics Division, Lawrence Berkeley National Laboratory, 2021.
available at:
<https://www.desy.de/garutti/LECTURES/ParticleDetectorSS12/spieler.pdf>
(accessed in August 2021)
- [Stock 2018] M. Stock *et al.*, *The technological basis for adaptive ion beam therapy at MedAustron: status and outlook*, *Z Med Phys* 28, 196–210, 2018.
- [Surti 2007] S. Surti *et al.*, Performance of Philips Gemini TF PET/CT Scanner with Special Considerations for Its Time-of-Flight Imaging Capabilities, *Nucl. Med.* 48, 471–48, 2007.

-
- [Surti 2015] S. Surti, Update on time-of-flight PET imaging, *J. Nucl. Med.* 56, 98-105, 2015.
- [Surti and Karp 2016] S. Surti and J.S. Karp, Advances in time-of-flight PET, *Phys. Med* 32, 12-22, 2016.
- [Sutcliffe 1996] J.F. Sutcliffe, A review of in vivo experimental methods to determine the composition of the human body, *Phys. Med. Biol.* 41 791, 1996.
- [Takyu 2017] S. Takyu *et al.*, Development of a DOI-based Compton camera for nuclear medicine applications, IEEE Medical Imaging Conference, M-08-003, Atlanta, 2017.
- [Takyu 2018] S. Takyu *et al.*, Development of a 4-layer DOI TOF-PET detector module with a 6 mm-pitch MPPC array, 2018, IEEE NSS/MIC Proceedings, M-07-035, 2018.
- [Takyu 2020] S. Takyu *et al.*, GAGG-MPPC detector with optimized light guide thickness for combined Compton-PET applications, *Nucl. Inst. Meth. A* 990, 164998, 2020.
DOI: 10.1016/j.nima.2020.164998.
- [Tavernier 2006] S. Tavernier *et al.* (eds.), Radiation Detectors for Medical Applications, 191–207, 2006.
- [Taya 2016] T. Taya *et al.*, First demonstration of real-time gamma imaging by using a handheld Compton camera for particle therapy, *Nucl. Inst. Meth. Phys. Res. A*, 831 355 – 361 (2016), proceedings of the 10th International Hiroshima Symposium on the Development and Application of Semiconductor Tracking Detectors.
doi : [http : //dx.doi.org/10.1016/j.nima.2016.04.028](http://dx.doi.org/10.1016/j.nima.2016.04.028).
- [Teledyne 2021] TELEDYNE LECROY, WaveRunner 6 Zi Oscilloscopes - datasheet, 2021.
downloaded from: [https : //cdn.teledynelecroy.com/files/pdf/waverunner-6zi-datasheet.pdf](https://cdn.teledynelecroy.com/files/pdf/waverunner-6zi-datasheet.pdf) (November 2021).
- [Ter-Pogossian 1975] M.M. Ter-Pogossian *et al.*, A positron-emission transaxial tomograph for nuclear imaging (PET), *Radiology* 114, 89-98, 1975.
doi : 10.1148/114.1.89
- [Thirolf 2014] P. Thirolf *et al.*, Development of a Compton Camera for Online Range Monitoring of Laser-Accelerated Proton Beams via Prompt-Gamma Detection, *EPJ Web of Conferences* 66 11036, 2014.
doi : 10.1051/epjconf/20146611036.
- [Thirolf 2015] P.G. Thirolf *et al.*, Perspectives for highly-sensitive PET-based medical imaging using β^+ - γ coincidences, *Acta. Phys. Pol.* A127, 1441–4, 2015.
- [Thariat 2012] J. Thariat *et al.*, Past, present, and future of radiotherapy for the benefit of patients, *Nat. Rev. Clin. Oncol.* 10, 52-60, 2013.

- [Thorlabs 2018] Thorlabs, LED with Ball Lens, 450 nm datasheet, QTN015134-S01 (Rev B), 2018. available at:
<https://www.thorlabs.com/thorproduct.cfm?partnumber = LED450L> (November 2021).
- [Todd 1974] R.W. Todd *et al.*, A proposed γ camera, *Nature* 251, 132–134, 1974.
<https://doi.org/10.1038/251132a0>
- [Trenn 1976] T. J. Trenn, Rutherford on the Alpha-Beta-Gamma Classification of Radioactive Rays 67, 61-75. Accessed August 1, 2021.
<http://www.jstor.org/stable/231134>, 1976.
- [Tschurlovits 2021] M. Tschurlovits, What is "*ionizing radiation*", downloaded from
<https://www.osti.gov/etdweb/servlets/purl/593131> (August 2021).
- [Tsang 1985] W.T. Tsang (Ed), Semiconductors and Semimetals: Lightwave Communication Technology, Part D, Photodetectors, Tsang W. T. (Ed), 1 309, Academic Press Inc., 978-0-12752-153-4, 1985.
- [Uenomachi 2021] M. Uenomachi *et al.*, Simultaneous in vivo imaging with PET and SPECT tracers using a Compton-PET hybrid camera, *Sci. Rep.* 11, 17933, 2021.
<https://doi.org/10.1038/s41598-021-97302-7>
- [Urakabe 2001] E. Urakabe *et al.*, Spot scanning using radioactive ^{11}C beams for heavy-ion radiotherapy, *Japanese Journal of Applied Physics, Part 1: Regular Papers and Short Notes and Review Papers* 40, 2540-2548, 2001.
- [vanDam 2011] H. T. van Dam *et al.*, Improved Nearest Neighbor Methods for Gamma Photon Interaction Position Determination in Monolithic Scintillator PET Detectors, *IEEE Transactions on nuclear Science* 58, 2139-2147, 2011.
- [vanSluis 2019] J. van Sluis *et al.*, Performance characterization of the digital Biograph Vision PET/CT system, *J. Nucl. Med.* 60, 1031-1036, 2019.
- [Vedia 2015] V. Vedia *et al.*, Enhanced time response of 1-in. LaBr₃(Ce) crystals by leading edge and constant fraction techniques, *Nucl. Instrum. Methods Phys. Res. A.*, Vol. 795, 2015.
DOI: 10.1016/j.nima.2015.05.058
- [Vedia 2017] V. Vedia *et al.*, Performance evaluation of novel LaBr₃(Ce) scintillator geometries for fast-timing applications, *Nucl. Inst. Meth. A* 857, 98-105, 2017.
<https://doi.org/10.1016/j.nima.2017.03.030>.
- [Verburg 2012] J.M. Verburg *et al.*, Simulation of prompt gamma-ray emission during proton radiotherapy, *Phys. Med. Biol.* 57, 5459 (2012)

-
- [Verhey 1999] L.J. Verhey, Comparison of three-dimensional conformal radiation therapy and intensity-modulated radiation therapy systems, *Seminars in Radiation Oncology*, Volume 9, Issue 1, pp. 78-98, 1999.
[https://doi.org/10.1016/S1053-4296\(99\)80056-3](https://doi.org/10.1016/S1053-4296(99)80056-3).
- [Viegas 2018] R. Viegas Bothelho Correia Rego, Development and Performance Evaluation of Detectors in a Compton Camera Arrangement for Ion Beam Range Monitoring in Particle Therapy, M.Sc. Thesis, Munich Univ. Coimbra (Portugal)/ LMU Munich, 2018.
- [Viegas 2020] R. Viegas Bothelho Correia Rego, Private conversation on personal contact with PETsys engineers, 2020.
- [Viegas 2021] R. Viegas Bothelho Correia Rego, MACACOp Compton Camera: performance improvement and tests at high photon energies, *IEEE Medical Imaging Conference 2021*, Contribution: M15-354, 2021.
- [Vinogradov 2015] S. Vinogradov, The Silicon Photomultiplier (SiPM) Concept and Design Development,
available at:
<https://www.appec.org/news/the-silicon-photomultiplier-sipm-concept-and-design-development>, 2015.
- [Watanabe 2018] T. Watanabe *et al.*, Development of an omnidirectional gamma-ray imaging Compton camera for low-radiation-level environmental monitoring, *Jpn. J. Appl. Phys.* 57, 026401, 2018.
- [Weber 2021] G. Weber, Compton scattering calculator, available at:
https://web-docs.gsi.de/stoe_exp/web_programs/compton/index.php, accessed September 2021, 2021.
- [Weber 2002] M. J. Weber, Inorganic scintillators: today and tomorrow, *Journal of Luminescence* 100, 35-45, 2002.
- [Wermes 2020] N. Wermes, Signal Formation and Signal Processing in Detectors, Lectures at the University of Freiburg, Lecture 2, 2002.
available at :
<https://www.grk2044.uni-freiburg.de/dateien/dateien/wermes-freiburg-lecture-2.pdf>
- [WHO 2020] World Health Organisation, WHO report on cancer: setting priorities, investing wisely and providing care for all, Geneva: World Health Organization, (License: CC BY-NC-SA 3.0 IGO), 2020.
- [Wilson 1946] R.R. Wilson, Radiological use of fast protons, *Radiology* 47, 487-91, 1946.
DOI: 10.1148/47.5.487.

- [Yamamoto 1984] Y.L. Yamamoto, Positron emission tomography, *Radiation Physics and Chemistry* 24, 385-403, 1984.
[https://doi.org/10.1016/0146-5724\(84\)90075-X](https://doi.org/10.1016/0146-5724(84)90075-X).
- [Yoshida 2020] E. Yoshida *et al.*, Whole gamma imaging: a new concept of PET combined with Compton imaging, *Phys. Med. Biol.* 65, 125013, 2020.
- [Zanzonico 2004] P. Zanzonico, Positron emission tomography: a review of basic principles, scanner design and performance, and current systems, *Seminars in Nuclear Medicine* 34, 87-111, 2004.
<https://doi.org/10.1053/j.semnuclmed.2003.12.002>.
- [Ziegler 1977] J. F. Ziegler *et al.*, *The Stopping and Ranges of Ions in Matter*, New York: Pergamon Press 1977.
- [Ziegler 1999] J. F. Ziegler, The Stopping of Energetic Light Ions in Elemental Matter, *J. Appl. Phys / Rev. Appl. Phys.*, 85, 1249-1272, 1999.
- [Zhou 2020] Y.J. Zhou, A Detailed Study of the Energy Resolution of a Compton Camera Prototype, Bachelor Thesis, LMU Munich, 2020.
- [Zoglauer 2005] A.C. Zoglauer, *First Light for the Next Generation of Compton and Pair Telescopes*, Doctoral Dissertation, Technical University of Munich, 2005.
- [Zoglauer 2008] A.C. Zoglauer *et al.*, MEGALib - Simulation and data analysis for low-to-medium-energy gamma-ray telescopes, *Proceedings of SPIE - The International Society for Optical Engineering*. 7011, 2008.
DOI: 10.1117/12.789537.
- [Zoglauer 2021] A.C. Zoglauer, MEGALib - The Medium-Energy Gamma-ray Astronomy library website:
<https://megalibtoolkit.com/documentation.html> (accessed September 2021), 2021.

Acknowledgement

I want to thank my family, friends and colleagues who contributed to this work by supporting me in many different ways over the course of the past

four years.

Thank you,...

... **Peter Thirof** for your continuous support. No matter at which time, I could always come to you for professional advice or personal conversations. You showed me how to achieve goals with passion and dedication.

... **Erin Grace** for your support in any situation. You give me strength everyday and in any situation of life!

... **Florian Schneiders** for introducing me to the topic of scintillation detectors. I could always come to you for (personal and professional) advise and discussion. Thank you for being my friend!

... **Katia Parodi** for supporting my work and giving me the chance to work in an international environment together with excellent scientists on various international projects.

... **Silvia Liprandi and Saad Aldawood**. This work would not have been possible without you. Thank you for the years of inspiring work in the laboratory and fun times in our office and especially at late night shifts during beamtimes.

... **Franz Engelbrecht** for being my friend in any situation!

... **Benedict Seiferle, Lars von der Wense, Kevin Scharl and Daniel Moritz** for all our very early lunch breaks and enjoyable times.

... **Munetaka Nitta, Mohammad Safari and Giulio Lovatti** for many fruitful discussions, your advice and help with the setup and/or image reconstruction and especially for the fun times during our two beamtime campaigns at GSI.

... **all students working with me over the past four years, Rita Viegas, Maria Kawula, Giovanni Vinci, Henning Geesmann, Yuzhen Zhou, Max Brünger, Jonas Schaible and Alexander Weinzierl**. I enjoyed the times with you and could learn a lot from you.

Silvia Wallner and Reinhard Fojt for supporting the collaboration between KETEK and the LMU Chair for Medical Physics. I am grateful that I could write my B.Sc, M.Sc. and my PhD thesis with KETEK.

... **all colleagues and friends from KETEK, Florian Wiest, Peter Iskra, Thomas Ganka, Eugen Engelmann, Ralph Brandmeier** for your support over the past eight years during my Bachelor's and Master's studies and finally my PhD the-

sis.

... all colleagues and friends from the Chair for Medical Physics

Kenji Shimazoe for many fruitful meetings and to a joint measurement campaign.

... my family and friends who supported me over the past ten years of my studies.

You always motivated me in times of doubts. You all contributed to this work as much as all my colleagues did.

... Opa, du warst immer da für mich und darum tut es umso mehr weh,
dass du in den beiden größten Momenten in meinem Leben nicht hier sein
hast können. Ich vermisse dich!